UNIVERSITY OF CALIFORNIA SAN DIEGO

Many-Body Approaches Towards Elevating Pure and Hybrid *Ab-Initio* Simulations

A dissertation submitted in partial satisfaction of the
requirements for the degree
Doctor of Philosophy

in

Chemistry

by

Eleftherios A.P. Lambros

Committee in charge:

Professor Francesco Paesani, Chair
Professor Micheal Galperin
Professor Shyue Ping Ong
Professor John Weare
Professor Mark Young

2022

The dissertation of Eleftherios A.P. Lambros is approved, and it is acceptable in quality and form for publication on microfilm and electronically.

University of California San Diego

2022

DEDICATION

To my plants

EPIGRAPH

Test

—Teri

TABLE OF CONTENTS

LIST OF FIGURES

LIST OF TABLES

ACKNOWLEDGEMENTS

Thanks to Blue Pepper, Tapioca Express, and to the Price Center Target.

A first and foremost thanks goes to my advisor, Professor Francesco Paesani, whose guidance and support has helped me develop into a better scientist and a better person. Thank you for being such an amazing mentor and pushing on through times thick and thin, and for not giving up on me during the lowest and hardest points during these years.

I'd also like to extend a thanks Dr. Andrés Cisneros and Dr. Filippo Lipparini for helping implement the QM/MB-pol scheme in LICHEM and Gaussian, as well as Dr. John Perdew for his assistance in our study for DC-SCAN. To my colleages at UCSD, I want to thank Dr. Andreas Götz for his wonderful advice particularly in the beginning of my time at UCSD. A heartfelt thanks goes to Dr. Colin Egan, Dr. Marc Riera, Kartik Lakshmi, Kelly Hunter, Etienne Palos, Dr. Saswata Dasgupta, Alessandro Caruso, Ching-Hwa Ho, Hilliary Frank, Graham Griffin, Yaoguang Zhai, Yuanhui Pan, Dr. Sigbjørn Bore, Dr. Vinicius Cruziero, Dr. Raja Ghosh, Ruihan Zhou, Henry Agnew, Cianna Calia, Ethan Bull-Vulpe, Xuanyu Zhu, Richa Rashmi, as well as to my wonderful students Jie Hu and Steven Swee.

A great heap of thanks goes to my friends and family, without whose support I would not have succeded. To my sister Alexandra, my mother Mary, my father John, and to my great friends Raphael, Anthony, Dimitri, Kamyar, and the many others along the way who I have not mentioned, I would not have made it without you.

Chapter 2 is in full a reprint of the material as it appears in "Lambros, E., & Paesani, F. (2020). How good are polarizable and flexible models for water: Insights from a many-body perspective. *The Journal of Chemical Physics*" The dissertation author was the primary author of this paper.

Chapter 3 is in full a reprint of the material as it appears in "Lambros, E., Lipparini, F., Cisneros, G. A., & Paesani, F. (2020). A Many-Body, Fully Polarizable Approach to QM/MM

Simulations. *Journal of Chemical Theory and Computation*" The dissertation author was the primary author of this paper.

Chapter 4 is in full a reprint of the material as it appears in "Lambros, E., Dasgupta, S., Palos, E., Swee, S., Hu, J., & Paesani, F. (2021). General many-body framework for data-driven potentials with arbitrary quantum mechanical accuracy: Water as a case study. *Journal of Chemical Theory and Computation*" The dissertation author was the co-primary author of this paper.

Chapter 5 is in full a reprint of the material as it appears in "Lambros, E., Hu, J., & Paesani, F. (2021). Assessing the accuracy of the SCAN functional for water through a many-body analysis of the adiabatic connection formula. *Journal of Chemical Theory and Computation*" The dissertation author was the primary author of this paper.

Chapter 6 is in full a reprint of the material as it appears in "Dasgupta, S., Lambros, E., Perdew, J., & Paesani, F. (2021). Elevating Density Functional Theory to Chemical Accuracy for Water Simulations through a Density-Corrected Many-Body Formalism. *Nature Communications*" The dissertation author was the co-primary author of this paper.

VITA

2017	B. S. in Mathematics, University of California Irvine
2017	B. S. in Biochemistry and Molecular Biology, University of California Irvine
2022	Ph. D. in Chemistry and Biochemistry, University of California San Diego

PUBLICATIONS

Greene, D. A., Botello-Smith, W. M., Follmer, A., Xiao, L., **Lambros, E.**, & Luo, R. (2016). Modeling membrane protein–ligand binding interactions: the human purinergic platelet receptor. *The Journal of Physical Chemistry B*

Riera, M., **Lambros, E.**, Nguyen, T. T., Götz, A. W., & Paesani, F. (2019). Low-order many-body interactions determine the local structure of liquid water. *Chemical science*

Lambros, E., & Paesani, F. (2020). How good are polarizable and flexible models for water: Insights from a many-body perspective. *The Journal of Chemical Physics*

Lambros, E., Lipparini, F., Cisneros, G. A., & Paesani, F. (2020). A Many-Body, Fully Polarizable Approach to QM/MM Simulations. *Journal of Chemical Theory and Computation*

Cruzeiro, V. W. D., **Lambros, E.**, Riera, M., Roy, R., Paesani, F., & Götz, A. W. (2021). Highly accurate many-body potentials for simulations of N2O5 in water: Benchmarks, development, and validation. *Journal of Chemical Theory and Computation*

Lambros, E., Hu, J., & Paesani, F. (2021). Assessing the accuracy of the SCAN functional for water through a many-body analysis of the adiabatic connection formula. *Journal of Chemical Theory and Computation*

Lambros, E., Dasgupta, S., Palos, E., Swee, S., Hu, J., & Paesani, F. (2021). General many-body framework for data-driven potentials with arbitrary quantum mechanical accuracy: Water as a case study. *Journal of Chemical Theory and Computation*

Dasgupta, S., **Lambros, E.**, Perdew, J., & Paesani, F. (2021). Elevating Density Functional Theory to Chemical Accuracy for Water Simulations through a Density-Corrected Many-Body Formalism. *Nature Communications*

Gartner III, T.E., Hunter, K.M., **Lambros, E.**, Caruso, A., Riera, M., Medders, G.R., Panagiotopoulos, A.Z., Debenedetti, P.G., & Paesani, F. (2021). The Anomalies and Local Structure of Liquid Water from Many-Body Molecular Dynamics Simulations. *The Journal of Physical Chemistry Letters*

Palos, E., **Lambros, E.**, Swee, S., Hu, J., Dasgupta, S., & Paesani, F. (2022). Assessing the Interplay Between Functional-Driven and Density-Driven Errors in DFT Models of Water. *Journal of Chemical Theory and Computation*

Palos, E., **Lambros, E.**, Dasgupta, S., & Paesani, F. (2022). Density Functional Theory of Water with a Machine Learned Functional: A Many-Body Analysis of the DM21 Functional. *The Journal of Chemical Physics*

ABSTRACT OF THE DISSERTATION

Many-Body Approaches Towards Elevating Pure and Hybrid *Ab-Initio* Simulations

by

Eleftherios A.P. Lambros

Doctor of Philosophy in Chemistry

University of California San Diego, 2022

Professor Francesco Paesani, Chair

A precise and accurate description of the fundamental interactions between molecules in solution is imperative to develop models that represent chemical reactions in solutions at a predictive level. Here, we develop a set of many-body approaches which elevate the accuracy of both hybrid QM/MM and pure *ab-initio* methods. In order to address the boundary discontinuity problem in QM/MM simulations, where because the QM and MM regions are represented by two different potential energy surfaces, there is an energetic discontinuity at the QM/MM boundary, a generalized MB-QM model trained to the specific level of theory used in the QM region is chosen to represent the MM region. Using this scheme, the entire QM/MM system is treated under the same numerically ”effective” Hamiltionian, just with different analytical representations

in the QM and MM regions, in essence, describing the entire system at a full *ab-initio* level of accuracy at the cost of a much cheaper QM/MM calculation. Finally, in a separate vein, after characterizing the effects of exact exchange for aqueous systems using hybrid SCAN functionals derived from the adiabatic connection formula, DC-SCAN, which evaluates the SCAN functional on the Hartree-Fock density, is developed. This density corrected functional is shown to provide gold-standard CCSD(T)/CBS level of accuracy for aqueous systems at the computational cost of a Hartree-Fock calculation, and represents the first DFT based model which is able to quantitatively represent the structural and energetic properties of water from the gas to condensed phases.

Chapter 1

Introduction

Challenges in contemporary aqueous chemistry include the control of chemical reactions in bulk solutions and interfaces and the ability to predictively model physiochemical properties and transformations which span many orders of magnitude in size, from molecular scale hydrogen bond rearrangements in the microscopic regime to macroscopic fluid flows. Towards this end, a precise description of chemical processes in solution requires an accurate account of the interactions between the various chemical species in aqueous solutions, multi-component mixtures, and other complex condensed-phase systems. For chemical reactions, chemical transformations like bond rearrangements, steric orientation, and the electronic structure of the reactive species in solution must be accurately represented, and the ability to reliably control and predict the corresponding structures, phases, and reactivities which emerge in these fluid environments necessitates a fundamental understanding of the underlying interactions between the individual components of these systems.

At the smallest scales, individual molecules with a small number of electrons can be modeled using purely quantum mechanical (QM) methods, which find approximate solutions to Schrödinger's equation and are used to calculate the electronic structure of a group of atoms. Correlated *ab-initio* methods like configuration interaction (CI)[7] or coupled cluster (CC)[8, 9]

are of the most accurate methods available, with coupled cluster with singles, douples, and perturbative triples (CCSD(T)) regarded as the gold standard for electronic struture calculations. These methods recover almost all of the exact energy of the system due to their explicit description of electronic correlation. More efficient methods like 2^{nd} order Møller-Plesset perturbation theory[10, 11] and density functional theory (DFT)[12, 13] can be used to simulate larger systems, which can reach on the order of hundreds of atoms, with DFT being particularly efficient in this regard.

Extended systems with periodic conditions in the condensed phase such as bio-molecular complexes in solution, liquid water, and crystalline solids including metal-organic frameworks (MOFs) are prohibitively large for treatment by purely QM methods and so are treated with force-fields (FFs) whose simpler analytic form is only crudely accurate, but allows for orders-of-magnitude faster evaluation than QM techniques. FFs are built upon a formalism of inter and intramolecular interactions which does not explicitly account for the electrons in the systems and therefore cannot model the electronic structure of the system. Despite these limitations, FFs are useful for simulating large systems over extended timescales inaccessible to pure QM methods, and can therefore be used to calculate time dependent and thermodynamic quantities including diffusion coefficients, free energies, and densities among many others within a defined statistical ensemble.

In actual practice, a combination of traditional FF's, *ab-initio* DFT, and a new classes of machine learned models have been used to study aqueous and other condensed phase systems. While the physics of such large systems are most efficiently studied by classical molecular mechanics models due to their large size and need for extended sampling over long timescales, owing to their relative efficiency over other *ab-inito* methods and higher accuracy over simple FFs, a variety of density functional approximations (DFAs) have been used to study the condensed phase physics of aqueous systems with the SCAN density functional [14] recently gaining traction in this area.[15–18] In a similar vein, Machine learned models trained on *ab-initio* data have

emerged as viable models to study both gas and condensed phase systems. [19–29] These models, which seek to retain the accuracy of the data to which they are trained while offering a computational cost similar to that of a traditional FF, have been consequently extended to study condensed phase systems in the place of raw *ab-intio* calculations, with many such potentials being trained on the SCAN functional and its hybrids to study liquid water and ice. [5, 30–32]

In situations where neither QM methods nor FFs can be used on their own, hybrid quantum mechanics / molecular mechanics (QM/MM) schemes are used. These schemes, which treat a small subsytem according to QM and the rest of the system using a FF, are useful for modelling reactive systems embedded within a larger environment. This can range from relatively simple systems such as a reactive complex in solution[33] to more intricate systems like an active site embedded in a larger protein or a catalytic center on a material.[34–36] QM/MM simulations are necessary for these sorts of systems as the electronic structure of the subsystem needs to be solved in order to understand bond rearrangements, orbital properties, and electronic excitations which be described by a FF, but where the size of the extended environment prohibits a full quantum mechanical treatment.

1.1 Overview

This dissertation will focus on the development of many-body approaches to QM/MM simulations, as well as a simple scheme to drastically raise the accuracy of certain density functionals. Chapter 2 overviews a characterization of contemporary polarizable water models in the context of the many-body expansion, and shows that many such popular models suffer from severe error cancellation between their many-body terms, so that while those models predict qualitatively correct energetic, structural, and thermodynamic properties, they are getting the right answers for the wrong reasons. It is also highlighted in this work, although a great deal of progress has been made in this field, particularly with more advanced models such as AMOEBA+CF

which don't suffer from the same error cancellation that plagued their predecessors, the simple functional forms adopted by these models inhibit a quantitative description of the entire energy landscape.

Chapter 3 introduces a many-body approach to fully polarizable QM/MM simulations, where by using a many-body model trained to reproduce the potential energy surface of the specific level of theory used in the QM region, boundary discontinuities between the QM and MM regions can be suppressed, treating the entire system consistently under the same "effective" Hamiltonian, just with different representations in the QM and MM regions. Importantly, this allows for the system to be represented at a full *ab-initio* level of accuracy at the cost of a QM/MM simulation. Also covered in this chapter is the effect of using a fully self consistent polarizable embedding over a partially self consistent implementation, where it is shown that while a fully self-consistent cross polarization between the QM and MM regions is certainly more ideal, the partially self-consistent polarizable embedding performs quite well, recovering most of the polarization energy for small systems.

In chapter 4, the many-body models introduced in chapter 3 are generalized so that all of their non-fitted parameters are derived from a specific level of theory so that in a QM/MM implementation, the underlying QM/MM electrostatics are as close to the pure QM representation as possible. More importantly, we show that in particular certain density functionals, particularly GGAs, are not amenable to be captured by our many-body models. These functionals have large density driven errors and often suffer from severe electronic over-delocalization, leading to larger magnitude higher-order terms which cannot be adequately captured by the classical polarization used in our models for those terms. It is shown that using density corrected versions of such functionals drastically reduces the amount of error in the higher order terms, making them much more amenable to reproduction by our many-body models.

Finally, chapters 5 and 6 cover new developments in raising the accuracy of the SCAN functional through the incorporation of Hartree-Fock exchange. In chapter 5, the fraction of

Hatree-Fock exchange using in SCAN hybrids is modulated in order to tune the energetic and structural properties of gas and condensed phase water. Contrary to the value of 25% HF exchange used in the SCAN0 hybrid functional, we show that a value closer to that of 15% is much more optimal for reproducing the structure of liquid water. In chapter 6, building off the information from chapters 4 and 5, shows that by simply evaluating the SCAN functional on the Hartree-Fock density, SCAN can recover CCSD(T) level accuracy. This not only hold for the energetics of small clusters, but extends to the structural and thermodynamic properties of water in the condensed phase, and represents the first DFT based model that can quantitatively reproduce the properties of water from the gas to condensed phases.

1.2 Many-Body Formalism and the MB-pol model

Irrespective of the method used to analyze the system, within the many-body formalism, the total potential energy of a system can expressed in a many-body expansion (MBE), which partitions the energy of a system as the sum of individual n-body contributions in a system of N molecules with $n \leq N$.[37–39]

This expansion is formally expressed as:[40]

$$E_N(r_1,..,r_N) = \sum_{i=1}^{N} \varepsilon_{1B}(r_i) + \sum_{i<j}^{N} \varepsilon_{2B}(r_i,r_j) + \sum_{i<j<k}^{N} \varepsilon_{3B}(r_i,r_j,r_k) + ... + \varepsilon_{NB}(r_1,..,r_N) \qquad (1.1)$$

where ε_{1B} is the distortion energy of an individual molecule, and where ε_{nB} with $n > 1$ are the n-body energies which are defined recursively as:

$$\varepsilon_{nB} = \varepsilon_n(1,...,n) - \sum_{i=1}^{N} \varepsilon_{1B}(r_i) - \sum_{i<j}^{N} \varepsilon_{2B}(r_i,r_j) - \sum_{i<j<k<...<n-1}^{N} \varepsilon_{(n\text{-}1)B}(r_i,r_j,..r_{n-1}). \qquad (1.2)$$

This expansion converges quickly for molecules with large band gaps and localized electron densities such as water, and most other conventional small molecules, with the 2-body

and 3-body energies composing ∼90-95% of the total interaction energy.[41–44] Models based on the MBE exploit its low order convergence, explicitly representing the first few terms at a high level of accuracy, and either truncating the higher order terms, or representing them implicitly with a simpler description.

With respect to water, there have been a number of previously developed explicit many-body models [45], as well as many implicit many-body models which use classical polarization to capture the higher order terms in the MBE such as the TTM type models[46–53], and the well known AMOEBA family of potentials. [54–60] The MB-pol[37–39], MB-DFT[61], and generalized MB-nrg[62, 63] models include explicit representations for the first three terms of the MBE, while all higher order, $n > 3$ body terms, are implicitly accounted for through a classical polarization term,

$$E_N(r_1,..,r_N) = \sum_{i=1}^{N} \varepsilon_{1B}(r_i) + \sum_{i>j}^{N} \varepsilon_{2B}(r_i,r_j) + \sum_{i>j>k}^{N} \varepsilon_{3B}(r_i,r_j,r_k) + E_{pol} \tag{1.3}$$

The 1B term represents the energy required to distort a molecule from its equilibrium configuration. In MB-pol, this is represented by the Partridge-Schwenke potential energy surface[64], which is parameterized using the high-level multi-reference configuration interaction (MRCI) level of theory, while in the more generalized MB-nrg potentials[62, 63], this term is represented using a permutationally invariant polynomial (PIP)[65] fit to an arbitrary level of theory. The 2-body term is written as:

$$\varepsilon_{2B} = E_{2B}^{sr} + E_{elec} + E_{disp} \tag{1.4}$$

where E_{2B}^{sr} is a 4^{th}-degree PIP[65] which represents short-range quantum mechanical interactions within a water dimer. E_{elec} is represented by Coulomb interactions between geometry dependent point charges which reproduce the *ab initio* dipole moment surface of a water molecule. [64] The

2-body dispersion interaction is written as

$$E_{disp} = -\sum_{i,j} f(\delta_{ij}) \frac{C_{6,ij}}{R_{ij}^6} \tag{1.5}$$

where i and j are indices for atoms on two water monomers, $f(\delta_{ij})$ is the Tang-Toennies damping function with a fitted damping parameter δ_{ij},[66] and $C_{6,ij}$ are the dispersion coefficients calculated from the asymptotic reference energies of the water dimer as in CC-pol.[45] The 3-body interactions are represented by an explicit short range 4^{th}-degree PIP[65]:

$$\varepsilon_{3B} = E_{3B}^{sr} \tag{1.6}$$

In MB-pol, the 2B and 3B terms are fitted on top of the core electrostatic and dispersion components, to recover the CCSD(T) level of theory,[37, 38], though these can be fit, in principle, to an arbitrary level of theory.[61]

Chapter 2

How good are polarizable and flexible models for water: Insights from a many-body perspective

We present a systematic analysis of state-of-the-art polarizable and flexible water models from a many-body perspective, with a specific focus on their ability to represent the Born-Oppenheimer potential energy surface of water, from the gas to the liquid phase. Using coupled cluster data in the completed basis set limit as a reference, we examine the accuracy of the polarizable models in reproducing individual many-body contributions to interaction energies and harmonic frequencies of water clusters, and compare their performance with that of MB-pol, an explicit many-body model that has been shown to correctly predict the properties of water across the entire phase diagram. Based on these comparisons, we use MB-pol as a reference to analyze the ability of the polarizable models to reproduce the energy landscape of liquid water at ambient conditions. We find that, while correctly reproducing the energetics of minimum-energy structures, the polarizable models examined in this study suffer from inadequate representations of many-body effects for distorted configurations. To investigate the role played by geometry-

dependent representations of 1-body charge distributions in reproducing coupled cluster data for both interaction and many-body energies, we introduce a simplified version of MB-pol that adopts fixed atomic charges and demonstrate that the new model retains the same accuracy as the original MB-pol model. Based on the analyses presented in this study, we believe that future developments of both polarizable and explicit many-body models should continue in parallel and would benefit from synergistic efforts aimed at integrating the best aspects of the two theoretical/computational frameworks.

2.1 Introduction

Since the early days of computer simulations, molecular models of water have provided the scientific community with a means of investigating aqueous environments at the microscopic level.[67, 68] Despite significant progress achieved in the last two decades, the accurate prediction of the molecular properties of water across the entire phase diagram remains an outstanding challenge, with the overall predictive power of any computer simulation heavily depending on the accuracy with which the underlying model is able of representing the interactions between water molecules.[69–72]

Starting from the seminal work by Bernal and Fowler[73] and taking advantage of increasing computational power, the field of computer simulations of water has witnessed the continued development of progressively more sophisticated models. Early models, such as ST2,[74] and the subsequent TIPnP [75–77] and SPC* [78] families of models, have been instrumental in shedding light on the structural, thermodynamic and dynamical properties of liquid water at the molecular level. These models adopt relatively simple functional forms, representing the water molecules as rigid bodies, and describe electrostatic interactions via Coulomb potentials between effective atomic point charges, and repulsive and dispersion interactions via Lennard-Jones potentials.[69–72]

Motivated by the recognition of the importance of many-body effects in determining the properties of the hydrogen-bond network, several models have been developed building upon the many-body expansion (MBE) of the total energy, E_N, which is expressed as[40]

$$E_N(r_1,..,r_N) = \sum_{i=1}^{N} \varepsilon_{1B}(r_i) + \sum_{i<j}^{N} \varepsilon_{2B}(r_i,r_j) + \sum_{i<j<k}^{N} \varepsilon_{3B}(r_i,r_j,r_k) + ... + \varepsilon_{NB}(r_1,..,r_N) \qquad (2.1)$$

where N is the number of water molecules and r_i collectively denotes the coordinates of the oxygen (O) and hydrogen (H) atoms of the i-th water molecule. Eq. 6.4 shows that E_N can be rigorously obtained by summing all contributions due to individual n-body energies, with the 1-body energy, ε_{1B}, representing the deformation energy of a water monomer (which is set to zero for rigid models) and ε_{nB} corresponding to the n-body energies defined recursively as

$$\varepsilon_{nB} = \varepsilon_n(1,...,n) - \sum_{i=1}^{N} \varepsilon_{1B}(r_i) - \sum_{i<j}^{N} \varepsilon_{2B}(r_i,r_j) - \sum_{i<j<k<...<n-1}^{N} \varepsilon_{(n\text{-}1)B}(r_i,r_j,..r_{n-1}) \qquad (2.2)$$

From Eqs. 6.4 and 5.7, it follows that the interaction energy, E_{int}, between N water molecules can be expressed as

$$E_{int} = E_N(r_1,..,r_N) - \sum_{i=1}^{N} \varepsilon_{1B}(r_i) \qquad (2.3)$$

In polarizable models, all many-body energies, from ε_{3B} to ε_{NB} in Eq. 6.4 are effectively accounted for by a single term representing classical many-body polarization.[79] Building upon the pioneering work by Kollman and coworkers,[80] several polarizable water models, with different degrees of sophistication, have been developed and used in molecular dynamics (MD) and Monte Carlo (MC) simulations of aqueous systems. [43, 46–57, 59, 60, 81–108] Among the most popular polarizable water models, which takes into account monomer flexibility, are the TTM[47–53] and AMOEBA[54–57, 59, 60] families.

The TTM models are based on Thole's polarization schemes[109] and were primarily fitted to *ab initio* data for small water clusters.[46–53] The development of the TTM models began

with the parameterization of a polarizable model derived from *ab initio* data for the water dimer, which was then used to investigate the properties of water clusters and ice.[46] A subsequent analysis of the water dimer potential energy surface (PES) demonstrated that models that were able to more closely reproduce the *ab initio* PES were also able to more accurately reproduce the experimental second virial coefficient.[47] Starting from the polarizable model of Ref. 46, the TTM2-R model,[49] a polarizable model of water with rigid monomers, was developed to reproduce the *ab initio* dimer PES of Ref. 47. TTM2-R was shown to reproduce both gas-phase properties and *ab initio* data calculated at the second-order Møller-Plesset (MP2) level of theory in the complete basis set (CBS) for small water clusters, as well as several bulk properties, including the diffusion coefficient and the radial distribution functions (RDFs) of liquid water, and the lattice constants of ice I_h.[49] Building upon the TTM2-R parameterization, the TTM2-F model[50] and its refined TTM2.1-F version[51] were the first flexible water models to adopt a highly accurate 1-body term rigorously derived from high-level *ab initio* potential energy and dipole moment surfaces reported for an isolated water molecule reported in Ref. 64. While maintaining the same level of accuracy as TTM2-R in reproducing several properties of water,[110–113] TTM2-F and TTM2.1-F were the first models able to correctly predict the widening of the HOH angle going from small gas-phase clusters to liquid water and ice.[114] Subsequent developments led to two distinct TTM models, TTM3-F[52] and TTM4-F[53], which were parameterized with specific focus on reproducing the dynamical properties and vibrational spectra of water. Both TTM3-F and TTM4-F were shown to provide better agreement with the experimental infrared spectra of liquid water and ice compared to TTM2-F, although some discrepancies with the experimental spectra were found in both lineshapes and vibrational shifts, particularly in the OH stretching frequency region.[52, 53, 115, 116]

The original AMOEBA model, AMOEBA03, was built upon a polarizable atomic multipole description of electrostatic interactions, including multipoles up to the quadrupole, and representing polarization via self-consistently induced atomic dipoles within a modified Thole

scheme.[54] AMOEBA03 was shown to reproduce several experimental properties and *ab initio* data for both water clusters and liquid water.[55] Subsequent developments and reparametrizations using the ForceBalance algorithm,[117] led to iAMOEBA[60] and AMOEBA14[58]. In contrast to AMOEBA03, iAMOEBA uses a direct approximation to polarization, with the induced dipoles being only determined from the permanent multipole electric fields.[60] Besides being computationally less expensive, iAMOEBA was shown to provide better agreement with experiment than AMOEBA03 for several properties of water in the gas, liquid, and solid phases.[60] It has recently been shown, however, that iAMOEBA is not able to correctly reproduce the sharp increase of the isothermal compressibility in the supercooled regime.[118] Extensive comparisons with experimental data showed that AMOEBA14 correctly reproduces the temperature dependence of several structural, thermodynamic, and dynamical properties of water.[58] Most recent developments of the AMOEBA models include AMOEBA+[57] and AMOEBA+CF.[56] Besides providing improved description of many-body polarization, repulsion, and dispersion compared to its predecessor models, AMOEBA+ incorporates an effective description of charge penetration by damping multipole–multipole interactions as well as an explicit pairwise charge transfer term fitted to reproduce the results of energy decompositions calculated at the symmetry-adapted perturbation theory (SAPT) level. AMOEBA+ was shown to perform well in both reproducing individual SAPT components and the properties of liquid water.[57] AMOEBA+CF represents a further refinement of AMOEBA+, which was achieved by implementing a geometry-dependent charge flux (CF) scheme within each water molecule. This resulted in a noticeable improvement in the description of both the energetics of water clusters and the properties of liquid water.[56]

Closely related to the AMOEBA models is MB-UCB, which was derived from a variational energy decomposition analysis.[108] Similarly to AMOEBA+, MB-UCB includes terms describing permanent electrostatics, polarization, repulsion, dispersion, and charge transfer which were parameterized from electronic structure data for the water monomer and small water clusters. MB-UCB was shown to reproduce the relative energies of large data sets of water clusters as well

as the structural, thermodynamic, and dynamical properties of liquid water.[108]

It was recognized quite early that Eq. 6.4 also provides a rigorous theoretical framework for the development of explicit many-body models that aim to quantitatively reproduce each individual term of the MBE.[119–122] With continued progress in both hardware technology and efficient algorithms for correlated electronic structure calculations, the development of explicit many-body models of water has witnessed a significant acceleration in the last decade. Since, on average, the sum of 2-body and 3-body energies contributes $\sim$95% to E_{int}, in these explicit many-body models, low-order n-body energies up to 3-body contributions (ε_{3B}) are treated individually, while all higher-body energies are either approximated by an effective $(n-3)B$-term or represented by classical polarization as in polarizable models. To date, the most notable explicit many-body models of water are CC-pol,[45, 123–125] which was the first explicit many-body water model with rigid monomers capable to reproduce both the properties of the water dimer and the radial distribution functions (RDFs) of liquid water at 300 K, WHBB,[126–129] which was the first explicit many-body water model with flexible monomers, and HBB2-pol and MB-pol,[37–39, 130, 131] which were the first explicit many-body water models with flexible monomers capable to correctly predict the properties of water across all phases.[1, 132] In particular, MB-pol has been shown to quantitatively reproduce the vibration-rotation tunneling spectrum of the water dimer,[37] the energetics, isomeric equilibria, tunneling splittings, and vibrational spsctra of small water clusters,[38, 133–144] the structural, thermodynamic, and dynamical properties as well as the infrared and Raman spectra of liquid water,[39, 145–149] the sum-frequency generation spectra of the air/water interface,[150–154] and the energetics and the infrared and Raman of various ice phases.[155–157] More recently, molecular configurations extracted from MD simulations with MB-pol have been used in many-body perturbation theory calculations to model the X-ray absorption spectrum of liquid water[158] as well as to determine the electron affinity of water, both in the bulk and at the air/water interface.[159] MB-pol was also used as a reference for the development of an optimized exchange-correlation density functional for

water.[160]

Given the renewed interest in polarizable water models, we present here a systematic analysis of the TTM, AMOEBA, and MB-UCB models, with particular focus on the ability of these models to reproduce many-body effects in water systems from the gas to the condensed phase. Results obtained with the polarizable models are compared with the corresponding values obtained with MB-pol, and, when possible, the accuracy of each model is assessed relative to reference values calculated at the coupled cluster level of theory, including single, double, and perturbative triple excitations, in the CBS limit, i.e., CCSD(T)/CBS, the current "gold standard" for chemical accuracy. To determine the effects of geometry-dependent representations of the 1-body charge distribution on interaction and many-body energies, we also introduce a simplified version of MB-pol (fq-MB-pol) which employs fixed point charges, and assess the accuracy of the new model relative to MB-pol and CCSD(T)/CBS. This study aims to investigate the accuracy of state-of-the-art polarizable and flexible water models through a many-body perspective, and determine how possibly shortcomings inherent to a description of many-body effects entirely based on classical polarization may affect the predictions of the properties of water calculated from computer simulations.

The article is organized as follows: Section II provides a brief description of both polarizable and explicit many-body models analyzed in this study, while Section III provides computational details specific to the comparisons presented in the following sections. Section IV presents comparisons for interaction and many-body energies calculated for small water clusters, associated harmonic frequencies, and interaction energies for liquid configurations. A general discussion along with an outlook is presented in Section V.

2.2 Molecular models

2.2.1 Polarizable models

The TTM, AMOEBA, and MB-UCB models approximate Eq. 6.4 as

$$E_N(r_1,..,r_N) = \sum_{i=1}^{N} \varepsilon_{1B}(r_i) + E_{MB}^{eff} \tag{2.4}$$

where E_{MB}^{eff} effectively accounts for all many-body interactions among N water molecules. As mentioned in the Introduction, the TTM models employ an accurate representation of $\varepsilon_{1B}(r_i)$ derived from high-level *ab initio* calculations of the water monomer which were then refined to reproduce the experimental line positions of the rovibrational spectrum of an isolated water molecule.[64] The 1-body term in the AMOEBA and MB-UCB models is instead represented by empirically parameterized anharmonic bond-stretching and angle-bending potentials, along with a bond-angle cross term that was found necessary in the original developments of AMOEBA03 to improve the description of the splitting between symmetric and asymmetric OH stretching vibrations.[54]

The TTM, AMOEBA, and MB-UCB models further decompose E_{MB}^{eff} into distinct physical contributions to the interaction energy according to

$$E_{MB}^{eff} = E_{elec} + E_{pol} + E_{rep} + E_{disp} + E_{CT} \tag{2.5}$$

where E_{elec}, E_{pol}, E_{rep}, E_{disp}, and E_{CT} are individual terms parameterized to represent permanent electrostatics, polarization, repulsion, dispersion, and charge transfer, respectively. Since the TTM, AMOEBA, and MB-UCB models adopts different functional forms to describe each contribution to E_{MB}^{eff}, we briefly summarize here the main features of all models. The interested reader is referred to the original references for specific details.

TTM2.1-F. In TTM2.1-F, E_{elec} is described by Coulomb interactions between geometry-dependent point charges placed on the H atoms and the fictitious M-site site located along the bisector of the HOH angle.[51] The geometry-dependent point charges were determined to reproduce the *ab initio* dipole moment surface of an isolated water molecule derived from high-level *ab initio* calculations in Ref. 64. E_{pol} is represented according to a Thole's damping scheme,[109] with inducible point dipoles placed on the O and H atoms. Both E_{elec} and E_{pol} in TTM2.1-F are fully damped to mimic charge penetration effects. TTM2.1-F does not include an explicit charge transfer term and combines E_{rep} and E_{disp} in a single term representing pairwise additive van der Waals interactions between the oxygen atoms,

$$E_{rep} + E_{disp} = E_{vdW} = \sum_{i<j} \left[De^{-\alpha R_{ij}} - \frac{A}{R_{ij}^6} - \frac{B}{R_{ij}^{10}} - \frac{C}{R_{ij}^{12}} \right] \tag{2.6}$$

where R_{ij} is the distance between the O atoms of molecules i and j, and D, α, A, B, and C are fitting parameters.

TTM3-F. Although adopting the same functional form as TTM2.1-F, the TTM3-F model was specifically parameterized to improve the description of vibrational spectra of water.[52] For this purpose, the original geometry-dependent point charges of TTM2.1-F, were empirically modified to mimic the increase in magnitude of the charges on the H atoms when the OH bonds elongate in liquid water. In contrast to TTM2.1-F, the TTM3-F model employs a single inducible point dipole placed on the M-site as well as a different expression for the van der Waals interactions,[52]

$$E_{rep} + E_{disp} = E_{vdW} = \sum_{i<j} \frac{\varepsilon}{1-6/\lambda} \left[\frac{6}{\lambda} e^{\lambda\left(1-\frac{R_{ij}}{\sigma}\right)} \left(\frac{\sigma}{R_{ij}}\right)^6 \right] \tag{2.7}$$

where, as in TTM2.1-F, R_{ij} is the distance between the O atoms of molecules i and j, and ε, σ, and λ are fitting parameters.

TTM4-F. Directly building upon TTM2-F,[50] the TTM4-F model was parameterized

to reproduce the polarizability surface of the water monomer calculated at the MP2 level of theory.[53] As a result, although TTM4-F employs the same functional form as TTM2-F to describe permanent electrostatics and polarization, it adopts a modified Thole's damping scheme along with an expanded pairwise additive term representing van der Waals interactions,

$$E_{rep} + E_{disp} = E_{vdW} = \sum_{i<j} \sum_{l=3}^{8} \frac{A_{2l}}{R_{ij}^{2l}} \tag{2.8}$$

where, as in TTM2.1-F and TTM3-F, R_{ij} is the distance between the O atoms of molecules i and j, and A_{2l} are fitting parameters.

AMOEBA03. As mentioned above, the 1-body term of AMOEBA03, which includes anharmonic representations of both stretching and bending vibrations along with an additional Urey-Bradley term representing the coupling between stretching and bending vibrations, was parameterized to reproduce the gas-phase vibrational frequencies of the water monomer at the experimental geometry.[54] AMOEBA03 employs a multipole expansion, with atomic monopole, dipole, and quadrupole moments placed on each atom, to represent E_{elec} in Eq. 2.5. These moments were derived from a distributed multipole analysis carried out on *ab initio* data for the water monomer. E_{pol} in Eq. 2.5 is represented through the interactions of inducible point dipoles placed on the atomic sites. While AMOEBA03 adopts a Thole's scheme to damp E_{pol} at short range, no damping is applied to E_{elec}. As the TTM models, AMOEBA03 does not include an explicit charge transfer term, but, differently from the TTM models, includes van der Waals interactions between all pairs of atoms through a sum of pairwise additive buffered 14-7 potentials,

$$E_{vdW} = \sum_{i<j} \varepsilon_{ij} \left(\frac{1+\delta}{\rho_{ij}+\delta} \right)^7 \left(\frac{1+\gamma}{\rho_{ij}^7+\gamma} - 2 \right) \tag{2.9}$$

Here, i and j thus indicate O and H atoms on different water molecules within each dimer, ε_{ij} is the potential well depth of the corresponding 14-7 potential, and $\rho_{ij} = R_{ij}/R_{ij}^0$, with R_{ij} being the distance between atoms i and j, and R_{ij}^0 being the corresponding minimum energy distance. The

values of $\delta = 0.07$ and $\gamma = 0.12$ were taken from Ref. 161. All fitting parameters in AMOEBA03 were optimized to reproduce *ab initio* data for gas-phase clusters as well as the temperature and pressure dependence of several properties of liquid water.

iAMOEBA. Although iAMOEBA adopts the same functional form as AMOEBA03, it employs a simplified expression for the polarization term in which the induced dipoles are only determined by the electric fields generated by permanent multipoles and mutual polarization between the induced dipoles is neglected.[60] Including only direct polarization implies that iAMOEBA only accounts for at most 3-body interactions where an induced dipole interacts with two other multipole moments. iAMOEBA was parameterized using the ForceBalance algorithm that allows for simultaneously fitting to experimental and *ab initio* training data.[117]

AMOEBA14. AMOEBA14[58] represents an updated version of the original AMOEBA03 model which was obtained by using the ForceBalance algorithm[117] to determine a refined set of fitting parameters.

AMOEBA+. Although it was built upon previous versions of the AMOEBA models, AMOEBA+ employs a different representation of E_{MB}^{eff} in which Thole's damping is applied not only to E_{pol} but also to the interactions between the permanent multipoles of E_{elec}.[57] In addition, AMOEBA+ includes an explicit term describing charge transfer. Starting from energy decompositions derived from SAPT calculations, all fitting parameters in AMOEBA+ were optimized to reproduce both *ab initio* and experimental data using the ForceBalance algorithm.[117]

AMOEBA+CF. Representing a further development of AMOEBA+, AMOEBA+CF adopts a more advanced description of permanent electrostatics which is achieved by implementing a geometry-dependent charge-flux (CF) scheme within each monomer.[56] Similarly to the TTM models, the charge flux in AMOEBA+CF explicitly depends on the local geometry of a water molecule and was found to improve the transferability of the model across different phases.

MB-UCB. Closely related to AMOEBA+ and AMOEBA+CF, the MB-UCB model adopts a similar functional form for E_{elec}, with fully damped interactions between permanent multipoles,

although, differently from the AMOEBA models, the multipole expansion is truncated at the dipole moment.[108] Furthermore, MB-UCB implements anisotropic dipole polarizabilities to better reproduce anisotropic electric fields in nonhomogenous media. While MB-UCB adopts the same buffered 14-7 expression for E_{vdW} as AMOEBA+ and AMOEBA+CF, differently from the AMOEBA+ models that account only for pairwise charge transfer, MB-UCB includes a many-body charge transfer term that is solved self-consistently.[108] All parameters of the MB-UCB model were optimized on training data for the water monomer, dimer, trimer, tetramer, and pentamer clusters, with the E_{CT} term being specifically parameterized to reproduce charge transfer energies derived from a variational absolutely localized molecular orbitals energy decomposition analysis (ALMO-EDA). Based on the analyses reported in Ref. 108, it was claimed that MB-UCB achieves comparable performance to MB-pol.

2.2.2 Explicit many-body models

Both MB-pol and fq-MB-pol approximate Eq. 6.4 as

$$E_N(r_1,..,r_N) = \sum_{i=1}^{N} \varepsilon_{1B}(r_i) + \sum_{i>j}^{N} \varepsilon_{2B}(r_i,r_j) + \sum_{i>j>k}^{N} \varepsilon_{3B}(r_i,r_j,r_k) + E_{pol} \tag{2.10}$$

where ε_{1B} represents the same *ab initio* PES of the water monomer of Ref. 64 adopted by the TTM models, ε_{2B} and ε_{3B} are explicit 2-body and 3-body terms, and $\varepsilon_{>3B}$ is an implicit term representing all many-body interactions involving more than three water molecules at a time.

MB-pol. The 2-body term of MB-pol includes three contributions,[37]

$$\varepsilon_{2B} = E_{2B}^{sr} + E_{elec} + E_{disp} \tag{2.11}$$

Here, E_{2B}^{sr} describes short-range 2-body interactions that are represented by a 4^{th}-degree permutationally invariant polynomial (PIP)[65] in variables that are functions of the distances between

all pairs of the (six) sites of the MB-pol water monomer. As in TTM2.1-F and TTM4-F, E_{elec} in MB-pol is described by Coulomb interactions between geometry-dependent point charges that reproduce the *ab initio* dipole moment surface of a water molecule determined in Ref. [64]. E_{disp}) is a 2-body dispersion term expressed as

$$E_{disp} = -\sum_{i,j} f(\delta_{ij}) \frac{C_{6,ij}}{R_{ij}^6} \tag{2.12}$$

where the sum runs over all pairs of O and H atoms i and j on different water molecules within a dimer, R_{ij} is the distance between atoms i and j, $f(\delta_{ij})$ is the Tang-Toennies damping function with fitting parameter δ_{ij},[66] and $C_{6,ij}$ are the dispersion coefficients calculated from fits to the asymptotic *ab initio* reference energies of the water dimer as in CC-pol.[45]

In Eq. 5.8,

$$\varepsilon_{3B} = E_{3B}^{sr} \tag{2.13}$$

describes 3-body short-range interactions that, as in the analogous 2-body term E_{3B}^{sr}, are represented by a 4^{th}-degree PIP[65] in variables that are functions of the distances between all sites within a trimer.[38] The coefficients of the 2-body and 3-body PIPs were optimized using Tikhonov regression (also known as ridge regression)[162] to reproduce 2-body and 3-body energies calculated at the CCSD(T)/CBS level of theory. It was shown that the E_{2B}^{sr} and E_{3B}^{sr} terms of MB-pol quantitatively reproduce 2-body and 3-body quantum-mechanical effects that cannot be described by purely classical expressions (e.g., charge transfer and penetration, and Pauli repulsion).[163] Finally, E_{pol} in Eq. 5.8 represents N-body polarization and is described by a modified version of the Thole-type model adopted by TTM4-F.[37, 38]

fq-MB-pol. fq-MB-pol is introduced here to assess the importance of employing 1-body geometry-dependent atomic charges in reproducing CCSD(T)/CBS interaction and many-body energies. For this purpose, fq-MB-pol adopts the same functional form as MB-pol, with explicit representations of short-range 2-body and 3-body interactions in terms of PIPs that are combined

with classical representations of permanent electrostatics, polarization, and dispersion. fq-MB-pol was developed from the same sets of CCSD(T)/CBS data for 1-body, 2-body, and 3-body energies used in the development of MB-pol.[37, 38] However, differently from MB-pol that employs geometry-dependent charges to reproduce the *ab initio* dipole moment surface of Ref. 64, fq-MB-pol employs fixed multipole-derived charges[164] calculated at the ωB97M-V/aug-cc-pVQZ level of theory,[165–167] for an isolated water molecule in the corresponding optimized geometry. The multipole-derived charges were then mapped into the M-site (q_M) and the two H atoms (q_H) according to the same scheme adopted by MB-pol and originally introduced in the TTM2.1-F model, resulting in $q_M = -1.151790e$ and $q_H = 0.575895e$.

2.3 Computational details

All TTM2.1-F, TTM3-F, TTM4-F, MB-pol, and fq-MB-pol calculations were carried out using in-house software based on DL_POLY2,[168] while all AMOEBA03, AMOEBA14, iAMOEBA, AMOEBA+, and AMOEBA+CF calculations were carried out using Tinker.[169] The 2-body and 3-body CCSD(T)/CBS reference energies are taken from Refs. 37 and 38. The reference structures for the water clusters, along with the associated interaction and many-body energies calculated at the CCSD(T)/CCSD(T)-F12 level of theory within the SAMBA scheme,[170] are taken from Ref. 1. The reference harmonic frequencies calculated at the 2-body:many-body CCSD(T):MP2 level of theory are taken from Refs. 2 and 3, while the harmonic frequencies for all polarizable and explicit many-body models were calculated from the corresponding optimized cluster structures.

2.4 Results

To assess the ability of the different models considered in this study to represent many-body effects in water from the gas to the condensed phase, the following sections present a systematic analysis of interaction energies, many-body energy decompositions, and harmonic frequencies for small clusters (Fig. 2.1), as well as relative energies for configurations extracted from centroid molecular dynamics (CMD)[171–175] simulations of liquid water carried out at ambient conditions with MB-pol in Ref. 148.

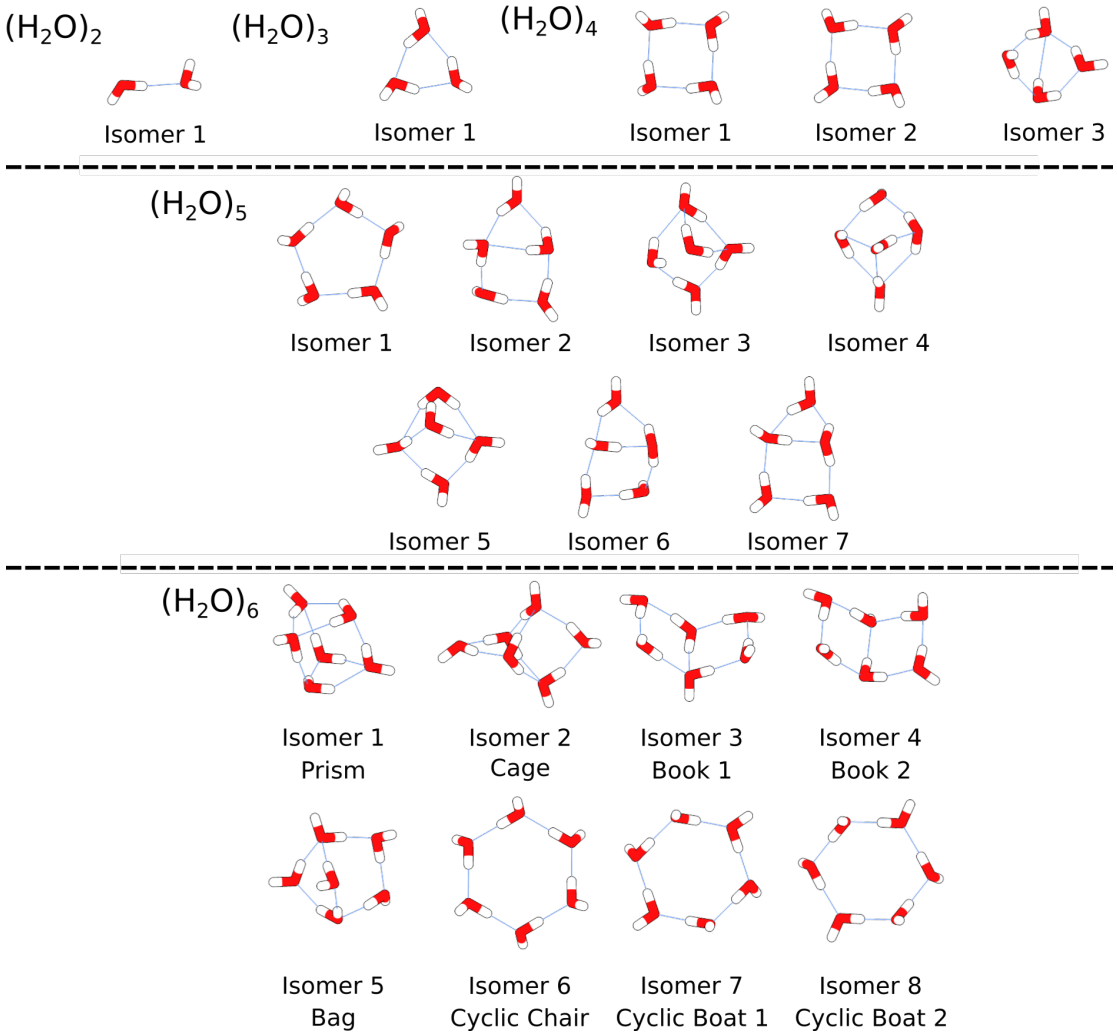

Figure 2.1: Structures of the $(H_2O)_n$ clusters, with $n = 1 - 6$, used in the analysis of interaction and many-body energies as well as harmonic frequencies.

2.4.1 Analysis of 2-body and 3-body energies

The interaction energies (E_{int} in Eq. 2.3) for the minimum-energy structures of the water dimer and trimer (isomers 1 in Fig. 2.1) calculated using both polarizable and explicit many-body models are listed in Table 2.1. Also reported in Table 2.1 are the corresponding 2-body and 3-body energies contributing to the interaction energy of the water trimer. We note here that, by definition (Eq. 2.3), the interaction energy for the water dimer also corresponds to the 2-body energy.

At the 2-body level, all polarizable models predict interaction energies for the water dimer that are close to the CCSD(T)/CBS reference value. Only the TTM3-F and MB-UCB models predict noticeably more attractive interactions, with 2-body energies of -5.30 kcal/mol and -5.44 kcal/mol, respectively, which are $\sim$5% lower than the reference CCSD(T)/CBS value. Although most polarizable models predict reasonably accurate interaction energies for the water trimer, large deviations from the CCSD(T)/CBS reference values are found for TTM4-F, which underestimates the interaction strength by 1.90 kcal/mol, and AMOEBA+, which instead overestimates the

Table 2.1: Interaction energies (E_{int}) for the minimum-energy structures of the water dimer and trimer (isomers 1 of $(H_2O)_2$ and $(H_2O)_3$ in Fig. 2.1). Also listed are the 2-body and 3-body energies contributing to E_{int} of the water trimer. All energies are in kcal/mol.

Model	$(H_2O)_2$	$(H_2O)_3$		
	E_2	E_3	E_{2B}	E_{3B}
CCSD(T)	-5.06	-16.21	-13.74	-2.47
TTM2.1-F	-5.07	-15.82	-13.59	-2.22
TTM3-F	-5.30	-16.23	-15.01	-1.21
TTM4-F	-5.03	-14.31	-11.80	-2.51
AMOEBA03	-5.21	-16.00	-13.18	-2.81
iAMOEBA	-5.22	-15.58	-13.91	-1.67
AMOEBA14	-4.91	-16.23	-12.99	-3.25
AMOEBA+	-5.20	-17.09	-14.29	-2.80
AMOEBA+CF	-5.00	-16.32	-13.75	-2.57
MB-UCB	-5.44	-16.40	-14.21	-2.20
fq-MB-pol	-5.07	-16.20	-13.74	-2.46
MB-pol	-5.05	-16.15	-13.69	-2.45

interaction strength by 0.88 kcal/mol. For both water dimer and trimer, MB-pol and fq-MB-pol provide quantitative agreement with CCSD(T)/CBS, with deviations being always within 0.06 kcal/mol of the reference values.

When the interaction energy of the water trimer is decomposed into the corresponding individual many-body contributions, it is found that TTM3-F overestimates 2-body effects and underestimates 3-body effects by more than 1.0 kcal/mol. Similar trend, although to a lesser extent, is found for AMOEBA14, which instead underestimates 2-body effects and overestimates 3-body effects by $\sim$0.8 kcal/mol. This analysis indicates that the apparent agreement with the CCSD(T)/CBS interaction energy for the water trimer exhibited by TTM3-F and AMOEBA14 results from nearly perfect error compensation between 2-body and 3-body effects.

On the other hand, TTM4-F significantly underestimates 2-body energies by $\sim$2.0 kcal/mol but is able to quantitatively reproduce 3-body energies. The opposite trend is predicted by iAMOEBA which is able to correctly reproduce 2-body energies but underestimates 3-body contributions by $\sim$1.0 kcal/mol. The different performance exhibited by TTM4-F and iAMOEBA in reproducing 3-body energies is directly correlated to the different representations used by these two models to describe polarization effects, with TTM4-F being specifically parameterized to reproduce the polarizability of a water molecule and iAMOEBA neglecting mutual polarization between water molecules.

Table 2.1 shows that both MB-pol and fq-MB-pol quantitatively reproduce the CCSD(T)/CBS reference values for the 2-body and 3-body energies of the water trimer. This demonstrates that the ability of these models to accurately predict the interaction energies of both water dimer and trimer thus results from a quantitative account of both 2-body and 3-body effects.

While the comparisons reported in Table 2.1 demonstrate that, although with different levels of accuracy, most polarizable models are able to represent 2-body and 3-body energies for the minimum-energy structures of the water dimer and trimer, they do not provide any information about 2-body and 3-body effects for distorted configurations that exist in liquid water at different

temperatures and pressures. Therefore, to assess the ability of both polarizable and explicit many-body models to describe the multidimensional 2-body and 3-body energy landscapes, Figs. 2.2 and 2.3 show correlations between 2-body and 3-body energies calculated with each model and the corresponding CCSD(T)/CBS reference values for 1000 dimer and trimer configurations randomly extracted from the original MB-pol training sets.[37, 38] To guarantee fair comparisons between all models, the MB-pol and fq-MB-pol models shown in Figs. 2.2 and 2.3 were re-fitted to the reduced 2-body and 3-body training sets obtained after removing from the original training sets the same 1000 configurations used for the correlation analysis.

Fig. 2.2 shows that all polarizable models exhibit significant deviations from the reference CCSD(T)/CBS 2-body energies. This is particularly evident for TTM4-F and AMOEBA+ that are associated with RMSDs of 2.28 and 4.38 kcal/mol, respectively. Overall, among the polarizable models, TTM3-F, AMOEBA03, iAMOEBA, AMOEBA+CF, and MB-UCB display similar RMSDs of $\sim$1.2-1.3 kcal/mol, while TTM2.1-F and AMOEBA14 provide the closer agreement with the CCSD(T)/CBS reference energies, with RMSDs of $\sim$1.0 kcal/mol. In contrast, both MB-pol and fq-MB-pol exhibit the same accuracy as CCSD(T)/CBS over the entire range of 2-body energies, with RMSDs of $\sim$0.05 kcal/mol, which are more than one order of magnitude smaller than those associated with the polarizable models.

Importantly, both AMOEBA+CF and MB-UCB do not display the large (positive) deviations from the CCSD(T)/CBS 2-body energies that are instead associated with AMOEBA+. Considering the progressive development of the AMOEBA models described in Section II, these differences can be traced back to the fact that both AMOEBA+CF and MB-UCB include explicit terms parameterized to mimic charge transfer, which improves the description of short-range interactions in more distorted water dimers. In this regard, it should be noted that, although these parameterized charge transfer terms adopt relatively simple functional forms and, therefore, are not sufficient to achieve CCSD(T)/CBS accuracy over a wide range of 2-body energies as shown in Fig. 2.2, they effectively mimic the same role played by the 2-body PIP adopted by MB-pol

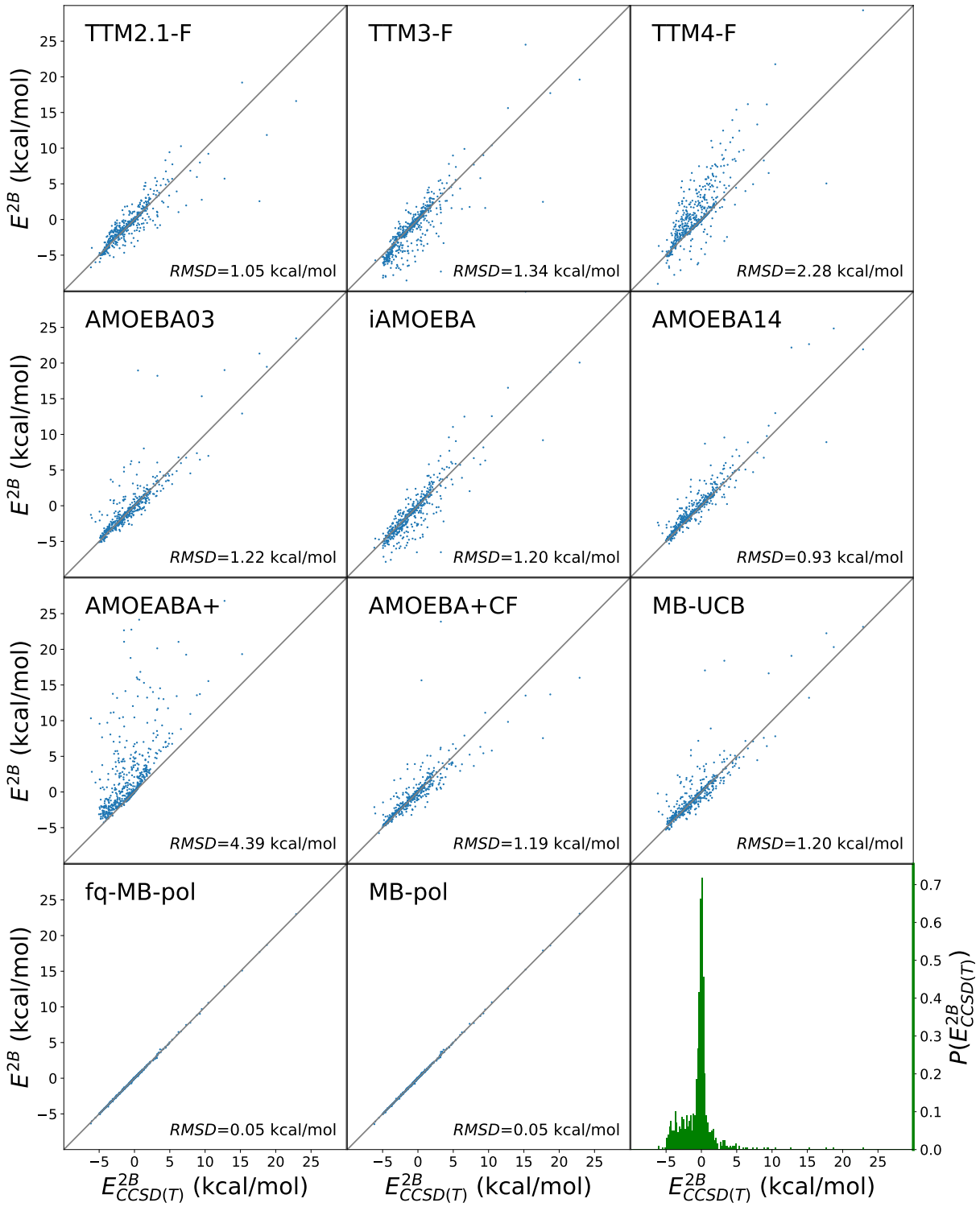

Figure 2.2: Correlation plots for the 2-body energies. Plotted on the x axes are the 2-body CCSD(T)/CBS reference energies from Ref. 37. On the y axes are the corresponding 2-body energies calculated with both polarizable and explicit many-body models. Also shown in the bottom right panel is the distribution of 2-body energies in the test set used for this analysis.

and fq-MB-pol. Using a multidimensional 2-body PIP to supplement a classical description of permanent electrostatics, polarization and dispersion was found to be necessary to guarantee an accurate representation of the global energy landscape of the water dimer over a wide range of molecular distortions.[37, 163]

Fig. 2.3 shows that, with the exception of TTM3-F, all polarizable models considered in this study are able to reproduce CCSD(T)/CBS 3-body energies relatively better than the corresponding 2-body energies. Specifically, all models are associated RMSDs smaller than $\sim$0.2 kcal/mol relative to the reference values. This is in agreement with previous observations that 3-body energies in water are primarily due to polarization, which can be properly accounted for using classical representations based on physically-motivated parameterizations of molecular polarizabilities.[130] TTM3-F not only displays the largest RMSDs ($\sim$0.4 kcal/mol) but also provides a poor correlation with the reference CCSD(T)/CBS values, significantly underestimating attractive 3-body energies. Since Fig. 2.3 shows that the closely related TTM2.1-F and TTM4-F models perform significantly better than TTM3-F, the large deviations associated with TTM3-F can be attributed to the fact that this model employs a single polarizable site that may not be sufficient for a correct representation of the anisotropy of 3-body effects within a Thole's damping scheme.

Fig. 2.3 shows that all AMOEBA models, with the exception of iAMOEBA, tend to slightly overestimate the strength of 3-body interactions, which results in a slope greater than 1. Among the polarizable models, AMOEBA+CF overall provides the best correlation with the CCSD(T)/CBS reference data with an RMSD of $\sim$0.13 kcal/mol. As in the case of 2-body energies, Fig. 2.3 shows that both MB-pol and fq-MB-pol also provide quantitative agreement with the CCSD(T)/CBS 3-body energies a, with RMSDs of $\sim$0.04 kcal/mol. Considering that the core representation of 3-body energies in both MB-pol and fq-MB-pol builds upon a slightly modified version of the polarization scheme adopted by TTM4-F, the different level of accuracy achieved by MB-pol and fq-MB-pol compared to that of polarizable models can be attributed to

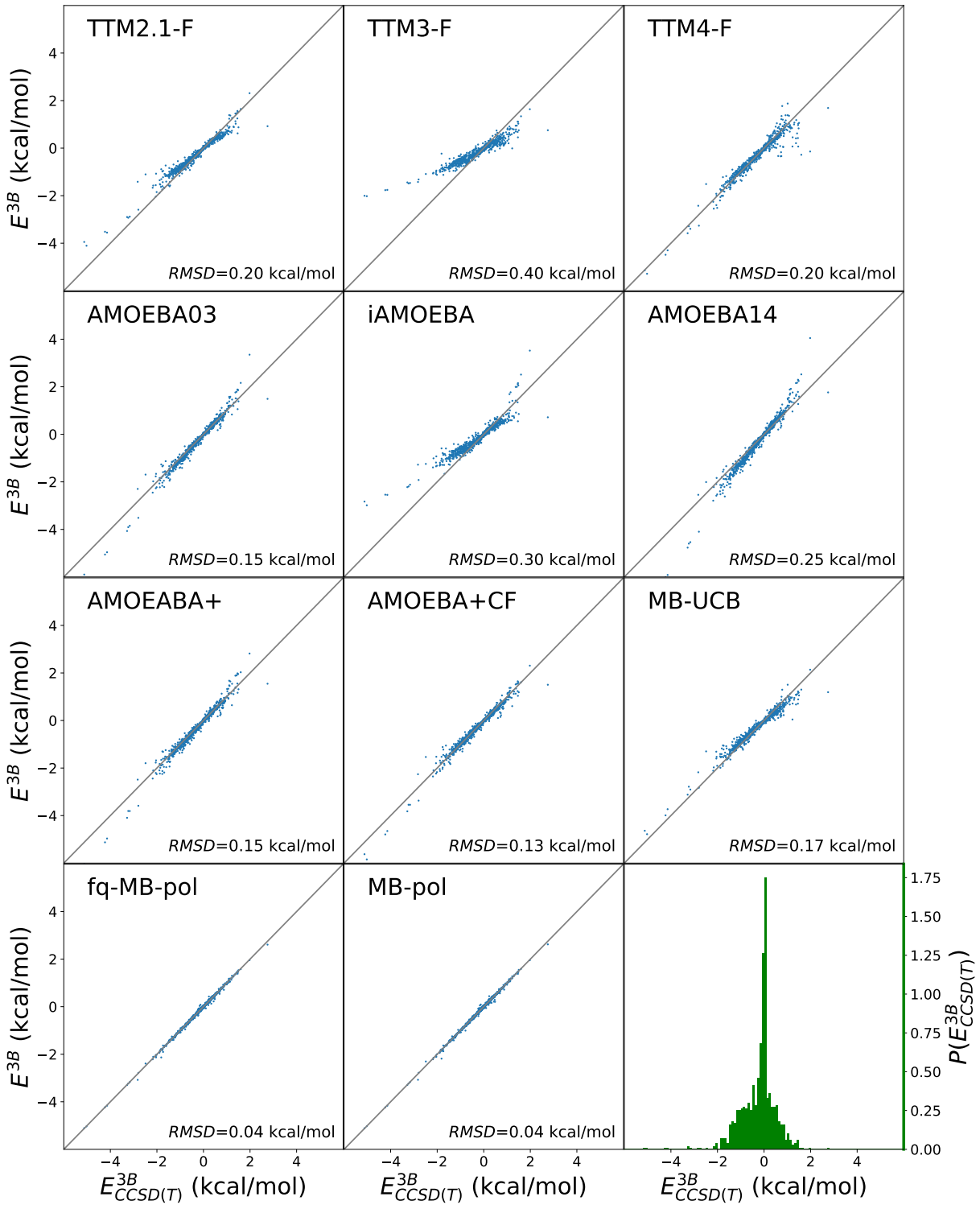

Figure 2.3: Correlation plots for the 3-body energies. Plotted on the x axes are the 3-body CCSD(T)/CBS reference energies from Ref. 38. On the y axes are the corresponding 3-body energies calculated with both polarizable and explicit many-body models. Also shown in the bottom right panel is the distribution of 3-body energies in the test set used for this analysis.

the ability of the 3-body PIP to correct for intrinsic deficiencies associated with purely classical representations of 3-body interactions based on many-body polarization. This is particularly relevant at short range where the overlap of the monomer electron densities is responsible for 3-body effects (e.g., 3-body exchange-repulsion, correlation, and dispersion, as well as more subtle effects such as coupling of exchange and correlation to the dispersion interaction) that do not have well-defined classical analogs.

2.4.2 Analysis of many-body energies is small water clusters

The deviations from the reference many-body energies calculated for $(H_2O)_n$ clusters, with $n = 4-6$, using the TTM, AMOEBA, MB-UCB, and MB-pol models are compared in Fig. 2.4. As shown in Eq. 2.3, the interaction energy for each cluster is defined as the difference between the total energy of the cluster and the energies of the individual water molecules kept at the same geometry as in the cluster. By removing the contributions associated with the monomer distortions, the interaction energies thus allow for direct comparisons of molecular interactions as predicted by the different models, without being "contaminated" by differences in the description of the 1-body energies specific to each model.

Fig. 2.4 shows that TTM2.1-F, TTM3-F, AMOEBA03, iAMOEBA, and AMOEBA14 benefit from significant error compensation between individual many-body terms. For example, the absolute 2-body deviations for the hexamer isomers are as large as 2.65 kcal/mol for TTM2.1-F, 5.31 kcal/mol for TTM3-F, 1.38 kcal/mol for AMOEBA03, 3.91 kcal/mol for iAMOEBA, and 3.81 kcal/mol for AMOEBA14. These models are correspondingly associated with large, but of opposite sign, 3-body deviations whose absolute values are up to 2.85 kcal/mol for TTM2.1-F, 5.12 kcal/mol for TTM3-F, 0.95 kcal/mol for AMOEBA03, 3.91 kcal/mol for iAMOEBA, and 2.31 kcal/mol for AMOEBA14. The observed error compensation in these models stems primarily from an insufficient representation of 2-body permanent electrostatics and van der Waals energies that need to be compensated by unphysically large contributions from many-body polarization, which

is particularly evident at the 3-body level. Interestingly, the analysis of many-body energies shows that TTM3-F displays notably larger errors than its predecessor model TTM2.1-F. This can be partially attributed to the TTM3-F model employing a single polarizable site, which was a choice made during the parameterization as a compromise between accuracy and computational efficiency but may be insufficient to correctly reproduce anisotropic electric fields.[52] In the AMOEBA03, iAMOEBA, and AMOEBA14 models, the aforementioned deficiencies in the representation of permanent electrostatics may be due to the adoption of undamped interactions between the multipoles. Since, by construction, iAMOEBA only includes up to 3-body contributions, the iAMOEBA errors for all ε_{nB} terms with $n > 3$ are equal, but opposite in sign, to the corresponding CCSD(T)/CCSD(T)-F12 reference values. It should be noted that AMOEBA14 exhibits larger deviations than the original AMOEBA03 model, indicating that the representation of permanent electrostatics and polarization worsened during the parameterization of AMOEBA14 when the the ForceBalance algorithm was used to simultaneously reproduce both *ab initio* and experimental data.

On the other hand, TTM4-F, AMOEBA+, AMOEBA+CF, and MB-UCB do not benefit from significant error compensation and exhibit, overall, relatively smaller deviations than their predecessor models. For example, the absolute deviations on the 2-body energies of the hexamer isomers are up to 4.0 kcal/mol for TTM4-F, 1.70 kcal/mol for AMOEBA+, 0.91 kcal/mol for AMOEBA+CF, and 2.06 kcal/mol for MB-UCB, while the corresponding absolute 3-body deviations are as large as 0.70 kcal/mol for TTM4-F, 0.90 kcal/mol for AMOEBA+, 0.30 kcal/mol for AMOEBA+CF, and 0.73 kcal/mol for MB-UCB. The improved description of many-body effects in these polarizable models can be attributed to the adoption of more advanced representations of both permanent electrostatics and polarization. Specifically, TTM4-F uses the same fully damped scheme for the electrostatics as TTM2.1-F and TTM3-F but employs a more flexible damping function along with distinct Thole parameters for intermolecular and intramolecular interactions. On the other hand, contrary to previous AMOEBA models, both AMOEBA+, AMOEBA+CF

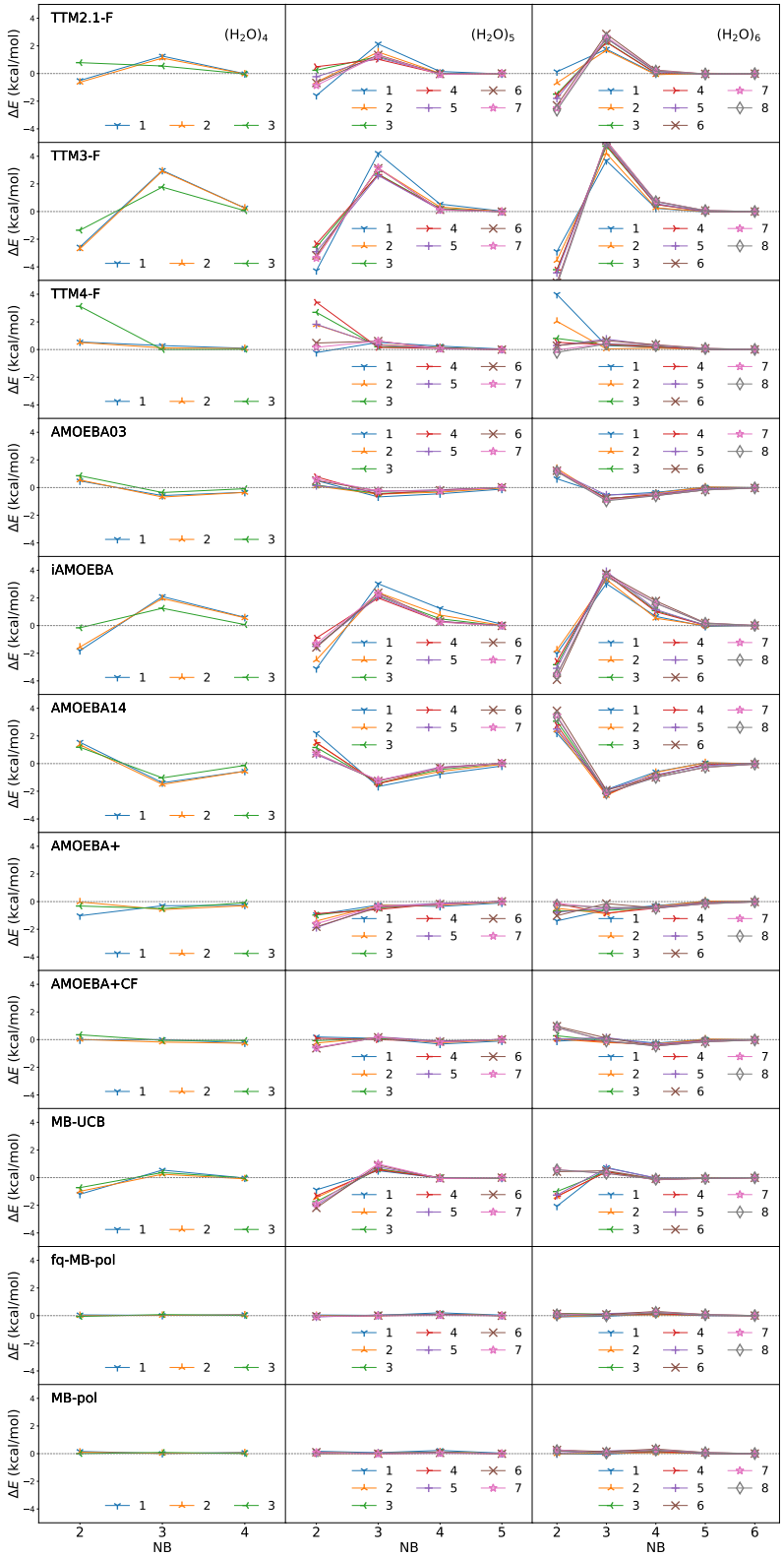

Figure 2.4: Deviations, ΔE, from the CCSD(T)/CCSD(T)-F12 reference values for individual many-body energies calculated for $(H_2O)_n$ clusters, with $n = 4-6$, using both polarizable and explicit many-body models.

and MB-UCB adopt fully damped expressions for permanent electrostatics and include explicit charge penetration and charge transfer terms. Interestingly, the analysis of many-body energies for the water clusters indicates that the MB-UCB model predicts relatively larger 2-body errors for non-cyclic than cyclic isomers of the pentamer and hexamer clusters. This suggests that MB-UCB describes relatively more accurately water arrangements with cooperative hydrogen-bonding than those with anti-cooperative hydrogen-bonding, which is likely owed to MB-UCB using anisotropic atomic polarizabilities that provide better representations of planar structures with concerted water arrangements.

Finally, independently of the cluster size and structure, MB-pol, which includes explicit 2-body and 3-body terms integrated with a classical representation of polarization similar to that adopted by the TTM4-F model, exhibits small deviations for each individual n-body energy. In particular, the 2-body and 3-body deviations for the hexamer isomers never exceed 0.27 kcal/mol and 0.14 kcal/mol, respectively, with the larger deviations (0.33 kcal/mol) being associated with 4-body energies. Importantly, fq-MB-pol, which adopts a simplified representation of permanent electrostatics, exhibits 2-body and 3-body deviations ($\sim$0.15 kcal/mol) comparable to those associated with those predicted by the original MB-pol model.

Overall, the deviations on the interaction energies shown in Fig. 2.5 are found to increase with cluster size for all models, since the errors associated with each individual term of the MBE adds up. Importantly, the cyclic isomers of each clusters are associated, on average, with the largest deviations. Since these isomers are characterized by extended hydrogen-bonded chains of (nearly) equivalent water molecules, the difficulties in reproducing the CCSD(T)/CCSD(T)-F12 reference energies suggest that purely classical polarization terms may be insufficient for a quantitative description of water structures dominated by cooperative effects.

Motivated by a similar analysis carried out for density functional theory (DFT) models of water,[176] we apply the same scoring scheme developed in Ref. 1 to quantify the accuracy of both polarizable and explicit many-body models in reproducing the CCSD(T)/CCSD(T)-F12

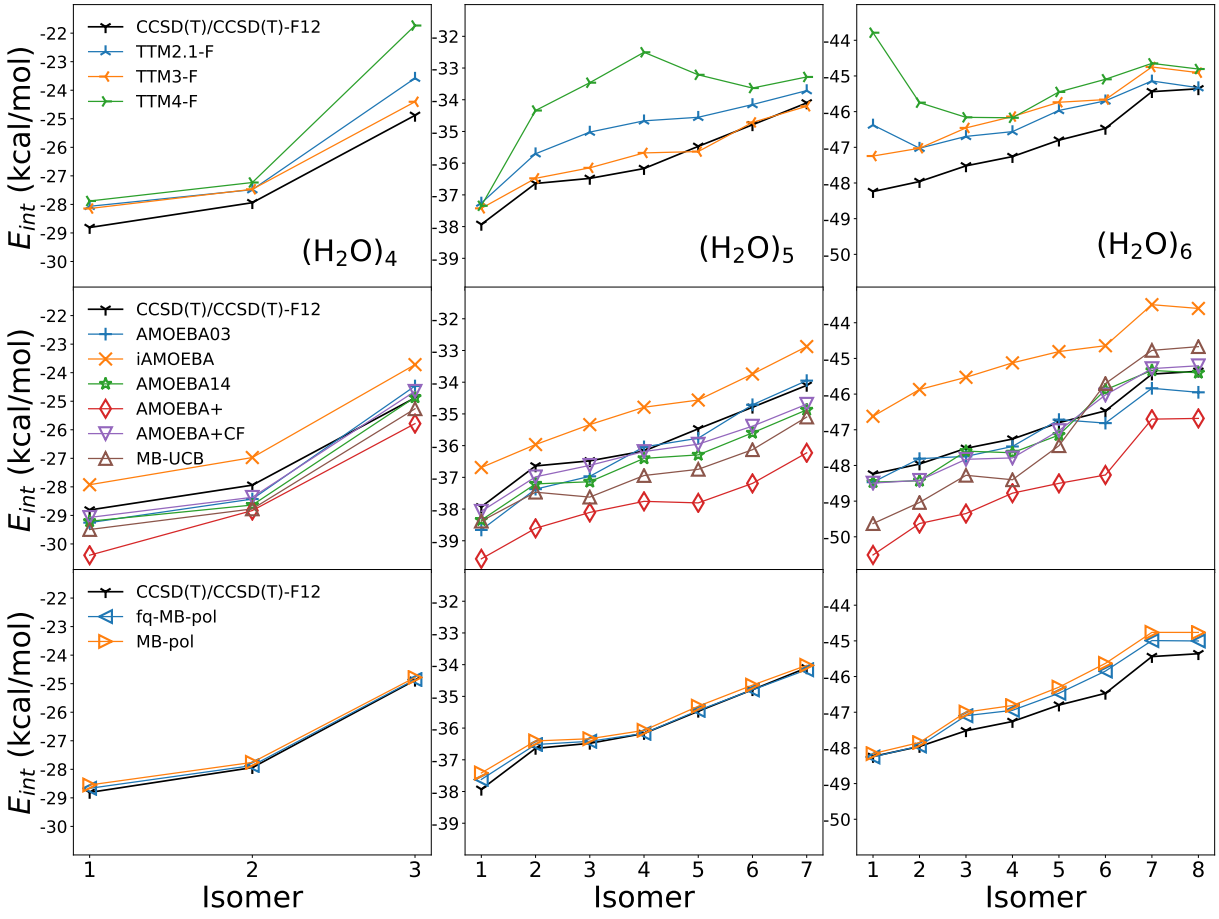

Figure 2.5: Comparisons between the interaction energies of the low-lying isomers of $(H_2O)_n$ clusters, with n=4-6, (see Fig. 2.1) obtained at the CCSD(T)/CCSD(T)-F12 level of theory within the SAMBA scheme in Ref. 1 and the corresponding values calculated with both polarizable and explicit many-body models.

reference data. The resulting scores assigned to each model based on the ability to reproduce interaction and many-body energies for $(H_2O)_n$ clusters with n = 4, 5, and 6 are reported in Table 2.2. In this analysis, the maximum total unsigned error over all isomers of each $(H_2O)_n$ cluster is defined as:

$$\Delta E^{MB}_{unsigned,\,max} = max_i \left[\left(\sum_j^{NB} |E^j_{model} - E^j_{ref}| \right) \right] \tag{2.14}$$

The maximum absolute error in the interaction energy over all isomers of each $(H_2O)_n$ cluster is

defined as:

$$\Delta E^{MB}_{int,\,max} = max_i \left[\left| \left(\sum_j^{NB} E^j_{model} - E^j_{ref} \right) \right| \right] \tag{2.15}$$

The relative energy difference between isomer 1 and isomer 2 of each $(H_2O)_n$ cluster is defined as:

$$\Delta E_{diff} = E^{isomer1}_{int} - E^{isomer2}_{int} \tag{2.16}$$

Following Ref. 1, the scores for the maximum total unsigned error and maximum absolute error are equal to 100 points if these errors are less than 1.0 kcal/mol, with additional 10 points deducted for each increment of 0.5 kcal/mol in the error. Using the CCSD(T)/CCSD(T)-F12 reference values of -0.87, -1.29, and -0.29 kcal/mol, for the tetramer, pentamer, and hexamer clusters, respectively,[1] a score of 100 points is assigned if the relative energy difference between isomers 1 and 2 is within 0.1 kcal/mol of the reference value and 10 points are deducted for every additional 0.1 kcal/mol thereafter. If a positive value is predicted for the relative energy difference, 0 points are assigned to the model. For scores that are negative, the sign of the relative energy difference is correct, but the difference is greater than 1.0 kcal/mol from the reference, and the value falls outside the bounds of chemical accuracy.

For each cluster, a small value for $\Delta E^{MB}_{int,\,max}$ accompanied by a large value for $\Delta E^{MB}_{unsigned,\,max}$ indicates that the model benefits from error compensation between individual many-body contributions. Table 2.2 shows that TTM3-F displays the largest difference between the scores of the maximum unsigned error (-110) and maximum absolute error (90) for the hexamer cluster. This indicates that, while the total interaction energy is apparently accurate, it is the result of significant error compensation between individual terms of the MBE. Similar trends, although less pronounced, are found for iAMOEBA and AMOEBA14. On the other hand, among the polarizable models, AMOEBA+CF and MB-UCB earn high scores for both $\Delta E^{MB}_{int,\,max}$ and $\Delta E^{MB}_{unsigned,\,max}$. It should be noted that MB-pol and fq-MB-pol score perfectly for each cluster size, indicating that these models do not rely on error compensation to correctly reproduce the corresponding

CCSD(T)/CCSD(T)-F12 reference interaction energies.

In the case of the tetramer, all models predict the correct sign for ΔE_{diff}, and the associated errors fall within 1.0 kcal/mol of the reference value, with only AMOEBA+ having a notably smaller score of 30. For the pentamer, the TTM4-F score is -80 points, indicating that, while

Table 2.2: Errors and associated scores assessing the accuracy of both polarizable and explicit many-body models in describing interaction and many-body energies for $(H_2O)_n$ clusters, with $n = 4-6$. $\Delta E^{MB}_{unsigned,max}$ (Eq. 2.14) and $\Delta E^{MB}_{int,max}$ (Eq. 2.15) are the maximum total unsigned error and maximum absolute total error in the many-body energy decomposition, respectively, while ΔE_{diff} (Eq. 2.16) is the energy difference between the interaction energies of isomers 1 and 2 of each cluster. All energies are in kcal/mol.

Model	Cluster	$\Delta E^{MB}_{unsigned,\,max}$	Score	$\Delta E^{MB}_{int,\,max}$	Score	ΔE_{diff}	Score
TTM2.1-F	$(H_2O)_4$	1.78	80	1.30	90	-0.58	70
	$(H_2O)_5$	3.90	40	1.50	80	-1.55	70
	$(H_2O)_6$	5.45	10	1.86	80	0.64	0
TTM3-F	$(H_2O)_4$	5.87	0	0.67	100	-0.67	80
	$(H_2O)_5$	9.06	-70	0.51	100	-0.95	60
	$(H_2O)_6$	11.18	-110	1.12	90	-0.21	100
TTM4-F	$(H_2O)_4$	3.15	50	3.15	50	-0.65	70
	$(H_2O)_5$	3.67	40	3.67	40	-3.00	-80
	$(H_2O)_6$	4.46	30	4.45	30	1.96	0
AMOEBA03	$(H_2O)_4$	1.58	80	0.49	100	-0.83	100
	$(H_2O)_5$	1.75	80	0.73	100	-1.29	100
	$(H_2O)_6$	2.94	60	0.59	100	-0.65	60
iAMOEBA	$(H_2O)_4$	4.50	20	1.16	90	-0.95	100
	$(H_2O)_5$	7.47	-30	1.38	90	-0.72	40
	$(H_2O)_6$	9.66	-80	2.14	70	-0.75	50
AMOEBA14	$(H_2O)_4$	3.48	50	0.70	100	-0.57	60
	$(H_2O)_5$	4.79	20	0.82	100	-1.14	80
	$(H_2O)_6$	7.05	-30	0.59	100	-0.03	70
AMOEBA+	$(H_2O)_4$	1.58	80	1.58	80	-1.56	30
	$(H_2O)_5$	2.43	70	2.40	70	-0.96	60
	$(H_2O)_6$	2.32	70	2.27	70	-0.88	40
AMOEBA+CF	$(H_2O)_4$	0.47	100	0.43	100	-0.71	80
	$(H_2O)_5$	0.96	100	0.60	100	-1.09	70
	$(H_2O)_6$	1.72	80	0.53	100	-0.07	70
MB-UCB	$(H_2O)_4$	1.77	80	0.83	100	-0.72	80
	$(H_2O)_5$	3.15	50	1.34	90	-0.91	60
	$(H_2O)_6$	2.85	60	1.39	90	-0.59	70
fq-MB-pol	$(H_2O)_4$	0.14	100	0.14	100	-0.79	100
	$(H_2O)_5$	0.31	100	0.31	100	-1.01	70
	$(H_2O)_6$	0.62	100	0.62	100	-0.31	100
MB-pol	$(H_2O)_4$	0.26	100	0.26	100	-0.80	100
	$(H_2O)_5$	0.51	100	0.51	100	-1.10	80
	$(H_2O)_6$	0.84	100	0.84	100	-0.32	100

getting the ranking of the isomers correct, this model predicts an overly large energy difference. In the case of the hexamer, both the TTM2.1-F and TTM4-F models score 0 points, meaning that they predict an incorrect order for isomers 1 (prism) and 2 (cage). AMOEBA03 earns a perfect score for the tetramer and pentamer clusters, but fails at correctly reproducing the energetics of the hexamer isomers. MB-pol and fq-MB-pol, on the other hand, score perfectly for the tetramer and hexamer clusters, but perform slightly less well for the pentamer cluster. Since MB-pol and fq-MB-pol are built on top of a classical representation of permanent electrostatics and polarization similar to that adopted by TTM4-F, their performance for the pentamer isomers indicates that the 2-body and 3-body PIPs have more difficulties compensating for the relatively large errors predicted by TTM4-F for these clusters.

2.4.3 Harmonic frequencies of water clusters

While the comparisons reported in the previous sections allow for a quantitative assessment of the ability of the different models to represent interaction and many-body energies for various minimum-energy structures of small water clusters, they do not provide any information about the overall morphology of the underlying multidimensional PES. Specific insights into the PES curvature in the neighborhoods of the minimum-energy structure of each isomer can be obtained from the analysis of the corresponding harmonic frequencies. For this purpose, Fig. 2.6 shows the deviations associated with both polarizable and explicit many-body models relative to the reference 2-body:many-body CCSD(T):MP2 harmonic frequencies reported in Ref. 2, 3.

Among the polarizable models, all TTM models, which employ a 1-body term exhibiting spectroscopic accuracy,[64] are able to quantitatively reproduce the harmonic frequencies of an isolated water molecule. However, differences in the representation of many-body effects discussed in the previous sections lead to large variations in the ability of these models to reproduce the harmonic frequencies of larger clusters. In particular, independently of the cluster size and structure, TTM2.1-F systematically overestimates the harmonic frequencies of both free

and hydrogen-bonded OH stretches. TTM3-F displays the opposite behavior, predicting relatively large redshifts for all OH stretching vibrations, while TTM4-F exhibits intermediate behavior, overestimating the vibrational frequencies of the free OH stretches while underestimating those of the hydrogen-bonded OH stretches. These trends indicate that TTM2.1-F predicts hydrogen bonds that are too weak while both TTM3-F and TTM4-F overestimate the strength of the hydrogen bonds. All TTM models accurately reproduce the harmonic frequencies of the bending vibrations. Qualitative differences are found in the low-frequency region of the spectra, with

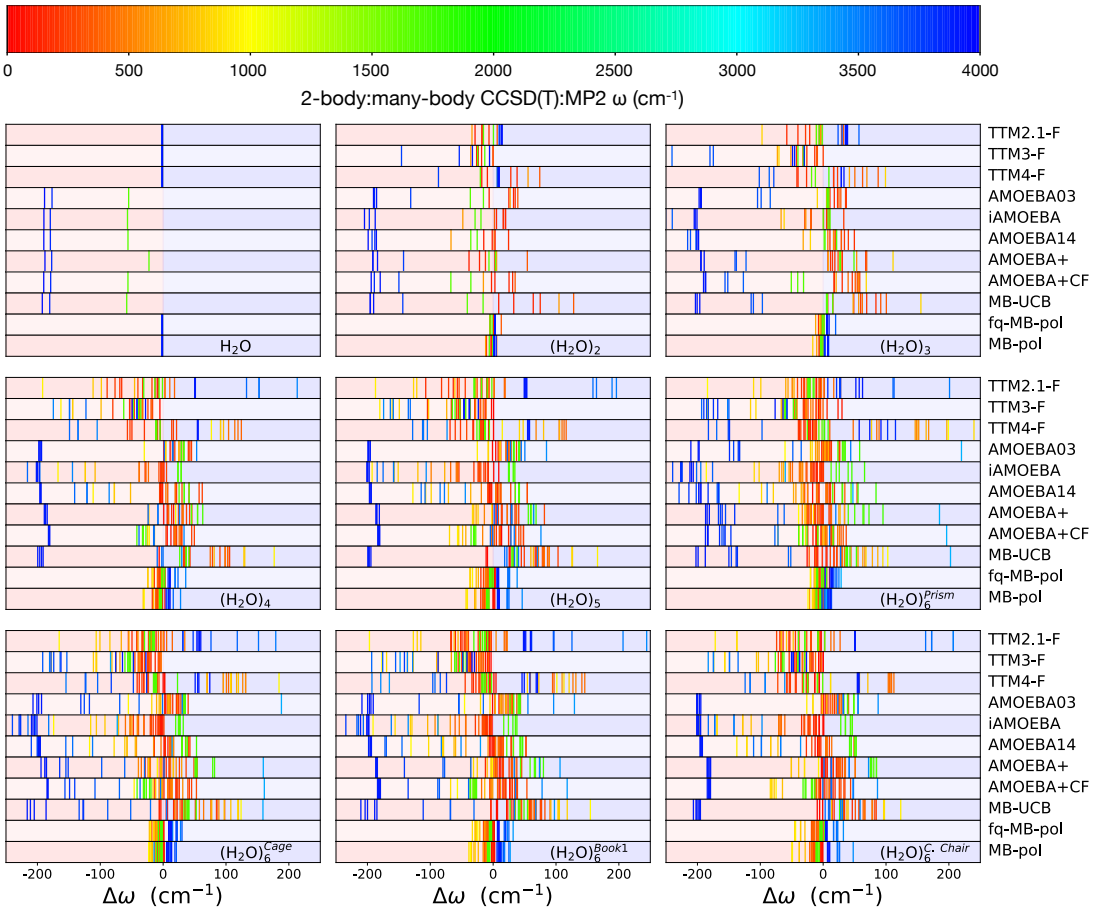

Figure 2.6: Deviations from reference 2-body:many-body harmonic frequencies of $(H_2O)_n$ clusters, with $n = 1-6$,[2, 3] calculated with both polarizable and explicit many-body models. The light red and blue backgrounds correspond to red and blue shifts relative to the reference values. Each harmonic mode, indicated by a stick line, is colored based on the associated frequency according to the colorbar displayed at the top of the figure.

TTM4-F, in general, overestimating (by up to $\sim$150 cm^{-1}) the harmonic frequencies of vibrational modes between 500 cm^{-1} and 1000 cm^{-1}, and both TTM2.1-F and TTM3.F systematically underestimating the harmonic frequencies of most of these modes. Since vibrational modes below 1000 cm^{-1} correspond to collective rearrangements of the hydrogen-bond network, these differences suggest that all TTM models, for different reasons, may have difficulties in correctly representing the hydrogen-bond dynamics in liquid water and its temperature dependence, which is in agreement with previous observations.[113, 116, 177]

Fig. 2.6 shows that AMOEBA03, AMOEBA+, AMOEBA+CF, and MB-UCB tend to largely underestimate, up to 200 cm^{-1}), the frequencies of the free OH stretching vibrations above 3700 cm^{-1}, which is traced back to the inability of these models to correctly predict the harmonic frequencies of an isolated water molecule. On the other hand, while these models still underestimate by $\sim$100 cm^{-1} the frequencies of weakly hydrogen-bonded OH stretches (at $\sim$3500 cm^{-1}), they significantly overestimate, by up to $\sim$150-200 cm^{-1}, the frequencies of strongly hydrogen-bonded OH stretches of the prism, cage, book1, and cyclic chair isomers of the hexamer cluster. Considering that these models underestimate the harmonic frequencies of the symmetric and asymmetric OH stretches of an isolated water molecule, the relatively large blueshifts predicted for OH stretches at $\sim$3200 cm^{-1} imply that the effective "solvochromatic shifts" for these vibrational fequencies can be up to $\sim$400 cm^{-1}, pointing to some deficiencies of these models in representing strong hydrogen bonds. AMOEBA03, AMOEBA+, AMOEBA+CF, and MB-UCB predict similar deviations within 100 cm^{-1} of the reference values for the bending vibrations ($\sim$1700 cm^{-1}), although larger variations are found in the ability of these models to reproduce collective vibrations (below 1000 cm^{-1}). In particular, while AMOEBA03, AMOEBA+, and AMOEBA+CF still exhibit deviations within 100 cm^{-1} of the reference values, relatively larger deviations of up to $\sim$150 cm^{-1} are associated with MB-UCB in this frequency region. These relatively large deviations suggest that, as the TTM models, MB-UCB may not be able to correctly describe the dynamical rearrangements of the water hydrogen-bond network.

Table 2.3: Absolute deviation (AD), average absolute devitation (AAD), and maximum absolute deviation (MAD) in cm^{-1} for the harmonic frequencies of selected isomers of $(H_2O)_n$ clusters with $n = 1-6$ calculated with both polarizable and explicit many-body models.

		H_2O isomer 1	$(H_2O)_2$ isomer 1	$(H_2O)_3$ isomer 1	$(H_2O)_4$ isomer 1	$(H_2O)_5$ isomer 1	$(H_2O)_6$ isomer 1	$(H_2O)_6$ isomer 2	$(H_2O)_6$ isomer 3	$(H_2O)_6$ isomer 6
TTM2.1-F	AD	-1.38	-5.39	-0.44	-1.01	1.59	2.25	2.12	1.75	3.80
	AAD	1.38	14.57	27.47	60.28	62.91	46.32	50.88	59.79	60.70
	MAD	2.36	33.66	97.25	213.33	252.42	384.57	352.9	293.6	259.55
	Score	100	90	60	0	-20	-90	-70	-40	-20
TTM3-F	AD	-1.38	-31.71	-56.61	-66.37	-65.18	-62.14	-64.37	-64.44	-62.25
	AAD	1.38	31.71	56.62	66.37	65.22	64.64	64.37	64.44	62.26
	MAD	2.36	145.79	240.43	174.67	180.29	193.36	191.60	193.22	182.82
	Score	100	30	-20	20	10	10	10	10	10
TTM4-F	AD	-1.38	7.75	7.75	10.41	1.82	7.29	9.32	9.13	-2.88
	AAD	1.38	30.19	46.30	62.17	53.73	89.70	66.78	60.31	52.33
	MAD	2.36	86.99	101.60	148.92	128.08	449.83	327.32	192.82	124.14
	Score	100	60	50	30	40	-120	-60	10	40
AMOEBA03	AD	-140.08	-49.6	-29.7	-6.9	-4.0	-17.3	-11.1	-4.9	-5.9
	AAD	140.08	76.0	54.3	47.3	48.8	46.0	46.3	49.4	46.5
	MAD	188.6	190.3	197.3	197.9	199.1	220.0	207.0	208.7	201.1
	Score	10	10	10	10	10	-10	0	0	0
iAMOEBA	AD	-141.95	-74.6	-73.0	-73.0	-74.4	-68.0	-72.1	-71.6	-72.1
	AAD	141.95	84.6	80.1	80.4	82.6	76.8	78.6	79.1	82.0
	MAD	189.7	269.2	264.0	215.8	200.5	239.5	239.8	234.3	200.8
	Score	10	-30	-30	0	0	-10	-10	-10	0
AMOEBA14	AD	-141.7	-73.4	-47.6	-39.2	-37.9	-44.4	-41.0	-38.5	-39.9
	AAD	141.7	78.3	74.2	66.1	59.7	65.8	63.6	61.1	59.9
	MAD	189.8	198.8	215.6	195.9	196.7	229.2	209.7	198.2	195.4
	Score	10	10	0	10	10	-10	0	10	10
AMOEBA+	AD	-129.3	-60.2	-20.5	-9.7	-5.5	-23.3	-17.9	-9.0	-3.1
	AAD	129.3	71.2	72.7	47.5	48.7	54.4	52.5	48.7	51.4
	MAD	188.0	191.4	194.7	189.0	186.2	187.0	194.3	186.4	184.3
	Score	10	10	10	10	10	10	10	10	10
AMOEBA+CF	AD	-141.61	-61.61	-28.82	-21.99	-22.86	-28.90	-23.17	-21.02	-26.31
	AAD	141.61	77.29	78.01	46.00	47.10	48.36	47.03	50.04	47.06
	MAD	189.94	193.98	190.30	182.44	183.37	196.42	184.40	183.95	184.36
	Score	10	10	10	10	10	10	10	10	10
MB-UCB	AD	-143.54	-30.73	-4.59	27.54	26.73	-1.40	12.86	20.04	11.77
	AAD	143.54	99.58	83.23	80.75	78.39	61.38	70.42	73.05	62.48
	MAD	192.23	195.65	203.18	199.47	199.15	202.58	216.20	210.44	206.40
	Score	10	10	0	10	10	0	0	0	0
fq-MB-pol	AD	-1.39	0.45	0.56	-0.91	-3.64	0.35	-0.85	-3.31	-6.26
	AAD	1.39	3.93	4.92	10.55	12.96	9.04	10.03	11.58	13.07
	MAD	2.37	12.95	19.81	35.92	38.20	28.58	30.00	33.05	45.06
	Score	100	100	100	90	90	90	90	90	80
MB-pol	AD	-1.38	-1.84	-1.67	-5.13	-6.00	-2.75	-3.28	-5.44	-7.29
	AAD	1.38	4.36	4.67	11.58	15.61	7.78	8.88	12.65	16.52
	MAD	2.36	11.97	16.53	31.40	46.22	24.10	23.02	38.55	49.37
	Score	100	100	100	90	80	90	90	90	80

As shown in Fig. 2.6, independently of the cluster size, both MB-pol and fq-MB-pol accurately reproduce the harmonic frequencies of all vibrational modes, with deviations always being within 50 cm^{-1} of the reference values. Since MB-pol and fq-MB-pol adopt the same 1-body term as the TTM models, the higher accuracy displayed in reproducing the harmonic frequencies is a direct consequence of both MB-pol and fq-MB-pol being able to quantitatively reproduce each individual term of the MBE in Eq. 6.4, as discussed in Section IVB.

Table 2.3 reports the average deviations (AD), average absolute deviations (AAD), and maximum absolute deviations (MAD) from the reference 2-body:many-body CCSD(T):MP2

harmonic frequencies[2, 3] calculated for the same water clusters analyzed in Fig. 2.6. To quantify the accuracy of each model in reproducing the reference values, we follow Ref. 1 and assign a score of 100 if the MAD is below 20 cm^{-1} and deduct 10 points for each additional increment of 20 cm^{-1}, until 0 points are reached. Since the TTM models use a highly accurate 1-body term, they score perfectly for the water monomer. However, the agreement with the reference harmonic frequencies deteriorates significantly for larger clusters, which can be attributed to deficiencies in the representation of the underlying interactions as discussed in Section IVB. On the other hand, the AMOEBA and MB-UCB models tend to suffer from large average absolute errors, with all models, except iAMOEBA, benefiting from error compensation as indicated by smaller average errors. Since these models already exhibit large deviations from the reference harmonic frequencies of the water monomer, the deviations observed for larger clusters result from inaccuracies in the description of both intramolecular and intermolecular potential energy surfaces. It should be noted that all polarizable models exhibit large maximum deviations on the order of 200-400 cm^{-1}, which, as shown in Fig. 2.6, are associated with OH stretching vibrations. Since these vibrations report directly on the local hydrogen-bonding environment,[178] these large deviations indicate that the TTM, AMOEBA, and MB-UCB models may not be able to correctly describe the structural and dynamical properties of the hydrogen-bond network. In contrast, both MB-pol and fq-MB-pol perform uniformly well for all cluster sizes and structures, with the corresponding MAD never exceeding 50 cm^{-1}, which is in agreement with previous studies of vibrational spectra of water in both gas and condensed phases.[137, 145, 148–151, 156, 157]

2.4.4 Liquid water

After determining the accuracy in reproducing interaction and many-body energies of small water clusters, and associated harmonic frequencies, this section investigates the ability of the different models to reproduce the energy landscape of liquid water. Since CCSD(T)/CBS simulations for liquid water in periodic boundary conditions are currently unaffordable, in the

following comparisons MB-pol is used as a reference. Although this choice is arbitrary, it can be justified by considering that several studies have demonstrated that MB-pol correctly reproduces structural, thermodynamic, dynamical, and spectroscopic properties of liquid water across a wide range of temperatures.[1, 39, 145, 148–151] For this analysis, we use molecular configurations corresponding to 5 ps of a longer CMD trajectory, which includes nuclear quantum effects,[171–175] carried out with MB-pol at 298.15 K for a system containing 256 water molecules.[148]

Fig. 2.7 shows that, among the polarizable models, TTM3-F and iAMOEBA more closely follows MB-pol, with average deviations per molecules of -0.15 kcal/mol and 0.31 kcal/mol, respectively, and maximum absolute deviations of 0.26 kcal/mol and 0.45 kcal/mol, respectively. These models are followed by AMOEBA14 that displays average and maximum absolute deviations of 0.48 kcal/mol and 0.57 kcal/mol, respectively. Interestingly, these three models perform rather well in this analysis despite displaying relatively poor agreement with the reference CCSD(T)/CCSD(T)-F12 many-body energies for small clusters. This suggests that, as already discussed in Section III B, the apparent better agreement with the MB-pol binding energies for liquid water likely results from error compensation between individual many-body

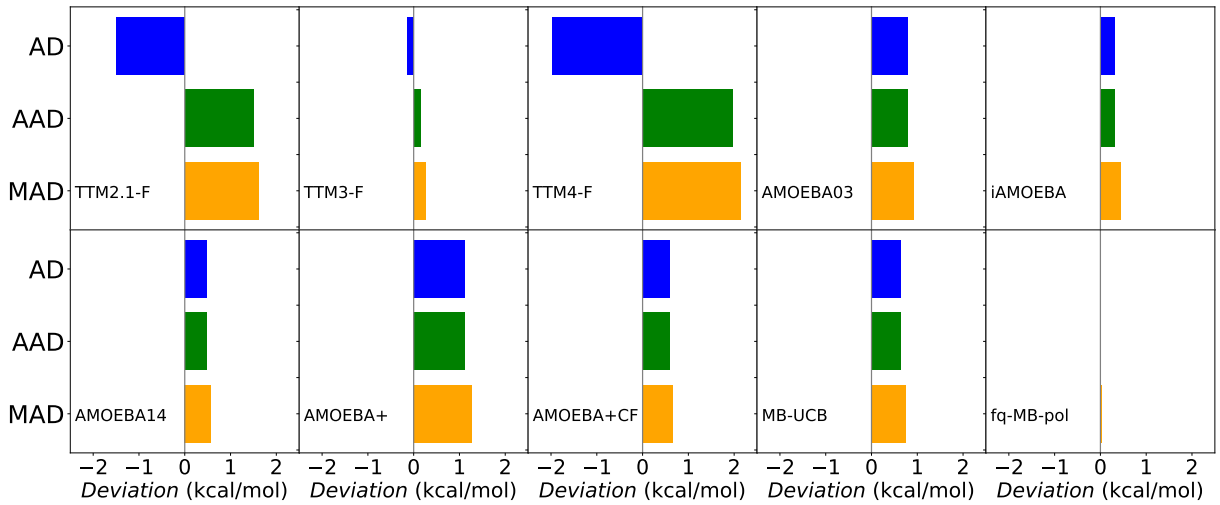

Figure 2.7: Average (AD), average absolute (AAD), and maximum absolute (MAD) deviations of the binding energy per molecule relative to the corresponding MB-pol values along 5 ps of a longer MB-pol CMD trajectory carried out at 298.15 K in Ref. 148.

Table 2.4: Average deviation (AD), average absolute deviation (AAD), and maximum absolute deviation (MAD) per molecule, calculated with both polarizable and explicit many-body models relative to the MB-pol binding energies per molecule along 5 ps of a MB-pol CMD trajectory carried out at 298.15 K in Ref. 148.

Model	AD (kcal/mol)	AAD (kcal/mol)	MAD (kcal/mol)
TTM2.1-F	-1.50	1.50	1.61
TTM3-F	-0.15	0.15	0.26
TTM4-F	-1.98	1.98	2.16
AMOEBA03	0.80	0.80	0.94
iAMOEBA	0.31	0.31	0.45
AMOEBA14	0.48	0.48	0.57
AMOEBA+	1.13	1.13	1.28
AMOEBA+CF	0.59	0.59	0.67
MB-UCB	0.64	0.64	0.75
fq-MB-pol	-0.02	0.02	0.03

contributions.

Relatively larger average deviations per molecule are instead found for TTM2.1-F (-1.50 kcal/mol), TTM4-F (-1.98 kcal/mol) and AMOEBA+ (1.13 kcal/mol), while AMOEBA+CF and MB-UBC provides similar average deviations on the order of 0.6 kcal/mol.

The comparisons in Fig. 2.7 show that the use of fixed atomic charges does not prevent fq-MB-pol from quantitatively reproducing the original MB-pol trajectory. Considering that permanent electrostatics is purely pairwise additive in both MB-pol and fq-MB-pol, the agreement shown in Fig. 2.7 provides further evidence for the ability of the 2-body PIP adopted by these models to correct for inherent deficiencies in classical representations of molecular interactions at short range and demonstrates that (small) differences in the representation of the 1-body charge distributions do not affect the accuracy of explicit many-body models in describing the interactions between water molecules, from small clusters to the liquid phase.

To provide a more immediate assessment of the ability of each model to reproduce the energy landscape of liquid water, Table 2.5 ranks all models based on the corresponding standard deviations shown in Fig. 2.7. Considering that ~ 4.5 molecules are within the first hydration shell as determined from the oxygen-oxygen radial distribution function (RDF) calculated with

Table 2.5: Average absolute deviations and corresponding scores calculated for the first hydration shell in liquid water using both polarizable and explicit many-body models relative to the MB-pol binding energies along 5 ps of a MB-pol CMD trajectory carried out at 298.15 K in Ref. 148. See text for details.

Model	Average absolute deviation (kcal/mol) for the first hydration shell	Score
TTM2.1-F	6.750	89
TTM3-F	0.675	99
TTM4-F	8.910	85
AMOEBA03	3.600	94
iAMOEBA	1.395	98
AMOEBA14	2.160	96
AMOEBA+	5.085	91
AMOEBA+CF	2.655	95
MB-UCB	2.880	95
fq-MB-pol	0.090	100

MB-pol at 298.15 K and 1 atm (which quantitatively agrees with the experimental RDF[39]), a score of 100 points is assigned if the average absolute deviation per molecule multiplied by 4.5 from the MB-pol binding energies is within 0.593 kcal/mol, which corresponds to k_BT at 298.15 K, with k_B being Boltzmann's constant, and 1 point is then deducted for each additional increment of k_BT. As already inferred from the analysis of Fig. 2.7, Table 2.5 shows that most polarizable models, with the exception of TTM4-F and AMOEBA+, provides similar performance relative to MB-pol, with scores between 81 and 88. This analysis shows that, already considering only the energetics of the first hydration shell in liquid water, this analysis the deviations of the TTM, AMOEBA, and MB-UCB models from MB-pol are, in all cases, larger than k_BT, which suggests that MD simulations of liquid water carried out with these polarizable models would likely sample different regions of the underlying multidimensional energy landscape from those sampled with MB-pol and, consequently, would lead to different molecular structures.

2.5 Conclusion

In this study we presented an assessment of state-of-the-art polarizable water models with flexible monomers based on a systematic analysis of interaction energies, many-body effects, and harmonic frequencies calculated for molecular systems of increasing size. For water clusters, comparisons were made with reference data calculated at the CCSD(T)/CBS level of theory, the current "gold standard" for chemical accuracy, while MB-pol was used as a reference for liquid water since it has been shown that this model accurately reproduces structural, thermodynamic, dynamical, and spectroscopic properties of water across the phase diagram.

Overall, our analysis indicates that significant progress has been made in the development of polarizable water models, although the path has not always been smooth and straight as demonstrated by early models (e.g., TTM2.1-F and AMOEBA03) often outperforming most recent models (e.g., TTM3-F, TTM4-F, iAMOEBA, and AMOEBA14). In particular, comparisons of interaction and many-body energies provide support for an early observation by **(author?)** that models able to more closely reproduce high-level *ab initio* data also appear to provide a more balanced description of the properties of water from the gas to the condensed phase.[47] This suggests that some caution should be used in relying on the agreement with experimental data for bulk properties during the parameterization procedure since, given the high dimensionality of the parameter space, the apparent agreement with experiment may often be the result of fortuitous error compensation. In particular, several polarizable models considered in our analysis appear to benefit from significant error compensation between 2-body and 3-body energies, which consequently leads to incorrect representations of hydrogen-bond strengths depending on the system size and structure as demonstrated by relatively large deviations from the reference OH-stretch harmonic frequencies of water cluster which are associated with all polarizable models.

The errors associated with 2-body and 3-body energies calculated with polarizable models

for distorted dimer and trimer configurations indicate that it may be difficult to tune the relatively simple functional forms adopted by popular polarizable models (e.g., TTM and AMOEBA models) to quantitatively account for each individual many-body contribution and, at the same time, be able to correctly describe structural, thermodynamic, and dynamical properties of liquid water. Even the most advanced polarizable models (e.g., AMOEBA+CF and MB-UCB), which provide improved descriptions of the energetics of small water clusters by adopting relatively more sophisticated parameterizations of various physical contributions to the interaction energies, do not display significant improvement in the description of the harmonic frequencies of water cluster and the energy landscape of liquid water. This suggests that, while rigorous and systematic physics-based parameterizations certainly improves the description of water systems in the neighborhoods of minimum-energy structures, the relatively simple functional forms adopted by polarizable models may not allow for a quantitative representation of the entire multidimensional energy landscape.

On the other hand, our analysis indicates that, independently of the system size and specific water arrangements, explicit many-body models (e.g., MB-pol and fq-MB-pol) effectively provide CCSD(T)/CBS accuracy for both minimum-energy and distorted structures. As discussed in previous studies,[132] this accuracy is owed to the flexibility of short-range 2-body and 3-body PIPs to correct for inherent deficiencies associated with classical representations of molecular interactions. Despite recent claims about certain polarizable models being comparable in performance to MB-pol,[108] the present analysis demonstrates that, as it should be expected after considering the different theoretical frameworks these models are built upon and the nature of the approximations used in the parameterization process, many-body models provide significantly higher accuracy and predictive power than existing polarizable models. Importantly, the analyses presented in this study also demonstrated that, with the development of more advanced representations of low-order n-body interactions, foregoing geometry-dependent atomic charges appear to have negligible impact on reproducing the CCSD(T)/CBS reference values, as illustrated by the

accuracy achieved by the fq-MB-pol model, which is able to accurately reproduce interaction and many-body energies and harmonic frequencies of small water clusters as well as the energetics of liquid water despite adopting fixed atomic charges.

Moving forward we believe that future developments of both polarizable and many-body models should continue in parallel and exploit synergies instead of aiming to compete. In particular, many-body models should serve as a reference for side-by-side comparisons that would provide guidance for systematic parameterizations of new polarizable models. In this regard, Ref. 1 provides extensive reference data calculated with MB-pol for various properties of water across the entire phase diagram which could be used to develop more balanced parameterizations of polarizable models capable of approaching "the right answers for the right reasons". On the other hand, while it has been shown that the same theoretical/computational framework adopted by MB-pol can be applied to more complex aqueous systems[179–190] and molecular fluids,[63, 191] future efforts should focus on the development of explicit many-body models for simulations of larger molecular systems in both gas and condensed phases, with the same accuracy exhibited by MB-pol for water.

2.6 Supplementary Material

Tables with interaction energies and harmonic frequencies of water clusters calculated with both polarizable and many-body explicit models.

2.7 Data Availability

The coordinates of all optimized clusters used in the analyses of the interaction and many-body energies as well as harmonic frequencies, along with the coordinates of the CMD trajectory used in the analysis of the energetics of liquid water are available at:

https://github.com/paesanilab/polarizable_water_models. Any other data generated and analyzed for this study that are not included in this Article and its Supplementary Material are available from the authors upon request.

2.8 Acknowledgements

We thank Colin Egan, Kartik Rallapalli, Kelly Hunter, and Jay Hu for useful discussion. We also thank Pengyu Ren, Jean-Philip Piquemal, and Chengwen Liu for guidance with the AMOEBA+ and AMOEBA+CF models, and Akshaya Das and Theresa Head-Gordon for providing all the data for the MB-UCB model. This research was supported by the U.S. Department of Energy, Office of Science, Office of Basic Energy Science through Grant No. DE-SC0019490. All graphs were generated using Matplotlib.[192] All calculations used resources of the Extreme Science and Engineering Discovery Environment (XSEDE), which is supported by the National Science Foundation through Grant No. ACI-1053575, under allocation TG-CHE110009, and the Triton Shared Computing Cluster (TSCC) at the San Diego Supercomputer Center (SDSC).

Chapter 2 is in full a reprint of the material as it appears in "Lambros, E., & Paesani, F. (2020). How good are polarizable and flexible models for water: Insights from a many-body perspective. *The Journal of Chemical Physics*" The dissertation author was the primary author of this paper.

Chapter 3

A Many-Body, Fully Polarizable Approach to QM/MM Simulations

We present a new development in quantum mechanics/molecular mechanics (QM/MM) methods by replacing conventional MM models with data-driven many-body (MB) representations rigorously derived from high-level QM calculations. The new QM/MM approach builds on top of mutually polarizable QM/MM schemes developed for polarizable force fields with inducible dipoles and uses permutationally invariant polynomials to effectively account for quantum-mechanical contributions (e.g., exchange-repulsion, and charge transfer and penetration) that are difficult to describe by classical expressions adopted by conventional MM models. Using the many-body MB-pol and MB-DFT potential energy functions for water, which include explicit 2-body and 3-body terms fitted to reproduce the corresponding CCSD(T) and PBE0 2-body and 3-body energies for water, we demonstrate a smooth energetic transition as molecules are transferred between QM and MM regions, without the need of a transition layer. By effectively elevating the accuracy of both the MM region and the QM/MM interface to that of the QM region, the new QM/MB-MM approach achieves an accuracy comparable to that obtained with a fully QM treatment of the entire system.

3.1 Introduction

Quantum mechanics/molecular mechanics (QM/MM) approaches that integrate quantum chemistry (QM) with molecular mechanics (MM), have been used to describe systems that cannot be completely modeled by a pure QM or MM approach. These methods, which treat a smaller subsystem (S) via a quantum mechanical framework and the surrounding environment (E) using a force field, were initially described by Warshel and co-workers in 1972, wherein they partitioned the σ and π electrons of a molecule into separate empirical and semi-empirical treatments.[193] The current QM/MM formalism was originally proposed in the seminal 1976 study by Warshel and Levitt, where a protein was split into separate QM and MM subsystems, which interacted via a dielectric coupling.[194]

In their infancy these QM/MM approaches were used to study small chemical reactions, such as halide exchange reactions of the form $CH_3Cl + Cl^-$ which needed a solvent to be accurately modeled.[33] Following the development of efficient interfaces between popular QM and MM software,[33] along with advances in computational power, it became possible to simulate larger and more complex systems, such as enzymatic and other biomolecular reactions.[34, 35] Furthermore, QM/MM saw success in the simulation of spectroscopic experiments of complex molecular systems.[36]

With regards to the formalism, most QM/MM approaches rely on an "effective Hamiltonian" which couples the properties of the electronic density of the subsystem S to a set of point charges representing the environment E. This coupling, known as the electrostatic embedding (EE), is commonly used with non-polarizable force-fields, as all electrostatic interactions between the two regions can be taken into account in a relatively straightforward and cost-effective way. However, in EE only the QM density is polarized by the environment and not vice versa. In particular, this implies that the interaction between the QM subsystem and the environment is the same, independently of the electronic state of the QM subsystem and/or the effects of an

external field. The solution to this conundrum, known as a "polarizable embedding" (PE), allows for the self-consistent equilibration of the classical degrees of freedom used to represent the electrostatic distribution of the environment, described with a polarizable force field[195–198], with the electronic density in the QM region. Early approaches to the PE method involved simple iterations over an electrostatic embedding scheme where the inducible dipoles could be back-polarized by point charges fit to the electronic density until the system converged.[199–202] A related approximation to the polarizable embedding was introduced with the LICHEM interface, which couples generic QM and MM software using a partially self-consistent polarization scheme, compromising some accuracy for a more generalized interface and grater computational efficiency.[203, 204]

By solving the QM equations and the MM polarization equations in a fully coupled fashion, some recent approaches adopt a more intimate coupling between the electron density in the QM region and the polarization in the MM region, with the latter being modeled by inducible point dipoles (IPD)[205–213], fluctuating charges[214–219], Drude oscillators.[220–225], or using a response kernel.[226, 227] In this contribution, we limit our discussion to IPD-based approaches, as this is the polarization model adopted by both the MB-pol [37–39] and AMOEBA [54, 58] models used in this analysis. We note, in passing, that an IPD polarization scheme is also present in other advanced QM/MM methods, such as the effective fragment potential method[228] and the X-pol method[229].

Several implementations exist of fully polarizable IPD-based QM/MM schemes[205, 209, 211, 230–232]. Over the years, these implementations have been extended to simulations of various molecular properties, with the QM subsystem in either the ground or an excited state, hydration properties and, more recently, *ab initio* multiscale molecular dynamics[210, 211, 218, 219, 223–225, 233, 234].

Beyond the issues associated with coupling the QM and the MM regions, QM/MM faces another methodological roadblock: diffusive breakup of the QM region. During a molecular

dynamics simulation in solution, molecules that were originally assigned to the QM region can diffuse apart, which lead to an effective exchange between QM and MM molecules. Such situations can result in low-accuracy MM molecules, which, by construction, cannot undergo any chemical transformation, moving into the original QM region of interest, while high-accuracy QM molecules are dispersed in the original MM region. So-called adaptive QM/MM schemes attempt to overcome this limitation by adaptively partitioning the molecules in the QM and MM regions at each step.[235–238] Although appealing, adaptive QM/MM schemes suffer from some drawbacks associated with the inherent differences between QM and MM descriptions of the energies and corresponding forces. Due to this, when a molecule is switched between QM and MM treatments during re-partitioning, the whole system can experience a large change in energy causing a discontinuity in the force. This can, for example, happen if the minima of the QM and MM energy landscapes are shifted relative to each other, which implies that a molecule located in a minimum energy configuration on the MM energy landscape can be thrust into a high-energy configuration when transitioned to the QM energy landscape.[235, 236, 239] In simulations, this behavior is manifested as unphysical dynamics along with structural artifacts at the QM/MM boundary.[34, 235, 236, 239, 240] In this thread, advances in adaptive QM/MM have focused on suppressing and reducing energetic discontinuities at the QM/MM boundary, often by using a transition layer to smoothly transition atoms between QM and MM treatments.[238] These techniques range from simple smoothing functions to more complex distance-based partitioning approaches which have been shown to conserve energy and smooth forces. [34, 236–239, 241–254]

Unfortunately, while these adaptive approaches improve energy conservation and alleviate some of the discontinuities in the forces, which, consequently, smooth out boundary artifacts that may occur, they do not solve the underlying issue in that the system is being represented by two different potential energy functions.[238] Furthermore, adoption of transition layers increases the computational cost of QM/MM simulations, as some schemes can result in up to 2^N additional

QM calculations for N molecules in the transition layer, though more modern partitioning schemes have been shown to significantly reduce that number. [236, 238, 239, 246, 250]

Other approaches using advanced representations of the energy landscape have attempted a more rigorous treatment of QM/MM systems. Effective and exchange fragment models (EFP and XFP respectively) partition the system into *ab initio* and effective fragment (EF) components, where the two regions interact via one electron integrals between *ab initio* and EF molecules.[255–259] Recent EFP approaches have further developed this by integrating exchange-repulsion style interaction potentials across the QM/MM boundary in order to account for some quantum effects missing from the core EFP interaction. [260] The Gaussian electrostatic model (GEM) uses a density fitting formalism to represent the MM region using molecular electron densities. [261] Incorporated into a QM/MM approach, GEM allows both the QM and the MM regions to be represented by an electron density, and thus affords the scheme much greater accuracy when evaluating QM/MM interactions. [262, 263] Building on these previous QM/MM approaches, we propose a new development, QM/MB-MM, in which the MM region is represented by data-driven models rigorously derived from the many-body expansion of the interaction energy. In this study, we describe the QM/MB-MM scheme using water as a prototypical example where the MB-MM region is described by the MB-pol[37–39] and MB-DFT[61] models. MB-pol and MB-DFT are many-body water models that include explicit terms fitted to reproduce 2-body and 3-body energies calculated at the CCSD(T) and DFT levels of theory, respectively. We demonstrate that QM/MB-MM combined with a polarizable embedding scheme effectively elevate QM/MM calculations to quantum mechanical levels of accuracy, specifically, CCSD(T) for MB-pol and PBE0 for MB-DFT. Importantly, by combining a PBE0 representation of the QM region with a MB-DFT model fitted to PBE0 2-body and 3-body data to represent the MM region, we demonstrate that energy discontinuities at the QM/MM boundary are largely suppressed and reduced to negligible effects.

3.2 Theory and Computational Details

All QM/MM calculations were carried out with the PBE0 functional along with the D3 dispersion correction using the aug-cc-pVQZ basis set.[166, 264–266] Gaussian16[267] was used for the QM calculations while an in-house code was used to handle the MB-pol and MB-DFT components incorporated into the QM/MM coupling framework.

3.2.1 Explicit many-body models: MB-pol and MB-DFT

MB-pol and MB-DFT are explicit many-body models based on the many-body expansion (MBE) which represents the energy of a system as the sum of individual n-body contributions in a system of N molecules with $n \leq N$.[37–39]

This is formally expressed as:[40]

$$E_N(r_1,..,r_N) = \sum_{i=1}^{N} \varepsilon_{1B}(r_i) + \sum_{i<j}^{N} \varepsilon_{2B}(r_i,r_j) + \sum_{i<j<k}^{N} \varepsilon_{3B}(r_i,r_j,r_k) + ... + \varepsilon_{NB}(r_1,..,r_N) \qquad (3.1)$$

where ε_{1B} represents the energy required to distort an individual monomer from its equilibrium geometry, and ε_{nB} with $n > 1$ are the n-body energies that are recursively defined as:

$$\varepsilon_{nB} = \varepsilon_n(1,...,n) - \sum_{i=1}^{N} \varepsilon_{1B}(r_i) - \sum_{i<j}^{N} \varepsilon_{2B}(r_i,r_j) - \sum_{i<j<k<...<n-1}^{N} \varepsilon_{(n\text{-}1)B}(r_i,r_j,..r_{n-1}). \qquad (3.2)$$

For molecules with localized electron density and large band gap, such as water, this expansion converges very quickly, with the sum of 2-body and 3-body energies contributing $\sim$90-95% to the total interaction energy.

The MB-pol[37–39] and MB-DFT[61] models include explicit representations for the first three terms of the MBE, while implicitly accounting for all higher order, $n > 3$ body terms

through a classical polarization term,

$$E_N(r_1,..,r_N) = \sum_{i=1}^{N} \varepsilon_{1B}(r_i) + \sum_{i>j}^{N} \varepsilon_{2B}(r_i,r_j) + \sum_{i>j>k}^{N} \varepsilon_{3B}(r_i,r_j,r_k) + E_{pol} \tag{3.3}$$

In these models, the 1B term is described by the Partridge-Schwenke potential energy surface, which was originally calculated at the configuration interaction level of theory and subsequently refined to quantitatively reproduce the experimental rovibrational transitions.[64] The 2-body term consists of three contributions:

$$\varepsilon_{2B} = E_{2B}^{sr} + E_{elec} + E_{disp} \tag{3.4}$$

where E_{2B}^{sr} is a 4^{th}-degree permutationally invariant polynomial (PIP)[65] representing short-range interactions within a water dimer. E_{elec} is described by Coulomb interactions between geometry dependent point charges which reproduce the *ab initio* dipole moment surface of a water molecule. [64] Lastly, the 2-body dispersion interaction is expressed as

$$E_{disp} = -\sum_{i,j} f(\delta_{ij}) \frac{C_{6,ij}}{R_{ij}^6} \tag{3.5}$$

where i and j are indices for atoms on two separate water monomers, $f(\delta_{ij})$ is the Tang-Toennies damping function with a fitted parameter δ_{ij},[66] and $C_{6,ij}$ are the dispersion coefficients calculated from the asymptotic reference energies of the water dimer as in CC-pol.[45] The explicit 3-body term,

$$\varepsilon_{3B} = E_{3B}^{sr} \tag{3.6}$$

represents short-range 3-body interactions and is represented by a 4^{th}-degree PIP[65]. In MB-pol, these explicit 2B and 3B terms were fitted on top of an implicit many-body polarizable term (E_{pol} in Eq. 5.8) to reproduce 2B and 3B energies calculated at the CCSD(T) level of theory in the complete basis set (CBS) limit.[37, 38] In the MB-DFT model, the explicit ε_{2B} and ε_{3B} terms

were instead fitted to 2B and 3B energies calculated at the PBE0-D3/aug-cc-pVQZ level of theory using the same procedure described in Ref. 61.

3.2.2 The QM/MM interaction with MB-pol and MB-DFT

In this section, we briefly overview the theory of IPD-based polarizable QM/MM at the self-consistent field level of theory, i.e., Hartree-Fock (HF) or DFT. A more detailed overview can be found in a recent review[268]. The MB-pol and MB-DFT polarization energy is variational with respect to the polarization degrees of freedom, which means that the coupled QM/MM equations and energy can be conveniently obtained starting from a variational energy functional[209, 212] of the SCF density $\mathbf{P}$ and the IPDs $\boldsymbol{\mu}$

$$\mathscr{E}(\mathbf{P},\boldsymbol{\mu}) = \mathscr{E}^{QM}(\mathbf{P}) + \mathscr{E}^{MM}(\boldsymbol{\mu}) + \mathscr{E}^{Coup}(\mathbf{P},\boldsymbol{\mu}) \tag{3.7}$$

where $\mathscr{E}^{QM}(\mathbf{P})$ and $\mathscr{E}^{MM}(\boldsymbol{\mu})$ represent the purely quantum mechanical and classical contributions to the energy, and $\mathscr{E}^{Coup}(\mathbf{P},\boldsymbol{\mu})$ describes the coupling between the two regions. The MM and coupling terms can then be combined into a general "environmental" $\mathscr{E}^{Env}(\mathbf{P},\mu)$ term:

$$\mathscr{E}(\mathbf{P},\boldsymbol{\mu}) = \mathscr{E}^{QM}(\mathbf{P}) + \mathscr{E}^{Env}(\mathbf{P},\boldsymbol{\mu}) \tag{3.8}$$

which is expressed as a sum of the MM contribution ($\mathscr{E}^{FF}$), the polarization energy ($\tilde{\mathscr{E}}^{Pol}$), and the electrostatic QM/MM coupling ($\mathscr{E}^{QM/MM}$):

$$\mathscr{E}^{Env}(\mathbf{P},\boldsymbol{\mu}) = \mathscr{E}^{FF} + \tilde{\mathscr{E}}^{Pol}(\mathbf{P},\boldsymbol{\mu}) + \mathscr{E}^{QM/MM}(\mathbf{P}) \tag{3.9}$$

The first term in Eq. 3.9 represents the energy of the MM region as described by a force field, which depends on neither the electron density nor the induced dipoles on the MM atoms, as well as any non-electrostatic interactions between the QM and MM regions, such as van der Waals

interactions between molecules in the QM and MM regions:

$$\mathscr{E}^{FF} = E^{MM}_{non-elec} + E^{QM/MM}_{non-elec}. \tag{3.10}$$

For the MB-pol and MB-DFT models which, besides the standard dispersion energy term, also incorporate 2B and 3B PIPs to account for short-range quantum-mechanical effects (e.g., charge transfer and penetration) missing in standard force fields, the first term of Eq. 3.10 becomes

$$E^{MB-pol}_{non-elec} = E_{disp} + E_{2b,sr} + E_{3b,sr} \tag{3.11}$$

Here, $E^{MB-pol}_{non-elec}$ sums up all the dispersion, and short-range 2B and 3B terms for the MM region alone, as well as all possible cross terms for pairs and triples of molecules split between the QM and MM regions. The 2B and 3B PIPs included in the QM/MM interaction, therefore, act as correction terms, allowing, in principle, the QM/MM energy to achieve the same accuracy as in purely QM calculations. In contrast, when the MM region is described with a standard polarizable force field, such as AMOEBA, the non-electrostatic QM/MM interaction only includes a van der Waals term represented by a force-field specific functional force, such as a standard 12-6 potential, or, for AMOEBA, a buffered 14-7 potential[54, 58, 203, 209, 212]:

$$E^{AMOEBA}_{non-elec} = E_{vdW} \tag{3.12}$$

We note here that in the QM/MB-pol scheme, the non-electrostatic interactions are modeled in a purely classical fashion, i.e., the associated energy contribution does not depend on the QM density, but only on geometrical parameters. This allows one to achieve high accuracy on the energy and structures without complicating the QM equations, but cannot reproduce quantum confinement effects on the QM density, which might be relevant to compute properties and model spectroscopies[228, 269, 270]. A density-dependent correction for MB-pol and MB-DFT is

currently under active investigation.

The second term of Eq. 3.9 is the most relevant one for the coupling of the QM and classical subsystems, as it describes the QM/MM polarization:

$$\tilde{\mathscr{E}}^{Pol}(\mathbf{P},\boldsymbol{\mu}) = \frac{1}{2}\boldsymbol{\mu}^{\dagger}\mathbf{T}\boldsymbol{\mu} - \boldsymbol{\mu}^{\dagger}(\mathbf{E}^{\mathrm{MM}} + \mathbf{E}^{\mathrm{QM}}(\mathbf{P})), \tag{3.13}$$

where μ is a vector that collects all the IPD, $\mathbf{T}$ describes the Thole-damped dipole interaction tensor, and

$$E_i^{QM}(\mathbf{P}) = \sum_{\alpha} Z_{\alpha}\frac{R_{\alpha}-r_i}{|R_{\alpha}-r_i|^3} - \sum_{\mu\nu} P_{\mu\nu}\int \chi_{\mu}(r)\chi_{\nu}(r)\frac{r-r_i}{|r-r_i|^3}d^3r \tag{3.14}$$

is the electric field due to the QM density at the i-th polarizable site.[37, 232] We remark that the QM field is the sum of the contributions of the nuclei, with charges Z_{α} at positions R_{α}, and of the electronic density, that has been expanded in a basis of atomic orbitals χ. Finally, the third term in Eq. 3.9 represents the interaction of the electron density with the static charges:

$$\mathscr{E}^{QM/MM}(\mathbf{P}) = \boldsymbol{q}^{\dagger}\boldsymbol{V}^{QM}(\boldsymbol{P}), \tag{3.15}$$

where $\boldsymbol{V}^{QM}$ is the QM electrostatic potential and $\boldsymbol{q}$ is a vector that collects all the point charges, that represent the permanent electrostatic distribution in MB-pol and MB-DFT. The coupled QM/MM equations are easily obtained by minimizing the variational energy functional in eq. 3.7 with respect to the QM density and the IPDs, taking into account the constraints on the density. In particular, by differentiating with respect to the elements of the density matrix, we get the QM/MM Fock (Kohn-Sham, KS) matrix:

$$F_{\mu\nu} = F_{\mu\nu}^{\mathrm{vac}} + \boldsymbol{q}^{\dagger}\boldsymbol{V}_{\mu\nu} - \boldsymbol{\mu}^{\dagger}\mathbf{E}_{\mu\nu}, \tag{3.16}$$

where F^{vac} is the standard Fock (KS) matrix and $\boldsymbol{V}_{\mu\nu}, \boldsymbol{E}_{\mu\nu}$ are standard potential and electric field one-electron integrals.[209] The polarization equations are obtained by differentiating with

respect to the IPD:

$$\mathbf{T}\boldsymbol{\mu} = \mathbf{E}^{\mathrm{MM}} + \mathbf{E}^{\mathrm{QM}}(\mathbf{P}). \tag{3.17}$$

We note that the QM and polarization equations are coupled, as the Fock (KS) matrix depends on the IPDs, while the right-hand side of the polarization equations depends on the QM density. Within a SCF approach, the coupled equations are solved by computing the IPDs at each SCF cycle by solving eq. 3.17 either with a direct method or iteratively, and then using them to assemble the environment contribution to the Fock (KS) matrix, which is in turn diagonalized to get a new density, until convergence is achieved.

For the QM/AMOEBA polarizable QM/MM scheme, a few modifications need to be introduced, as the model is non variational and includes higher order multipolar moments into the permanent electrostatic distribution. A detailed derivation of the electrostatic and polarization interactions can be found in the relevant literature.[209, 212]

In our analysis, we also consider a simplified polarizable embedding scheme implemented in the LICHEM software.[203, 204] In this scheme, the electrostatic interaction between QM and MM regions is separated into two components. The first component accounts for the polarization of the QM region induced by the point charges in the MM region, while the second component accounts for the back-polarization of the the MM region induced by the polarized QM charges. For multipolar models that contain permanent dipoles and quadrupoles, such as AMOEBA, a set of six point charges are octahedrally distributed about each atom to guarantee that the permanent multipole moments are correctly described.[203]

In this work, the fully self-consistent polarizable QM/MM scheme is referred to as fsc-QM/MB-MM, and the partially self-consistent polarizable QM/MM scheme implemented in LICHEM is referred to as psc-QM/MB-MM.

3.3 Results and discussion

3.3.1 Water dimer

As an initial demonstration, Fig. 3.1 shows the QM/MB-MM interaction energies of the water dimer calculated along MP2/aug-cc-pVQZ scans obtained by optimizing the positions of the hydrogen atoms for each fixed oxygen-oxygen distance. In this analysis, both possible QM/MB-MM partitions were examined, with the QM region containing either the hydrogen-bond donor or the hydrogen-bond acceptor. The QM/MB-MM energies, calculated using both the fully self-consistent polarizable (fsc-QM/MB-MM)[209, 212, 213] and the partially self-consistent polarizable (psc-QM/MB-MM)[203, 204] schemes, are compared against the corresponding full MB-MM and QM values calculated with MB-pol and PBE0-D3, respectively. The kink in the plot occurring at $\sim$2.7 Å corresponds to configurations that shift from a "sheared" geometry, where the two water molecules are symmetrically flipped, to a "hydrogen-bonded" geometry, as displayed in the upper left panel of Fig. 3.1.

When the QM water molecule donates the hydrogen bond, the fsc-QM/MB-pol energies lie close to the MB-pol reference values in the neighborhood of minimum-energy geometry (between 2.7 and 3.2 Å), with the largest deviation of $\sim$ 0.1 kcal/mol occurring near the kink at 2.7 Å. The psc-QM/MB-pol scheme yields comparable results, although it tends to slightly overestimate the interaction strength, giving rise to a larger maximum error of $\sim$ 0.25 kcal/mol in correspondence of the kink. When the partition is reversed, such that the QM water molecule becomes the hydrogen-bond acceptor, a much larger overall error is observed in both QM/MB-MM schemes. In this case, the fsc-QM/MB-pol scheme overestimates the interaction energy by $\sim$ 0.3 kcal/mol at the kink, while underestimating the interaction energy at the minimum by about 0.2 kcal/mol. The psc-QM/MB-pol scheme predicts a larger error of $\sim$ 0.5 kcal/mol at the kink but reproduces the minimum energy within 0.05 kcal/mol of the reference MB-pol value.

The bottom panels of Fig. 3.1 compare the reference MB-pol and PBE0-D3 interaction

energies to the corresponding QM/MB-DFT values where, as described in Section 4.2, the MB-DFT model was fitted to reproduce 2B and 3B PBE0-D3/aug-cc-pVQZ energies. Similar to the QM/MB-pol case, when the QM water molecule is the hydrogen-bond donor, the fsc-QM/MB-DFT scheme underestimates the PBE0-D3 interaction energies, with the largest error of about 0.1 kcal/mol found at the kink. The psc-QM/MB-DFT scheme predicts an error of $\sim$ 0.2 kcal/mol for the same configuration. When the QM/MM partition is switched and the QM water molecule becomes the hydrogen-bond acceptor, both the fully and partially self-consistent schemes overestimate the reference PBE0-D3 interaction energy at the kink, with the errors being $\sim$0.3 and $\sim$0.5 kcal/mol, respectively. The fsc-QM/MB-DFT scheme underestimates the interaction energy at the minimum by $\sim$0.1 kcal/mol, while the psc-QM/MB-DFT scheme overestimates it by $\sim$0.1 kcal/mol.

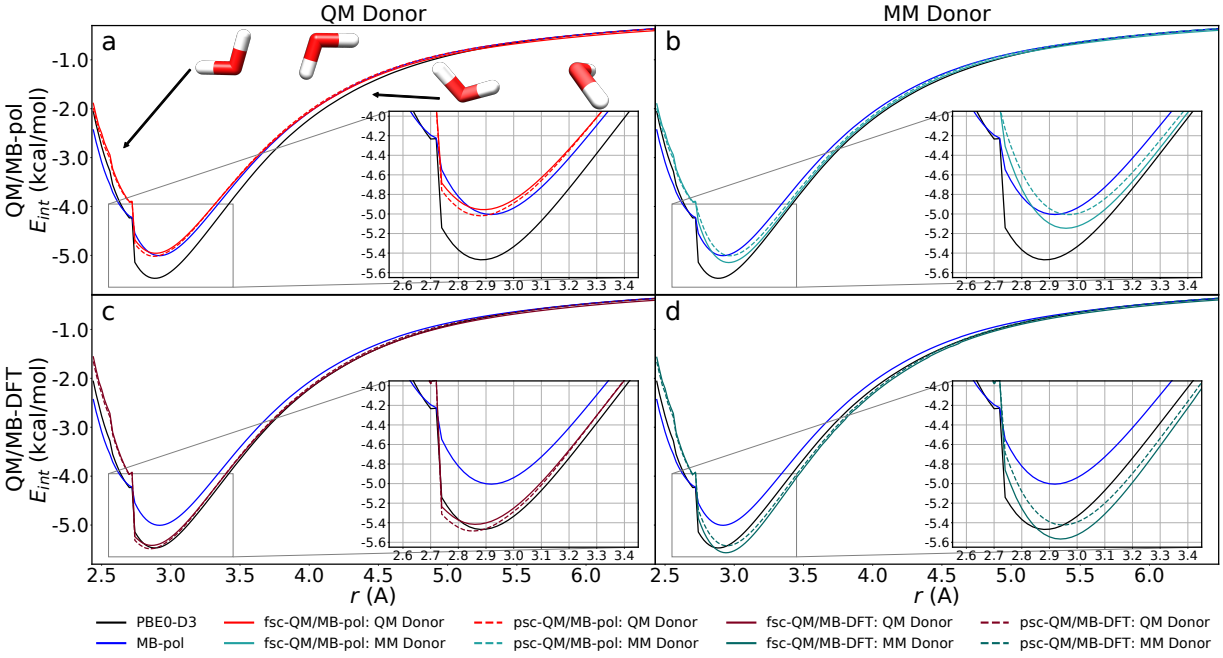

Figure 3.1: Comparison of the QM/MM interaction energy against the MB-pol and PBE0-d3 values over the MP2/aug-cc-pvqz optimized dimer scan. a) QM/MB-pol results with the QM water molecule as the hydrogen-bond donor. b) QM/MB-pol results with the MM water molecule as the hydrogen-bond donor. c) QM/MB-DFT results with the QM water molecule as the hydrogen-bond donor. d) QM/MB-DFT results with the MM water molecule as the hydrogen-bond donor.

Because QM/MB-pol and QM/MB-DFT only differ in the identity of the 2B and 3B PIPs (along with the Tang-Toennies damped dispersion), the shift in the interaction energies from QM/MB-pol, which closely reproduces the MB-pol values, to QM/MB-DFT, which instead closely reproduces the PBE0-D3 values, is due to the MB-DFT PIPs correctly compensating the core QM/MM electrostatic interaction. If the QM/MM electrostatic interaction is sufficiently similar to the core MM electrostatic interaction, these results suggest that the 2B and 3B corrections used in MB-pol and MB-DFT can be successfully integrated into a QM/MM scheme to correctly account for the deficiencies in the core QM/MM interaction. In both QM/MB-pol and QM/MB-DFT, smaller overall deviations from the corresponding MB-pol and PBE0-D3 reference values are observed when the QM water molecule donates the hydrogen bond compared to those found when the QM water is the hydrogen-bond acceptor. Furthermore, between these two partitions, the QM hydrogen-bond donor case predicts a minimum that is slightly shifted to a shorter distance, indicating a slightly more attractive interaction between water molecules. On the other hand, in the QM hydrogen-bond acceptor case, the minimum is shifted significantly to a larger distance (by $\sim$0.15 Å), indicating that both QM/MB-pol and QM/MB-DFT overall predict a more repulsive interaction relative to the MB-pol and PBE0-D3 references, respectively. This"repulsive shift" observed in the QM hydrogen-bond acceptor case carries out to the region beyond the minimum, where both QM/MB-pol and QM/MB-DFT consistently underestimate the interaction energies as the two water molecules are taken apart. This indicates that, depending on which molecule (QM or MM) is the hydrogen-bond donor, the difference between the QM/MB-MM and MB-MM descriptions of the underlying electrostatic interactions may become significant and possibly incompatible with the corrections provided by the PIPs at short range.

In the short-range region, where the two water molecules are closer than 2.7 Å, they adopt a symmetrically flipped "sheared" geometry. Due to the symmetry of these dimer configurations, the two possible QM/MM partitions are virtually identical and, consequently, predict the same QM/MM energies. The close vicinity of the water molecules in these configurations makes

the distinction of the QM and MM regions somewhat blurred, which implies that the QM/MM electrostatic interaction become more quantum mechanical in nature, with the point charges and dipoles of the MM molecule penetrating the electron density of the QM molecule. The consistently higher error of $\sim$0.5 kcal/mol observed for these configurations can thus be attributed to the expected incompatibility of the short-range PIPs, which were optimized for a purely MB-MM description of the interaction energies, with the QM/MM electrostatics.

3.3.2 Water 2-body energies

With the previous section evaluating the performance of QM/MB-pol and QM/MB-DFT for an optimized water dimer scan where the geometries of the two water molecules lied close to the corresponding minimum-energy conformation, this section explores the performance of QM/MB-pol and QM/MB-DFT for a set of 1000 dimers with more distorted molecular geometries randomly extracted from the original MB-pol 2B training set.[37] Fig. 3.2 shows correlations between 2-body energies calculated with the QM/MB-pol, QM/MB-DFT, and QM/AMOEBA14 schemes, and the corresponding CCSD(T) and PBE0-D3 reference values for this set of distorted dimers. For this analysis, the CCSD(T) 2B energies in the complete basis set limit were taken from the original MB-pol reference[37] while the corresponding PBE0-D3 values were calculated with Gaussian16 using the aug-cc-pVQZ basis set. In order to exclude from this analysis overly distorted dimers whose CCSD(T)-based geometry-dependent MB-pol charges may significantly deviate from those predicted by PBE0-D3, and thus provide a more electrostatically consistent QM/MM interaction, the RMSDs reported in Fig. 3.2 are calculated considering only configurations whose maximum intramolecular OH bond length is shorter than 1.16 Å, corresponding to the 90^{th} percentile of the entire set. It should be emphasized that, in actual QM/MM simulations, these distorted dimers with elongated OH bonds should effectively be included in the QM region since they represent configurations involved in the water autoionization process.

The RMSDs relative to the CCSD(T) 2B energies are 0.92, 0.60, and 0.69 kcal/mol for the

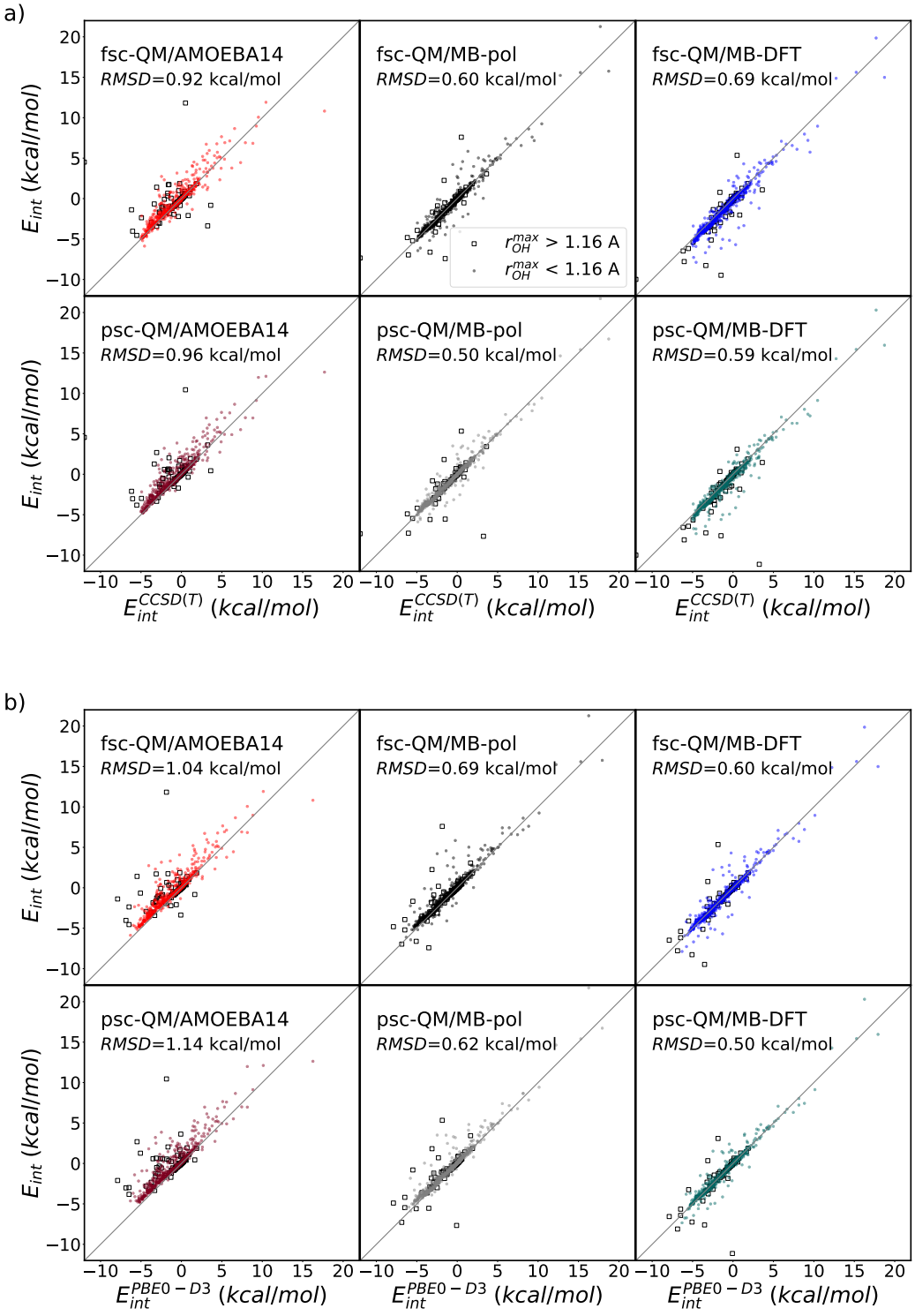

Figure 3.2: Correlations between the QM/MM interaction energies of 1000 water dimers calculated with AMOEBA14, MB-pol, and MB-PBE0 representing the MM region, and PBE0-D3 representing the QM region, and the corresponding CCSD(T) (panels a) and PBE0-D3 (panels b) values. Each RMSD is calculated for configurations whose maximum intramolecular OH bond length is shorter than 1.6 Å.

fsc-QM/AMOEBA14, QM/MB-pol, and QM/MB-DFT schemes, respectively. A similar trend is found for the RMSDs calculated relative to the PBE0-D3 2B energies, with values of 1.04, 0.69, and 0.60 kcal/mol for QM/AMOEBA14, QM/MB-pol, and QM/MB-DFT, respectively. Slightly smaller values are obtained using the partially self-consistent scheme, with QM/AMOEBA14, QM/MB-pol, and QM/MB-DFT being associated with RMSDs of 0.96, 0.50, and 0.59 kcal/mol, respectively, relative to the CCSD(T) 2B energies, and 1.14, 0.62, and 0.50 kcal/mol, respectively, relative to the PBE0-D3 2B energies.

The overall decrease in the RMSD values observed for the QM/MB-pol and QM/MB-DFT schemes relative to QM/AMOEBA14 is attributed to the ability of the PIPs adopted by the explicit many-body models to account for short-range quantum-mechanical effects (e.g., charge transfer and penetration) which cannot be quantitatively recovered by the purely classical expressions used in the QM/AMOEBA14 scheme. QM/MB-pol, which employs PIPs specifically fitted to account for the difference in 2B energies between the 2B CCSD(T) reference energies and the classical components of the 2B MB-pol energies, shows the smallest RMSD relative to CCSD(T). Correspondingly, QM/MB-DFT, which uses the same PIPs as MB-pol but fitted to PBE0-D3 2B reference energies, shows the smallest QM/MM RMSD relative to PBE0-D3. These results, which hold for both the fully and partially self-consistent schemes, suggest that, respective to their references, the PIPs fitted to CCSD(T) and PBE0-D3 are able to compensate, at least in part, for the differences between the actual quantum-mechanical 2B energies (ε_{2B} in Eq. 4) and the corresponding classical 2B terms (i.e., E_{elec} and E_{disp} in Eq. 4), even for distorted dimer configurations.

It is particularly interesting to note that the psc-QM/MB-pol and QM/MB-DFT exhibit lower RMSDs than their fully-consistent counterparts. This apparently counterintuitive result can be understood by considering that the partially self-consistent QM/MM scheme may benefit from a more "MM-like" representation of the QM/MM electrostatics, as part of the QM/MM polarization is evaluated using the MM functional form. Specifically, in the psc-QM/MB-MM, the

MB-MM region gets back-polarized by the polarized QM point charges, instead of the electron density as in the fully self-consistent QM/MB-MM scheme, which makes part of the QM/MM polarization more similar to that of the MM model. As a result, this more MM-like treatment of the QM/MM electrostatics within the psc-QM/MM scheme is, by construction, more compatible with the PIPs of the MB-pol and MB-DFT models which were fitted to the differences between the 2B CCSD(T) and PBE0-D3 energies, respectively, and the classical electrostatic and dispersion terms.

3.3.3 QM/MM partitions for the water hexamer

With the the two previous sections focusing on dimer configurations, which report at most on 2-body contributions to the interaction energies, in this section we examine the ability of the QM/MB-MM scheme to reproduce the energetics of the water hexamer isomers. Here, it should be emphasized that as MB-pol and MB-DFT were explicitly trained only up to the 3B energy, they do not have any prior knowledge of systems containing more than 3 water molecules.[37, 38, 61]

While the analysis described in the following will specifically focus on the prism isomer, which is the lowest-energy isomer of the water hexamer,[137] analogous analyses for other low-lying isomers are reported in the Supporting Information. Starting with the cluster containing one water molecule in the QM region, water molecules are successively included in the QM region until a total of five water molecules are placed in the QM region. As water molecules are added, one at a time, all possible QM/MM partitions are examined. This analysis thus examines the effects of adding (subtracting) water molecules to (from) the QM region, as it might happen during adaptive QM/MM simulations in solution. The interaction energies calculated for the different QM/MM partitions as a function of number of water molecules in the QM region are shown in Fig. 3.3 where they are compared with the corresponding MB-pol and PBE0-D3 values. Within each column of Fig. 3.3, the QM/MM partitions keep the number of QM and MM molecules constant but permute the QM and MM indices, which allow us to assess the performance of the

QM/MB-pol and QM/MB-DFT schemes depending on all possible spatial arrangements of the QM and MM water molecules within the prism cluster.

With one water in the QM region, the interaction energies calculated for the different QM/MM partitions using both the fully and partially self-consistent QM/MB-pol schemes lie,

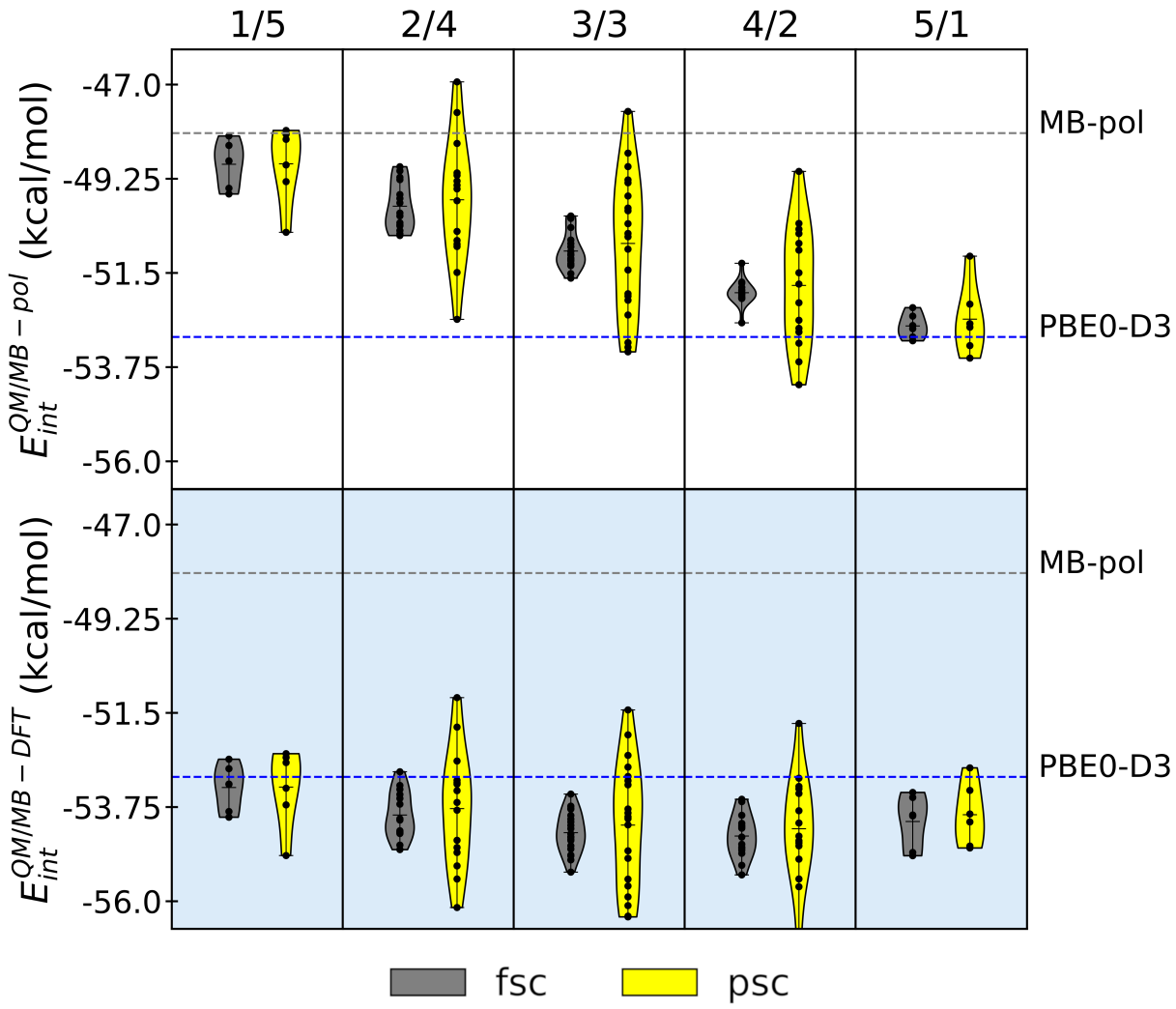

Figure 3.3: Interaction energies of the prism isomer (isomer 1 in Ref. 1) of the water hexamer calculated using QM/MB-pol and QM/MB-DFT for all possible QM/MM partitions involving 1 to 5 water molecules in the QM region using fully self-consistent (fsc) and partially self-consistent (psc) cross-polarization between the QM and MM regions. The grey line is the MB-pol reference energy and the blue line is the PBE0-D3 reference energy. The numbers at the top of each column determine the number of water molecules in the QM and MM regions (num QM / num MM).

on average, within $\sim$1.5 kcal/mol of the reference MB-pol energies, with only one partition of the psc-QM/MB-pol scheme displaying a deviation of $\sim$2.3 kcal/mol. Successively including one water to the QM region linearly shifts the distribution of QM/MB-pol energies towards the QM value. When the QM/MM partition contains five water molecules in the QM region, the QM/MB-pol energies lie within 0.6 and 1.5 kcal/mol of the PBE0-D3 value for the fsc-QM/MB-pol and psc-QM/MB-pol schemes, respectively. On the other hand, fsc-QM/MB-DFT and psc-QM/MB-DFT calculations for the partition with one water molecule in the QM region predict interaction energies that are within 1.0 and 2.0 kcal/mol, respectively, of the reference PBE0-D3 value. The successive addition of water molecules results in fsc-QM/MB-DFT and psc-QM/MB-DFT interaction energies that are within 1.5 and 1.3 kcal/mol, respectively, of the PBE0-D3 reference value for the partition containing five water molecules in the QM region. The largest deviations (up to 2.25 kcal/mol for fsc-QM/MB-DFT and up to 3.54 kcal/mol for psc-QM/MB-DFT) relative to the PBE0-D3 value are found for the symmetric partition with three water molecules in both the QM and MM regions. Furthermore, independently of using the partially or fully self-consistent schemes, the largest deviations in the distributions of both QM/MB-pol and QM/MB-DFT interaction energies are associated with configurations in which the QM water molecule is a double hydrogen-bond acceptor from two MM water molecules. This is consistent with the results in Section 3.3.1 where the case of the MM donor (QM acceptor) displays the largest error in the scan of the water dimer potential energy surface.

Compared to the QM/MB-pol interaction energies, which are increasingly weighted towards the PBE0-D3 reference value as the number of water molecules in the QM region increases, the QM/MB-DFT results remain relatively close to the PBE0-D3 reference value, independently of how the water molecules are partitioned in the QM and MM regions. The different trend found for interaction energies calculated with QM/MB-pol and QM/MB-DFT as a function of the number of water molecules in the QM region can be explained by considering that the only differences between the MB-pol and MB-DFT potential energy functions derive

from the differences in the corresponding 2B and 3B PIPs. Since the MB-pol PIPs were fitted to CCSD(T)/CBS 2B and 3B energies, this implies that, when the QM/MM partition includes only one water molecule in the QM region, all possible 2B and 3B energies within the hexamer contains contributions from the corresponding MB-pol PIPs. In the opposite limit, when five water molecules are placed in the QM region, only 6 out of 15 2B energies and 10 out of 20 3B energies include contributions from the corresponding MB-pol PIPs. As a result, the QM/MB-pol interaction energy approaches the PBE0-D3 reference value as the number of water molecules in the QM region increases because the contributions from the MB-pol PIPs become progressively smaller. In contrast, since the MB-DFT PIPs were fitted to PBE0-D3 2B and 3B energies, all possible 2B and 3B contributions to the QM/MB-DFT interaction energy, independently of the QM/MM partition, are effectively described at the PBE0-D3 level (either through actual PBE0-D3 calculations in the QM region or through the MB-DFT PIPs in the MM region). As a result, the QM/MB-DFT interaction energies remain relatively close to the PBE0-D3 reference value for all different partitions, that the QM/MB-DFT scheme enables smooth transitions between QM regions described by an arbitrary DFT model and MM regions described by the corresponding MB-DFT potential energy function, which is particularly appealing for QM/MM simulations in solution.

Fig. 3.3 shows that, while the psc-QM/MB-pol and psc-QM/MB-DFT scheme displayed smaller RMSDs than the corresponding fully self-consistent schemes for energetics of water dimers (Fig. 3.2), they predict wider spread than the corresponding fully self-consistent schemes in the interaction energies of the prism hexamer, depending on the spatial arrangements of the water molecules in the QM and MM regions. In particular, the psc-QM/MB-pol and psc-QM/MB-DFT calculations predict the largest spread of 4.5 kcal/mol for the symmetric QM/MM partition, with 3 water molecules in both QM and MM regions, which must be compared with a spread of $\sim$1.5 kcal/mol predicted by the corresponding fully self-consistent schemes. This symmetric QM/MM partition contains the largest number of different spatial arrangements of the QM and

MM molecules, resulting in 20 total permutations, as well as the largest number of 2B (9) and 3B (18) QM/MM energies. The large number of 2B and 3B QM/MM interactions serves to amplify possible inaccuracies of the 2B and 3B PIPs as even relatively small errors in the description of individual 2B and 3B energies add up, resulting in larger total errors and, consequently, wider spreads for interaction energies calculated for different QM/MM partitions. Importantly, as shown in Figs. S10 and S11 of the Supporting Information, both psc-QM/MB-DFT and fsc-QM/MB-DFT are able to reproduce, on average, the interaction energies and relative stabilities of the water hexamers predicted by PBE0-D3, independently of the QM/MM partition. This suggests that, when employed in adaptive QM/MM simulations, QM/MB-DFT would correctly sample the same water configurations as in fully QM simulations.

The analysis reported in Fig. 3.3 underscores the importance of many-body polarization effects in QM/MM calculations. In particular, the relatively wider spreads associated, on average, with interaction energies of the water hexamer calculated with the psc-QM/MB-pol and psc-QM/MB-DFT schemes are due to the neglect of fully self-consistent polarization effects between the QM and MM regions, which are included in the corresponding fsc-QM/MB-pol and fsc-QM/MB-DFT schemes. These findings are further underscored by observing that both fully and partially self-consistent polarization schemes predict similar spreads of the interaction energies for the two limiting QM/MM partitions, with 1 and 5 water molecules in the QM region, respectively, which correspond to the two QM/MM partitions with the smallest contributions from mutual polarization between the QM and MM regions.

3.4 Conclusions

We presented here a new development in QM/MM, integrating the MB-pol and MB-DFT models into a polarizable embedding, allowing the dipoles in the MM region to self-consistently equilibrate with the density in the QM region. On top of this embedding, the PIPs used in MB-pol

and MB-DFT, which are fitted to recover the CCSD(T) and PBE0-D3 energies at the 2B and 3B levels, are incorporated into the QM/MM interaction. We show that use of both QM/MB-pol and QM/MB-DFT increases the overall accuracy of the QM/MM interaction, as the PIPs account for the leading order dispersion and repulsion energies. Using both partially and fully self consistent mutual polarization between the QM and MM region, we show that a fully self consistent scheme is required to fully capture the polarization effects in larger and more complex water clusters. More importantly, we demonstrate a consistent treatment between QM and MM regions. Using MB-DFT, the MM region can be represented at the same level of accuracy as an arbitrary DFT functional used in the QM region. In our case, using PBE0-D3 as the functional of choice, we can consistently represent an entire QM/MM system, with the pure MM, QM, and QM/MM interactions at the PBE0-D3 level of theory. As demonstrated in our analysis of the water hexamer, this consistent scheme mitigates the change in energy when a molecule is added to or removed from the QM region, as might happen during an adaptive QM/MM simulation. The QM/MB-DFT scheme offers the advantage that, since both QM and MM components as well as the QM/MM interaction are treated at the same level of accuracy, the need for a transition layer is reduced or eliminated, though it should be noted that some levels of QM theory do not have analytical gradients, and can thus become prohibitively expensive for dynamical QM/MM simulations. In more succinct terms, this approach can be thought of as treating the entire system under the same ”effective” Hamiltonian, with different, but numerically equivalent representations for the QM and MM components.

3.5 Acknowledgements

E.L. thanks Kartik Lakshmi Rallapalli, Kelly Hunter, Colin Egan, Marc Riera, and Jay Hu for stimulating discussion about QM/MM. All figures in this paper were generated with UCSF Chimera and Matplotlib.[192, 271] This research was supported by the U.S. Department

of Energy, Office of Science, Office of Basic Energy Science, through grant No. DE-SC0019490 (F.P.), the National Science Foundation, through grant No. 1704063 (F.P.), and NIGMS/NIH through grant No. R01GM108583 (G.A.C.). F.L. acknowledges support from Gaussian, inc. The authors are grateful to the MoLECoLab group in Pisa for granting access to the LIFETimeS cluster, that was used to perform all the fsc-QM/MM calculations. This research used resources of the National Energy Research Scientific Computing Center, which is supported by the Office of Science of the U.S. Department of Energy under Contract DE- AC02-05CH11231, as well as the Triton Shared Computing Cluster (TSCC) at the San Diego Supercomputer Center (SDSC).

Chapter 3 is in full a reprint of the material as it appears in "Lambros, E., Lipparini, F., Cisneros, G. A., & Paesani, F. (2020). A Many-Body, Fully Polarizable Approach to QM/MM Simulations. *Journal of Chemical Theory and Computation*" The dissertation author was the primary author of this paper.

3.6 Supplementary Information

Analyses of the interaction energies of eight low-lying isomers of the water hexamer calculated using different QM/MM partitions.

Chapter 4

General many-body framework for data-driven potentials with arbitrary quantum mechanical accuracy: Water as a case study

We present a general framework for the development of data-driven many-body (MB) potential energy functions (MB-QM PEFs) that represent the interactions between small molecules at an arbitrary quantum-mechanical (QM) level of theory. As a demonstration, a family of MB-QM PEFs for water are rigorously derived from density functionals belonging to different rungs across Jacob's ladder of approximations within density functional theory (MB-DFT) as well as from Møller-Plesset perturbation theory (MB-MP2). Through a systematic analysis of individual many-body contributions to the interaction energies of water clusters, we demonstrate that all MB-QM PEFs preserve the same accuracy as the corresponding *ab initio* calculations, with the exception of those derived from density functionals within the generalized gradient approximation (GGA). The differences between the DFT and MB-DFT results are traced back to density-driven errors

that prevent GGA functionals from accurately representing the underlying molecular interactions for different cluster sizes and hydrogen-bonding arrangements. We show that this shortcoming may be overcome, within the many-body formalism, by using density-corrected functionals that provide a more consistent representation of each individual many-body contribution. This is demonstrated through the development of a MB-DFT PEF derived from density-corrected PBE-D3 data, which more accurately reproduce the corresponding *ab initio* results.

4.1 Introduction

Molecular mechanics (MM) models, with tunable parameters, are the workhorse of computer simulations. While the earliest MM models were parameterized using simple point-charge and pairwise potentials to reproduce experimental observables, recent MM models are constructed with first-principles approaches using parameters derived from high level *ab initio* reference data. Polarizable force fields (FFs)[72, 197, 272] and machine learning (ML) models[19–29] have now taken the center stage as the models of choice for molecular dynamics (MD) and Monte Carlo (MC) simulations.

Among ML models, neural networks (NNs) have become increasingly popular in computational molecular sciences. Atomistic NNs describe the target multidimensional potential energy surface (PES) using a set of descriptors that represent the immediate local environment around each atom.[19, 20, 23, 24] NN models rely on using regression algorithms to train flexible potential energy functions (PEFs) on large sets of reference data that are calculated at the highest level of theory compatible with the system's size and complexity.[19, 20, 23, 24, 273–275] While the restrictions on the functional forms used to represent the target PES are somewhat loose, ML models must satisfy rotational, translational, and permutational invariance, and must be able to uniquely describe a molecular configuration.[19, 20, 24, 65, 276–281] Some ML models are trained on gas-phase reference data and, while useful for studying individual molecules and small

clusters, are not adequate to accurately describe systems in the condensed phase where long-range many-body effects may play important roles.[282] On the other hand, since gas-phase reference data are generated for small systems, they are not only relatively cheap and fast to calculate, but can also be computed using higher levels of theory compared to models trained on large condensed-phase systems.[27] For small molecules the reference data are usually calculated using coupled cluster (CC) theory, including single, double, and perturbative triple excitations, i.e., CCSD(T), often in the complete basis set (CBS) limit, currently the "gold standard" for molecular interactions. Towards this end, some ML approaches, which include Δ-machine learning procedures applied to permutationally invariant polynomials (PIPs),[65] allow for a ML model to be trained to an effective higher level of theory by training a correction to a core potential generated at a lower level of theory, using a sparser number of higher-level data points.[283, 284] ML approaches based on NNs and PIPs have also been developed to model chemical reactions in the gas-phase and at solid surfaces.[277–280, 285–289] In order to implicitly include many-body effects, some ML models are trained on entire sets of condensed-phase configurations, which are expensive to generate and must consequently use a lower level of theory, commonly density functional theory (DFT), for the reference data.[15, 31, 290]

An alternative way to represent condensed-phase systems using ML approaches is to adopt a hybrid data-driven/physics-based scheme where a data-driven model, which captures (short-range) quantum-mechanical interactions, is integrated with a physics-based model of many-body interactions, which are represented by classical expressions.[291–293] Examples of hybrid data-driven/physics-based models are the MB-pol and related MB-nrg PEFs that are able to accurately predict the properties of water[1, 37–39] and various aqueous systems[179–181, 183–187], as well as molecular fluids,[62, 63] from the gas to condensed phases. Both MB-pol and MB-nrg PEFs are rigorously derived from the many-body expansion (MBE) of the energy and use PIPs[65] to capture short-range quantum-mechanical effects arising from the overlap of the electron densities of individual monomers (e.g., Pauli repulsion, and charge transfer

and penetration), which are missing in conventional force fields. The MB-DFT PEFs generalize the MBE formalism adopted to develop the MB-pol PEF of water by replacing the 2-body (2B) and 3-body (3B) terms, which were originally calculated at the CCSD(T)/CBS level of theory, with corresponding terms calculated using an arbitrary density functional.[61] It has been shown that the MB-DFT PEFs closely reproduce the structural properties of liquid water calculated from fully *ab initio* MD simulations carried out with the same density functional.[61]

The MB-DFT family of hybrid data-driven/physics-based PEFs is particularly appealing for quantum mechanics/molecular mechanics (QM/MM) simulations of systems that are either too computationally expensive to be treated at a fully quantum-mechanical (QM) level or cannot be described using molecular mechanics (MM) models since they involve rearrangements of chemical bonds. Likewise, while ML approaches can, by construction, model bond rearrangements, their behavior is highly dependent on the composition the datasets and level of theory used in the training process. In principle, these problems do not affect QM/MM simulations where the total system is divided into a smaller QM subsystem, which includes all molecular species that are involved in the chemical transformation, and a MM region, which describes environmental effects.[193, 194] However, conventional QM/MM approaches suffer from energy discontinuities at the boundary between the QM and the MM region which appear due to the different accuracy of the QM and MM models in representing the underlying molecular interactions. Another shortcoming of conventional QM/MM calculations arises when they are applied to studying chemical reactions in solutions where, due to diffusion, molecules initially assigned to the MM region may enter the QM region and, vice versa, molecules initially assigned to the QM region may enter the MM region during the MD simulation. To overcome this problem, several adaptive QM/MM schemes have been proposed where the QM region is dynamically repartitioned at every MD step in order to prevent diffusive breakup. This is generally accomplished by introducing transition layers that smooth over the QM/MM boundary discontinuity.[34, 235, 236, 236–239, 239–254] This suggests that "elevating" the accuracy of the MM model to the same level as the

QM model would effectively remove these discontinuities and significantly improve the realism and predictive power of QM/MM calculations.[294]

In this context, pure ML models of the MM region do not lend themselves well to QM/MM simulations since point charges must, at least, be assigned to the MM atoms to capture Coulombic interactions between the MM region and the QM electronic density through a minimal electrostatic embedding scheme.[295] In contrast, MB-DFT PEFs[61] and other polarizable models like AMOEBA[54, 58] can directly couple to the QM region using a polarizable embedding scheme which allows the environment to dynamically respond to the QM density via the polarization of inducible multipole moments on the MM atoms.[205–213, 294] In principle, when used in QM/MM calculations, the MB-DFT PEFs can not only elevate the accuracy of the MM region to be consistent with that of the QM region but, by construction, their 2B and 3B PIPs help recover quantum-mechanical effects in the QM/MM interaction which are missing in QM/MM calculations with conventional (either polarizable or nonpolarizable) force fields, thus allowing the entire QM/MM system to be consistently treated at the same level of theory.[294] However, in the case of water, the original MB-DFT PEFs[180] were built upon the same Thole-type scheme adopted by MB-pol to represent permanent electrostatics and polarization derived from high-level QM calculations,[37–39] which implies that they are not able to strictly reproduce many-body energies calculated *ab initio* using the corresponding DFT models. This is a problem in QM/MM calculations in water where the MM region is described by a MB-DFT PEF and the QM region by the corresponding DFT model because the associated QM/MM electrostatic interactions may be substantially different from those predicted by the original MB-pol electrostatic model underlying the MB-DFT PEFs, which results in an unbalanced representation of short-range many-body effects between the QM and MM regions.[294] This problem is particularly evident in configurations with strong polarization. For example, we observed that when the hydrogen-bond donor in the water dimer is assigned to the QM region described by a DFT model and the hydrogen-bond acceptor is described by the corresponding MB-DFT PEF, the underlying

QM/MM electrostatic interactions are very similar to the pure MM electrostatic interactions provided by the MB-DFT PEF. This allows the 2B and 3B PIPs of the MB-DFT PEFs to correctly recover the reference QM energy of the water dimer. In contrast, when the QM/MM partition is flipped such that the hydrogen-bond donor is assigned to the MM region represented by the MB-DFT PEF, the QM/MM electrostatic interactions become appreciably different from the pure MM electrostatic interactions provided by the MB-DFT PEF, which prevents the PIPs of the MB-DFT PEFs from correctly recovering the *ab initio* DFT energy.[294] Furthermore, the higher-body nB terms ($n \geq 4$) of the MB-DFT PEFs are fully described by the polarization term of MB-pol, which implies that they are identical in all MB-DFT PEFs, regardless to which density functional a particular MB-DFT PEF is derived from.[61] As a consequence, if a given density functional displays sufficiently different polarization effects from those represented by MB-pol, the original MB-DFT PEFs[61] are not able to correctly reproduce higher-body nB interactions ($n \geq 4$) provided by that density functional. Finally, the 1B term of the original MB-DFT PEFs for water, which describes the intramolecular distortions in an isolated water molecule, is represented by the same Partridge-Schwenke PEF[64] used in MB-pol[37–39], which was derived from high-level QM calculations and further refined to reproduce the rovibrational transitions of an isolated water molecule in the gas phase. This implies that the intramolecular distortion energies in the original MB-DFT PEFs do not properly reproduce the corresponding DFT 1B energies.[61]

In this study, we introduce an efficient theoretical/computational framework for the development of MB-QM PEFs that consistently reproduce each individual many-body energy contribution calculated *ab initio* using the corresponding QM model. While MB-QM PEFs can be developed for generic (small) molecular fluids at an arbitrary QM level of theory, the present study focuses on MB-QM PEFs for water derived from *ab initio* data calculated using various density functionals belonging to different rungs across the Jacob's ladder of DFT approximations as well as from second-order Møller-Plesset (MP2) perturbation theory. While these MB-QM PEFs are intended for use in future QM/MM simulations, this first study focuses on the theoretical

details and assessment of the accuracy of the MB-QM PEFs through a systematic analysis of the energetics of small water clusters. By analyzing each many-body contribution to the interaction energies, we find that density functionals derived within the generalized gradient approximation (GGA) and hybrid density functionals suffer from relatively large density-driven errors. This leads to the over-delocalization of the electron density which, in turn, results in (unphysically) larger higher-body energies whose magnitude cannot correctly be captured by the purely classical, many-body polarization term adopted by the MB-DFT PEFs. We show that, within the theoretical framework based on the many-body formalism that is introduced here, it is possible to develop density-corrected MB-DFT PEFs that remove, at least partially, these density-driven errors and provide a more accurate description of individual many-body contributions to the interactions between water molecules.

4.2 Theory

4.2.1 MB-QM

The MBE expresses the total energy, E_{tot}, of an N-body system as the sum of individual n-body energy contributions, ε_{nB}, where $n \leq N$,[40]

$$E_{tot}(r_1,..,r_N) = \sum_{i=1}^{N} \varepsilon_{1B}(r_i) + \sum_{i<j}^{N} \varepsilon_{2B}(r_i,r_j) + \sum_{i<j<k}^{N} \varepsilon_{3B}(r_i,r_j,r_k) + ... + \varepsilon_{NB}(r_1,..,r_N) \quad (4.1)$$

Here, ε_{1B} represents the energy of an isolated monomer, and the n-body energies are defined recursively as

$$\varepsilon_{nB} = \varepsilon_n(1,...,n) - \sum_{i=1}^{N} \varepsilon_{1B}(r_i) - \sum_{i<j}^{N} \varepsilon_{2B}(r_i,r_j) - \sum_{i<j<k<...<n-1}^{N} \varepsilon_{(n-1)B}(r_i,r_j,..r_{n-1}). \quad (4.2)$$

It has been shown that the MBE converges quickly for systems with localized electron densities and large band gaps. For example, the sum of 2B and 3B energies contributes to ∼96-99% of the total interaction energy in water.[40, 170, 296–301] Exploiting the fast convergence of the MBE, several many-body PEFs for water[37–39, 45, 127] and other molecular fluids[62, 63, 302, 303] have been derived from high-level QM data. In this study, we generalize the many-body formalism originally adopted by the MB-pol PEF[37–39] to the development of many-body PEFs for generic (small) molecules at an arbitrary QM level of theory. As examples, we introduce several MB-DFT PEFs for water derived from various density functionals belonging to different rungs across the Jacob's ladder of DFT approximations (MB-DFT) as well as from MP2 perturbation theory (MB-MP2).

Briefly, the MB-QM PEFs approximate eq 6.4 to the sum of explicit 1B, 2B, and 3B terms along with a polarization term implicitly representing classical many-body interactions:

$$E_{tot}(r_1,..,r_N) = \sum_{i=1}^{N} \varepsilon_{1B}(r_i) + \sum_{i>j}^{N} \varepsilon_{2B}(r_i,r_j) + \sum_{i>j>k}^{N} \varepsilon_{3B}(r_i,r_j,r_k) + E_{pol} \tag{4.3}$$

Each term of eq 5.8 is fitted to reproduce the corresponding *ab initio* data calculated at the same QM level of theory. Specifically, the 1B term is represented by a PIP[65] that accurately describes intramolecular distortions. The 2B term incorporates three different energy contributions:

$$\varepsilon_{2B} = E_{2B}^{sr} + E_{elec} + E_{disp} \tag{4.4}$$

where E_{2B}^{sr} describes short-range 2B interactions and is represented by a 4^{th}-degree PIP.[37, 61] E_{elec} represents permanent electrostatics between point charges that reproduce the *ab initio* dipole moment of an isolated molecule. Following ref 294, in the MB-QM PEFs for water introduced here, the point charges are kept fixed to the values that reproduce the dipole moment of a water molecule in its equilibrium geometry. However, the present MB-QM scheme is general and allows for using geometry-dependent charges if deemed necessary for achieving higher accuracy.

The last term in eq 5.9, E_{disp}, describes the 2B dispersion energy that is expressed as

$$E_{disp} = -\sum_{i,j} f(\delta_{ij}) \frac{C_{6,ij}}{R_{ij}^6} \tag{4.5}$$

where $f(\delta_{ij})$ is the Tang-Toennies damping function[66], i and j are atom indices on two separate water monomers, and $C_{6,ij}$ are the dispersion coefficients. The 3B term of the MB-QM PEFs describes short-range 3-body interactions and, as in the case of ε_{2B}, is represented by a 4^{th}-degree PIP,

$$\varepsilon_{3B} = E_{3B}^{sr}. \tag{4.6}$$

4.2.2 Density-corrected DFT

The Kohn-Sham theory allows for minimizing the exchange-correlation (XC) functional given by[13]

$$F[n] = T_{\mathrm{S}}[n] + E_{\mathrm{H}}[n] + E_{\mathrm{XC}}[n]. \tag{4.7}$$

where $n(r)$ is the ground-state density of the system, T_{S} is the non-interacting kinetic energy, and E_{H} and E_{XC} define Hartree and exchange-correlation energies, respectively. The exact $F[n]$ gives rise to derivative discontinuities for total energies at integer values of the number of electrons (N),[304] a feature that is missing in GGA and hybrid GGA density functionals which, by construction, provide smooth functions of N. As a consequence, the derivatives of these density functionals are inaccurate,[304] which results in an incorrect Kohn-Sham potential and, in turn, poor orbital energies. As the potential generated by these density functionals show a constant shift with respect to the exact potential, these errors do not affect the density. Unsurprisingly, for this reason, most density functionals engender accurate electron densities, which suggests that DFT errors are primarily functional-driven rather than density-driven. In this regard, it should, however, be noted that density functionals constructed in unconstrained forms may give rise to unphysical electron densities despite providing a good representation of the energies.[305]

Probably the most significant contributor to density-driven errors is the self-interaction error (SIE). In wavefunction theory, Coulomb interactions are incorporated as pairwise two-electron potentials, where an electron does not interact with itself. However, in Kohn-Sham theory, since the energy is a functional of the one-electron density, it is impossible to remove the interaction of the electrons with themselves as each electron interacts with the entire density. As a consequence, most density functionals are unable to satisfy the following conditions for the one-electron system,[306]

$$T_{\mathrm{s}} = \int \mathrm{d}^3 r \frac{|\nabla n|^2}{8n}, \quad E_{\mathrm{X}} = -E_{\mathrm{H}}, \quad E_{\mathrm{C}} = 0. \tag{4.8}$$

where E_{X} and E_{C} are the exchange and correlation energies. The inability to satisfy eq 4.8 gives rise to the SIE. Although for many-electron systems the self-interaction energy can be formally defined as the sum of the energies of each orbital interacting with itself,[307] correcting for the SIE has been found not to be straightforward.[308] For hybrid density functionals, mixing a fraction of Hartree-Fock exchange with the XC functional leads to incomplete cancellation of the SIE, thus giving rise to smaller density-driven errors compared to pure functionals.[309–311]

Besides the SIE, another contributor to density-driven errors is the delocalization error, which is a many-electron effect resulting in unphysical delocalization of the electrons and low energies for the delocalized electrons.[308, 312–314]

One possible workaround to minimize DFT density-driven errors is the use of an accurate electron density. However, this effectively makes the minimization of density-driven errors impractical because finding a highly accurate electron density is more expensive than the DFT calculation itself. In this context, with the absence of derivative discontinuities in the energy provided by the GGA functionals, the use of the Hartree-Fock density, n^{HF}, in the orbital-dependent functionals is free from density-driven errors[306] and makes the overall computational

cost of the density-corrected energy, $E^{\mathrm{DC-DFT}}$, similar to that of the original DFT energy,

$$E^{\mathrm{DC-DFT}} \approx E^{\mathrm{HF}} + \left(\tilde{E}_{\mathrm{XC}}\left[n^{\mathrm{HF}}\right] - E_{\mathrm{X}}^{\mathrm{HF}}\right) \tag{4.9}$$

Although approximate, using the Hartree-Fock density, n^{HF}, to calculate $E^{\mathrm{DC-DFT}}$ in a non-self-consistent way has been shown to minimize density-driven errors in DFT calculations of various properties (e.g., electron affinities,[315] noncovalent interactions,[316–319] spin gaps for coordination compounds[319]) with minimal additional computational cost. It should be noted that other approaches have also been proposed in the literature to correct the SIE in DFT calculations.[320, 321]

4.3 Computational details

All MB-DFT PEFs were fitted to *ab initio* data calculated with GGA density functionals (BLYP[322, 323] and PBE[324] belonging to rung 2 functionals), meta-GGA density functionals (B97M-rV[325] belonging to rung 3 functionals), hybrid density functionals (B3LYP,[323, 326] PBE0,[327] and M06-2X,[328] belonging to rung 4 functionals) and range-separated density functionals (ωB97M-V[329] belonging to rung 4 functionals). The empirical D3 correction was added to all density functionals that do not account for dispersion energy.[330] Similarly, the MB-MP2 PEF was derived from the corresponding data calculated at the MP2 level of theory. Both DFT and MP2 calculations were carried out with the aug-cc-pVQZ basis set[166, 266] using Q-Chem[331] and ORCA[332] quantum chemistry packages. The Euler-Maclaurin-Lebedev (99,590) grid[333, 334] was used in all DFT calculations to minimize possible grid errors since it has been shown that the accuracy of more recent density functionals are particularly sensitive to the choice of the integration grid.[335]

The 1B, 2B, and 3B training sets used in the development of each MB-DFT and MB-MP2 PEF comprise 5000 monomers, 42508 dimers, and 12347 trimers, respectively. The 1B training

set was generated using in-house software following the same procedure described in previous studies,[62, 63] while we used the same 2B and 3B training sets used in the development of the MB-pol PEF.[37, 38]

The dipole polarizabilities for the free O and H atoms were computed at the corresponding DFT and MP2 levels of theory. The effective polarizabilities used in the MB-DFT and MB-MP2 PEFs were calculated as:

$$\alpha_{eff} = \alpha_{free} \left(\frac{V_{eff}}{V_{free}} \right)^{4/3} \tag{4.10}$$

where V_{eff} and V_{free} are the effective and free volumes of the O and H atoms in H_2O calculated via the XDM model[336–338] as implemented in Q-Chem.[339] The atomic charges were calculated using the CM5 method[340] and then distributed on the actual sites representing the MB-QM H_2O molecule (i.e., the fictitious site along the bisector of the HOH angle and the two H atoms)[37] according to the procedure described in ref 51.

All the density-corrected DFT calculations were performed in two steps, where a fully self-consistent Hartree-Fock calculation was performed prior to a single non-self-consistent DFT calculation where the orbitals of the HF calculation were used to generate the DFT density.

In the analysis of the energetics of the water clusters presented in section 4.4, the binding energies are defined as

$$E_{bind} = E^{\text{cluster}} - nE_{opt}^{\text{H}_2\text{O}} \tag{4.11}$$

where E^{cluster} is the total energy of n-molecule cluster and $E_{opt}^{\text{H}_2\text{O}}$ is the energy of an isolated water molecule in the optimized geometry. The corresponding interaction energies are defined as

$$E_{int} = E^{\text{cluster}} - \sum_i E_i^{\text{H}_2\text{O}} \tag{4.12}$$

where E^{cluster} is the same total energy as in eq 4.11 and $E_i^{\text{H}_2\text{O}}$ is the energy of the i-th water molecule in the same geometry as in the cluster. All MP2 optimized geometries used in the

analyses of the energetics of the water clusters are taken from ref 1.

4.4 Results and discussions

4.4.1 Many-body analysis of the MB-QM PEFs

In this section we analyze the ability of the MB-DFT and MB-MP2 PEFs to reproduce results obtained from *ab initio* calculations carried out at the corresponding QM level of theory. Correlation plots between the 2B and 3B energies calculated with the different QM methods and the corresponding values obtained with the MB-QM PEFs are shown in Figures 4.1 and 4.2, respectively. Analogous correlation plots for the 1B energies are included in the Supporting Information.

Independently of the QM level of theory, the MB-QM PEFs are able to quantitatively reproduce the 1B, 2B, and 3B reference energies, with RMSDs of $\sim$0.08, $\sim$0.12, and $\sim$0.03 kcal/mol respectively. In the case of the 2B and 3B energies, the high correlation between the QM data and the corresponding MB-QM values indicates that the 4th-degree PIPs used to supplement the representation of short-range 2B and 3B interactions in the MB-QM PEFs are sufficiently flexible to "capture" quantum-mechanical contributions (e.g., Pauli repulsion, charge transfer and penetration) which, arising from the overlap of the monomers' electron densities, cannot be quantitatively represented by classical expressions commonly used in conventional force fields.

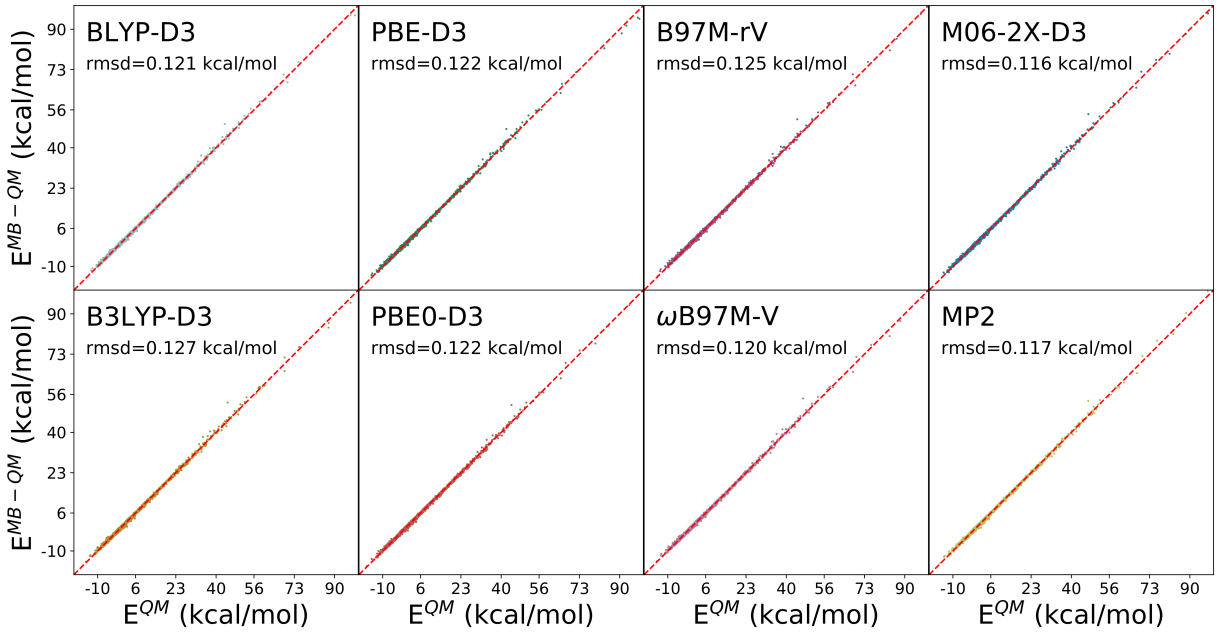

Figure 4.1: Correlation plots between the 2B QM reference energies and the values obtained with the corresponding MB-QM PEFs calculated for the 42508 configurations of the 2B training set.

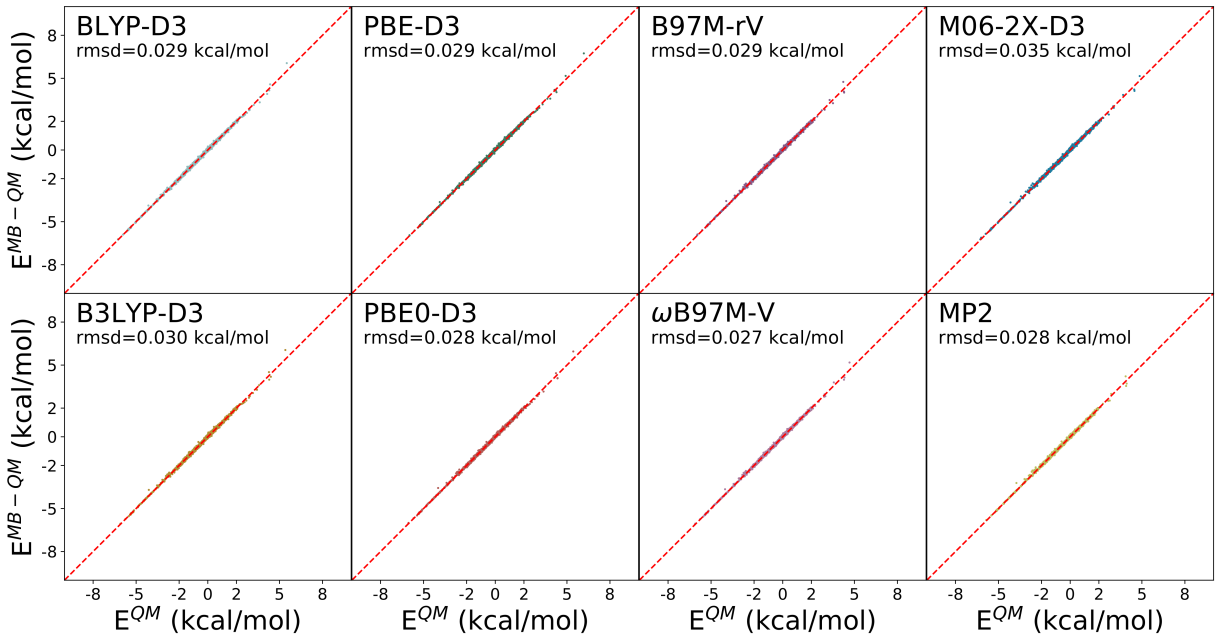

Figure 4.2: Correlation plots between the 3B QM reference energies and the values obtained with the corresponding MB-QM PEFs calculated for the 12347 configurations of the 3B training set.

As discussed in previous studies,[1, 72] the analysis of individual many-body contributions to the interaction energies of small water clusters allows for an overall assessment of the accuracy of a given water model. In this context, it should be emphasized that, since the MB-QM PEFs are trained on data that contain information only up to 3B term of the MBE, they do not have any prior knowledge of systems containing more than three water molecules. Figure 4.3 displays the MB-QM errors relative to the corresponding QM values for each individual many-body contribution (i.e., from 2B to 6B energies) to the interaction energy of the prism isomer that corresponds to the minimum-energy isomer of the water hexamer.[137, 341–343] While the corresponding analyses for the first eight low-energy hexamer isomers are reported in the Supporting Information, Table 4.1 lists the MB-DFT and MB-MP2 errors for each individual nB energy averaged over all eight isomers. As discussed in section 4.3, since the interaction energies, by definition, remove all contributions due to monomer distortions, the present many-body analysis allows for a direct and quantitative comparison of the MB-DFT and MB-MP2 PEFs in their ability to reproduce the corresponding QM nB contributions to the interaction energy.

Figure 4.3 shows that the absolute magnitude of the 2B and 3B errors associated with the

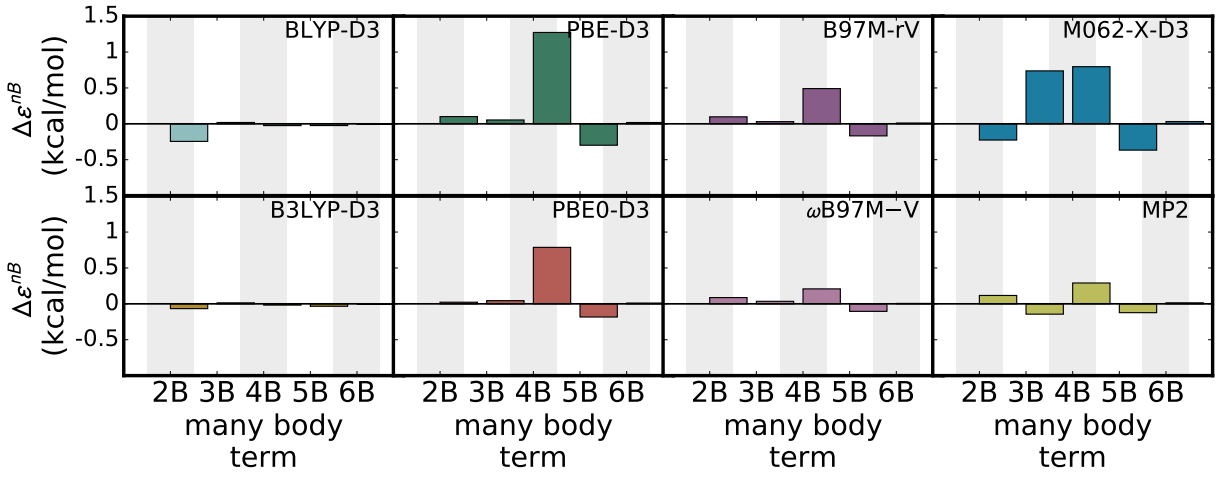

Figure 4.3: Errors in individual many-body energies, nB, associated with the MB-QM PEFs relative to the corresponding QM reference values for the prism isomer of the water hexamer. The MP2 optimized geometry of the prism isomer is from ref 1.

MB-QM PEFs range between 0.1 and 0.3 kcal/mol, with the MB-DFT PEFs fitted to M06-2X-D3 and BLYP-D3 data displaying the largest 2B errors. The overall low errors for the 2B and 3B energies are consistent with the low RMSDs reported in Figures 4.1 and 4.2. In the case of M06-2X-D3, relatively larger errors are not only associated with the 3B term but are also found at the 4B and 5B levels, as discussed in more detail in ref 72. The large average 3B error (0.7 kcal/mol) associated with M06-2X-D3 can be explained by considering that the water hexamer contains 20 distinct trimers and M06-2X-D3 displays the largest 3B RMSD of 0.035 kcal/mol (Figure 4.2). It should be noted that, although similar trends are also found for the other isomers as shown in Figures S3 - S10 of the Supporting Information, the more planar hexamer isomers (i.e., the book, boat, and chair isomers) display significantly larger 2B and 3B errors compared to the three-dimensional isomers (i.e., the prism and cage isomers). This difference is primarily due to error accumulation in the highly symmetric planar isomers, where repeated dimer and trimer subunits contribute many-body energies with same signed errors, resulting in the total error to add up.

As shown in Table 4.1, the average 4B error is disproportionately large relative to the magnitude of the total error for all MB-QM PEFs, except those derived from B3LYP-D3 and MP2 data. The largest 4B error (1.07 kcal/mol) is associated with the MB-DFT PEF fitted to PBE-D3

Table 4.1: Average errors associated with the QM methods considered in this study relative to the reference QM values calculated for the first low-energy isomers of the water hexamers. The MP2 optimized geometries of the water hexamer isomers are from ref 1.

	ΔE_{avg}^{NB} (kcal/mol)					
Method	2B	3B	4B	5B	6B	Total
BLYP-D3	0.19	0.08	0.45	0.06	0.00	0.79
B3LYP-D3	0.36	0.08	0.24	0.03	0.01	0.72
PBE-D3	0.46	0.07	1.07	-0.06	0.02	1.57
PBE0-D3	0.38	0.07	0.72	-0.03	0.01	1.16
M06-2X-D3	-0.10	0.70	0.67	-0.08	0.01	1.20
B97M-rV	0.27	0.07	0.56	-0.03	0.00	0.89
ωB97M-V	0.31	0.07	0.42	-0.00	0.00	0.81
MP2	0.35	-0.06	0.33	0.01	-0.01	0.62

data. Importantly, despite 4B effects generally contributing less than 5% to the total interaction energy in water clusters,[72, 170, 297, 298, 344, 345] the error in the 4B term accounts for most of the total error associated with the MB-DFT PEFs. By construction (see section 4.2), 4B energies in the MB-QM PEFs are represented completely by a classical many-body polarization term that is expressed according to a modified Thole-type model.[53] Table I shows that MB-QM PEFs fitted to ωB97M-V and MP2 data are associated with relatively small 4B errors, similar to those found for MB-pol relative to CCSD(T)/CBS,[1] while large 4B errors are associated with MB-DFT PEFs fitted to PBE-D3, PBE0-D3, and M06-2X-D3 data. Given the trend observed in the 4B errors associated with MB-DFT PEFs fitted to density functionals belonging to different rungs across the Jacob's ladder of DFT approximations, we posit that the magnitude of the 4B errors stems from density-driven errors (i.e., self-interaction and delocalization errors) which plague, to various extent, all density functionals. As discussed in section 4.4, the electron self-repulsion is explicitly non-local and should, in principle, be removed via the exchange-correlation energy. In practice, most exchange-correlation functionals contain substantial local components and are thus unable to correctly compensate for the interactions of the electrons with themselves. This results in (unphysical) over-delocalization of the electron density in order to minimize the electron self-repulsion. In turn, this over-delocalization of the electron density causes the higher-order terms of the MBE to be (artificially) more quantum-mechanical in nature and, consequently, not amenable to the purely classical representation based on many-body polarization which is adopted by the MB-QM PEFs.

4.4.2 Density-driven errors in the DFT description of molecular interactions in water

In this section we analyze density-driven errors in DFT models of water with a particular focus on the dependence of these erorrs on both the rung of the density functional and the cluster size.

Interaction energies of water clusters

Our analysis indicates that common GGA functionals tend to overbind the water clusters, likely due to the presence of relatively large density-driven errors (Figure S11 and S12). To test this hypothesis, we use HF orbitals in non-self-consistent DFT calculations of the interaction and many-body energies of water clusters, which was shown to reduce the impact of density-driven errors.[346] Figure 4.4 shows the errors in the interaction energies (ΔE_{int}^{DC}) calculated for various water clusters, from the dimer to the hexamer, using both the self-consistent (SC) and density-corrected (DC) versions of the GGA BLYP-D3 and PBE-D3 functionals, and corresponding hybrid GGA B3LYP-D3 and PBE0-D3 functionals. For all clusters, PBE-D3 is found to be the most susceptible to the density-driven errors. Independently of the density functional, the density-driven error defined as $\Delta E_{int}^{DC} = E_{int}^{DC} - E_{int}^{SC}$ increases from the dimer to the hexamer. In particular, ΔE_{int}^{DC} per molecule lies within 0.73 and 0.82 kcal/mol for BLYP-D3 and decreases to 0.39-0.44 kcal/mol for B3LYP-D3,[323, 326] which contains 20% Hartree-Fock exchange (Figure S13). A similar trend is found for the PBE-D3 and PBE0-D3 functionals, with the former displaying ΔE_{int}^{DC} per molecule between 0.93 and 1.06 kcal/mol, and the latter between 0.44 and 0.56 kcal/mol. It should be noted that PBE0-D3 contains 25% Hartree-Fock exchange.[327]

To assess the overall accuracy of the density-corrected functionals, Table 4.2 lists the errors associated with each density-corrected functional relative to the CCSD(T)/CBS reference values[1] for the interaction energies of the first eight low-energy isomers of the water hexamer. For this analysis, the errors are defined as $\Delta E_{int}^{CCSD(T)} = E_{int}^{DC} - E_{int}^{CCSD(T)}$, where E_{int}^{DC} and $E_{int}^{CCSD(T)}$ are the interaction energies calculated with the density-corrected functionals and at CCSD(T)/CBS level of theory, respectively. A large mean unsigned error (MUEs) of 4.91 kcal/mol is found for BLYP-D3(DC), whereas PBE-D3(DC) and B3LYP-D3(DC) provide comparable MUEs of 2.56 kcal/mol and 2.05 kcal/mol, respectively. Despite being a hybrid functional as B3LYP-D3(DC), PBE0-D3(DC) provides a much smaller MUE of 0.43 kcal/mol, which is comparable to that found for M06-2X-D3(DC) (MUE = 0.42 kcal/mol) and ωB97M-V(DC) (MUE = 0.56 kcal/mol).

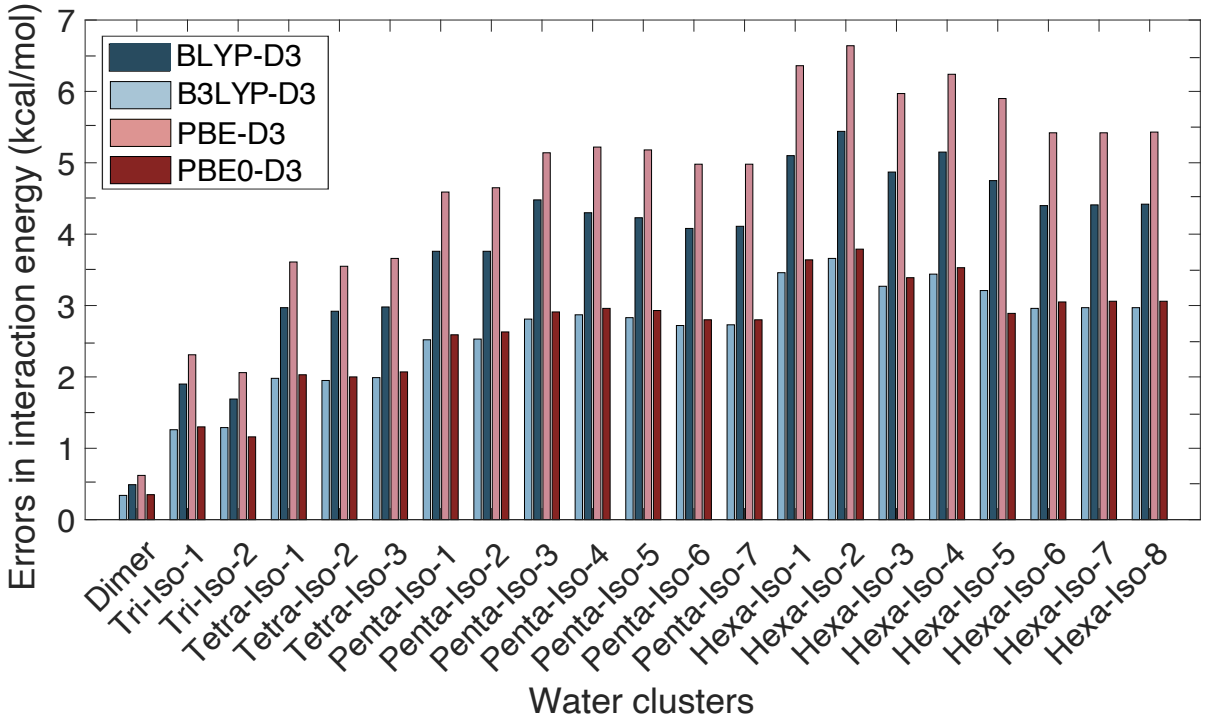

Figure 4.4: Density-driven errors in the interaction energies of $(H_2O)_n$ clusters, with $n = 2-6$, associated with BLYP-D3, B3LYP-D3, PBE-D3, PBE0-D3 relative to the corresponding density-corrected functionals. The errors are defined as $\Delta E_{int}^{DC} = E_{int}^{DC} - E_{int}^{SC}$, where E_{int}^{DC} and E_{int}^{SC} are the interaction energies calculated with the density-corrected and self-consistent functionals, respectively.

It should be noted that the hexamer isomers can be broadly classified in two distinct groups, one containing three-dimensional structures, where each water molecule is involved in three hydrogen bonds (i.e., the prism and cage isomers), and one containing two-dimensional structures, where each water molecule is involved in two hydrogen bonds (i.e., the cyclic isomers), with the book-type isomers being in between and sharing features that are common to both groups. In this context, it is worth mentioning that, with the exception of BLYP-D3(DC) and ωB97M-V(DC), all density-corrected functionals analyzed in this study exhibit significantly lower accuracy for the three-dimensional isomers.

Table 4.2: Errors (in kcal/mol) in interaction energies for the first eight low-energy isomers of the water hexamer associated with the density-corrected functionals PBE-D3(DC), PBE0-D3(DC), BLYP-D3(DC), B3LYP-D3(DC), M06-2X-D3(DC) and ωB97M-V(DC) relative to the CCSD(T)/CBS reference values. The errors are defined as $\Delta E_{int}^{CCSD(T)} = E_{int}^{DC} - E_{int}^{CCSD(T)}$, where the reference $E_{int}^{CCSD(T)}$ values are taken from ref 1.

Isomer	PBE-D3 (DC)	PBE0-D3 (DC)	BLYP-D3 (DC)	B3LYP-D3 (DC)	M06-2X-D3 (DC)	ωB97M-V (DC)
Prism	3.76	1.05	5.44	2.82	-1.16	0.50
Cage	3.32	0.67	5.26	2.54	-0.66	0.73
Book1	2.55	-0.01	4.92	2.06	-0.21	0.65
Book2	2.51	-0.03	4.91	2.06	-0.12	0.68
Bag	2.48	-0.05	4.91	2.05	-0.20	0.58
Cyclic chair	1.97	-0.56	4.65	1.62	-0.40	0.42
Cyclic boat 1	1.92	-0.54	4.57	1.61	-0.32	0.45
Cyclic boat 2	1.98	-0.50	4.61	1.63	-0.33	0.43
MUE	2.56	0.43	4.91	2.05	0.42	0.56

Many body decomposition analysis

It has been shown that 2B and 3B effects contribute to 96-99% of the total interaction energy in water,[41, 72, 297] which implies that the ability of a given water model to correctly reproduce 2B and 3B energies mainly determines the accuracy with which the model is able to describe the total interaction energy and relative stability of different water clusters.

Figure 4.5 shows the density-driven errors, $\Delta E_{nB}^{DC} = E_{nB}^{DC} - E_{nB}^{SC}$ $(n = 2-6)$, calculated for each individual nB contribution to the interaction energies of the first eight low-energy isomers of the water hexamer. Here, E_{int}^{DC} and E_{int}^{SC} are the interaction energies calculated with the density-corrected and self-consistent functionals, respectively. Due to relatively large density-driven errors, the MUE for ΔE_{2B}^{DC} is 6.22 kcal/mol for PBE-D3 and 4.69 kcal/mol for BLYP-D3. Adding a fraction of Hartree-Fock exchange systematically reduces these errors, with the corresponding MUEs being 3.45 kcal/mol and 3.25 kcal/mol for PBE0-D3 and B3LYP-D3, respectively. More recent functionals show significantly smaller errors, resulting in MUEs of 1.08 kcal/mol and 0.93 kcal/mol for M06-2X-D3 and ωB97M-V, respectively, which confirms that density-driven errors are less severe for hybrid, meta-GGA and range-separated functionals.

The analysis of ΔE_{2B}^{DC} shown in Figure 4.5 also indicates that, at the 2B level, density-driven errors tend to overbind the water clusters, as the 2B errors are positive for all density functionals examined in this study. This is in agreement with similar results recently obtained with the SCAN functional.[16] The trend in 3B density-driven errors is not as consistent as for the 2B errors. The largest MUE (0.47 kcal/mol) is found for M06-2X-D3, with the MUE for all other density functionals ranging from 0.14 kcal/mol to 0.34 kcal/mol. Interestingly, with the exception of the cyclic isomers, PBE-D3 and PBE0-D3 display negative ΔE_{3B}^{DC} for all hexamer isomers, which implies that 3B density-driven errors tend to underbind these clusters. Independently of the cluster structure, all other density functionals display positive 3B density-driven errors, except B3LYP-D3 that provide negative ΔE_{3B}^{DC} for the prism and cage isomers.

The comparisons with the reference CCSD(T)/CBS n-body energies shown in Figure 4.6 indicate that the PBE0-D3(DC) and M06-2X-D3(DC) functionals provide the smallest MUE at both 2B (0.27 kcal/mol and 0.65 kcal/mol, respectively) and 3B (0.27 kcal/mol and 0.53 kcal/mol, respectively) levels. Relatively large 2B errors are still found for the GGA functionals

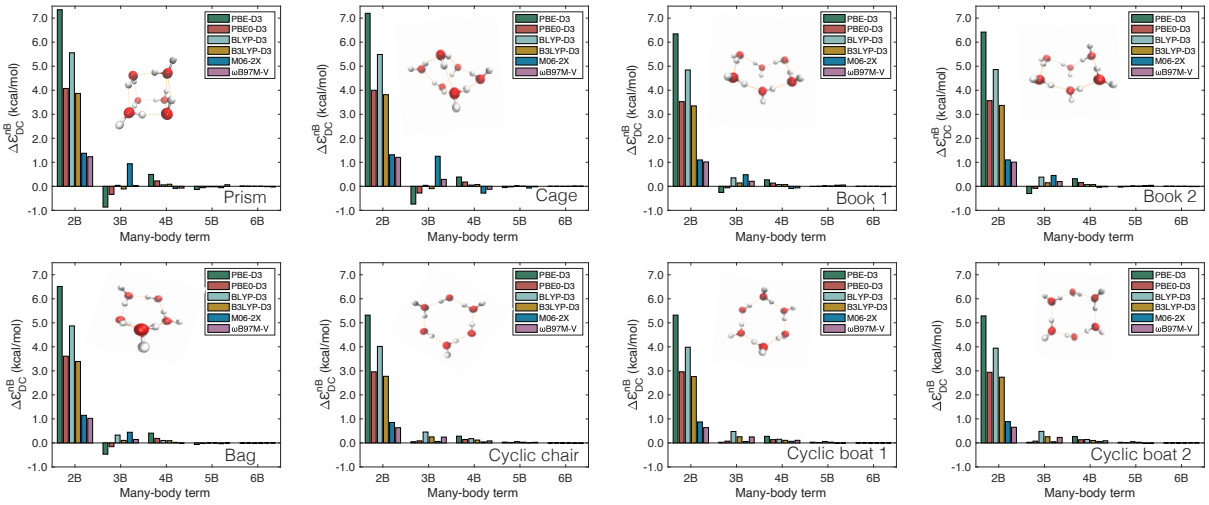

Figure 4.5: Errors in nB energies ($n = 2-6$) associated with PBE-D3, PBE0-D3, BLYP-D3, B3LYP-D3, M06-2X-D3 and ωB97M-V relative to the corresponding density-corrected values calculated for the first eight low-energy isomers of the water hexamer. Errors are defined as $\Delta E_{nB}^{DC} = E_{nB}^{DC} - E_{nB}^{SC}$, where E_{int}^{DC} and E_{int}^{SC} are the interaction energies calculated with the density-corrected and self-consistent functionals, respectively.

(although significantly smaller than those associated with the corresponding self-consistent density functionals), with MUEs of 2.77 kcal/mol and 6.47 kcal/mol for the PBE-D3(DC) and BLYP-D3(DC) functionals, respectively. The 2B MUE for the ωB97M-V(DC) functional is 0.94 kcal/mol for the 2B. Interestingly, independently of the isomer structure, all density-corrected functionals are associated with 2B and 3B errors of opposite signs relative to the CCSD(T)/CBS reference values. This results in fortuitous error compensation between 2B and 3B energies which, in turn, leads to apparently better agreement with the CCSD(T)/CBS total interactions energies for all hexamer isomers. Considering that the density-corrected functionals provide an approximate, yet reliable, representation of the interactions which is, at least, partially "free" of density-driven errors, the remaining deviations from the CCSD(T)/CBS values are likely due to inaccuracies in the density functionals, along with the localization errors associated with using Hartree-Fock densities in DFT calculations.[347]

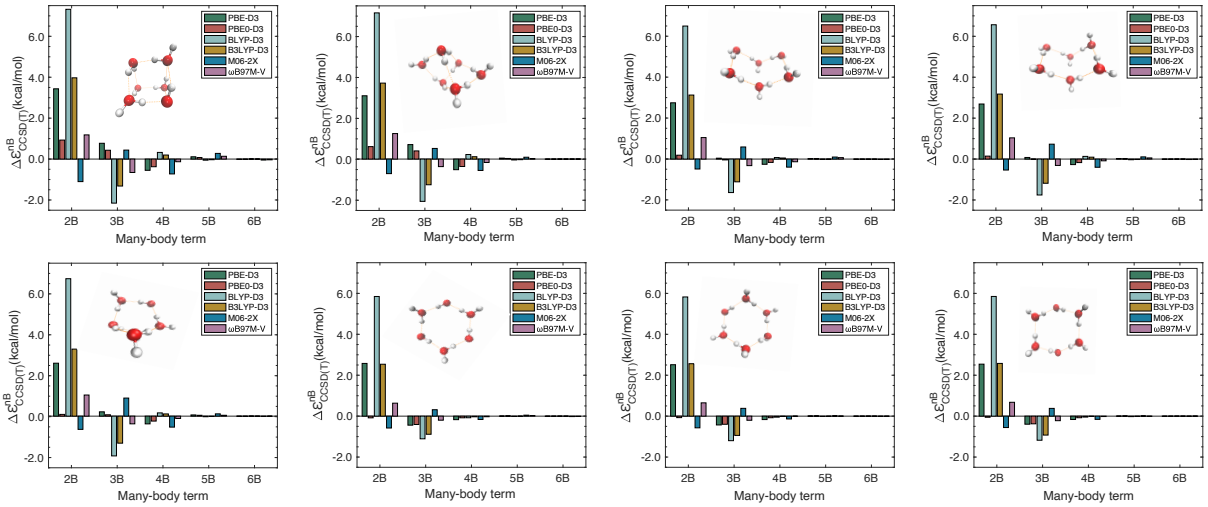

Figure 4.6: Errors in nB energies ($n = 2-6$) associated with the density corrected PBE-D3(DC), PBE0-D3(DC), BLYP-D3(DC), B3LYP-D3(DC), M06-2X-D3(DC) and ωB97M-V(DC) relative to the corresponding CCSD(T)/CBS reference values[1] calculated for the first eight low-energy isomers of the water hexamer. Errors are defined as $\Delta E_{nB}^{CCSD(T)} = E_{nB}^{DC} - E_{nB}^{CCSD(T)}$, where E_{nB}^{DC} and $E_{nB}^{CCSD(T)}$ are the nB energies calculated with the density-corrected functionals and at the CCSD(T)/CBS level of theory,[1] respectively.

Binding energies of the water hexamer isomers

Since the binding energies of all hexamer isomers lie within $\sim$1 kcal/mol, following ref 16, we focus our attention to the prism, cage, book-2, and cyclic chair-2 isomers. Based on the CCSD(T)/CBS reference values, the binding energies for these four hexamer isomers follow this order: prism $<$ cage $<$ book-2 $<$ cyclic chair-2, with the prism isomer being the most strongly bound isomer. The energy difference between the prism and cyclic chair-2 isomers is 0.88 kcal/mol at the CCSD(T)/CBS level. As shown in Figure 4.7a, the GGA functionals largely overbind all hexamer isomers, with MUE from the reference CCSD(T)/CBS data being 5.19 kcal/mol and 2.15 kcal/mol for PBE-D3 and BLYP-D3, respectively. The hybrid GGA functionals provides smaller MUE of 3.24 kcal/mol and 1.69 kcal/mol for PBE0-D3 and B3LYP-D3, respectively. Importantly, all these functionals provide the incorrect energy ordering of the isomers, predicting the cage isomer to be the most stable isomer. On the other hand, the more recent functionals (i.e., M06-2X and ωB97M-V) predict the correct energy ordering, with the ωB97M-V binding energies being very close to the reference CCSD(T)/CBS values, which results in a MUE of 0.58 kcal/mol. The relatively large MUE of 2.71 kcal/mol associated with the M06-2X-D3 functional is mainly due to this functional largely overbinding the prism and cage isomers.

Figure 4.7b shows that the overbinding tendency associated with all self-consistent density functionals is removed upon applying the density correction. Overall, the density-corrected functionals provide binding energies that are in significantly closer agreement with the reference CCSD(T)/CBS values, although they tend to slightly underbind all hexamer isomers, which may be related to localization errors associated with using Hartree-Fock densities.[347] Specifically, the density correction decreases the MUE associated with the PBE-D3 and PBE0-D3 functionals to 1.72 kcal/mol and 0.81 kcal/mol, respectively. Relatively large MUE are still obtained with the density-corrected BLYP-D3 (3.70 kcal/mol) and B3LYP-D3 (2.23 kcal/mol) functionals. As for the corresponding self-consistent density functionals, none of the density-corrected PBE-D3,

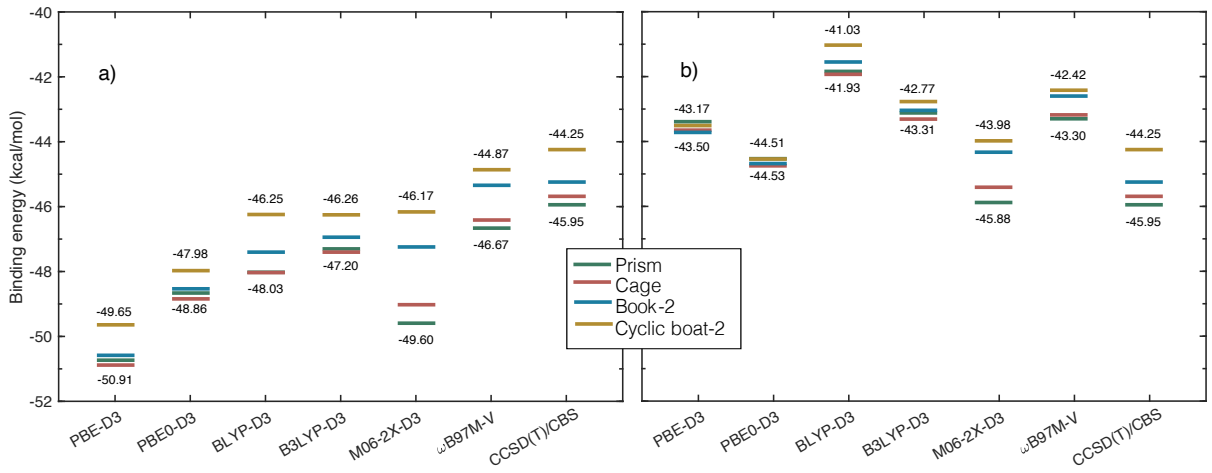

Figure 4.7: Binding energies of the prism, cage, book-2 and cyclic chair-2 isomers of the water hexamer calculated with PBE-D3, PBE0-D3, BLYP-D3, B3LYP-D3, M06-2X-D3 and ωB97M-V, along with the corresponding CCSD(T)/CBS reference values. Panels a) and b) report binding energies calculated with the self-consistent and density-corrected functionals, respectively.

PBE0-D3, BLYP-D3, and B3LYP-D3 functionals is able to reproduce the correct energy ordering of the hexamer isomers, with all four density functionals predicting the cage isomer to be the lowest-energy isomer.

Since hybrid, meta-GGA and range-separated functionals are less prone to density-driven errors, the differences in binding energies calculated with the self-consistent and density-corrected versions of M06-2X-D3 and ωB97M-V are significantly smaller than those obtained with the GGA and hybrid GGA functionals. Specifically, the MUE associated with the density corrected M06-2X-D3 and ωB97M-V functionals are 0.39 kcal/mol and 2.41 kcal/mol, respectively. Interestingly, this analysis indicates that applying the density correction somewhat deteriorates the ability of ωB97M-V to reproduce the CCSD(T)/CBS binding energies of the water hexamer isomers.

Density-corrected MB-DFT PEFs

To further investigate the effects of density-driven errors on the ability of density functionals to reproduce many-body interactions in water, we developed a density-corrected MB-DFT

PEF, dubbed MB-PBE(DC), which was trained on 1B, 2B, and 3B energies calculated with the corresponding density-corrected PBE-D3(DC) functional. Due to the lack of a suitable machinery for calculating atomic charges, polarizabilities and C_6 coefficients using density-corrected functionals, the corresponding PBE0-D3 values were used for these quantities, which seems to be a good compromise as the presence of a fraction of Hartree-Fock exchange partially reduces density-driven errors.

Figure 4.8 shows the errors associated with the MB-PBE and MB-PBE(DC) PEFs for each individual many-body contribution to the interaction energies of the first eight low-energy hexamer isomers relative to the corresponding values calculated with the self-consistent PBE-D3 and density-corrected PBE-D3(DC) functionals, respectively. As the density-driven errors are minimized in the MB-PBE(DC) PEF, the corresponding 4B energies, which, as discussed in section 4.2, are entirely represented by classical polarization in the MB-DFT PEFs, are significantly closer to the reference CCSD(T)/CBS values. Specifically, the 4B MUE associated with the MB-PBE(DC) PEF is 0.64 kcal/mol which must be compared to a value of 1.07 kcal/mol

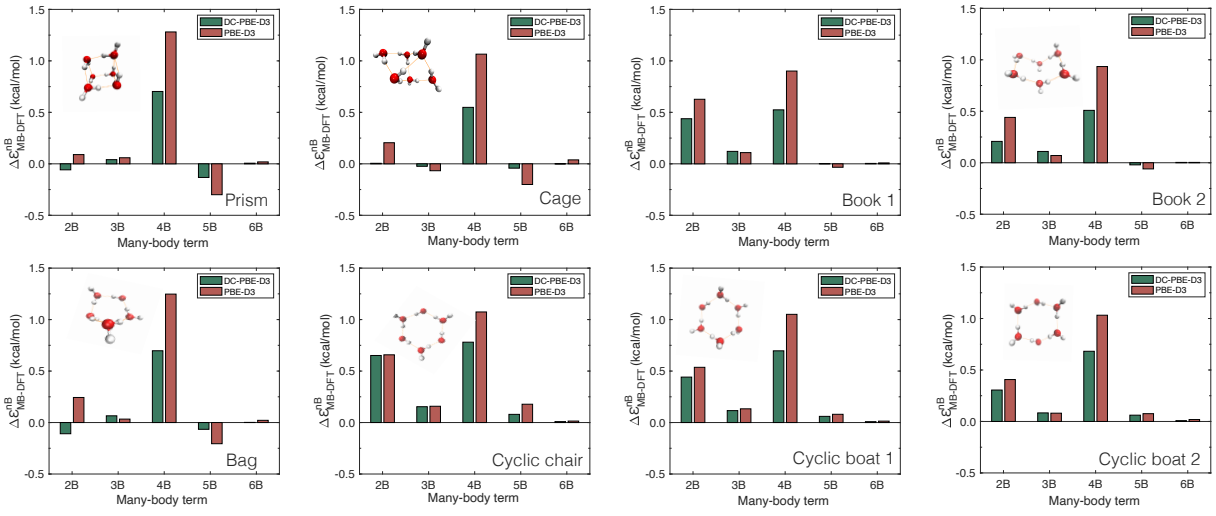

Figure 4.8: Errors in nB energies ($n = 2-6$) associated with MB-PBE and MB-PBE(DC) relative to the corresponding PBE-D3 and PBE-D3(DC) values calculated for the first eight low-energy isomers of the water hexamer. Errors are defined as $\Delta E^{MB-DFT}_{nB} = E^{MB-DFT}_{nB} - E^{DFT}_{nB}$, where E^{MB-DFT}_{nB} and E^{DFT}_{nB} are the nB energies calculated with the MB-DFT PEFs and corresponding (self-consistent and density-corrected) functionals, respectively.

reported in Table 4.1 for the analogous MB-PBE PEF trained on PBE-D3 data. Importantly, Figure 4.8 shows that not only the 4B error but also the errors for all other nB terms are significantly smaller when the density correction is taken into account as demonstrated by the higher accuracy provided by the MB-PBE(DC) PEF compared to the analogous MB-PBE PEF.

Figure 4.9 shows the interaction energies calculated with PBE-D3, PBE-D3(DC) and their corresponding MB-PBE and MB-PBE(DC) PEFs, respectively, along with the CCSD(T)/CBS reference values. As density-driven errors tend to overbind the isomers of the water hexamer, PBE-D3 predicts lower interaction energies than CCSD(T)/CBS. On the other hand, PBE-D3(DC) systematically underbinds all isomers. The density correction significantly improves the description of the interaction energies of the MB-PBE(DC) PEF, by effectively reducing the errors associated with all nB contributions to the interaction energy (Figure 4.8). The MB-PBE PEF displays a MUE of -1.51 kcal/mol relative to PBE-D3 whereas the density-corrected MB-PBE(DC)

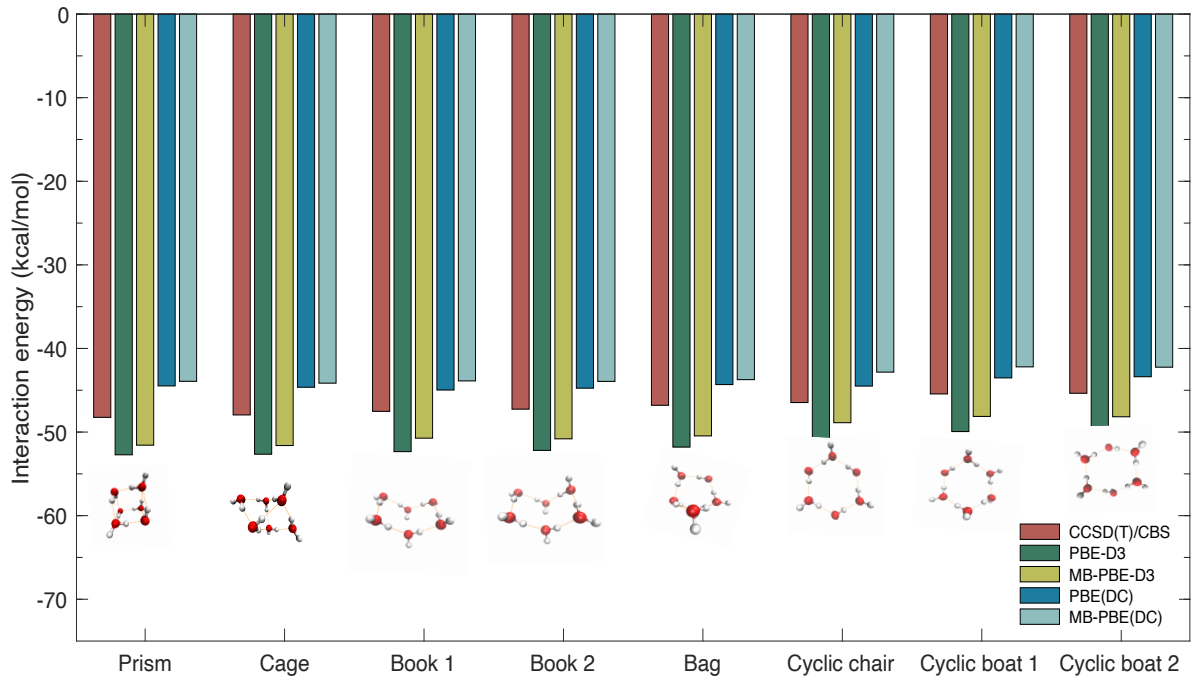

Figure 4.9: Interaction energies of the first eight low-energy isomers of the water hexamer calculated with the PBE-D3 and PBE-D3(DC) functionals, and the corresponding MB-PBE and MB-PBE(DC) PEFs along with the reference CCSD(T)/CBS values.

PEF displays a MUE of -0.96 kcal/mol relative to PBE-D3(DC). A direct comparison of the errors are shown in Figure S14.

It should be noted that, while PBE-D3(DC) displays a significantly lower MUE (2.56 kcal/mol) relative to CCSD(T)/CBS than PBE-D3 (4.67 kcal/mol), the MB-PBE(DC) PEF is associated with a slightly higher MUE (3.52 kcal/mol) relative to CCSD(T)/CBS than the MB-PBE PEF (3.16 kcal/mol). This is due to the signs of $\Delta E^{CCSD(T)}$ (Figure 4.6) and ΔE^{MB-DFT} (Figure 4.8), which make these errors add up for the MB-PBE(DC) PEF while partially cancelling out for the MB-PBE PEF.

4.5 Conclusions

In this study, we have presented a general theoretical framework for the development of data-driven many-body PEFs (MB-QM) in which the individual terms of the many-body expansion of the energy are rigorously derived from electronic structure data calculated at an arbitrary QM level of theory. As a demonstration, we have introduced a family of MB-QM PEFs for water which are rigorously derived from density functionals belonging to different rungs across Jacob's ladder of DFT approximations (MB-DFT) as well as from Møller-Plesset perturbation theory (MB-MP2).

All MB-QM PEFs, except those derived from the GGA functionals, are shown to retain the same accuracy of the corresponding QM methods for the energetics of small water clusters and associated many-body energy contributions. Due to the presence of relatively large density-driven errors, *ab initio* DFT calculations carried out with the GGA functionals analyzed in this study (PBE-D3 and BLYP-D3) yield appreciable smaller 4B energies compared to analogous calculations carried out with the corresponding MB-DFT PEFs. Since in the MB-DFT PEFs all higher-than-3B contributions are described by classical many-body polarization, the difference between the MB-DFT and DFT results can be traced back to density-driven errors that prevent

density functionals, in particular those derived within the GGA, from accurately representing individual many-body contributions. In this regard, the analysis of the energetics of the isomers of the water hexamer shows that density-driven errors in the DFT representations of the interactions in water primarily affect 2B and 3B energies.

To further investigate the effects of density-driven errors in the DFT descriptions of the interactions in water, for each density functional considered in this study, we have analyzed a corresponding density-corrected functional obtained by using Hartree-Fock densities in non-self-consistent DFT calculations. Except for ωB97M-V, all density-corrected functionals provide better agreement with the reference CCSD(T)/CBS data. Motivated by the improved performance of the density-corrected functionals, we have developed a density-corrected MB-DFT PEF, MB-PBE(DC) from density-corrected PBE-D3 data, and shown that it more closely reproduces the corresponding *ab initio* many-body energies than the analogous MB-DFT derived from self-consistent PBE-D3 data. The different performance of self-consistent and density-corrected functionals in reproducing the energetics of water clusters indicates that, while not essential for hybrid and range-separated functionals, accounting for density-driven errors is a necessary requirement in the development of MB-DFT PEFs derived from GGA functionals. These findings suggest that density-driven errors affect the convergence of the many-body expansion in water and indicate that the accuracy of a given density functional may vary significantly depending on both the size and hydrogen-bonding arrangements of the system under examination.

Acknowledgements

This research was supported by the U.S. Department of Energy, Office of Science, Office of Basic Energy Science, through grant no. DE-SC0019490. This research used resources of the National Energy Research Scientific Computing Center (NERSC), which is supported by the Office of Science of the U.S. Department of Energy under Contract DE-AC02-05CH11231,

the Extreme Science and Engineering Discovery Environment (XSEDE), which is supported by the National Science Foundation grant number ACI-1548562, and the Triton Shared Computing Cluster (TSCC) at the San Diego Supercomputer Center (SDSC) Supercomputer Center (SDSC).

Chapter 4 is in full a reprint of the material as it appears in "Lambros, E., Dasgupta, S., Palos, E., Swee, S., Hu, J., & Paesani, F. (2021). General many-body framework for data-driven potentials with arbitrary quantum mechanical accuracy: Water as a case study. *Journal of Chemical Theory and Computation*" The dissertation author was the co-primary author of this paper.

Chapter 5

Assessing the accuracy of the SCAN functional for water through a many-body analysis of the adiabatic connection formula

We present a systematic analysis of the accuracy of a series of SCANα functionals for water, with varying fractions (α) of exact exchange, which are constructed through the adiabatic connection formula. Our results indicate that that all SCANα functionals exhibit substantial errors in the representation of the water 2-body energies. Importantly, the inclusion of exact exchange is found to have opposite effects on the ability of the SCANα functionals to describe the interaction energies of water clusters with 2-dimensional and 3-dimensional hydrogen-bonding arrangements. These errors are found to directly affect the ability of the SCANα functionals to describe the structure of liquid water at ambient conditions, which is investigated using explicit many-body models (MB-SCANα) derived from the corresponding SCANα data. In particular, it is found that all MB-SCANα models predict a more compact first hydration shell, which results in a denser liquid with a more ice-like structure. These apparent opposite trends can be explained by the inability of the SCANα functionals to provide a balanced description of the water 2B and

3B energies at the fundamental level. The analyses presented in this study provide new insights that can guide future developments of improved exchange-correlation functionals for aqueous systems.

5.1 Introduction

Density functional theory (DFT) approaches have been used to calculate the properties of various molecular systems, from small molecules to liquids and solids where more expensive, post-Hartree-Fock methods become prohibitively inefficient.[348–351] Originally built upon the Hohenberg and Kohn theorems,[12] DFT was later formulated in its modern version by Kohn and Sham who introduced the exchange-correlation energy functional in the expression of the total energy functional.[13] Although in principle exact, the solution of the Kohn-Sham equations becomes approximate in practice because the exact exchange-correlation energy functional is unknown.[352]

The earliest approximation to the exact density functional, known as the local density approximation (LDA), was inspired by work by Slater who, a decade earlier, had proposed an approximation to the exact exchange term in Hartree-Fock theory based on a functional of the electron density.[353] Formally, the LDA is derived from the corresponding terms of the homogeneous electron gas, and assumes that the electron density is purely "local". This assumption of locality implies that the LDA approximation holds only for systems with very slowly varying densities as the density is assumed to be uniform at every point.[13] Besides its tendency to overestimate atomization energies,[354] the LDA also tends to overestimate the strength of hydrogen bonds in aqueous systems, predicting shorter oxygen-oxygen distances in small water clusters.[355, 356] Despite these aforementioned problems, the LDA also provided some of the first theoretical predictions of crystal structures under pressure. [357] First order corrections to the LDA, initially proposed in 1969 by Herman, Van Dyke, and Ortenburger,

were based on an analytic approach that eventually became the modern-day generalized gradient approximation (GGA) as developed by Langreth, Perdew, and Becke, among others.[358–363]

Modern GGA functionals, such as the PBE functional,[364] perform relatively better than the LDA functional for aqueous systems, but still result in broad disagreement with various experimental data, including the over-structuring of liquid water at ambient conditions.[176, 365] These GGA functionals were further extended to incorporate second-order corrections to the LDA using the Laplacian of the electron density, leading to meta-GGA functionals. [360, 366] By the late 90s, several meta-GGA functionals had been developed,[360, 367–369] which eventually evolved into more recent implementations, such as the B97M-V[370] and SCAN [14] functionals. It should be noted that most modern meta-GGA functionals use the kinetic energy density, τ, rather than an explicit Laplacian of the density. Both SCAN, which satisfies all 17 known constraints on the exact meta-GGA functional, and B97M-V are able to partially overcome the over-structuring of liquid water and provide better agreement to experiment for various properties,[4, 15, 371, 372] albeit often the comparisons with the experimental data are made with results obtained from simulations carried out at higher temperature.[4, 372]

In an attempt to improve the accuracy of DFT models, hybrid exchange-correlation functionals were developed starting from the adiabatic connection formula,[373]

$$E_{xc}[\rho] = \int_0^1 E_{xc,\lambda}\, d\lambda \tag{5.1}$$

In practical applications, the hybrid exchange-correlation functionals approximate the integral in eq 5.1 as a fractional sum of the non-interacting limit, which is described by the exact exchange, and the fully interacting limit, which is described by the exchange-correlation energy calculated with a given GGA or meta-GGA functional.[373] The original expression for $E_{xc}[\rho]$ was later refined into a 3-parameter fractional sum, with separate coefficients for the exact exchange term representing $E_{xc,0}$, and the exchange and correlation terms representing $E_{xc,1}$.[374] Following

the rationale introduced by Perdew, Ernzerhof, and Burke,[375] PBE0 and, later on, SCAN0 were proposed as hybrid versions of the corresponding base functionals (i.e., PBE and SCAN, respectively) without using any fitted parameters and adopting 25% exact exchange.[264, 376] Bundled with SCAN0, the double-hybrid SCAN0-2 functional was also shown to provide an accurate description of various molecular systems.[376]

Recently, the SCAN functional has been gaining popularity as a functional suitable for studies of liquid water. Yao and Kanai used SCAN to characterize the temperature dependence of nuclear quantum effects in liquid water.[15] Sharkas *et. al.* used small water clusters to show that the self-interaction error in the SCAN functional primarily affects the two-body (2B) term of the many-body expansion (MBE) of the energy.[16] Other studies used SCAN to analyze the equilibrium of high- and low-density liquid water at negative pressure.[17, 18] More recently, Xu *et. al.* studied the isotope effects in liquid H_2O and D_2O using a deep neural network potential (NNP) trained on the SCAN functional.[30]. A similar NNP was used to investigate the properties of supercooled water,[31] as well as the equilibrium between liquid water, ice I_h, and I_c,[5] and the ice I_h/XI transition.[32]

Building upon these studies, particularly the many-body analysis reported in ref 16, we provide here an assessment of the accuracy of the SCAN functional in predicting the properties of water. Our analysis uses the adiabatic connection formula to systematically investigate the effects of exact exchange on the individual terms of the MBE as well as on the structure of liquid water at ambient conditions and the description of hydrogen bonding in the water dimer. We demonstrate that, by modulating the fraction of exact exchange, small errors in the representation of the low-order terms of the MBE can lead to substantial changes in the structure of liquid water. Interestingly, our analysis indicates that the inclusion of exact exchange has opposite effects on the description of different hydrogen-bonding motifs, improving the accuracy of SCAN for 3-dimensional structures, while deteriorating its performance for 2-dimensional arrangements of water molecules.

5.2 Theory and Computational Details

All electronic structure calculations were performed with Q-Chem[331] using the SCAN functional[14] with the aug-cc-pVQZ basis set.[166, 266] The amount of exact exchange was specified using the "general" exchange functional section in Q-Chem. All molecular dynamics (MD) simulations were carried out in the isobaric-isothermal (NPT) ensemble for 1 ns with a 0.2 fs timestep using in-house software based on the DL_POLY2 simulation package,[168] which was modified to include the MB-DFT models.[61] The temperature was controlled via Nosé–Hoover chains (NHC) of four thermostats coupled to each degree of freedom.[377] The NPT ensemble was generated according to the algorithm described in ref. 378. A radial atom–atom cutoff distance of 9.0 Å was applied to the non-bonded interactions and the Ewald sum was used to treat long-range electrostatics.[379] The reference structures for the water hexamers, with their associated many-body interaction energies calculated at the CCSD(T)/CCSD(T)-F12 level of theory within the SAMBA scheme,[170] are taken from ref 1.

5.2.1 Hybrid Density Functionals

Hybrid density functionals are derived from the adiabatic connection formula[380–384]:

$$E_{xc}[\rho] = \int_0^1 E_{xc,\lambda}\, d\lambda \tag{5.2}$$

In eq 5.2, the electron-electron coupling goes through a continuum of partially interacting states, where the integration variable, λ, varies from 0 to 1, changing the system from a non-interacting Kohn-Sham reference system to a fully interacting system, with each intermediate state having the same ground-state electron density. The integrand in eq 5.2 is formally expressed as the

exchange-correlation potential energy at a given λ,

$$E_{xc,\lambda} = \langle \Psi_\lambda | V_{ee} | \Psi_\lambda \rangle - \frac{e^2}{2} \int \int \frac{\rho(r)\rho(r')}{|r-r'|} dr\, dr' \tag{5.3}$$

where V_{ee} is the electron-electron interaction operator and ρ is the density. At the non-interacting limit ($\lambda = 0$), the integrand becomes the exact exchange energy of the Kohn-Sham orbitals, while at the fully interacting limit the integrand is calculated using a given density functional approximation (DFA). As discussed in the introduction, the integral in eq 5.2 is approximated by a linear interpolation of the $\lambda = 0$ and $\lambda = 1$ states, and becomes a fractional sum of the two.[373] The most general formulation of this sum is given by

$$E_{xc} = \alpha E_x^{exact} + (1-\alpha) E_x^{DFA} + E_c^{DFA} \tag{5.4}$$

where E_x^{exact} is the exact exchange, and E_x^{DFA} and E_c^{DFA} are the DFA exchange and correlation terms. Eq. 5.4 can be rewritten as[375]

$$E_{xc} = \frac{1}{n} E_x^{exact} + \left(1 - \frac{1}{n}\right) E_x^{DFA} + E_c^{DFA} \tag{5.5}$$

for an integer n corresponding to the lowest order of Moller-Plesset perturbation theory needed to reproduce the atomization energies. Given the overall good performance of 4^{th} order Moller-Plesset perturbation theory (MP4), PBE0 and SCAN0 use $n = 4$ (corresponding to α=0.25).[264, 376] In this work, we refer to the hybrid SCAN functionals with varying fractions of exact exchange, α, as SCANα.

5.2.2 Explicit Many-Body Models: MB-pol and MB-DFT

MB-pol[37–39] and MB-DFT[61] are explicit many-body models derived from the MBE of the energy, which represents the energy of a system of N "bodies" (i.e., distinct atoms or

molecules) as the sum of all the individual n-body contributions, with $n \leq N$.[40] The MBE is formally expressed as

$$E_N(r_1,..,r_N) = \sum_{i=1}^{N} \varepsilon_{1B}(r_i) + \sum_{i<j}^{N} \varepsilon_{2B}(r_i,r_j) + \sum_{i<j<k}^{N} \varepsilon_{3B}(r_i,r_j,r_k) + ... + \varepsilon_{NB}(r_1,..,r_N) \quad (5.6)$$

where ε_{1B} represents the distortion energy of an individual monomer from its equilibrium geometry, and each ε_{nB} with $n > 1$ represents the n-body energy which is defined recursively as

$$\varepsilon_{nB} = \varepsilon_n(1,...,n) - \sum_{i=1}^{N} \varepsilon_{1B}(r_i) - \sum_{i<j}^{N} \varepsilon_{2B}(r_i,r_j) - \sum_{i<j<k<...<n-1}^{N} \varepsilon_{(n\text{-}1)B}(r_i,r_j,..r_{n-1}). \quad (5.7)$$

The MBE converges quickly for atoms and molecules with localized electron densities and sufficiently large band gaps, such as water[170] and other molecular fluids.[62**?**]

The MB-pol and MB-DFT models include explicit representations of the first three terms of the MBE, implicitly accounting for all higher-order ($n > 3$) body terms via classical polarization,

$$E_N(r_1,..,r_N) = \sum_{i=1}^{N} \varepsilon_{1B}(r_i) + \sum_{i>j}^{N} \varepsilon_{2B}(r_i,r_j) + \sum_{i>j>k}^{N} \varepsilon_{3B}(r_i,r_j,r_k) + E_{pol} \quad (5.8)$$

The 1B term in both MB-pol and MB-DFT models is described by the Partridge-Schwenke potential energy surface calculated at the configuration interaction level of theory and subsequently refined to quantitatively reproduce the experimental rovibrational transitions of a water molecule.[64] The 2B term consists of three contributions:

$$\varepsilon_{2B} = E_{2B,sr} + E_{elec} + E_{disp} \quad (5.9)$$

where $E_{2B,sr}$ is represented by a 4^{th}-degree permutationally invariant polynomial (PIP)[65]

describing the short-range interactions within a water dimer. E_{elec} is described by a Coulomb potential between geometry dependent point charges that reproduce the *ab initio* dipole moment surface of a water molecule.[64] Finally, the 2B dispersion energy is given by

$$E_{disp} = -\sum_{i,j} f(\delta_{ij}) \frac{C_{6,ij}}{R_{ij}^6} \tag{5.10}$$

where i and j are indices for two atoms on two separate water molecules, $f(\delta_{ij})$ is the Tang-Toennies damping function with a fitted parameter δ_{ij},[66] and $C_{6,ij}$ is the dispersion coefficient between atoms i and j which is calculated from the asymptotic reference energy of the water dimer as originally introduced in the CC-pol model.[45] The explicit 3-body (3B) term,

$$\varepsilon_{3B} = E_{3B,sr} \tag{5.11}$$

describes short-range 3B interactions and is represented by a 4^{th}-degree PIP[65]. In MB-pol, the 2B and 3B PIPs are fitted on top of an implicit many-body polarizable potential (E_{pol} in eq 5.8) in order to reproduce 2B and 3B energies calculated at the CCSD(T) level of theory in the complete basis set (CBS) limit.[37, 38] Similarly, the explicit ε_{2B} and ε_{3B} terms of the MB-DFT models are fitted to 2B and 3B energies calculated with a given DFA, using the same procedure described in ref 61.

In this study, we introduce a series of MB-DFT models for water, denoted as MB-SCANα, fitted to 2B and 3B energies calculated with the SCANα functionals, including different fractions (α) of exact exchange. The accuracy of each MB-SCANα model is assessed through a systematic analysis of the MBE, the structure of liquid water at ambient conditions, and the potential energy profile along the hydrogen-bonding coordinate in the water dimer.

5.3 Results and Discussion

5.3.1 Many-Body Analysis of the Water Hexamer

As a first demonstration of the role played by the exact exchange in determining the strength of the interactions between water molecules, Figure 5.2 plots the errors relative to the CCSD(T)/CBS reference values which are associated with the n-body (with $n = 2-6$) energies calculated using the SCANα functionals for the first eight low-energy isomers of the water hexamer displayed in Figure 5.1. Figure 5.3 shows the corresponding total interaction energies (panel a) and the relative interaction energies (panel b) as a function of α. The relative interaction energies are calculated by minimizing the total signed error with respect to the corresponding CCSD(T)/CBS reference values. By removing energy contributions due to monomer distortions, the analysis of the interaction energies allows for a direct comparison of the molecular interactions specific to each fraction of exact exchange. As discussed in section 2, the interaction energies were calculated at the SCANα/aug-cc-pVQZ level of theory with varying fractions of exact exchange corresponding to α=0.00 (pure SCAN functional), 0.05, 0.10, 0.15, 0.20, and 0.25 (hybrid SCAN0 functional).

In the analysis of the MBE for the prism isomer shown in Figure 5.2a, the 2B term calculated with α=0.00 exhibits an error of -5.74 kcal/mol. The error progressively decreases with increasing α, reaching a value of -4.96 kcal/mol at α=0.25. The 2B term for the cage isomer displays errors ranging from -5.69 kcal/mol for SCANα with α=0.00 to -4.98 kcal/mol for SCANα with α=0.25. Both book isomers display similar 2B errors of -4.83 and -4.90 kcal/mol for α=0.00, and reduced errors of -4.65 and -4.66 kcal/mol when α=0.25. Interestingly, the lowest errors (-4.63 and -4.65 kcal/mol for book-1 and book-2, respectively) are obtained when α=0.20. The bag isomer displays a 2B error of -4.95 kcal/mol when α=0.00, with an error of -4.63 kcal/mol when α=0.25. The cyclic isomers display opposite behavior as a function of α. Specifically, the 2B error in the cyclic chair is the smallest (-3.95 kcal/mol) at α=0.00 and

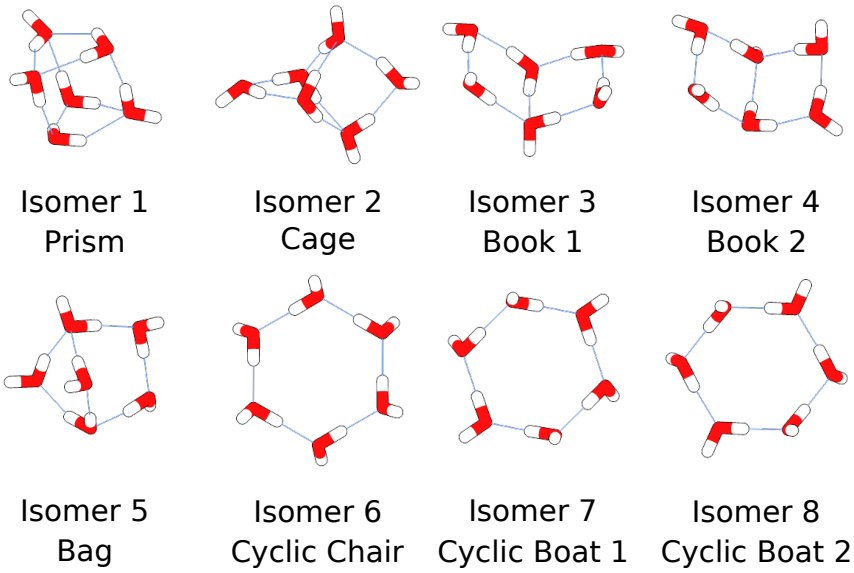

Figure 5.1: Structures of the first eight low-energy isomers of the water hexamer, $(H_2O)_6$.

the largest (-4.31 kcal/mol) at α=0.25. Similarly, the two cyclic boat isomers exhibit errors of -3.92 and -3.87 kcal/mol at α=0.00, and -4.22 and -4.19 kcal/mol at α=0.25. This general trend indicates that the accuracy of the 2B term in the SCANα functionals increases with α in isomers that display 3-dimensional hydrogen-bonding arrangements (i.e., prism and cage isomers). The opposite trend is observed for ring-like structures (i.e., the cyclic isomers) for which the addition of any fraction of exact exchange deteriorates the accuracy of the 2B term relative to the pure SCAN functional.

All SCANα functionals are associated with significantly smaller errors for all higher-body terms, which systematically decrease in magnitude as α increases. In particular, both prism and cage isomers, which are characterized by fully 3-dimensional hydrogen-bonded structures, display maximum errors of -0.08 and -0.12 kcal/mol for the 3B term, and a similarly small maximum error of -0.04 kcal/mol for the 4B term at α=0.00. Relatively larger 3B and 4B errors (on the order of -0.5 kcal/mol and 0.15 kcal/mol, respectively) are found for the book-1, book-2, and bag isomers described by the pure SCAN functional, with errors decreasing as α increases. All cyclic isomers exhibit 3B and 4B errors of approximately -0.8 kcal/mol and -0.25 kcal/mol when

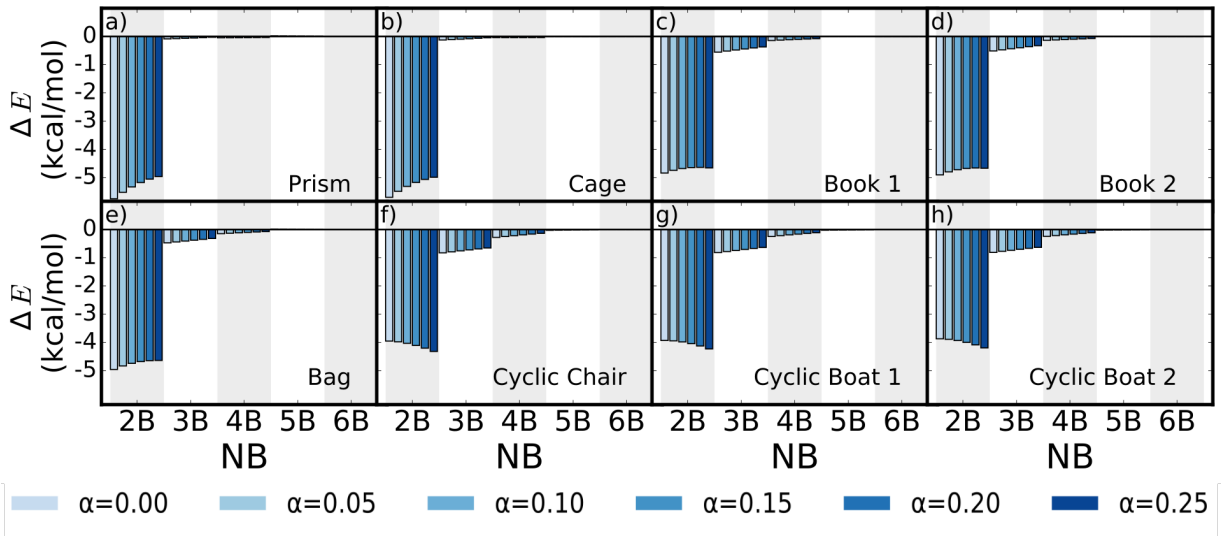

Figure 5.2: Errors in the individual terms of the MBE for the first eight low-energy isomers of the water hexamer calculated with the SCANα functionals relative to the CCSD(T)/CBS reference values of ref 1. The alternating grey and white shaded sectors separate each individual nB term of the MBE, with the corresponding errors associated with each SCANα functional shown as bars with varying shades of blue.

$\alpha = 0.00$, with errors decreasing as the fraction of exact exchange increases from α=0.00 to α=0.25. For all isomers, independently of α, the 5B and 6B errors are always small, ranging from 10^{-4} to 10^{-2} kcal/mol.

This analysis highlights the limitations of the pure SCAN functional (α=0.00) in providing a balanced representation of 2B and higher-body energies, with the former being largely overestimated. Importantly, this "asymmetry" is not corrected by including any fraction of exact exchange (up to $\alpha = 0.25$). In particular, while improving the description of 2B energies in the hexamer isomers with 3-dimensional hydrogen-bonding arrangements, the inclusion of any fraction of exact exchange deteriorates (approximately by the same amount) the description of 2B interactions in cyclic structures.

The errors in the individual terms of the MBE directly translate into the different ability of the SCANα functionals to predict the relative stability of the hexamer isomers. Figure 5.3a shows the total interaction energy for all isomers as a function of α. Starting from the prism isomer, the 3-dimensional isomers display substantially distinct interaction energies which become less

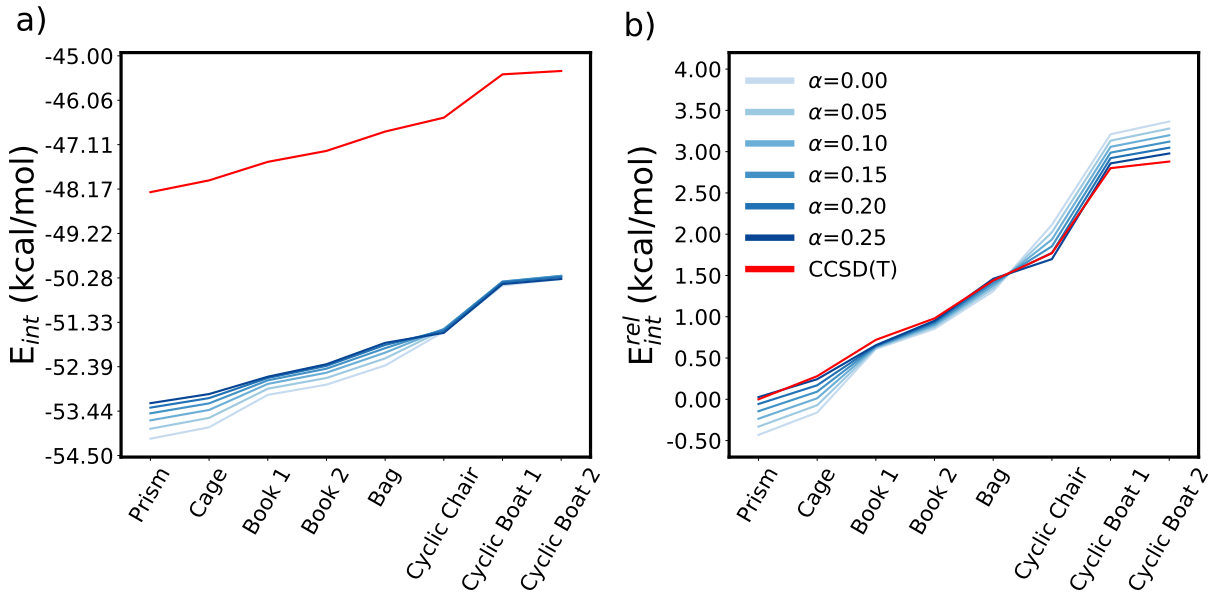

Figure 5.3: Total (panel a) and relative (panel b) interaction energies of the first eight low-energy isomers of the water hexamer calculated with the SCANα functionals. The CCSD(T)/CBS reference values are taken from ref 1. The relative interaction energies for each SCANα functional are aligned to the CCSD(T)/CBS reference values by minimizing the total signed error.

negative with increasing α. Moving from the cage to the book and bag isomers, the interaction energies become progressively more clustered, and closer to the values obtained with α=0.25. Once the 2-dimensional isomers (the cyclic chair and boat isomers) are reached, all SCANα functionals effectively predict the same interaction energy obtained with α=0.25.

As shown in Figure 5.3b, the SCANα functional with α=0.25 predicts relative interaction energies that closely follow the CCSD(T)/CBS reference values, while all other values of α display progressively divergent curves as α decreases. Importantly, the SCANα functionals with $\alpha < 0.25$ are found to progressively overbind the low-energy isomers and underbind the high-energy isomers. This results in the pure SCAN functional ($\alpha = 0.00$) predicting an energy difference of $\sim$4 kcal/mol between the prism and cyclic-boat-2 isomers, which is $\sim$1 kcal/mol larger than the corresponding CCSD(T)/CBS value.

The similarity of the total interaction energies between all values of α found in Figure 5.3a

for the three cyclic isomers may be explained by the opposite trend displayed by the corresponding 2B and higher-body terms. For these isomers, Figure 5.2 shows that the lower error in the 2B term found for small values of α is countered by higher errors in the 3B and 4B terms, and vice versa as α increases. This trend is further analyzed in Figure S3 of the Supporting Information which shows the $\Delta\Delta E$ relative to α=0.0 Finally, it should be noted that the 2B terms for the isomers with 3-dimensional structures show the largest variance in the associated errors, which correspondingly elicits the relatively wider distribution of interaction energies seen in Figure 5.3b. These results suggest that the fraction of exact exchange included in the SCANα functionals acts primarily on the 2B term of the MBE, leaving all other (higher-order) terms less dependent on α.

5.3.2 Liquid Water

While the previous section examines the effects of modulating the fraction of exact exchange within the SCAN functional on the energetics of small water clusters, this section seeks to connect the differences among the SCANα functionals to the ability of these functionals to describe the structure of liquid water at ambient conditions. For this purpose, MD simulations were carried out at 298.15 K and 1 atm in the NPT ensemble with the MB-SCANα models fitted to the corresponding SCANα 2B and 3B energies. Based on the analysis of the previous section, since the errors in the SCANα 4B and higher-body terms are effectively equivalent to those associated with MB-pol,[1] the MB-SCANα models provide an accurate representation of the SCANα functionals, despite only the corresponding 2B and 3B energies are explicitly used in their parameterization (see Figure S1 in the Supporting Information). Following ref 61, three distinct MB-SCANα models are constructed for each SCANα functional by progressively replacing the MB-pol 2B and 3B terms with the SCANα counterparts. The MB-SCANα models are thus labeled as (2B+3B)-MB-SCANα, (2B)-MB-SCANα, and (3B)-MB-SCANα to indicate that both the 2B and 3B, only the 2B, and only the 3B terms are represented by fits to the corresponding SCANα 2B and 3B energies, with all other terms being represented as in MB-

pol. As demonstrated in ref 61, the MB-DFT models are able to reproduce, at a fraction of the associated computational cost, the results obtained from the corresponding *ab initio* MD simulations.

Figure 5.4 displays the oxygen-oxygen (O-O) radial distribution functions (RDFs) calculated with the (2B+3B)-MB-SCANα (panel a), (2B)-MB-SCANα (panel b), and (3B)-MB-SCANα (panel c) models. All (2B+3B)-MB-SCANα models (panel a) predict O-O RDFs that are systematically shifted (by $\sim$0.3Å) to the left of the corresponding experimental curve,[385, 386] indicating overly attractive interactions between the water molecules. This is a direct consequence of all SCANα functionals overestimating, especially at the 2B level, the strength of the low-order many-body interactions between water molecules as shown in Figures 5.2 and 5.3. Besides this common feature, significant variation exists in the ability of the different (2B+3B)-MB-SCANα models to reproduce the experimental O-O RDF. In particular, the (2B+3B)-MB-SCANα model with α=0.00 predicts a significantly less structured second solvation shell. As α increases, the (2B+3B)-MB-SCANα models predict an increasingly more structured liquid. In this context, a value of α=0.15 appears to be the "optimal" compromise, leading to an O-O RDF that is in closer agreement with the experimental curve, although the peaks of the solvation shells are consistently higher and the "valleys" between consecutive shells are consistently deeper than in

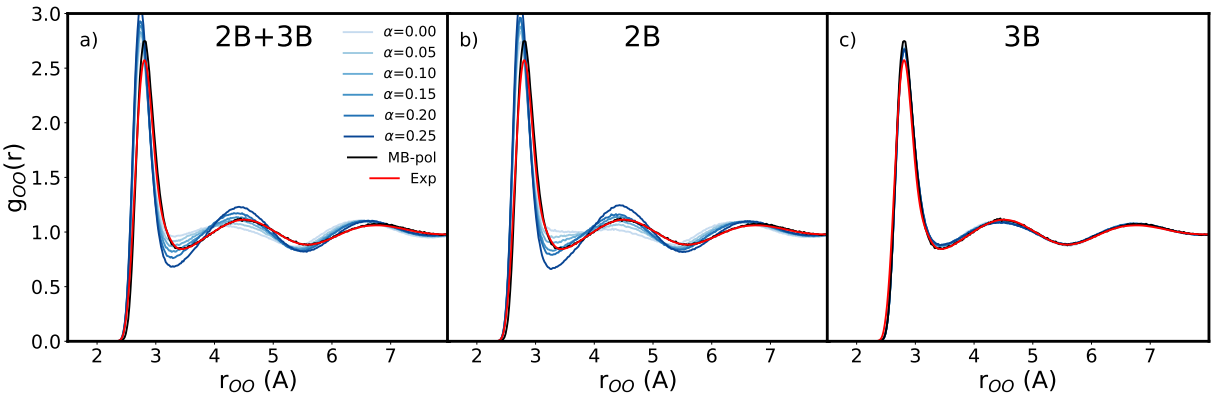

Figure 5.4: O-O RDFs calculated from NPT MD simulations carried out at 298 K and 1 atm using the (2B+3B)-MB-SCANα (panel a), (2B)-MB-SCANα (panel b), and (3B)-MB-SCANα (panel c) models. The experimental RDFs at 295 K are taken from refs 385 and 386.

the experimental RDF.

The general trend observed in the O-O RDFs calculated with the (2B+3B)-MB-SCANα models is also reproduced by the O-O RDFs calculated with the (2B)-MB-SCANα models (Figure 5.4b), where only the 2B term of MB-pol is replaced with the 2B term fitted to the corresponding SCANα 2B energies. On the other hand, all (3B)-MB-SCANα models, which replace only the 3B term of MB-pol with the corresponding SCANα 3B, closely reproduce the experimental O-O RDF (Figure 5.4c), effectively achieving the same accuracy of the MB-pol model. The close correspondence between the O-O RDFs calculated with the (2B+3B)-MB-SCANα and (2B)-MB-SCANα models combined with the agreement between the (3B)-MB-SCANα and experimental RDFs provide clear evidence that the inability of the pure SCAN functional ($\alpha = 0.00$) to reproduce the shape of the experimental RDF is primarily due to intrinsic deficiencies of the SCAN functional in correctly predicting the 2B energies as shown in Figure 5.2. Similar conclusions can be drawn from the analyses of the O-H and H-H RDFs reported in the Supporting Information.

The differences in the O-O RDFs calculated with the three sets of MB-SCANα models directly translate in the differences seen in the corresponding O-O cumulative distribution functions

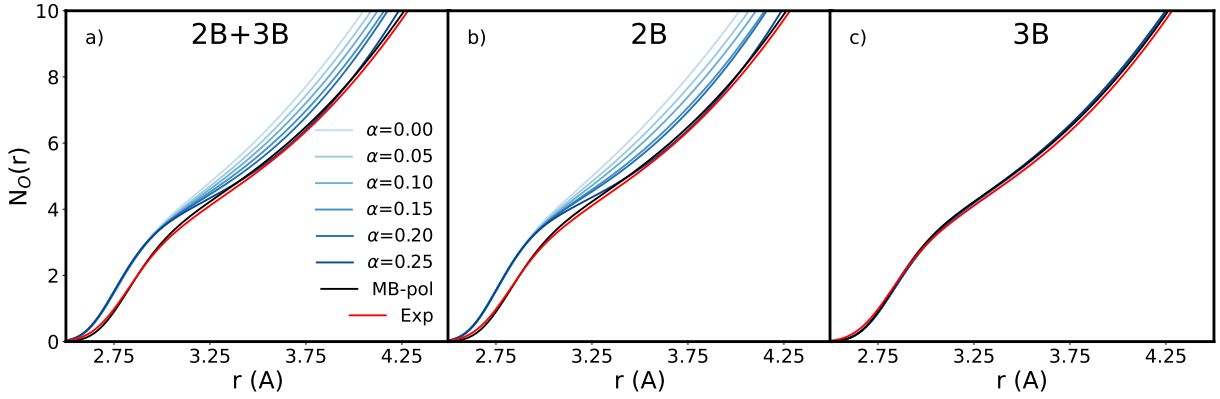

Figure 5.5: O-O CDFs calculated from NPT MD simulations carried out at 298 K and 1 atm using the (2B+3B)-MB-SCANα (panel a), (2B)-MB-SCANα (panel b), and (3B)-MB-SCANα (panel c) models. The experimental RDFs at 295 K are taken from refs 385 and 386, and 387 at 295K.

(CDFs) shown in Figure 5.5 and densities listed in Table 5.1. In particular, both the (2B+3B)-MB-SCANα and (2B)-MB-SCANα models predict CDFs that deviate significantly from the experimental and MB-pol curves, systematically overestimating the coordination number between 2.5 Åand 4.5 Å. On the contrary, all (3B)-MB-SCANα models are effectively indistinguishable from each other and in quantitative agreement with the experimental and MB-pol curves. As a consequence, both the (2B+3B)-MB-SCANα and (2B)-MB-SCANα models predict significantly higher densities, which systematically decrease as the fraction of exact exchange increases. On the other hand, all (3B)-MB-SCANα models predict densities that are in quantitative agreement with the experimental value of 0.997 g/cm^3, independently of α.

It should be noted that the density calculated with the (2B+3B)-MB-SCANα model with $\alpha = 0.00$ is larger than the values obtained in ref 4 using *ab initio* MD simulations carried out with the pure SCAN functional at 330 K (1.05$\pm$0.027 g/cm^3) and in ref 5 using MD simulations carried out with a DNN model trained on SCAN data for bulk configurations. In this context, it has been shown that density fluctuations in *ab initio* simulations of liquid water are particularly sensitive to both system's size and plane wave cutoff, which may be a possible reason for the differences considering that all MB-SCANα simulations were carried out for a system consisting of 256 water molecules while 64 molecules were used in the *ab initio* MD simulations of ref 4. Besides these technical differences, it should also be noted that, as discussed in ref 16, SCAN calculations of the water interactions are affected by non-negligible self-interaction errors that depend on the system's size. Since the (2B+3B)-MB-SCANα models are only trained on the low-order terms of the MBE, it follows that they cannot "capture" self-interaction errors that develop in larger systems. We believe that this is the main reason, besides the different temperatures and system sizes used in the simulations, for the different density values obtained from the *ab initio* MD simulations with SCAN reported in ref 4 and the present simulations with the (2B+3B)-MB-SCANα model (α = 0.0). To test this hypothesis, it would particularly interesting in the future to compare *ab initio* SCAN simulations corrected for the self-interaction error (e.g.,

Table 5.1: Density (in g/cm^3) of liquid water calculated from MD simulations carried out in the NPT ensemble at 298 K and 1 atm using the three sets of MB-SCANα models. As a reference, the experimental density is 0.997 g/cm^3, while the MB-pol density is 1.007 g/cm^3.[1]

α	(2B+3B)-MB-SCANα	(2B)-MB-SCANα	(3B)-MB-SCANα
0.00	1.14	1.16	1.00
0.05	1.12	1.14	1.00
0.10	1.10	1.12	1.00
0.15	1.08	1.09	1.01
0.20	1.07	1.08	1.01
0.25	1.04	1.04	1.01

using the FLOSIC scheme of ref 16) with simulations carried out with (2B+3B)-MB-SCANα models trained on 2B and 3B energies that are similarly corrected for the self-interaction error.

While the different nature of the training sets (bulk configurations for the DNN model of ref 5, and 1B, 2B, and 3B energies, along with 1B dipoles and polarizabilities, for the (2B+3B)-MB-SCANα models) may also be responsible for the different density values predicted by the two models, we believe that further investigations are needed to systematically determine both merits and shortcomings of DNN and MB-DFT models in reproducing *ab initio* data across the phase diagram of water.

While the RDFs report on the distributions of inter-atomic distances between pairs of atoms, direct insights into 3-dimensional arrangements of the water molecules in the liquid can be gained from the analysis of the tetrahedral order parameter, q_{tet}, defined as[388]

$$q_{tet} = 1 - \frac{3}{8} \sum_{j=1}^{3} \sum_{k=j+1}^{4} \left(cos(\psi_{jk}) + \frac{1}{3} \right)^2 \tag{5.12}$$

Here, ψ_{jk} is the angle between the O atom of the central water molecule and the O atoms of two neighboring water molecules. A q_{tet} value of 1 indicates a perfectly tetrahedral arrangement, while smaller values correspond to more disordered arrangements.

The analysis of q_{tet} calculated with the (2B+3B)-MB-SCANα models shown in figure 5.6a demonstrates that these models predict a progressively more tetrahedral structure as α increases,

as indicated by the rightward shift and heightening of the main peak at $q_{tet} \sim 0.75$. For small values of α, the observed larger values of q_{tet} relative to MB-pol can be explained by the larger coordination numbers predicted by the MB-SCANα models (Figure 5.5a) and the higher densities reported in Table 5.1. Since, by definition, q_{tet} only considers the four nearest water molecules, without accounting for any additional molecule in the solvation shell, the q_{tet} distribution for the MB-SCANα model with $\alpha = 0.00$, which corresponds to the pure SCAN functional, indicates a more compact, but geometrically ice-like structure of liquid water at ambient temperature. The results shown in Figure 5.5a also indicate that, as α increases, the (2B+3B)-MB-SCANα models approach a less compact structure, which is accompanied by a decrease in density and, at the same time, a more pronounced ice-like signature.

While an analogous trend is predicted by the (2B)-MB-SCANα models (Figure 5.6b), the (3B)-MB-SCANα models (Figure 5.6c) closely reproduce the MB-pol distribution. The close correspondence between the q_{tet} distributions for the (2B+3B)-MB-SCANα and (2B)-MB-SCANα models, along with the agreement between the (3B)-MB-SCANα and the MB-pol results further suggests that the compact, ice-like structure predicted by the (2B+3B)-MB-SCANα models with $\alpha = 0.00$ is rooted in the inability of the SCAN functional to correctly reproduce 2B interactions between water molecules (Figure 5.2).

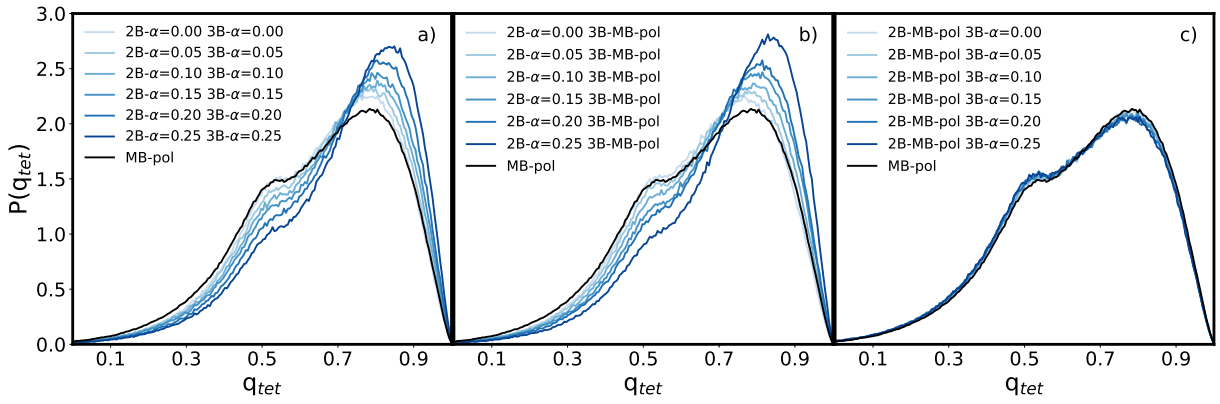

Figure 5.6: Distributions of the tetrahedral order parameter, q_{tet}, calculated from NPT MD simulations carried out at 298 K and 1 atm using the (2B+3B)-MB-SCANα (panel a), (2B)-MB-SCANα (panel b), and (3B)-MB-SCANα (panel c) models.

5.3.3 Hydrogen Bonding in the Water Dimer

In an attempt to rationalize the differences seen in the O-O RDFs, densities, and tetrahedral order parameters calculated with the three sets of MB-SCANα models, this section examines the ability of the SCANα functionals to describe hydrogen bonding in the water dimer. To this purpose, Figure 5.7 shows the deviations, $\Delta\tilde{\nu}$, in the harmonic frequencies of the water monomer and dimer calculated with the SCANα functionals relative to the reference CCSD(T):MP2 harmonic frequencies reported in refs 2 and 3. This analysis indicates that the deviations associated with the OH harmonic frequencies (marked in blue) of both H_2O and $(H_2O)_2$ systematically move from negative to positive values as α increases. In particular, for the water monomer, the pure SCAN functional (α=0.00) predicts a red shift of $\sim$30 cm^{-1}, while a blue shift of $\sim$75 cm^{-1} is associated with SCAN0 (α=0.25). While the same shifts are found for harmonic vibrations involving the free OH bonds in the water dimer, the harmonic frequency of the hydrogen-bonded OH (labeled as OH* in the figure) is appreciably underestimated by the pure SCAN functional, resulting in $\Delta\tilde{\nu} = -75$ cm^{-1}. This red shift, indicative of a relatively stronger hydrogen bond compared to the reference CCSD(T):MP2 value, directly correlates with the higher liquid density obtained from NPT simulations carried out with the (2B+3B)-MB-SCANα model with $\alpha = 0.00$. The progressive blue shift observed in the harmonic frequency of the hydrogen-bonded OH parallels the decrease in the liquid density predicted by the corresponding (2B+3B)-MB-SCANα models. Importantly, Figure 5.7 shows that the closest agreement between the CCSD(T):MP2 and SCANα harmonic frequencies of the hydrogen-bonded OH is obtained with $\alpha = 0.15$, which is the same fraction of exact exchange that provides the closet agreement with the experimental RDFs in the analysis of the (2B+3B)-MB-SCANα models (Figure 5.4).

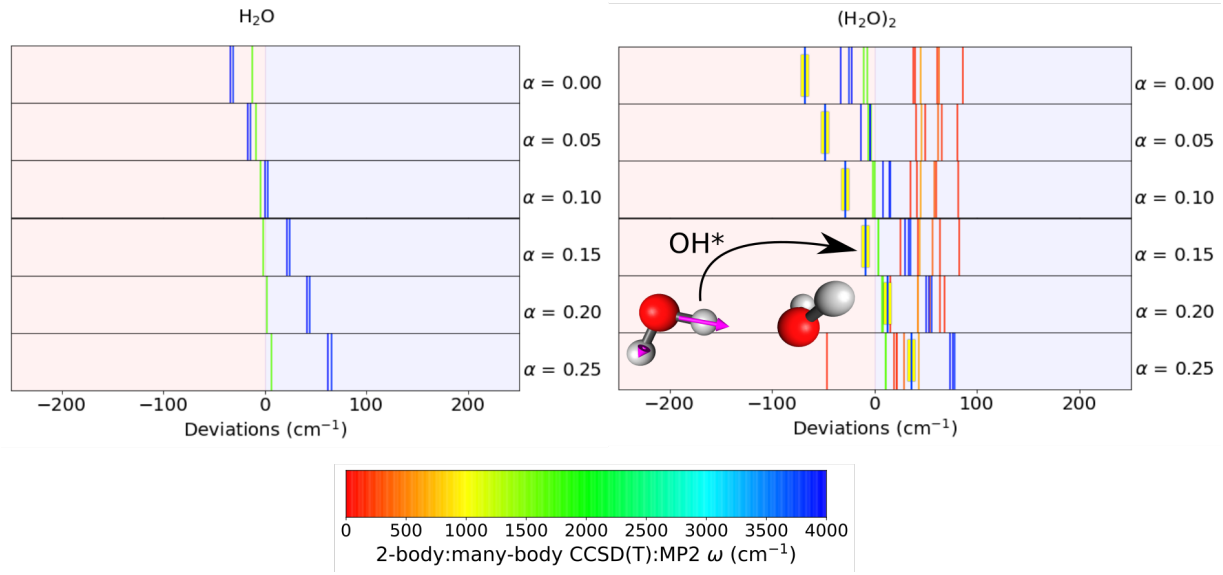

Figure 5.7: Deviations from the reference 2-body:many-body harmonic frequencies of $(H_2O)_n$, with $n = 1-2$,[2, 3] calculated using SCANα functionals with α=0.00-0.25. The light red and blue backgrounds correspond to red and blue shifts relative to the reference values. Each harmonic mode, indicated by a stick line, is colored according to the associated frequency according to the colorbar displayed at the bottom of the figure. For each value of α, the harmonic frequency for the hydrogen-bonded OH is highlighted with a yellow box, as indicated by the inset graphic.

5.4 Conclusion

In this study, we presented a systematic analysis of the role played by the exact exchange in describing the water interactions by investigating the accuracy of a series of SCANα functionals, with varying fractions (α) of exact exchange, which are constructed through the adiabatic connection formula. Our analysis demonstrates that all SCANα functionals are unable to correctly represent 2B interactions between water molecules, with errors relative to the CCSD(T)/CBS reference values that are on the order of 4-5 kcal/mol for the isomers of the water hexamer. Importantly, we show that the inclusion of exact exchange has opposite effects on the ability of the SCANα functionals to describe the interaction energies of the hexamer isomers with 2-dimensional and 3-dimensional hydrogen-bonding arrangements. Specifically, while the errors relative to the CCSD(T)/CBS reference values decrease going from $\alpha = 0.00$ (pure SCAN

functional) to $\alpha = 0.25$ (hybrid SCAN0 functional) for the prism and cage isomers, the opposite trend is found for the planar isomers (i.e., cyclic chair and cyclic boat isomers). These deficiencies are found to be directly related to the ability of the SCANα functionals to describe the structure of liquid water at ambient conditions, which is investigated through MD simulations carried out with the corresponding many-body MB-SCANα models. In particular, we have found that the MB-SCANα model with $\alpha = 0.00$, which corresponds to the pure SCAN functional, predicts a denser liquid, with a more compact first hydration shell. On the other hand, the MB-SCANα model with $\alpha = 0.25$, which corresponds to the hybrid SCAN0 functional, predicts a more ice-like structure. These differences can be explained by the different accuracy with which the SCANα functionals describe hydrogen bonding and the individual many-body contributions to the interaction energies at the fundamental level as determined from the analysis of the harmonic frequencies of the water dimer and the energetics of the hexamer isomers. The analysis of the dimer and hexamer clusters as well as the structure of liquid water at ambient conditions indicates that the SCANα functional with α=0.15 provides the closer agreement with the CCSD(T)/CBS reference energies and experimental O-O RDFs. However, it should be noted that this "optimal" MB-SCANα model with $\alpha = 0.15$ still provides a more attractive O-O RDF, which results in a higher liquid density at ambient conditions, although the overall structure of the liquid is predicted to be more ice-like. These apparent opposite trends can be explained by the inability of the SCANα functionals to provide a balanced description of 2B and 3B interactions between water molecules. While these findings suggest that some caution should be exercised when the SCAN functional is used in computer simulations of liquid water, ice, and other aqueous solutions,[4, 5, 15, 30, 32, 389] they also provide fundamental insights into both merits and shortcomings of the SCAN functional which can guide future theoretical developments.[16, 390]

5.5 Acknowledgements

E.L. thanks Kartik Lakshmi Rallapalli, Kelly Hunter, Colin Egan, and Marc Riera for stimulating discussion about DFT and for technical assistance with some calculations. All figures in this paper were generated with UCSF Chimera and Matplotlib.[192, 271] This research was supported by the U.S. Department of Energy, Office of Science, Office of Basic Energy Science, through grant No. DE-SC0019490. This research used resources of the National Energy Research Scientific Computing Center (NERSC), which is supported by the Office of Science of the U.S. Department of Energy under Contract DE- AC02-05CH11231, the Extreme Science and Engineering Discovery Environment (XSEDE), which is supported by the National Science Foundation (grant no. ACI-1548562), as well as the Triton Shared Computing Cluster (TSCC) at the San Diego Supercomputer Center (SDSC).

Chapter 5 is in full a reprint of the material as it appears in "Lambros, E., Hu, J., & Paesani, F. (2021). Assessing the accuracy of the SCAN functional for water through a many-body analysis of the adiabatic connection formula. *Journal of Chemical Theory and Computation*" The dissertation author was the primary author of this paper.

5.6 Supplementary Information

Comparison between the O-O RDFs obtained from *ab initio* simulations with the SCAN functional in ref 15 and MB-SCANα simulations in the NVT ensemble. Analyses of the O-O, O-H, and H-H RDFs obtained from MD simulations with the MB-SCANα models in the NPT ensemble. Figure showing $\Delta\Delta E$ =$\Delta E(\alpha)$-$\Delta E(\alpha = 0)$. Table with the deviations in the SCANα harmonic frequencies of the hydrogen-bonded OH of the water dimer relative to the reference CCSD(T):MP2 value.

Chapter 6

Elevating Density Functional Theory to Chemical Accuracy for Water Simulations through a Density-Corrected Many-Body Formalism

Density functional theory (DFT) has been extensively used to model the properties of water. While maintaining a good balance between accuracy and efficiency, no density functional has so far achieved the degree of accuracy necessary to correctly predict the properties of water across the entire phase diagram. Here, we present density-corrected SCAN (DC-SCAN) calculations for water which, minimizing density-driven errors, elevate the accuracy of the SCAN functional to that of coupled-cluster theory, the "gold standard" for chemical accuracy. Building upon the accuracy and efficiency of DC-SCAN within a many-body formalism, we introduce a data-driven many-body potential energy function, the MB-SCAN(DC)PEF, that can quantitatively reproduce coupled-cluster reference energetics of water clusters. Importantly, the properties of liquid water calculated from molecular dynamics simulations carried out with the MB-SCAN(DC)

PEF are found to be in excellent agreement with the experimental data, which thus demonstrates that MB-SCAN(DC) is effectively the first DFT-based model that correctly describes water from the gas to the liquid phase.

6.1 Introduction

Its anomalous behavior[391] and importance to life[392] make water one of the most studied chemical compounds. Among its many unique properties is the high value of the heat capacity which allows water to resist sudden temperature changes, thus permitting living organisms to survive without experiencing significant temperature fluctuations.[393] In addition, the dynamic nature of the water hydrogen-bond network plays a central role in several fundamental processes, including transport and diffusion in bulk solutions and at interfaces, and hydration of hydrophobic and hydrophilic solutes.[394] For example, protein folding is thought to be driven by the hydrophobic effect.[395] Finally, countless chemical reactions involving charged species take place efficiently in liquid water due to its high dielectric constant.[396–401] It thus not surprising that a myriad of simulation studies have been devoted to developing a fundamental understanding of both chemical and physical properties of water in different environments and under different thermodynamic conditions.[70, 72, 351]

Density functional theory (DFT)[12, 402] is one the most important tools available to computational chemists and physicists for *ab initio* simulations of molecular systems in the condensed phase since it offers a good balance between accuracy and computational cost.[403, 404] However, as discussed in the "Methods" section, the accuracy of a DFT calculation depends upon the accuracy of the underlying exchange-correlation (XC) functional, which allows for recasting the many-body electronic structure problem into a (self-consistent) single-particle problem formulated in terms of the Kohn-Sham equations.[13] The simplest XC functional, the local spin density approximation (LSDA),[13, 405, 406] was shown to correctly predict the

structure of metallic crystals under pressure,[407–409] but was unable to fulfill its promises for water simulations, overestimating the strength of the hydrogen bonds and, consequently, predicting a too packed and overstructured liquid phase.[355, 356] These limitations hindered the ability of the LSDA functional to describe the properties of water, even qualitatively.

Climbing the Jacob's ladder of DFT approximations,[410] the next generation of XC functionals, which were developed within the generalized gradient approximation (GGA),[363, 364, 411] dominated the scene of *ab initio* simulations of water for a long time, owing to their higher accuracy compared to LDA and affordable computational cost. Initial successes of the GGA functionals included relatively accurate binding energies for various water clusters and a reasonable description of the structure of liquid water.[348, 355, 412, 413] However, it became soon evident that serendipitous error cancellation was the primary reason behind the apparent accuracy of GGA simulations of liquid water, making the predictive power more accidental than consistent.[176, 414–416] For example, it was found that GGA functionals generally underestimate the density of liquid water, while predicting denser ice phases.[417]

The third rung of the Jacob's ladder of DFT approximations includes meta-GGA functionals [418, 419] that perform significantly better than both LDA and GGA functionals due to the inclusion of the kinetic energy density. Among them, the strongly constrained and appropriately normed (SCAN) functional has gained particular attention because it satisfies all 17 known exact constraints that can be satisfied by a meta-GGA functional.[14] Without being fitted to any bonded system, SCAN was shown to enable accurate predictions for various properties of molecules and solids.[420] In particular, for molecular dynamics (MD) simulations of liquid water, SCAN was found to outperform its predecessor GGA functionals.[4, 421] Importantly, accounting for intermediate-range dispersion interactions, the SCAN functional allows for a more accurate description of the energy differences among water clusters and ice phases,[420, 421] while, when used in MD simulations, it predicts a density of liquid water which is appreciably closer to the experimental value compared to values obtained with GGA functionals.[4]

Despite its relatively higher accuracy, SCAN, as all GGA and meta-GGA functionals, is still prone to density-driven errors (defined in the following section), including self-interaction[320] and delocalization errors.[312, 422–424] It was shown that self-interaction errors in the SCAN functional primarily affect 2-body contributions (defined in the "Results" section) to the interaction energies of water clusters.[16] On the other hand, inclusion of a fraction of Hartree-Fock exchange (also known as exact exchange) in a SCAN hybrid was found to partially reduce density-driven errors in calculations for various water systems.[6, 425] However, it was found that increasing the fraction of Hartree-Fock exchange beyond 15% did not improve the accuracy of hybrid SCAN functionals, progressively shifting the structure of liquid water towards that of ice.[425] A systematic analysis of hybrid SCAN functionals with varying fractions of Hartree-Fock exchange demonstrated the inability of these functionals to accurately represent 2-body interactions between water molecules, with errors up to $\sim$5 kcal/mol for the water hexamer relative to reference values calculated using coupled cluster theory with single, double, and perturbative triple excitations, i.e., CCSD(T), in the complete basis set (CBS) limit,[425] the 'gold standard" method for molecular interactions.[426] In this context, a neural-network potential, NNP-SCAN0, was recently trained on a modified SCAN0 functional that incorporates 10% Hartree-Fock exchange.[6] (It is worth noting that, in its original formulation, the SCAN0 functional mixes 25% Hartree-Fock exchange with 75% SCAN exchange.[376]) Despite providing better agreement with experimental data than SCAN for several properties of liquid water measured at ambient conditions, this improved agreement was achieved by actually performing the NNP-SCAN0 simulations at 330 K.[6]

While all previous studies suggest that SCAN is overall one of the most accurate XC functionals, they also indicate that any further improvement of the accuracy of DFT models for water requires removing, at least partially, the associated density-driven errors. To this end, we introduce here a data-driven many-body potential energy function (PEF) for water, MB-SCAN(DC), which is rigorously derived within a many-body formalism applied to density-

corrected SCAN (DC-SCAN) data for individual many-body contributions to the interaction energies between water molecules.

Density-corrected DFT (DC-DFT),[315, 346, 427–433] where the Hartree-Fock density is used instead of the Kohn-Sham density, is known to mitigate density-driven errors in GGA and meta-GGA functionals, especially nonempirical ones. In this regard, density-driven errors associated with calculations carried out on water clusters using the GGA PBE functional were found to be significant.[433]

Here, we show that both binding and interaction energies calculated with the DC-SCAN functional for various water clusters are close to the CCSD(T)/CBS reference values, with DC-SCAN correctly reproducing each individual many-body contribution to the interaction energies. Importantly, we demonstrate that the MB-SCAN(DC) PEF preserves the accuracy of DC-SCAN and enables simulations of liquid water with significantly higher accuracy than all previous DFT-based models reported in the literature (including both *ab initio* and neural network models), predicting structural, thermodynamic, and dynamical properties in quantitative agreement with experiment.

Results

6.1.1 Theoretical background.

In ground-state Kohn-Sham DFT,[13] the energy is self-consistently minimized as:

$$E = \min_{n} \left\{ F[n] + \int d^3 r\, n(\mathbf{r}) v(\mathbf{r}) \right\} \tag{6.1}$$

where the minimizing $n(\mathbf{r})$ is the ground-state density, $v(\mathbf{r})$ is the external potential, and $F[n]$ includes the exact non-interacting kinetic and Hartree electrostatic energy terms plus an exchange-correlation (XC) energy. Since the exact XC functional is unknown, different DFT approximations

have been developed to solve eq 6.1.

The total-energy error ΔE associated with different DFT approximations can be written as the sum of the functional-driven error, ΔE_{F}, and the density-driven error, ΔE_{D}:[431]

$$\Delta E = \Delta E_{\mathrm{F}} + \Delta E_{\mathrm{D}} \tag{6.2}$$

The functional-driven error $\Delta E_{\mathrm{F}} = E_{\mathrm{XC}}^{\mathrm{approx}}[n_{\mathrm{exact}}] - E_{\mathrm{XC}}^{\mathrm{exact}}[n_{\mathrm{exact}}]$ arises from the difference between the approximate XC functional, $F[n]$, and the (unknown) exact functional, while the density-driven error $\Delta E_{\mathrm{D}} = E_{\mathrm{XC}}^{\mathrm{approx}}[n_{\mathrm{approx}}] - E_{\mathrm{XC}}^{\mathrm{approx}}[n_{\mathrm{exact}}]$ arises from using an approximate density $n(\mathbf{r})$ to solve eq. 6.1. In most systems, the functional-driven error is the main contribution to the total error.[428, 431]

By many measures, the best nonempirical functionals predict more accurate densities for neutral atoms than the heavily-parameterized empirical functionals or even Hartree-Fock theory.[305] But they still make density-driven delocalization errors[304, 308] that can dominate the total error under special conditions.[307, 429]

Independent of the specific form and parametrization, standard approximate XC functionals still deviate from the piecewise-linear behavior of the exact functional for fractional charges,[304] causing excess charge delocalization and resulting in incorrect densities.[304, 308] For certain systems, the density-driven error thus become the dominant contributor to the total error.[431, 434] This error can be understood by considering that the classical electrostatic repulsion term that is part of $F[n]$ in eq. 6.1 contains a self-interaction contribution due to each electron interacting with itself.[307, 320] While this self-interaction contribution should, in theory, be compensated by the XC energy, approximate XC functionals contain substantial local components that prevent them from quantitatively removing electron self-interactions. As a result, the electron density thus tends to over-delocalize in order to minimize the many-electron self-interactions,[312–314] leading to fractional charges that underestimate the energy predicted

by the piecewise-linear behavior of the exact functional.[304, 435]

Using a more accurate density can mitigate errors due to the over-delocalization of the electron density.[315, 428, 436] However, obtaining an accurate density from wavefunction theories, such as Møller-Plesset peturbation theory and coupled cluster theory, is computationally significantly more expensive than the corresponding DFT calculations. An approximate, yet efficient, approach to reducing density-driven errors in DFT calculations consists in using the Hartree-Fock density, $n^{\mathrm{HF}}(\mathbf{r})$ because, by construction, it does not suffer from either electron over-delocalization or self-interaction errors.[315, 346, 428, 431, 433] The resulting density-corrected DFT (DC-DFT) energy can then be written as:

$$E^{\mathrm{DC-DFT}} \approx E^{\mathrm{HF}} + \left(E_{\mathrm{XC}}^{\mathrm{approx}}\left[n^{\mathrm{HF}}\right] - E_{\mathrm{X}}^{\mathrm{HF}}\right) \tag{6.3}$$

The occupied Hartree-Fock (HF) orbitals are used here in place of those from a self-consistent calculation with the approximated functional. If $E_{\mathrm{xc}}^{\mathrm{approx}}$ is not fitted to any bonded system, then neither is eq. 6.3. Eq. 6.3 takes advantage of the understood overall cancellation between semilocal approximations to the exchange and correlation energies; there is no corresponding overall cancellation in the potentials or functional derivatives. In meta-GGA functionals, the exchange-correlation energy depends explicitly not only on the electron density but also on the non-interacting kinetic energy density, and both these ingredients differ from HF to Kohn-Sham (KS) theory, but, importantly, for a meta-GGA functional like SCAN both the HF and the KS kinetic energy densities can be used to recognize iso-orbital and uniform density limits and to interpolate between them. In extensive molecular tests, SCAN evaluated on the Hartree-Fock density was found on average to be more accurate than self-consistent SCAN, and even more accurate than all but a few hybrid functionals.[437] It is very possible for a density functional to yield accurate energies on physical densities and yet have an inaccurate functional derivative and thus an inaccurate self-consistent electron density, because the functional derivative yields the

response of the functional to an arbitrary (and not necessarily physical) small density variation. For example, a self-consistent semilocal functional like SCAN cannot bind a full extra electron to an isolated neutral atom, but using the Hartree-Fock density for the negative ion yields an accurate electron affinity from such functionals.[438] It should be noted that density correction also has some limitations: (1) It can only correct part of the error of an approximate density functional. (2) Because it is not self-consistent, it cannot provide Hellmann-Feynman forces on the nuclei. (3) Going beyond the level of the Hartree-Fock approximation can incur not only the cost of the higher-level density but also the cost of inverting it to find an effective one-electron potential.[439]

Eq. 6.3 can be used to calculate individual n-body energies, $\varepsilon^{n\mathrm{B}}$, from one-body (1B) to N-body (NB), which enter the many-body expansion (MBE) of the energy for a system containing N (atomic or molecular) monomers:[40]

$$E_N(1,\ldots,N) = \sum_{i=1}^{N} \varepsilon^{1\mathrm{B}}(i) + \sum_{i<j}^{N} \varepsilon^{2\mathrm{B}}(i,j) + \sum_{i<j<k}^{N} \varepsilon^{3\mathrm{B}}(i,j,k) + \ldots + \varepsilon^{\mathrm{NB}}(1,\ldots,N), \qquad (6.4)$$

In the case of water, $\varepsilon^{1\mathrm{B}}(i)$ in eq 6.4 corresponds to the distortion energy of the ith water molecule in the system from the equilibrium geometry of the corresponding free molecule, and all higher-order n-body energies, $\varepsilon^{\mathrm{nB}}(2,\ldots,n)$, can be calculated recursively from the lower-order terms.[170] The data-driven many-body formalism originally introduced with the MB-pol PEF for water proceeds from monomer to dimer to trimer, successively calculating the 1B, 2B, and 3B energies over a wide distribution of molecular configurations and then fitting them to analytic potential energy functions. The 4B and higher-order terms of eq. 6.4 are replaced by a classical many-body polarization model. Once the PEFs are known, fast but very accurate classical molecular dynamics calculations for finite temperature or fully-relaxed geometry optimizations for zero temperature can be performed. It should be noted that for the equilibrium geometries of molecules and solids self-consistent SCAN already performs quite well.[14, 420] Here, we show

that DC-SCAN provides an accurate but inexpensive alternative to the accurate but expensive CCSD(T) parametrization of a data-driven many-body PEF for water, suggesting many possible future applications of DC-SCAN that we are beginning to explore.

6.1.2 2-body interactions in water.

Our analysis of the ability of the SCAN functional to represent the interactions between water molecules begins with the comparison in Fig. 6.1 between the total 2-body (2B) energies second term on the right-hand side of eq. 4) calculated for the low-energy isomers of the water hexamer using the (self-consistent) SCAN and SCAN0 functionals, and the corresponding (density-corrected) DC-SCAN and DC-SCAN0 functionals. Also shown for reference are the CCSD(T)/CBS values reported in ref. 1. It should be noted that the hexamer holds a special space along the path that connects individual water molecules in the gas phase to liquid water since it is the smallest water cluster for which the low-energy isomers are characterized by three-dimensional arrangements that are reminiscent of the three-dimensional structure of the hydrogen-bond network found in the liquid phase. In addition, the large number of low-energy isomers makes the hexamer cluster the prototypical system to assess the ability of different water models to correctly reproduce many-body interactions in water.[72] Fig. 6.1 shows that the SCAN functional displays fairly large errors compared to the reference values, with a maximum unsigned error (MUE) of 4.59 kcal/mol. In contrast, DC-SCAN predicts 2-body energies that are in quantitative agreement with the CCSD(T)/CBS values, resulting in a MUE of only 0.08 kcal/mol. By effectively eliminating the errors in the representation of 2-body interactions, the application of the density correction thus addresses the main shortcoming of the SCAN functional applied to water.[16] Fig. 6.1 also shows that SCAN0, the hybrid variant of SCAN with a 25% fraction of Hartree-Fock exchange, only provides a minor improvement in the representation of the 2-body energies, resulting in a MUE of 4.48 kcal/mol. It should be noted that SCAN0 provides a slightly more accurate description of the three-dimensional isomers (i.e., prism and

cage isomers) but a worse description of the planar isomers (i.e., cyclic isomers) compared to SCAN. Importantly, the density correction applied to SCAN0 does not result in a similarly dramatic improvement as found for SCAN, with DC-SCAN0 still displaying a relatively large MUE of 2.26 kcal/mol.

The analysis of the effects associated with various dispersion corrections, which is reported in Supplementary Fig. 1), indicates that the addition of any form of dispersion energy worsens the accuracy of both SCAN and DC-SCAN. Specifically, all the dispersion-corrected SCAN functionals considered in our analysis, SCAN-D3(0), SCAN-D3(BJ), and SCAN-VV10, are found to overbind the hexamer isomers, which results in larger deviations from the CCSD(T)/CBS values compared to their dispersion-free counterparts. Similarly, inclusion of larger fractions (α) of Hartree-Fock exchange deteriorates the ability of hybrid SCANα and DC-SCANα functionals to reproduce the interaction energies of the hexamer isomers, resulting in significant overbinding (Fig. S2). It is also worth noting that neither DC-SCAN+dispersion nor DC-SCANα (where α

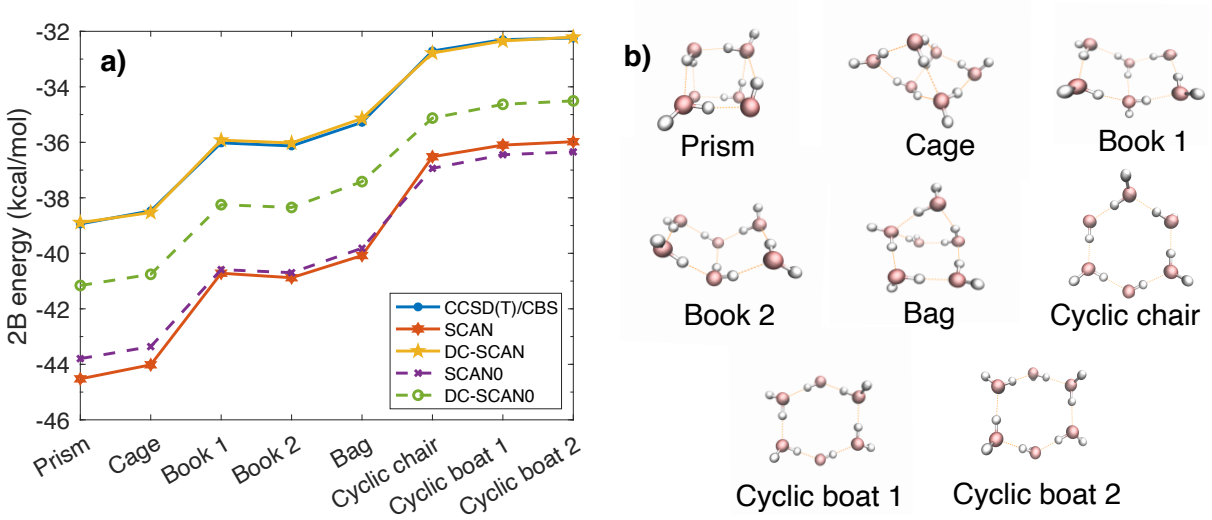

Figure 6.1: **2B energies of the water hexamer isomers.** 2-body energies calculated for the first eight low-energy isomers of the water hexamer using SCAN, DC-SCAN, SCAN0 (with 25% exact exchange), and DC-SCAN0, along with the corresponding CCSD(T)/CBS reference values from ref. 1. The 2-body energy, on average, contributes ∼80-85% to the total interaction energy in water.[72] The errors associated with a given functional relative to the CCSD(T)/CBS values are roughly the same for each isomer.

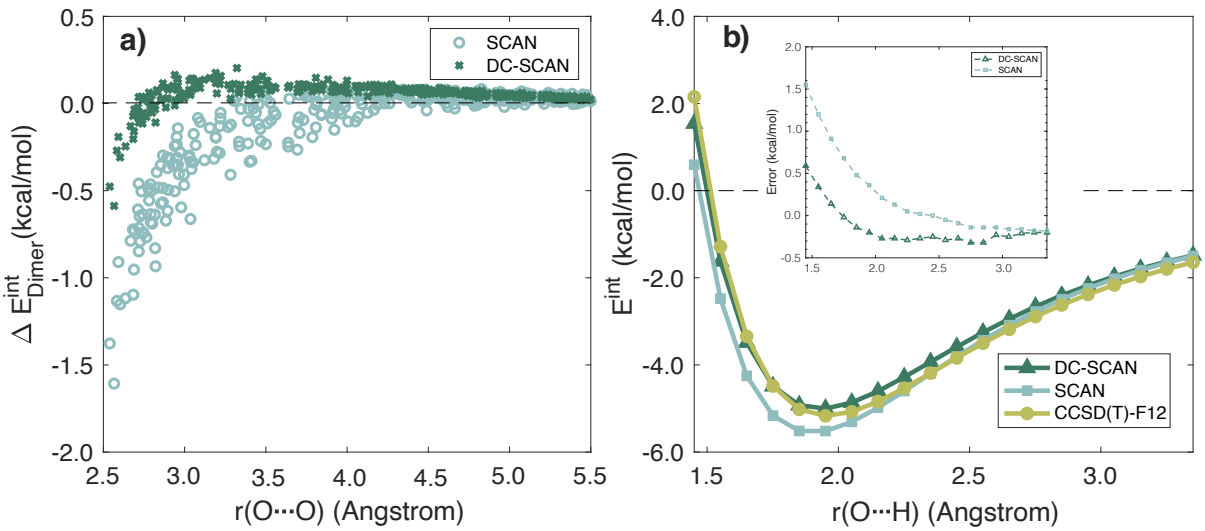

Figure 6.2: **Comparison of dimer interaction energies** a) Errors in 2-body energies calculated with SCAN and DC-SCAN relative to CCSD(T)-F12b values for dimers with an oxygen-oxygen distance shorter than 5.5 Å which were extracted from an NPT simulation of liquid water carried out with MB-pol[37–39] at ambient conditions. b) CCSD(T)-F12b, SCAN and DC-SCAN interaction energies calculated for an unrelaxed scan of the water dimer along the O···H distance. The inset of panel b shows the errors associated with DC-SCAN and SCAN relative to the CCSD(T)-F12b reference values as a function of r(O···H).

is the fraction of HF exchange) perform as well as DC-SCAN. This suggests that the addition of the dispersion correction and/or a fraction of Hartree-Fock exchange actually worsens the functional-driven error of SCAN for water.

To further investigate the impact of the density correction on the energetics of various water systems, in Fig. 6.2 we analyze the interaction energies of dimers extracted from a classical MD simulation of liquid water carried out in the isobaric-isothermal (NPT) ensemble at ambient conditions using the MB-pol PEF.[37–39] (The interaction energy is the binding energy without its 1-body contribution.) For this analysis, we consider dimers with an oxygen-oxygen (O···O) distance shorter than 5.5 Å, which approximately corresponds to the radius of the first two solvation shells in liquid water.[39, 385, 386] It should be noted that, by definition, the interaction energy of a water dimer exactly corresponds to the associated 2-body energy. Fig. 6.2a shows the errors, ΔE, in 2-body energies calculated with SCAN and DC-SCAN relative to the corresponding

reference values calculated at the CCSD(T)-F12b level of theory. As expected, DC-SCAN exhibits significantly smaller errors compared to SCAN for all dimers, independent of the O$\cdots$O distance. Specifically, the maximum error associated with DC-SCAN is -0.47 kcal/mol, which must be compared with a maximum error of -1.38 kcal/mol calculated with SCAN. It is also important to analyze the errors as a function of the O$\cdots$O distance since they directly affect the ability of the SCAN and DC-SCAN functionals to correctly predict the cohesive energy, and thus the structure, of liquid water. Fig. 6.2a shows that the 2-body energies calculated with SCAN only start to approach the CCSD(T)-F12b values at $\sim$4.5 Å, with a MUE of 0.25 kcal/mol associated with dimers with an O$\cdots$O distance up to 4.5 Å, and a MUE of 0.16 kcal/mol for all dimers up to an O$\cdots$O distance of 5.5 Å. In contrast, the 2-body energies calculated with DC-SCAN converge to the CCSD(T)-F12b values at 3.5Å, with a MUE of 0.09 kcal/mol obtained for dimers with an O$\cdots$O distance up to 3.5 Å, which decreases to 0.07 kcal/mol when all dimers up to an O$\cdots$O distance of 5.5 Å are considered.

Fig. 6.2b shows a comparison between the interaction energies calculated at the CCSD(T)-F12b, SCAN, and DC-SCAN levels of theory for an unrelaxed scan of the water dimer along the O$\cdots$H distance, starting from the dimer optimized geometry. This comparison provides further evidence for DC-SCAN predicting 2-body energies in close agreement with the CCSD(T)-F12b values. In contrast, SCAN systematically overbinds the water dimer, which is particularly evident in the minimum-energy region (r(O$\cdots$H) $\sim$ 1.9 Å). It is worth noting that SCAN gives slightly better agreement with CCSD(T)-F12b at long range, before asymptotically converging to DC-SCAN results. The reason behind SCAN giving slightly better result than DC-SCAN at long-range is the cancellation in SCAN of the density-driven errors (which overbind) with the lack of dispersion.

6.1.3 Binding energies of water clusters.

It is known that the binding energies of the low-energy isomers of the water hexamer lie within a few kcal/mol from each other[137] while the two most stable isomers (D_{2d} and S_4) of the water octamer are degenerate.[111] Table 6.1 shows that the SCAN functional predicts significantly different binding energies relative to the CCSD(T)-F12b results of ref. 440 for both sets of clusters, with an overall MUE of 6.54 kcal/mol. Interestingly, the error per water molecule is higher for the 3-dimensional isomers (prism and cage isomers) than for the planar isomers of the water hexamer, and increases for the two isoenergetic isomers of the octamer.

Table 6.1 also includes the binding energies calculated in ref. 16 with SCAN corrected for the self-interaction energy using the Fermi–Lowdin orbital self-interaction correction (FLOSIC) scheme.[441] Relative to SCAN, FLOSIC-SCAN is able to reduce the errors in the binding energies of all water clusters analyzed in Table 6.1, resulting in a MUE of 1.65 kcal/mol. The error per water molecule remains nearly constant for the prism, cage, and book-2 isomers of the hexamer but increases for the cyclic boat-2 isomer. The FLOSIC-SCAN error per molecule is smaller for the two isoenergetic isomers of the water octamer. The comparisons reported in Table 6.1 show that DC-SCAN performs better than FLOSIC-SCAN, with an overall MUE of 0.69 kcal/mol relative to CCSD(T)-F12b. As found with FLOSIC-SCAN, also in the case of

Table 6.1: Errors (in kcal/mol) in binding energies relative to the CCSD(T)-F12b values of ref. 440 calculated for representative isomers of the water hexamer and octamer using SCAN, FLOSIC-SCAN (from ref. 16) and DC-SCAN. The values in parentheses correspond to the errors per molecule. The last row reports the corresponding MUEs and MUEs per molecule.

	SCAN	FLOSIC-SCAN	DC-SCAN
Hexamer: Prism	5.69 (0.95)	-1.62 (-0.27)	-0.73 (-0.12)
Hexamer: Cage	5.68 (0.95)	-1.66 (-0.28)	-0.62 (-0.10)
Hexamer: Book 2	5.42 (0.90)	-1.56 (-0.26)	-0.41 (-0.07)
Hexamer: Cyclic boat 2	4.79 (0.80)	-2.43 (-0.41)	-0.12 (-0.02)
Octamer: D_{2d}	8.84 (1.10)	-1.31 (-0.16)	-1.15 (-0.14)
Octamer: S_4	8.84 (1.10)	-1.31 (-0.16)	-1.13 (-0.14)
MUE	6.54 (0.97)	1.65 (0.26)	0.69 (0.09)

DC-SCAN the error per molecule remains constant for the prism, cage, and book-2 isomers of the water hexamer but decreases for the cyclic boat-2 isomer. However, contrary to FLOSIC-SCAN, DC-SCAN predicts a slightly larger error per molecule for the two isoenergetic octamer isomers than for the prism, cage, and book-2 isomers of the hexamer. The overall MUE per molecule of 0.04 kcal/mol indicates that the binding energies predicted by DC-SCAN are in excellent agreement with the CCSD(T)-F12b reference values for all clusters analyzed in Table 6.1.

6.1.4 Many-body interactions in water.

Although the results presented in Fig. 6.1 and Table 6.1 demonstrate that, by correcting density-driven errors, DC-SCAN is able to accurately reproduce the interaction energies of small water clusters, the analyses of the previous sections do not provide any direct information about the ability of DC-SCAN to correctly describe many-body effects in water. The competition and interplay of many-body effects have been shown to play a critical role in determining structural, thermodynamic, and dynamical properties of aqueous systems, from small clusters to bulk solutions and interfaces.[44, 61, 137, 184, 341]

To investigate the impact of the density correction on individual n-body (nB) contributions to the interactions between water molecules, many-body decomposition analyses were carried out for the two isoenergetic isomers of the octamer. Errors relative to the CCSD(T)-F12b reference values are shown in Fig. 6.3 for each n-body energy calculated with the SCAN and DC-SCAN functionals. This analysis provides further evidence for the density-driven errors in the SCAN functional primarily affecting 2-body energies, with SCAN displaying large negative deviations from the CCSD(T)-F12b values, which confirms the tendency of the SCAN functional to overbind water clusters.[16] After application of the density correction, the errors in the 2-body energies reduce to only $\sim$0.3 kcal/mol for calculations carried out with the DC-SCAN functional. Importantly, Fig. 6.3 shows that the impact of the density correction is minimal for all nB energies with $n > 2$.

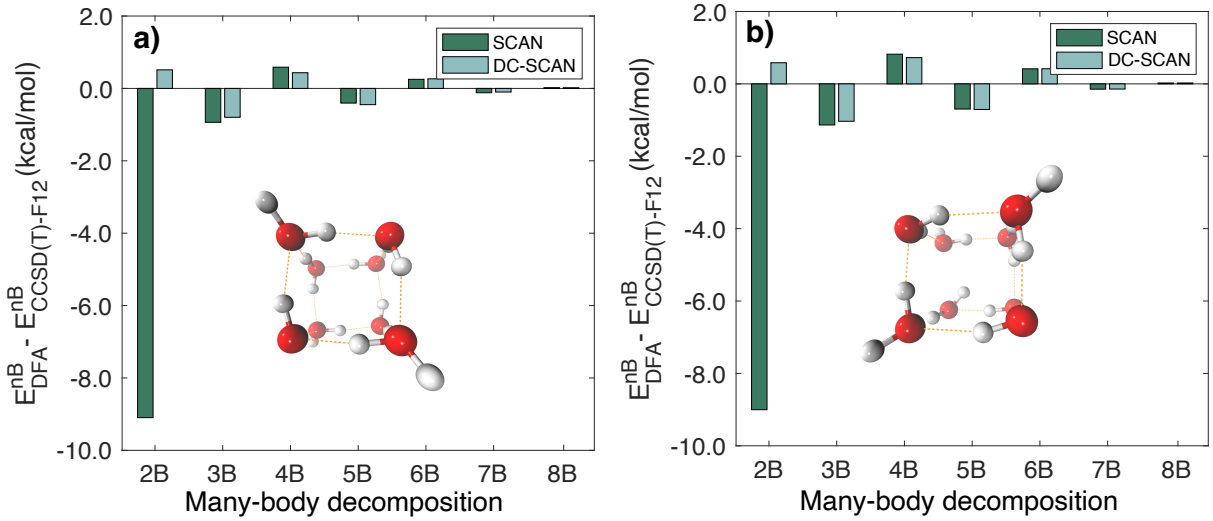

Figure 6.3: **Errors in *n*B interaction energy of water octamers.** Errors relative to CCSD(T)-F12b reference values for each *n*B energy contribution to the interaction energies calculated for the two isoenergetic isomers, a) D_{2d} and b) S_4, of the water octamer using the SCAN and DC-SCAN functionals.

After demonstrating that, by removing density-driven errors, the DC-SCAN functional effectively provides chemical accuracy for binding, interaction, and many-body energies of various water clusters, the 2B, 3B, and 4B energies, as well as the total interaction energies of the low-energy isomers of the water hexamer calculated using the SCAN and DC-SCAN functionals are compared in Fig. 6.4 with the analogous values calculated with the corresponding MB-SCAN and MB-SCAN(DC) potential energy functions (PEFs) described in the "Methods" section. Also shown for reference are the CCSD(T)/CBS values reported in ref. 1. The errors associated z many body energy components and interaction energies for SCAN, DC-SCAN along with their corresponding MB-PEFs, *i.e.* MB-SCAN and MB-SCAN(DC), with respect to the benchmark CCSD(T)/CBS are presented in Supplementary Figs. 7. As already discussed in the case of the octamer isomers, density-driven errors are most pronounced at the 2B level, with MUEs of 4.59 kcal/mol and 0.08 kcal/mol associated with SCAN and DC-SCAN, respectively. The MUEs reduce to 0.59 kcal/mol and 0.38 kcal/mol at the 3-body level. The comparisons shown in Fig. 6.4a and Fig. 6.4b demonstrate that both the MB-SCAN and MB-SCAN(DC) PEFs are

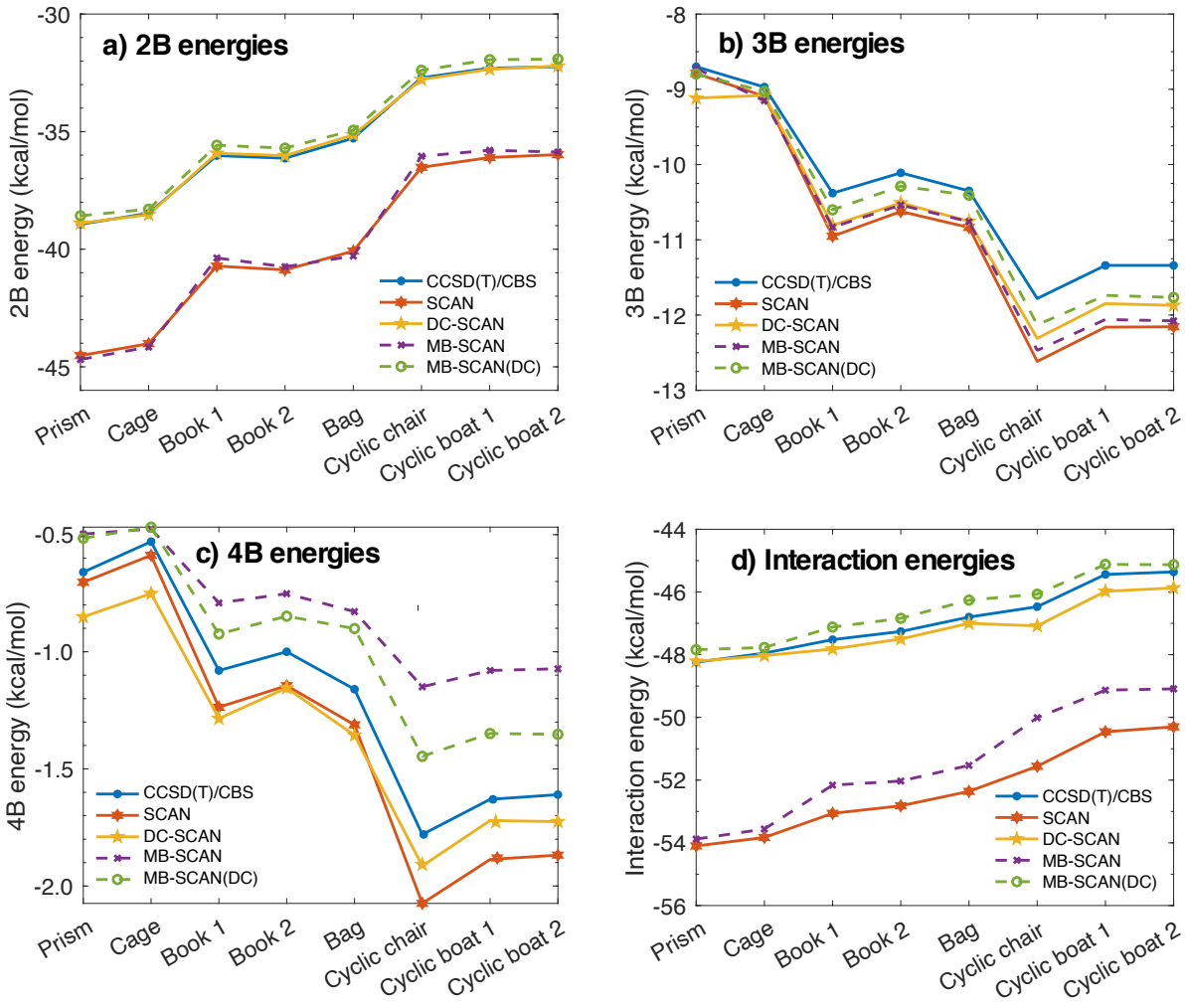

Figure 6.4: **Many-body and interaction energies for the isomers of the water hexamer.** a) 2-body (2B) b) 3-body (3B) c) 4-body (4B) and d) total interaction energies of the first eight isomers of the water hexamer calculated using SCAN, DC-SCAN, MB-SCAN, MB-SCAN(DC), along with the CCSD(T)/CBS reference values of ref. 1.

able to quantitatively reproduce the 2-body and 3-body energies calculated *ab initio* with the corresponding SCAN and DC-SCAN functionals. Since, by construction, nB energies with $n > 3$ in the MB-SCAN and MB-SCAN(DC) PEFs are entirely represented by a classical polarization term, the errors associated with these energies are not strictly related to those calculated *ab initio* with the corresponding SCAN and DC-SCAN functionals. In this regard, Fig. 6.4c shows that the 4-body energies predicted by the MB-SCAN and MB-SCAN(DC) PEFs tend to underbind

the hexamer isomers relative to CCSD(T)/CBS, whereas the 4-body energies calculated with the SCAN and DC-SCAN functionals tend to overbind the same clusters. However, it should be noted that in both cases the 4-body errors are small for all eight isomers, with SCAN and MB-SCAN providing MUEs of 0.17 kcal/mol and 0.35 kcal/mol, respectively. The corresponding MUEs for DC-SCAN and MB-SCAN(DC) are 0.16 kcal/mol and 0.21 kcal/mol, respectively.

The total interaction energies of the eight low-energy hexamer isomers calculated with the SCAN and DC-SCAN functionals, and the corresponding MB-SCAN and MB-SCAN(DC) PEFs are compared with the CCSD(T)/CBS reference values in Fig. 6.4d. Both DC-SCAN and MB-SCAN(DC) provide excellent agreement with the CCSD(T)/CBS reference values, displaying MUEs of 0.53 kcal/mol and 0.36 kcal/mol, respectively. In contrast, suffering from large density-driven errors at the 2-body level, SCAN and MB-SCAN systematically overbind all eight isomers.

6.1.5 Structural and dynamical properties of liquid water.

The last question that remains to be addressed is whether the high accuracy displayed by the MB-SCAN(DC) PEF in reproducing the multidimensional energy landscape of water clusters is sufficient to correctly predict the properties of liquid water. To this end, classical MD simulations for a periodic box containing 256 molecules were carried out with the MB-SCAN(DC) PEF in the NPT ensemble at 1 atm and various temperatures between $T = 250$ K and $T = 350$ K. The lengths of the MD trajectories were 2.6 ns for $T < 298$ K and 2 ns for $T \geq 298$ K. Fig. 6.5 shows that the MB-SCAN(DC) PEF correctly reproduces the temperature-dependence of the density of liquid water at 1 atm, underestimating the experimental values by only $\sim$0.01 g/cm^3 at all temperatures. At 298 K, MB-SCAN(DC) predicts a density of 0.986 g/cm^3, which is in close agreement with the experimental value of 0.997 g/cm^3. The temperature of maximum density calculated by fitting a 5$^{\text{th}}$-order polynomial to the MB-SCAN(DC) results is 280 K, in nearly quantitative agreement with the experimental value of 277 K. The MB-SCAN(DC)

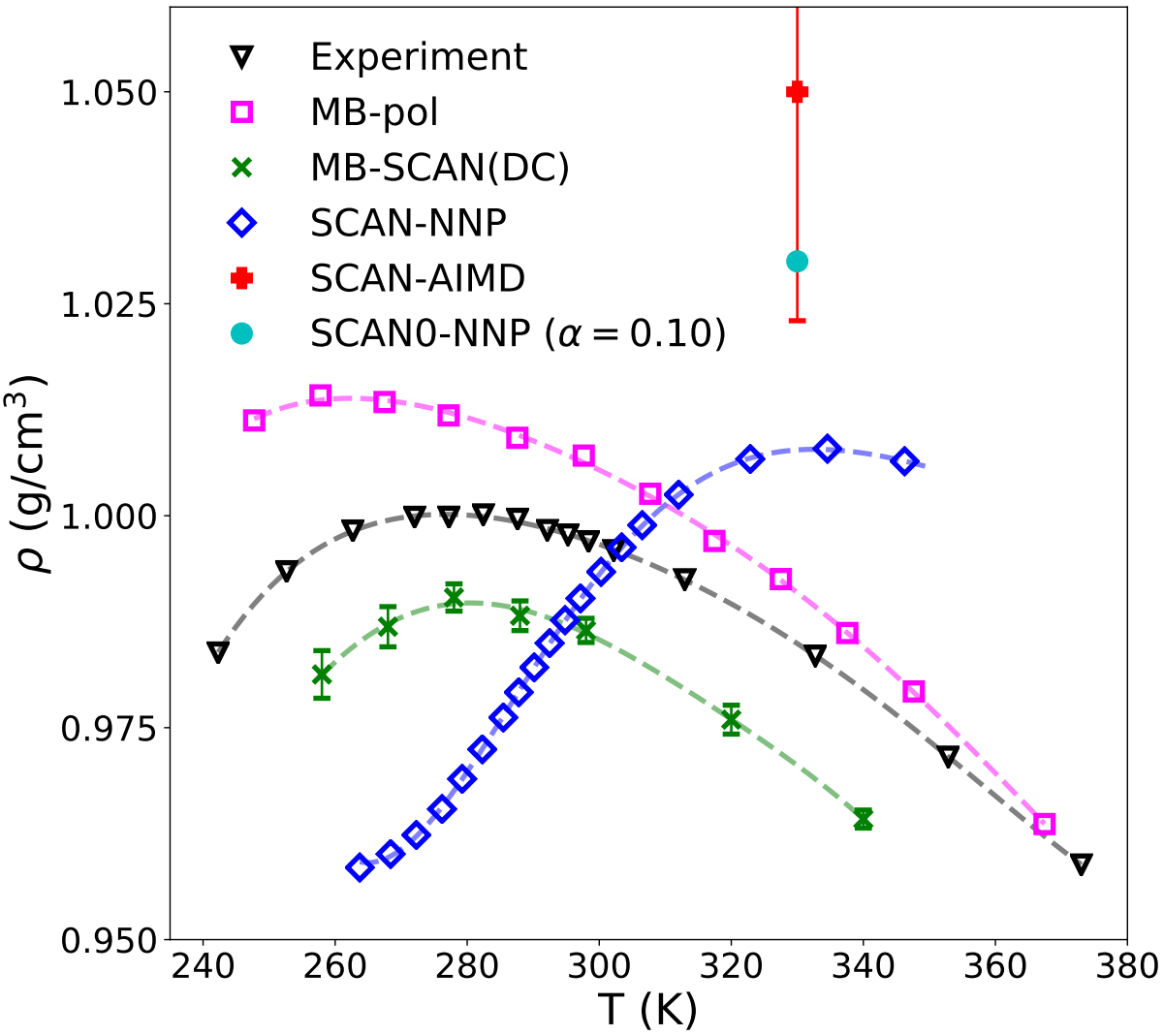

Figure 6.5: **Density of liquid water.** Temperature-dependence of the density of liquid water at 1 atm calculated from classical NPT simulations carried out with MB-SCAN(DC) along with the results from SCAN-AIMD,[4] SCAN-NNP,[5] and SCAN0-NNP (with 10% HF exchange)[6] simulations. The MB-pol results are from ref. 1, while the experimental data are from the NIST Chemistry WebBook.[442]

results are compared in Fig. 6.5 with those reported in the literature from MD simulations with SCAN[4] (SCAN-AIMD) as well as with NNPs trained on SCAN[5] (SCAN-NNP) and SCAN0[6] (SCAN0-NNP) data. These comparisons demonstrate that the MB-SCAN(DC) PEF predicts a liquid density at 330 K which is in significantly closer agreement with experiment than the value calculated in ref. 4 from *ab initio* MD simulations with SCAN.

Particularly interesting is the comparison of the MB-SCAN(DC) PEF with the two NNPs models trained on SCAN[5] and SCAN0[6] data. Fig. 6.5 shows that, despite being trained on SCAN data, the SCAN-NNP model is unable to correctly reproduce the density value calculated from *ab initio* MD simulations with SCAN at 330 K. A closer agreement between the density values calculated from the SCAN-AIMD and SCAN-NNP simulations was obtained after applying a reweighting procedure.[5] In addition, the SCAN-NNP model predicts a more pronounced temperature-dependence of the liquid density compared to experiment, overestimating both the value and the temperature of the density maximum.[5] A slightly more accurate prediction of the liquid density at 330 K is provided by the SCAN0-NNP model,[6] although no *ab initio* MD simulations with SCAN0 have been reported to compare with. Given the increased popularity of NNPs trained on DFT data, we believe that the differences between SCAN-AIMD and SCAN-NNP results deserve further investigation to assess the ability of NNPs to faithfully represent the target DFT models. In this context, it should be noted that in a previous study[425] we found that MD simulations carried out with the MB-SCAN PEF predict a liquid density of 1.14 g/cm^3 at 298 K, which is significantly different from the value of 1.05 g/cm^3 obtained from *ab initio* simulations with SCAN.[4] This difference is not due to the different size of the water systems studied in the two sets of simulations (256 molecules for MB-SCAN[425] and 64 molecules for SCAN-AIMD[4]). An explanation for this difference, proposed in ref. 425, considers that any PEF rigorously derived from the many-body expansion of the energy (MBE) is strictly faithful to its parent quantum-mechanical method only when the latter does not display spurious delocalization of the electron density which affects the convergence of the MBE in an unphysical manner. We believe that the present analysis of the SCAN and DC-SCAN functionals, along with the corresponding MB-SCAN and MB-SCAN(DC) PEFs, provides support for the interpretation presented in ref. 425 that density-driven errors are responsible for the differences between MD simulations carried out with the SCAN functional and the MB-SCAN PEF. The temperature dependence of the enthalpy of vaporization and isothermal compressibility calculated

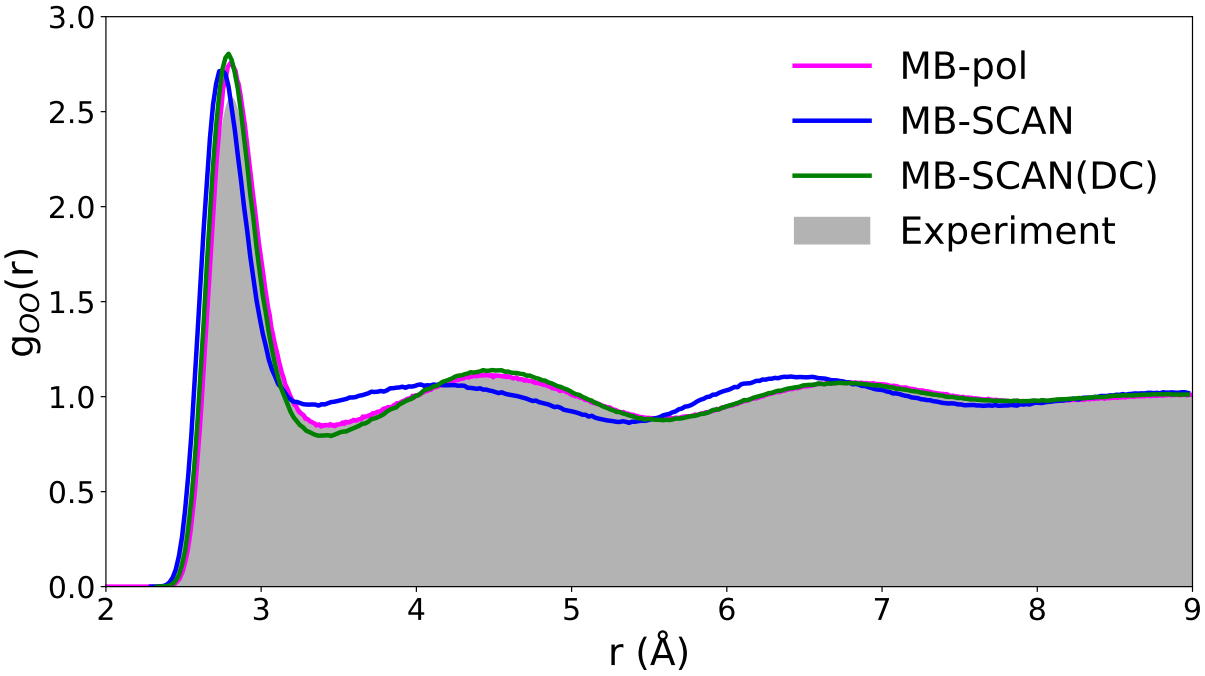

Figure 6.6: **Structure of liquid water.** Oxygen-oxygen (g_{OO}) radial distribution function (RDF) calculated from NPT simulations carried out with the MB-SCAN(DC) PEF at 298 K and 1 atm. The MB-pol RDF is from ref. 39, while the experimental RDF at 295 K is from ref. 385.

from classical MD simulations with MB-SCAN(DC) are shown in Supplementary Figs. 12 and 13.

Fig. 6.6 compares the oxygen-oxygen (g_{OO}) radial distribution function (RDF) calculated from MD simulations carried out with the MB-SCAN and MB-SCAN(DC) PEFs at 298 K and 1 atm with the corresponding experimental data.[385, 386] The MB-SCAN(DC) PEF provides excellent agreement with the experimental RDF, slightly overestimating the height of the first peak while underestimating the height of the "valley" between the first two peaks.

As shown in Supplementary Fig. 11, these small differences can be attributed to the neglect of nuclear quantum effects in classical MD simulations. The inclusion of nuclear quantum effects in path-integral molecular dynamics (PIMD) simulations with MB-SCAN(DC) indeed slightly lowers the height of the first peak and raise the "valley" between 3.2 Å and 4.0 Å similarly to what previously observed in the g_{OO} calculated with the MB-pol PEF.[39] As expected, the inclusion of

nuclear quantum effects also improves the agreement with the experimental oxygen-hydrogen and hydrogen-hydrogen RDFs (Supplementary Fig. 11). In contrast, as already discussed in ref. 425, the MB-SCAN PEF predicts a denser and more unstructured liquid. Based on the analyses discussed above, the differences between the MB-SCAN and MB-SCAN(DC) oxygen-oxygen RDFs can be unambiguously attributed to density-driven errors that affect SCAN many-body energies, particularly at the 2-body level, which are used to train the corresponding MB-SCAN PEF.

To provide further insights into the ability of the MB-SCAN(DC) PEF to describe the properties of liquid water, we also calculated the temperature dependence of the self-diffusion coefficient, D, from a 500 ps-long MD simulation carried out in the microcanonical (NVE) ensemble for a periodic box containing 256 molecules using the equilibrium density determined from the corresponding NPT simulations. D was calculated from the velocity autocorrelation function of the center of mass of each water molecule according to

$$D = \frac{1}{3}\int_0^\infty \langle v_i(t) v_i(0) \rangle dt, \tag{6.5}$$

where v_i is the center of mass velocity of the ith water molecule. Fig. 6.7 shows that the MB-SCAN(DC) PEF is able to correctly predict the diffusion coefficient between 250 K and 350 K. In particular, at 298 K, the diffusion coefficient predicted by the MB-SCAN(DC) PEF is 0.212 A^2/ps, which is in excellent agreement with the experimental value of 0.229 A^2/ps. At higher temperatures, larger fluctuations in the particle velocity lead to a wider distribution of self-diffusion. This is in contrast to the value of 0.106 A^2/ps obtained in ref. 15 from MD simulations carried out with an adaptive neural network model trained on SCAN data (SCAN-NNP in Fig. 6.7). In contrast to the MB-SCAN(DC) PEF, the SCAN-NNP model severely underestimates the diffusion coefficient of liquid water over the entire temperature range, although the agreement with experiment apparently improves as the temperature decreases.

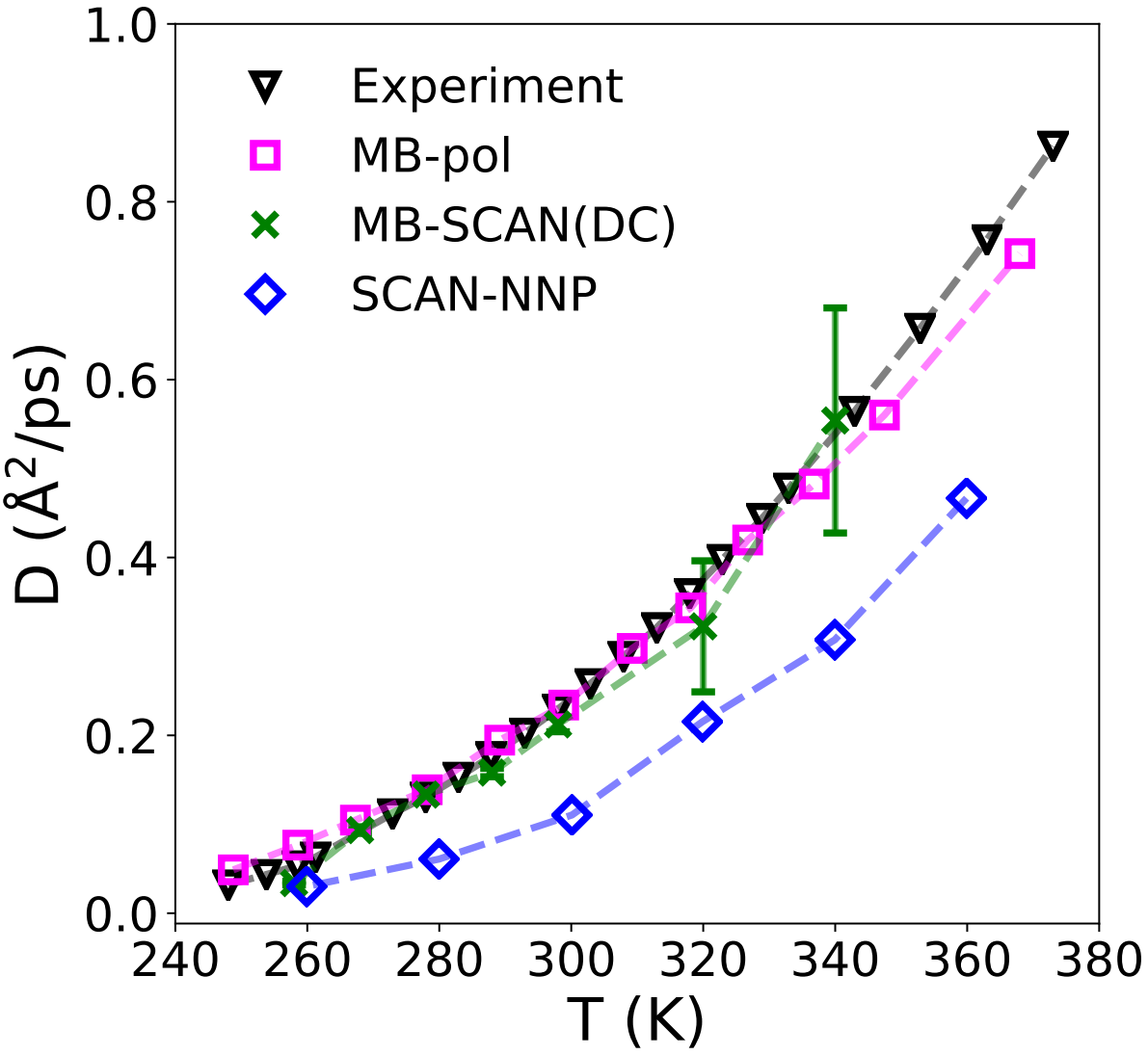

Figure 6.7: **Self-diffusion of liquid water.** Temperature-dependence of the self-diffusion coefficient of liquid water calculated from NVE simulations carried out with the MB-SCAN(DC) PEF. The SCAN-NNP data are from ref. 15, the MB-pol results are from ref. 1, while the experimental data are from refs. 443, 444 and 445.

Discussion

An *ab initio* representation of water across all the different phases has been an elusive goal since the early days of computer simulations.[119–122]. Although models based on correlated wavefunction theories (WFT) can, in principle, provide such a long-sought after *ab initio* repre-

sentation of water without resorting to *ad hoc* approximations or empirical parameterizations, the associated computational cost precludes the application of WFT models to systems containing more than a handful of water molecules. This effectively leaves DFT as the only viable approach to *ab initio* simulations of water.[351] However, it has been shown that existing XC functionals are not particularly accurate in their predictions of the properties of water,[72, 176] suffering from both functional-driven and density-driven errors.

In this study, we have demonstrated that the density-corrected SCAN (DC-SCAN) functional effectively removes density-driven errors from the water 2-body energies, which brings both binding and interaction energies of different water clusters very close to reference values calculated at CCSD(T)/CBS level of theory. Although not as pronounced as for the 2-body energies, the density correction also reduces density-driven errors in all higher-body terms of the many-body expansion (MBE) of the energy calculated for water using the DC-SCAN functional, with each individual many-body term being in quantitative agreement with the corresponding CCSD(T)/CBS reference values. In this context, it should be noted that a previous study[16] found a significant but less complete improvement for water clusters (Table 6.1) via a self-consistent FLOSIC self-interaction correction to SCAN. Ref. 16, however, did not find evidence for a major improvement from density correction, probably because the FLOSIC density is less localized than the Hartree-Fock and exact densities are. Although it should be kept in mind that the DC-SCAN functional, as does the parent SCAN functional, still suffers from functional-driven errors, which can be large for some chemical systems such as stretched H_2^+, the analyses presented here demonstrate that these functional-driven errors are negligible for water. In the future, it would be important to test the performance of DC-SCAN for more-general chemical applications. Importantly, our analyses suggest that, in principle, *ab initio* MD simulations with the DC-SCAN functional should be able to provide a consistently accurate description of the properties of water. However, the requirement of using the Hartree-Fock density in a non-self-consistent SCAN calculation at each MD step would make *ab initio* MD simulations with DC-SCAN not straightforward

to implement and expensive to perform.

While *ab initio* MD simulations with DC-SCAN are currently not feasible, we have shown that the improved accuracy of the DC-SCAN functional can be exploited to develop a data-driven many-body potential energy function, the MB-SCAN(DC) PEF, which indeed provides a highly accurate representation of water, from small clusters in the gas phase to the liquid phase. MB-SCAN(DC) is rigorously derived from the DC-SCAN MBE and adopts a hybrid data-driven/physics-based scheme, where a data-driven model, which captures (short-range) quantum-mechanical interactions arising from the overlap of the electron densities of individual molecules at the 2-body and 3-body levels (e.g., Pauli repulsion, and charge transfer and penetration), is integrated with a physics-based model of many-body interactions, which is represented by classical many-body electrostatics. Importantly, we have demonstrated that the MB-SCAN(DC) PEF achieves high accuracy by quantitatively reproducing each individual term of the DC-SCAN MBE for water, providing a correct representation of both short- and long-range many-body contributions. Since the DC-SCAN functional exhibits chemical accuracy for each individual term of the MBE for water and the MB-SCAN(DC) PEF quantitatively reproduces the DC-SCAN many-body energies, the MB-SCAN(DC) PEF effectively provides the first demonstration of a DFT-based model that correctly describes the properties of water, at the computational cost of advanced polarizable force fields.[72] Future applications of the MB-SCAN(DC) PEF will focus on modeling the phase diagram of water, which was shown to be only qualitatively reproduced by NNPs trained on SCAN data.[5, 446] We expect MB-SCAN(DC) to be especially well suited to modeling the liquid/vapor equilibrium, which involves the making and breaking of hydrogen bonds.

Finally, we want to emphasize that the many-body formalism adopted by the MB-SCAN(DC) PEF for water is general and has already been used in the development of data-driven many-body PEFs for various aqueous systems[179, 180] and molecular fluids[62, 63] which were trained on (expensive) CCSD(T) data. It thus follows that the significantly lower

computational cost associated with DC-SCAN calculations can enable the routine development of MB-SCAN(DC) PEFs for generic (small) molecules which are trained on DC-SCAN data but effectively display CCSD(T) accuracy. In this context, it should be noted that the MB-Fit software infrastructure[447] for many-body PEFs combined with the MBX many-body energy/force calculator[448] interfaced with i-PI[449] and LAMMPS[450] already provides a robust platform for MD simulations of generic molecules in the gas, liquid, and solid phases using MB-SCAN(DC) PEFs.

methods

Many-body expansion. Building upon the demonstrated accuracy of the MB-pol PEF for water[1, 37–39] and following the same theoretical/computational approach employed in development of DFT-based many-body PEFs,[61, 425, 451] we used eq. 6.4 to develop a data-driven many-body PEF, MB-SCAN(DC), that consistently reproduces each term of the MBE for water calculated using the DC-SCAN functional. Briefly, MB-SCAN(DC) includes explicit representations of 1B, 2B, and 3B energies, and describes all higher-order nB energy terms ($n > 3$) through classical many-body polarization. Specifically, ε^{1B} in eq. 6.4 is represented by the Partridge-Schwenke PEF,[64] while ε^{2B} and ε^{3B} are represented by terms describing permanent elecrostatics, dispersion energy, and induction, which are combined with short-range permutationally invariant polynomials (PIPs)[65] fitted to reproduce 2B and 3B energies calculated with DC-SCAN for the same training sets of water dimers and trimers used in the development of MB-pol.[37, 38] A detailed description of the theoretical and computational framework adopted in the development of data-driven many-body PEFs for water can be found in the original references.[37, 38, 61, 425, 451] It should be noted that, since our many-body PEFs directly target the underlying molecular interactions, differences in the representation of the 1-body (1B) term of eq. 5 have been found to be negligible for modeling the properties of liquid water[451]

and the air/water interface.[452]

All DFT calculations were performed with the aug-cc-pVQZ basis set[166, 266] using Q-Chem[453] quantum chemistry packages. Since the SCAN functional is particularly sensitive to the real-space grid, all SCAN and DC-SCAN calculations are performed on the highly dense Euler-Maclaurin-Lebedev (99,590) grid[333, 334] (58,410 points per atom). In this regard, the results of a sensitivity analysis reported in Table S1 suggest that the SG2 grid[335] ($\sim$8,000 points per atom) should also be sufficient to converge SCAN calculations. In case only smaller grids are available, we recommend to use r^{2}SCAN,[454] which often achieves an accuracy similar to SCAN. Single-point energy calculations using explicitly correlated coupled cluster, CCSD(T)-F12b, theory[455] were performed in the CBS limit by extrapolating [456, 457] the energy values obtained with the cc-pVTZ-F12 and cc-pVQZ-F12 basis sets along with associated auxiliary and complementary auxiliary (CABS) basis sets[458, 459] using the ORCA quantum chemistry package.[332]

Data availability

Any data generated and analyzed for this study that are not included in this Article and its Supplementary Information are available from the authors upon request.

Code availability

The MB-SCAN and MB-SCAN(DC) PEFs are available in MBX,[448] and can be used in MD simulations with LAMMPS[450] and i-PI.[449] All computer codes used in the analysis presented in this study are available from the authors upon request.

Acknowledgments

We thank Eunji Sim, Suhwan Song, and Kieron Burke for helpful and stimulating discussions. This research was supported by the U.S. Department of Energy, Office of Science, Office of Basic Energy Science, through grant no. DE-SC0019490 (F.P), and by the U.S. National Science Foundation through grant no. DMR-1939528, with a contribution from CTMC (J.P.P.). This research used resources of the National Energy Research Scientific Computing Center (NERSC), which is supported by the Office of Science of the U.S. Department of Energy under Contract DE-AC02-05CH11231, the Extreme Science and Engineering Discovery Environment (XSEDE), which is supported by the National Science Foundation grant number ACI-1548562, and the Triton Shared Computing Cluster (TSCC) at the San Diego Supercomputer Center (SDSC).

Chapter 6 is in full a reprint of the material as it appears in "Dasgupta, S., Lambros, E., Perdew, J., & Paesani, F. (2021). Elevating Density Functional Theory to Chemical Accuracy for Water Simulations through a Density-Corrected Many-Body Formalism. *Nature Communications*" The dissertation author was the co-primary author of this paper.

Chapter 7

Conclusion

First, many modern polarizable water models, which attempt to describe the interactions between water molecules using relatively simple, classical functional forms, often suffer from error cancellation between individual many-body terms and cannot quantitatively describe the entire energy landscape of water. More recent models such as AMOEBA+CF and MB-UCB which adopt more advanced electrostatics, as well as classical representations for charge-transfer interactions, perform more reliable across the terms in the many-body expansion, but still fail to quantitatively describe the free energy landscape around its minima. Based on our analyses, explicit many-body models such as MB-pol and fq-MB-pol provide CCSD(T)/CBS level accuracy for equilibrium and distorted geometries.

With respect to QM/MM simulations, we demonstrate that by using a many-body potential trained to match the level of theory in the QM region, the boundary discontinuity between the QM and MM regions can be suppressed. This allows for the entire QM/MM system to be treated under the same effective level of theory, so that the physics in both the QM and MM regions are quantitatively the same, and permitting the use of transition layer free adaptive QM/MM simulations, dramatically reducing computational expense and eliminating structural and dynamical artifacts due to a hybrid treatment between regions. In effect this many-body QM/MM

scheme allows for full *ab-initio* accuracy simulations at the cost of QM/MM. Furthermore for such QM/MM systems we have developed a set of generalized many-body PEFs called MB-QM which are trained to reproduce an arbitrary level of theory. These models are explicitly trained up to the 3B to a particular *ab-initio* method, while the underlying electrostatic parameters e.g. charges and polarizabilites are derived from the same level of theory, so that even the implicitly described higher order terms are treated at *ab-initio* level of accuracy. In this vein, certain classes of functionals, in particular GGAs like PBE suffer from large density over-delocalization, which leads to long-range quantum mechanical effects extending into higher-order many-body terms, which cannot be recovered by the implicit classical representation used in the MB-QM models. Instead, using using density-corrected versions of those functionals, where the functional is evaluated on the Hartree-Fock density reduces over-delocalization errors to tame the higher-order terms. This indicates, that while our potentials are technically generalizable to any level of theory, care must be taken to choose methods which do not suffer from severe over-delocalization so that the MB-QM model can faithfully reproduce its corresponding level of theory.

Regarding the SCAN functional, we presented a systematic analysis of the energetic and structural effects of the fraction of exact exchange (α) used in hybrid SCANα functionals, which are constructed through the adiabatic connection formula. We demonstrate that the SCANα functionals are unable to correctly describe the 2B interactions of water for all values of α, from α=0.0 to α=0.25, and that there is a structural heterogeneity in the response of water clusters to increasing the value of α. All low lying isomers of the water hexamer show large 2B errors on the order of 4-5 kcal/mol, but that this error decreases with larger α for isomers with 3-dimensional hydrogen bonding arrangements, while it correspondingly increases for 2-dimensional isomers whose hydrogen-bonds are confined within a plane. The errors that were observed for water cluster, extend to the ability of SCANα to describe the structure of liquid water, where through simulations of the corresponding many-body models of SCANα, MB-SCANα, increasing the fraction of exact exchange produces a more structured, ice-like water, with $alpha$=0.15 providing

the closest agreement with both the reference CCSD(T) energies and experimental O-O RDF at ambient conditions. Finally, we demonstrated that using DC-SCAN, a scheme where the SCAN functional is evaluated on the Hartree-Fock density, CCSD(T) level of accuracy can be achieved. By effectively suppressing the density driven errors in the SCAN functional, this scheme represents the first DFT based model that can quantitatively reproduce the properties of water from the gas to condensed phases.

Bibliography

[1] Sandeep K Reddy, Shelby C Straight, Pushp Bajaj, C Huy Pham, Marc Riera, Daniel R Moberg, Miguel A Morales, Chris Knight, Andreas W Götz, and Francesco Paesani. On the accuracy of the mb-pol many-body potential for water: Interaction energies vibrational frequencies and classical thermodynamic and dynamical properties from clusters to liquid water and ice. *J. Chem. Phys.*, 145(19):194504, 2016.

[2] J Coleman Howard, Jessica L Gray, Amanda J Hardwick, Linh T Nguyen, and Gregory S Tschumper. Getting down to the fundamentals of hydrogen bonding: Anharmonic vibrational frequencies of $(HF)_2$ and $(H_2O)_2$ from ab initio electronic structure computations. *J. Chem. Theory Comput.*, 10(12):5426–5435, 2014.

[3] J Coleman Howard and Gregory S Tschumper. Benchmark structures and harmonic vibrational frequencies near the ccsd(t) complete basis set limit for small water clusters:$(H_2O)_n$. *J. Chem. Theory Comput.*, 11(5):2126–2136, 2015.

[4] Mohan Chen, Hsin-Yu Ko, Richard C Remsing, Marcos F Calegari Andrade, Biswajit Santra, Zhaoru Sun, Annabella Selloni, Roberto Car, Michael L Klein, John P Perdew, and Xifan Wu. Ab initio theory and modeling of water. *Proc. Natl. Acad. Sci. USA*, 114(41):10846–10851, 2017.

[5] Pablo M Piaggi, Athanassios Z Panagiotopoulos, Pablo G Debenedetti, and Roberto Car. Phase equilibrium of water with hexagonal and cubic ice using the scan functional. *J. Chem. Theory Comput.*, 17(5):3065–3077, 2021.

[6] Chunyi Zhang, Fujie Tang, Mohan Chen, Linfeng Zhang, Diana Y Qiu, John P Perdew, Michael L Klein, and Xifan Wu. Modeling liquid water by climbing up jacob's ladder in density functional theory facilitated by using deep neural network potentials. *arXiv:2104.14410.*

[7] John A Pople, Rolf Seeger, and Raghavachari Krishnan. Variational configuration interaction methods and comparison with perturbation theory. *International Journal of Quantum Chemistry*, 12(S11):149–163, 1977.

[8] JA Pople, R Krishnan, HB Schlegel, and JS Binkley. Electron correlation theories and their application to the study of simple reaction potential surfaces. *International Journal of Quantum Chemistry*, 14(5):545–560, 1978.

[9] George D Purvis III and Rodney J Bartlett. A full coupled-cluster singles and doubles model: The inclusion of disconnected triples. *The Journal of Chemical Physics*, 76(4):1910–1918, 1982.

[10] Chr Møller and Milton S Plesset. Note on an approximation treatment for many-electron systems. *Physical review*, 46(7):618, 1934.

[11] Martin Head-Gordon, John A Pople, and Michael J Frisch. Mp2 energy evaluation by direct methods. *Chemical physics letters*, 153(6):503–506, 1988.

[12] Pierre Hohenberg and Walter Kohn. Inhomogeneous electron gas. *Phys. Rev.*, 136(3B):B864, 1964.

[13] Walter Kohn and Lu Jeu Sham. Self-consistent equations including exchange and correlation effects. *Phys. Rev.*, 140(4A):A1133, 1965.

[14] Jianwei Sun, Adrienn Ruzsinszky, and John P Perdew. Strongly constrained and appropriately normed semilocal density functional. *Phys. Rev. Lett.*, 115(3):036402, 2015.

[15] Yi Yao and Yosuke Kanai. Temperature dependence of nuclear quantum effects on liquid water via artificial neural network model based on scan meta-gga functional. *J. Chem. Phys.*, 153(4):044114, 2020.

[16] Kamal Sharkas, Kamal Wagle, Biswajit Santra, Sharmin Akter, Rajendra R Zope, Tunna Baruah, Koblar A Jackson, John P Perdew, and Juan E Peralta. Self-interaction error overbinds water clusters but cancels in structural energy differences. *Proc. Natl. Acad. Sci. USA*, 117(21):11283–11288, 2020.

[17] Gang Zhao, Shuyi Shi, Huijuan Xie, Qiushuang Xu, Mingcui Ding, Xuguang Zhao, Jinliang Yan, and Dehua Wang. Equation of state of water based on the scan meta-gga density functional. *Phys. Chem. Chem. Phys.*, 22(8):4626–4631, 2020.

[18] Mengli Li, Lu Chen, Lirong Gui, Shuo Cao, Di Liu, Gang Zhao, Mingcui Ding, Jinliang Yan, and Dehua Wang. Born–oppenheimer molecular dynamics simulations on structures of high-density and low-density water: A comparison of the scan meta-gga and pbe gga functionals. *Phys. Chem. Chem. Phys.*, 2021.

[19] Jörg Behler. Neural network potential-energy surfaces in chemistry: A tool for large-scale simulations. *Phys. Chem. Chem. Phys.*, 13(40):17930–17955, 2011.

[20] Jörg Behler. Representing potential energy surfaces by high-dimensional neural network potentials. *J. Phys. Condens. Matter*, 26(18):183001, 2014.

[21] Katja Hansen, Franziska Biegler, Raghunathan Ramakrishnan, Wiktor Pronobis, O Anatole Von Lilienfeld, Klaus-Robert Müller, and Alexandre Tkatchenko. Machine learning predictions of molecular properties: Accurate many-body potentials and nonlocality in chemical space. *J. Phys. Chem. Lett.*, 6(12):2326–2331, 2015.

[22] Jörg Behler. First principles neural network potentials for reactive simulations of large molecular and condensed systems. *Angew. Chem. Int. Ed.*, 56(42):12828–12840, 2017.

[23] Stefan Chmiela, Alexandre Tkatchenko, Huziel E Sauceda, Igor Poltavsky, Kristof T Schütt, and Klaus-Robert Müller. Machine learning of accurate energy-conserving molecular force fields. *Sci. Adv.*, 3(5):e1603015, 2017.

[24] Justin S Smith, Olexandr Isayev, and Adrian E Roitberg. Ani-1: An extensible neural network potential with dft accuracy at force field computational cost. *Chem. Sci.*, 8(4):3192–3203, 2017.

[25] Justin S Smith, Olexandr Isayev, and Adrian E Roitberg. Ani-1 a data set of 20 million calculated off-equilibrium conformations for organic molecules. *Sci. Data*, 4(1):1–8, 2017.

[26] Mojtaba Haghighatlari and Johannes Hachmann. Advances of machine learning in molecular modeling and simulation. *Curr. Opin. Chem. Eng.*, 23:51–57, 2019.

[27] Sergei Manzhos and Tucker Carrington Jr. Neural network potential energy surfaces for small molecules and reactions. *Chem. Rev.*, page https://doi.org/10.1021/acs.chemrev.0c00665, 2020.

[28] Frank Noé, Alexandre Tkatchenko, Klaus-Robert Müller, and Cecilia Clementi. Machine learning for molecular simulation. *Annu. Rev. Phys. Chem.*, 71:361–390, 2020.

[29] Paraskevi Gkeka, Gabriel Stoltz, Amir Barati Farimani, Zineb Belkacemi, Michele Ceriotti, John D Chodera, Aaron R Dinner, Andrew L Ferguson, Jean-Bernard Maillet, Hervé Minoux, Peterm Christine, Fabio Pietrucci, Ana Silveira, Alexandre Tkatchenko, Zofia Trstanova, Rafal Wiewiora, and Tony Lelièvre. Machine learning force fields and coarse-grained variables in molecular dynamics: Application to materials and biological systems. *J. Chem. Theory Comput.*, 16(8):4757–4775, 2020.

[30] Jianhang Xu, Chunyi Zhang, Linfeng Zhang, Mohan Chen, Biswajit Santra, and Xifan Wu. Isotope effects on molecular structures and electronic properties of liquid water via deep potential molecular dynamics based on scan functional. *Phys. Rev. B*, 102(21):214113, 2020.

[31] Thomas E Gartner, Linfeng Zhang, Pablo M Piaggi, Roberto Car, Athanassios Z Panagiotopoulos, and Pablo G Debenedetti. Signatures of a liquid–liquid transition in an ab initio deep neural network model for water. *Proc. Natl. Acad. Sci. USA*, 117(42):26040–26046, 2020.

[32] Pablo M Piaggi and Roberto Car. Enhancing the formation of ionic defects to study the ice ih/xi transition with molecular dynamics simulations. *arXiv:2101.09308*, 2021.

[33] U Chandra Singh and Peter A Kollman. A combined ab initio quantum mechanical and molecular mechanical method for carrying out simulations on complex molecular systems:

Applications to the $ch_3cl + cl^-$ exchange reaction and gas phase protonation of polyethers. *J. Comput. Chem.*, 7(6):718–730, 1986.

[34] Adam W Duster, Christina M Garza, Baris O Aydintug, Mikias B Negussie, and Hai Lin. Adaptive partitioning qm/mm for molecular dynamics simulations: 6. proton transport through a biological channel. *J. Chem. Theory Comput.*, 15(2):892–905, 2019.

[35] Hans Martin Senn and Walter Thiel. Qm/mm methods for biomolecular systems. *Angew. Chem. Int. Ed.*, 48(7):1198–1229, 2009.

[36] Uriel N Morzan, Diego J Alonso de Armino, Nicolas O Foglia, Francisco Ramirez, Mariano C Gonzalez Lebrero, Damian A Scherlis, and Dario A Estrin. Spectroscopy in complex environments from qm–mm simulations. *Chem. Rev.*, 118(7):4071–4113, 2018.

[37] Volodymyr Babin, Claude Leforestier, and Francesco Paesani. Development of a "first principles" water potential with flexible monomers: Dimer potential energy surface vrt spectrum and second virial coefficient. *J. Chem. Theory Comput.*, 9(12):5395–5403, 2013.

[38] Volodymyr Babin, Gregory R Medders, and Francesco Paesani. Development of a "first principles" water potential with flexible monomers. ii: Trimer potential energy surface third virial coefficient and small clusters. *J. Chem. Theory Comput.*, 10(4):1599–1607, 2014.

[39] Gregory R Medders, Volodymyr Babin, and Francesco Paesani. Development of a "first principles" water potential with flexible monomers. iii. liquid phase properties. *J. Chem. Theory Comput.*, 10(8):2906–2910, 2014.

[40] D Hankins, JW Moskowitz, and FH Stillinger. Water molecule interactions. *J. Chem. Phys.*, 53(12):4544–4554, 1970.

[41] Sotiris S Xantheas. Ab initio studies of cyclic water clusters $(h_2o)_n$ n. *J. Chem. Phys.*, 100(10):7523–7534, 1994.

[42] Sotiris S Xantheas. Cooperativity and hydrogen bonding network in water clusters. *Chemical Physics*, 258(2-3):225–231, 2000.

[43] Albert Defusco, Daniel P Schofield, and Kenneth D Jordan. Comparison of models with distributed polarizable sites for describing water clusters. *Mol. Phys.*, 105(19-22):2681–2696, 2007.

[44] Matthew J Elrod and Richard J Saykally. Many-body effects in intermolecular forces. *Chem. Rev.*, 94(7):1975–1997, 1994.

[45] Robert Bukowski, Krzysztof Szalewicz, Gerrit C Groenenboom, and Ad Van der Avoird. Predictions of the properties of water from first principles. *Science*, 315(5816):1249–1252, 2007.

[46] Christian J Burnham, Jichen Li, Sotiris S Xantheas, and Maurice Leslie. the parametrization of a thole-type all-atom polarizable water model from first principles and its application to the study of water clusters (n. *J. Chem. Physics*, 110(9):4566–4581, 1999.

[47] Christian J Burnham and Sotiris S Xantheas. Development of transferable interaction models for water. i. prominent features of the water dimer potential energy surface. *J. Chem. Phys.*, 116(4):1479–1492, 2002.

[48] Sotiris S Xantheas, Christian J Burnham, and Robert J Harrison. Development of transferable interaction models for water. ii. accurate energetics of the first few water clusters from first principles. *J. Chem. Phys.*, 116(4):1493–1499, 2002.

[49] Christian J Burnham and Sotiris S Xantheas. Development of transferable interaction models for water. iii. reparametrization of an all-atom polarizable rigid model (ttm2-r) from first principles. *J. Chem. Phys.*, 116(4):1500–1510, 2002.

[50] Christian J Burnham and Sotiris S Xantheas. Development of transferable interaction models for water. iv. a flexible all-atom polarizable potential (ttm2-f) based on geometry dependent charges derived from an ab initio monomer dipole moment surface. *J. Chem. Phys.*, 116(12):5115–5124, 2002.

[51] George S Fanourgakis and Sotiris S Xantheas. The flexible polarizable thole-type interaction potential for water (ttm2-f) revisited. *J. Phys. Chem. A*, 110(11):4100–4106, 2006.

[52] George S Fanourgakis and Sotiris S Xantheas. Development of transferable interaction potentials for water. v. extension of the flexible polarizable thole-type model potential (ttm3-f v. 3.0) to describe the vibrational spectra of water clusters and liquid water. *J. Chem. Phys.*, 128(7):074506, 2008.

[53] CJ Burnham, DJ Anick, PK Mankoo, and GF Reiter. The vibrational proton potential in bulk liquid water and ice. *J. Chem. Phys.*, 128(15):154519, 2008.

[54] Pengyu Ren and Jay W Ponder. Polarizable atomic multipole water model for molecular mechanics simulation. *J. Phys. Chem. B*, 107(24):5933–5947, 2003.

[55] Pengyu Ren and Jay W Ponder. Temperature and pressure dependence of the amoeba water model. *J. Phys. Chem. B*, 108(35):13427–13437, 2004.

[56] Chengwen Liu, Jean-Philip Piquemal, and Pengyu Ren. Implementation of geometry dependent charge flux into polarizable amoeba+ potential. *J. Phys. Chem. Lett.*, 11(2):419–426, 2020.

[57] Chengwen Liu, Jean-Philip Piquemal, and Pengyu Ren. Amoeba+ classical potential for modeling molecular interactions. *J. Chem. Theory Comput.*, 15(7):4122–4139, 2019.

[58] Marie L Laury, Lee-Ping Wang, Vijay S Pande, Teresa Head-Gordon, and Jay W Ponder. Revised parameters for the amoeba polarizable atomic multipole water model. *J. Phys. Chem. B*, 119(29):9423–9437, 2015.

[59] Jay W Ponder, Chuanjie Wu, Pengyu Ren, Vijay S Pande, John D Chodera, Michael J Schnieders, Imran Haque, David L Mobley, Daniel S Lambrecht, Robert A DiStasio Jr, Martin Head-Gordon, Gary N. I. Clark, Margaret E. Johnson, and Teresa Head-Gordon. Current status of the amoeba polarizable force field. *J. Phys. Chem. B*, 114(8):2549–2564, 2010.

[60] Lee-Ping Wang, Teresa Head-Gordon, Jay W Ponder, Pengyu Ren, John D Chodera, Peter K Eastman, Todd J Martinez, and Vijay S Pande. Systematic improvement of a classical molecular model of water. *J. Phys. Chem. B*, 117(34):9956–9972, 2013.

[61] Marc Riera, Eleftherios Lambros, Thuong T Nguyen, Andreas W Götz, and Francesco Paesani. Low-order many-body interactions determine the local structure of liquid water. *Chem. Sci.*, 10(35):8211–8218, 2019.

[62] Marc Riera, Alan Hirales, Raja Ghosh, and Francesco Paesani. Data-driven many-body models with chemical accuracy for ch_4/h_2o mixtures. *J. Phys. Chem. B*, 124(49):11207–11221, 2020.

[63] Marc Riera, Eric P Yeh, and Francesco Paesani. Data-driven many-body models for molecular fluids: Co_2/h_2o mixtures as a case study. *J. Chem. Theory Comput.*, 16(4):2246–2257, 2020.

[64] Harry Partridge and David W Schwenke. The determination of an accurate isotope dependent potential energy surface for water from extensive ab initio calculations and experimental data. *J. Chem. Phys.*, 106(11):4618–4639, 1997.

[65] Bastiaan J Braams and Joel M Bowman. Permutationally invariant potential energy surfaces in high dimensionality. *Int. Rev. Phys. Chem.*, 28(4):577–606, 2009.

[66] KT Tang and J Peter Toennies. An improved simple model for the van der waals potential based on universal damping functions for the dispersion coefficients. *J. Chem. Phys.*, 80(8):3726–3741, 1984.

[67] JA Barker and RO Watts. Structure of water; a monte carlo calculation. *Chem. Phys. Lett.*, 3(3):144–145, 1969.

[68] Aneesur Rahman and Frank H Stillinger. Molecular dynamics study of liquid water. *J. Chem. Phys.*, 55(7):3336–3359, 1971.

[69] Bertrand Guillot. a reappraisal of what we have learnt during three decades of computer simulations on water. *J. Mol. Liq.*, 101(1-3):219–260, 2002.

[70] Carlos Vega and Jose LF Abascal. Simulating water with rigid non-polarizable models: A general perspective. *Phys. Chem. Chem. Phys.*, 13(44):19663–19688, 2011.

[71] I Shvab and Richard J Sadus. Atomistic water models: Aqueous thermodynamic properties from ambient to supercritical conditions. *Fluid Phase Equilib.*, 407:7–30, 2016.

[72] Gerardo Andrés Cisneros, Kjartan Thor Wikfeldt, Lars Ojamäe, Jibao Lu, Yao Xu, Hedieh Torabifard, Albert P Bartók, Gábor Csányi, Valeria Molinero, and Francesco Paesani. Modeling molecular interactions in water: From pairwise to many-body potential energy functions. *Chem. Rev.*, 116(13):7501–7528, 2016.

[73] John D Bernal and Ralph H Fowler. a theory of water and ionic solution with particular reference to hydrogen and hydroxyl ions. *J. Chem. Phys.*, 1(8):515–548, 1933.

[74] Frank H Stillinger and Aneesur Rahman. Improved simulation of liquid water by molecular dynamics. *J. Chem. Phys.*, 60(4):1545–1557, 1974.

[75] William L Jorgensen, Jayaraman Chandrasekhar, Jeffry D Madura, Roger W Impey, and Michael L Klein. Comparison of simple potential functions for simulating liquid water. *J. Chem. Phys.*, 79(2):926–935, 1983.

[76] Michael W Mahoney and William L Jorgensen. a five-site model for liquid water and the reproduction of the density anomaly by rigid nonpolarizable potential functions. *J. Chem. Phys.*, 112(20):8910–8922, 2000.

[77] Hans W Horn, William C Swope, Jed W Pitera, Jeffry D Madura, Thomas J Dick, Greg L Hura, and Teresa Head-Gordon. Development of an improved four-site water model for biomolecular simulations: Tip4p-ew. *J. Chem. Phys.*, 120(20):9665–9678, 2004.

[78] HJC Berendsen, JR Grigera, and TP Straatsma. the missing term in effective pair potentials. *J. Phys. Chem.*, 91(24):6269–6271, 1987.

[79] AJ Stone. *the Theory of Intermolecular Interactions*. Clarendon, Oxford, 1996.

[80] James Caldwell, Liem X Dang, and Peter A Kollman. Implementation of nonadditive intermolecular potentials by use of molecular dynamics: Development of a water–water potential and water–ion cluster interactions. *J. Am. Chem. Soc.*, 112(25):9144–9147, 1990.

[81] Liem X Dang and Tsun-Mei Chang. Molecular dynamics study of water clusters liquid and liquid–vapor interface of water with many-body potentials. *J. Chem. Phys.*, 106(19):8149–8159, 1997.

[82] Claude Millot and Anthony J Stone. Towards an accurate intermolecular potential for water. *Mol. Phys.*, 77(3):439–462, 1992.

[83] Claude Millot, Jean-Christophe Soetens, Marília TC Martins Costa, Matthew P Hodges, and Anthony J Stone. Revised anisotropic site potentials for the water dimer and calculated properties. *J. Phys. Chem. A*, 102(4):754–770, 1998.

[84] Bin Chen, Jianhua Xing, and J Ilja Siepmann. Development of polarizable water force fields for phase equilibrium calculations. *J. Phys. Chem. B*, 104(10):2391–2401, 2000.

[85] Kwang-Hwi Cho, Kyoung Tai No, and Harold A Scheraga. a polarizable force field for water using an artificial neural network. *J. Mol. Struct.*, 641(1):77–91, 2002.

[86] Harry A Stern, F Rittner, BJ Berne, and Richard A Friesner. Combined fluctuating charge and polarizable dipole models: Application to a five-site water potential function. *J. Chem. Phys.*, 115(5):2237–2251, 2001.

[87] Lars Ojamäe, Isaiah Shavitt, and Sherwin J Singer. Potential models for simulations of the solvated proton in water. *J. Chem. Phys.*, 109(13):5547–5564, 1998.

[88] Satoru Iuchi, Akihiro Morita, and Shigeki Kato. Molecular dynamics simulation with the charge response kernel: Vibrational spectra of liquid water and n-methylacetamide in aqueous solution. *J. Phys. Chem. B*, 106(13):3466–3476, 2002.

[89] Tatsuya Ishiyama and Akihiro Morita. Analysis of anisotropic local field in sum frequency generation spectroscopy with the charge response kernel water model. *J. Chem. Phys.*, 131(24):244714, 2009.

[90] Guillaume Lamoureux, Alexander D MacKerell Jr, and Benoıt Roux. a simple polarizable model of water based on classical drude oscillators. *J. Chem. Phys.*, 119(10):5185–5197, 2003.

[91] Wenbo Yu, Pedro EM Lopes, Benoît Roux, and Alexander D MacKerell Jr. Six-site polarizable model of water based on the classical drude oscillator. *J. Chem. Phys.*, 138(3):034508, 2013.

[92] Haibo Yu, Tomas Hansson, and Wilfred F van Gunsteren. Development of a simple self-consistent polarizable model for liquid water. *J. Chem. Phys.*, 118(1):221–234, 2003.

[93] Haibo Yu and Wilfred F van Gunsteren. Charge-on-spring polarizable water models revisited: From water clusters to liquid water to ice. *J. Chem. Phys.*, 121(19):9549–9564, 2004.

[94] Anna-Pitschna E Kunz and Wilfred F van Gunsteren. Development of a nonlinear classical polarization model for liquid water and aqueous solutions: Cos/d. *J. Phys. Chem. A*, 113(43):11570–11579, 2009.

[95] Péter T Kiss and András Baranyai. a systematic development of a polarizable potential of water. *J. Chem. Phys.*, 138(20):204507, 2013.

[96] Kjartan Thor Wikfeldt, ER Batista, FD Vila, and H Jónsson. a transferable h_2o interaction potential based on a single center multipole expansion: Scme. *Phys. Chem. Chem. Phys.*, 15(39):16542–16556, 2013.

[97] Vlad P Sokhan, Andrew P Jones, Flaviu S Cipcigan, Jason Crain, and Glenn J Martyna. Signature properties of water: Their molecular electronic origins. *Proc. Natl. Acad. Sci. U.S.A.*, 112(20):6341–6346, 2015.

[98] Revati Kumar, Fang-Fang Wang, Glen R Jenness, and Kenneth D Jordan. a second generation distributed point polarizable water model. *J. Chem. Phys.*, 132(1):014309, 2010.

[99] Parminder K Mankoo and Thomas Keyes. Polir: Polarizable flexible transferable water potential optimized for ir spectroscopy. *J. Chem. Phys.*, 129(3):034504, 2008.

[100] Taisuke Hasegawa and Yoshitaka Tanimura. a polarizable water model for intramolecular and intermolecular vibrational spectroscopies. *J. Phys. Chem. B*, 115(18):5545–5553, 2011.

[101] G Andres Cisneros. Application of gaussian electrostatic model (gem) distributed multipoles in the amoeba force field. *J. Chem. Theory Comput.*, 8(12):5072–5080, 2012.

[102] Robert E Duke, Oleg N Starovoytov, Jean-Philip Piquemal, and G Andres Cisneros. Gem*: A molecular electronic density-based force field for molecular dynamics simulations. *J. Chem. Theory Comput.*, 10(4):1361–1365, 2014.

[103] Hedieh Torabifard, Oleg N Starovoytov, Pengyu Ren, and G Andrés Cisneros. Development of an amoeba water model using gem distributed multipoles. *Theor. Chem. Acc.*, 134(8):101, 2015.

[104] Robert E Duke and G Andres Cisneros. Ewald-based methods for gaussian integral evaluation: Application to a new parameterization of gem. *J. Mol. Model.*, 25(10):307, 2019.

[105] N Gresh. Inter- and intramolecular interactions. inception and refinements of the sibfa molecular mechanics (smm) procedure a separable polarizable methodology grounded on ab initio scf/mp2 computations. examples of applications to molecular recognition problems. *J. Chim. Phys. Phys.- Chim. Biol.*, 7(94):1365–1416, 1997.

[106] Jean-Philip Piquemal, Nohad Gresh, and Claude Giessner-Prettre. Improved formulas for the calculation of the electrostatic contribution to the intermolecular interaction energy from multipolar expansion of the electronic distribution. *J. Phys. Chem. A*, 107(48):10353–10359, 2003.

[107] Nohad Gresh, G Andrés Cisneros, Thomas A Darden, and Jean-Philip Piquemal. Anisotropic polarizable molecular mechanics studies of inter-and intramolecular interactions and ligand–macromolecule complexes. a bottom-up strategy. *J. Chem. Theory Comput.*, 3(6):1960–1986, 2007.

[108] Akshaya K Das, Lars Urban, Itai Leven, Matthias Loipersberger, Abdulrahman Aldossary, Martin Head-Gordon, and Teresa Head-Gordon. Development of an advanced force field for water using variational energy decomposition analysis. *J. Chem. Theory Comput.*, 15(9):5001–5013, 2019.

[109] B Thole. Molecular polarizabilities calculated with a modified dipole interaction. *Chem. Phys.*, 59(3):341–350, 1981.

[110] Bernd Hartke. Size-dependent transition from all-surface to interior-molecule structures in pure neutral water clusters. *Phys. Chem. Chem. Phys.*, 5(2):275–284, 2003.

[111] Sotiris S Xantheas and Edoardo Aprà. The binding energies of the d_2d and s_4 water octamer isomers: High-level electronic structure and empirical potential results. *J. Chem. Phys.*, 120(2):823–828, 2004.

[112] CJ Burnham, GF Reiter, J Mayers, T Abdul-Redah, H Reichert, and H Dosch. on the origin of the redshift of the oh stretch in ice ih: Evidence from the momentum distribution of the protons and the infrared spectral density. *Phys. Chem. Chem. Phys.*, 8(34):3966–3977, 2006.

[113] Francesco Paesani, Satoru Iuchi, and Gregory A Voth. Quantum effects in liquid water from an ab initio-based polarizable force field. *J. Chem. Phys.*, 127(7):074506, 2007.

[114] George S Fanourgakis and Sotiris S Xantheas. the bend angle of water in ice ih and liquid water: The significance of implementing the nonlinear monomer dipole moment surface in classical interaction potentials. *J. Chem. Phys.*, 124(17):174504, 2006.

[115] Scott Habershon, George S Fanourgakis, and David E Manolopoulos. Comparison of path integral molecular dynamics methods for the infrared absorption spectrum of liquid water. *J. Chem. Phys.*, 129(7):074501, 2008.

[116] Francesco Paesani, Sotiris S Xantheas, and Gregory A Voth. Infrared spectroscopy and hydrogen-bond dynamics of liquid water from centroid molecular dynamics with an ab initio-based force field. *J. Phys. Chem. B*, 113(39):13118–13130, 2009.

[117] Lee-Ping Wang, Jiahao Chen, and Troy Van Voorhis. Systematic parametrization of polarizable force fields from quantum chemistry data. *J. Chem. Theory Comput.*, 9(1):452–460, 2012.

[118] Alexander Späh, Harshad Pathak, Kyung Hwan Kim, Fivos Perakis, Daniel Mariedahl, Katrin Amann-Winkel, Jonas A Sellberg, Jae Hyuk Lee, Sangsoo Kim, Jaehyun Park, Ki Hyun Nam, Tetsuo Katayama, and Anders Nilsson. Apparent power-law behavior of water's isothermal compressibility and correlation length upon supercooling. *Phys. Chem. Chem. Phys.*, 21(1):26–31, 2019.

[119] O Matsuoka, E Clementi, and M Yoshimine. Ci study of the water dimer potential surface. *J. Chem. Phys.*, 64(4):1351–1361, 1976.

[120] GC Lie and E Clementi. Molecular-dynamics simulation of liquid water with an ab initio flexible water–water interaction potential. *Phys. Rev. A*, 33(4):2679, 1986.

[121] MW Evans, K Refson, KN Swamy, GC Lie, and E Clementi. Molecular-dynamics simulation of liquid water with an ab initio flexible water–water interaction potential. ii. the effect of internal vibrations on the time correlation functions. *Phys. Rev. A*, 36(8):3935, 1987.

[122] U Niesar, G Corongiu, E Clementi, GR Kneller, and DK Bhattacharya. Molecular dynamics simulations of liquid water using the ncc ab initio potential. *J. Phys. Chem.*, 94(20):7949–7956, 1990.

[123] Robert Bukowski, Krzysztof Szalewicz, Gerrit C Groenenboom, and Ad van der Avoird. Polarizable interaction potential for water from coupled cluster calculations. i. analysis of dimer potential energy surface. *J. Chem. Phys.*, 128(9):094313, 2008.

[124] Robert Bukowski, Krzysztof Szalewicz, Gerrit C Groenenboom, and Ad van der Avoird. Polarizable interaction potential for water from coupled cluster calculations. ii. applications to dimer spectra virial coefficients and simulations of liquid water. *J. Chem. Phys.*, 128(9):094314, 2008.

[125] Krzysztof Szalewicz, Claude Leforestier, and Ad Van Der Avoird. Towards the complete understanding of water by a first-principles computational approach. *Chem. Phys. Lett.*, 482(1-3):1–14, 2009.

[126] Xinchuan Huang, Bastiaan J Braams, and Joel M Bowman. Ab initio potential energy and dipole moment surfaces of $(h_2o)_2$. *J. Phys. Chem. A*, 110(2):445–451, 2006.

[127] Yimin Wang, Xinchuan Huang, Benjamin C Shepler, Bastiaan J Braams, and Joel M Bowman. Flexible ab initio potential and dipole moment surfaces for water. i. tests and applications for clusters up to the 22-mer. *J. Chem. Phys.*, 134(9):094509, 2011.

[128] Yimin Wang and Joel M Bowman. Ab initio potential and dipole moment surfaces for water. ii. local-monomer calculations of the infrared spectra of water clusters. *J. Chem. Phys.*, 134(15):154510, 2011.

[129] Yimin Wang, Benjamin C Shepler, Bastiaan J Braams, and Joel M Bowman. Full-dimensional ab initio potential energy and dipole moment surfaces for water. *J. Chem. Phys.*, 131(5):054511, 2009.

[130] Gregory R Medders, Volodymyr Babin, and Francesco Paesani. a critical assessment of two-body and three-body interactions in water. *J. Chem. Theory Comput.*, 9(2):1103–1114, 2013.

[131] Volodymyr Babin, Gregory R Medders, and Francesco Paesani. Toward a universal water model: First principles simulations from the dimer to the liquid phase. *J. Phys. Chem. Lett.*, 3(24):3765–3769, 2012.

[132] Francesco Paesani. Getting the right answers for the right reasons: Toward predictive molecular simulations of water with many-body potential energy functions. *Acc. Chem. Res.*, 49(9):1844–1851, 2016.

[133] Jeremy O Richardson, Cristóbal Pérez, Simon Lobsiger, Adam A Reid, Berhane Temelso, George C Shields, Zbigniew Kisiel, David J Wales, Brooks H Pate, and Stuart C Althorpe. Concerted hydrogen-bond breaking by quantum tunneling in the water hexamer prism. *Science*, 351(6279):1310–1313, 2016.

[134] William TS Cole, James D Farrell, David J Wales, and Richard J Saykally. Structure and torsional dynamics of the water octamer from thz laser spectroscopy near 215 μm. *Science*, 352(6290):1194–1197, 2016.

[135] Joel D Mallory and Vladimir A Mandelshtam. Diffusion monte carlo studies of mb-pol $(h_2o)_2 - 6$ and $(d_2o)_2 - 6$ clusters: Structures and binding energies. *J. Chem. Phys.*, 145(6):064308, 2016.

[136] Pablo E Videla, Peter J Rossky, and D Laria. Communication: Isotopic effects on tunneling motions in the water trimer. *J. Chem. Phys.*, 144(6):061101, 2016.

[137] Sandra E Brown, Andreas W Götz, Xiaolu Cheng, Ryan P Steele, Vladimir A Mandelshtam, and Francesco Paesani. Monitoring water clusters "melt" through vibrational spectroscopy. *J. Am. Chem. Soc.*, 139(20):7082–7088, 2017.

[138] CL Vaillant, DJ Wales, and SC Althorpe. Tunneling splittings from path-integral molecular dynamics using a langevin thermostat. *J. Chem. Phys.*, 148(23):234102, 2018.

[139] Matthew Schmidt and Pierre-Nicholas Roy. Path integral molecular dynamic simulation of flexible molecular systems in their ground state: Application to the water dimer. *J. Chem. Phys.*, 148(12):124116, 2018.

[140] Kevin P Bishop and Pierre-Nicholas Roy. Quantum mechanical free energy profiles with post-quantization restraints: Binding free energy of the water dimer over a broad range of temperatures. *J. Chem. Phys.*, 148(10):102303, 2018.

[141] Pablo E Videla, Peter J Rossky, and Daniel Laria. Isotopic equilibria in aqueous clusters at low temperatures: Insights from the mb-pol many-body potential. *J. Chem. Phys.*, 148(8):084303, 2018.

[142] Nagaprasad Reddy Samala and Noam Agmon. Temperature dependence of intramolecular vibrational bands in small water clusters. *J. Phys. Chem. B*, 123(44):9428–9442, 2019.

[143] Nagaprasad Reddy Samala and Noam Agmon. Thermally induced hydrogen-bond rearrangements in small water clusters and the persistent water tetramer. *ACS Omega*, 4(27):22581–22590, 2019.

[144] Marko T Cvitaš and Jeremy O Richardson. Quantum tunnelling pathways of the water pentamer. *Phys. Chem. Chem. Phys.*, 22:1035–1044, 2020.

[145] Gregory R Medders and Francesco Paesani. Infrared and raman spectroscopy of liquid water through "first-principles" many-body molecular dynamics. *J. Chem. Theory Comput.*, 11(3):1145–1154, 2015.

[146] Piero Gasparotto, Ali A Hassanali, and Michele Ceriotti. Probing defects and correlations in the hydrogen-bond network of ab initio water. *J. Chem. Theory Comput.*, 12(4):1953–1964, 2016.

[147] Shelby C Straight and Francesco Paesani. Exploring electrostatic effects on the hydrogen bond network of liquid water through many-body molecular dynamics. *J. Phys. Chem. B*, 120(33):8539–8546, 2016.

[148] Sandeep K Reddy, Daniel R Moberg, Shelby C Straight, and Francesco Paesani. Temperature-dependent vibrational spectra and structure of liquid water from classical and quantum simulations with the mb-pol potential energy function. *J. Chem. Phys.*, 147(24):244504, 2017.

[149] Kelly M Hunter, Farnaz A Shakib, and Francesco Paesani. Disentangling coupling effects in the infrared spectra of liquid water. *J. Phys. Chem. B*, 122(47):10754–10761, 2018.

[150] Gregory R Medders and Francesco Paesani. Dissecting the molecular structure of the air/water interface from quantum simulations of the sum-frequency generation spectrum. *J. Am. Chem. Soc.*, 138(11):3912–3919, 2016.

[151] Daniel R Moberg, Shelby C Straight, and Francesco Paesani. Temperature dependence of the air/water interface revealed by polarization sensitive sum-frequency generation spectroscopy. *J. Phys. Chem. B*, 122(15):4356–4365, 2018.

[152] Paul E Ohno, Hong-fei Wang, Francesco Paesani, James L Skinner, and Franz M Geiger. Second-order vibrational lineshapes from the air/water interface. *J. Phys. Chem. A*, 122(18):4457–4464, 2018.

[153] Sanghamitra Sengupta, Daniel R Moberg, Francesco Paesani, and Eric Tyrode. Neat water–vapor interface: Proton continuum and the nonresonant background. *J. Phys. Chem. Lett.*, 9(23):6744–6749, 2018.

[154] Shumei Sun, Fujie Tang, Sho Imoto, Daniel R Moberg, Tatsuhiko Ohto, Francesco Paesani, Mischa Bonn, Ellen HG Backus, and Yuki Nagata. Orientational distribution of free oh groups of interfacial water is exponential. *Phys. Rev. Lett.*, 121(24):246101, 2018.

[155] C Huy Pham, Sandeep K Reddy, Karl Chen, Chris Knight, and Francesco Paesani. Many-body interactions in ice. *J. Chem. Theory Comput.*, 13(4):1778–1784, 2017.

[156] Daniel R Moberg, Shelby C Straight, Christopher Knight, and Francesco Paesani. Molecular origin of the vibrational structure of ice i. *J. Phys. Chem. Lett.*, 8(12):2579–2583, 2017.

[157] Daniel R Moberg, Peter J Sharp, and Francesco Paesani. Molecular-level interpretation of vibrational spectra of ordered ice phases. *J. Phys. Chem. B*, 122(46):10572–10581, 2018.

[158] Zhaoru Sun, Lixin Zheng, Mohan Chen, Michael L Klein, Francesco Paesani, and Xifan Wu. Electron-hole theory of the effect of quantum nuclei on the x-ray absorption spectra of liquid water. *Phys. Rev. Lett.*, 121(13):137401, 2018.

[159] Alex P Gaiduk, Tuan Anh Pham, Marco Govoni, Francesco Paesani, and Giulia Galli. Electron affinity of liquid water. *Nat. Commun.*, 9(1):247, 2018.

[160] Michelle Fritz, Marivi Fernández-Serra, and José M Soler. Optimization of an exchange-correlation density functional for water. *J. Chem. Phys.*, 144(22):224101, 2016.

[161] Thomas A Halgren. the representation of van der waals (vdw) interactions in molecular mechanics force fields: Potential form combination rules and vdw parameters. *J. Am. Chem. Soc.*, 114(20):7827–7843, 1992.

[162] Trevor Hastie, Robert Tibshirani, and Jerome Friedman. *the Elements of Statistical Learning: Data Mining Inference and Prediction*. Springer Science & Business Media, 2009.

[163] Francesco Paesani. Water: Many-body potential from first principles (from the gas to the liquid phase). *Handbook of Materials Modeling: Methods: Theory and Modeling*, pages 635–660, 2020.

[164] Andrew C Simmonett, Andrew TB Gilbert, and Peter MW Gill. an optimal point-charge model for molecular electrostatic potentials. *Mole. Phys.*, 103(20):2789–2793, 2005.

[165] Narbe Mardirossian and Martin Head-Gordon. ωb97m-v: A combinatorially optimized range-separated hybrid meta-gga density functional with vv10 nonlocal correlation. *J. Chem. Phys.*, 144(21):214110, 2016.

[166]

[167] David E Woon and Thom H Dunning Jr. Gaussian basis sets for use in correlated molecular calculations. iii. the atoms aluminum through argon. *J. Chem. Phys.*, 98(2):1358–1371, 1993.

[168] W Smith and TR Forester. Dl_poly_2.0: A general-purpose parallel molecular dynamics simulation package. *J. Mol. Graph.*, 14(3):136–141, 1996.

[169] Joshua A Rackers, Zhi Wang, Chao Lu, Marie L Laury, Louis Lagardère, Michael J Schnieders, Jean-Philip Piquemal, Pengyu Ren, and Jay W Ponder. Tinker 8: Software tools for molecular design. *J. Chem. Theory Comput.*, 14(10):5273–5289, 2018.

[170] Urszula Góra, Rafał Podeszwa, Wojciech Cencek, and Krzysztof Szalewicz. Interaction energies of large clusters from many-body expansion. *J. Chem. Phys.*, 135(22):224102, 2011.

[171] J. Cao and G.A. Voth. the formulation of quantum statistical mechanics based on the feynman path centroid density. i. equilibrium properties. *J. Chem. Phys.*, 100(7):5093–5105, 1994.

[172] J. Cao and G.A. Voth. the formulation of quantum statistical mechanics based on the feynman path centroid density. ii. dynamical properties. *J. Chem. Phys.*, 100(7):5106–5117, 1994.

[173] J. Cao and G.A. Voth. the formulation of quantum statistical mechanics based on the feynman path centroid density. iii. phase space formalism and analysis of centroid molecular dynamics. *J. Chem. Phys.*, 101(7):6157–6167, 1994.

[174] J. Cao and G.A. Voth. the formulation of quantum statistical mechanics based on the feynman path centroid density. iv. algorithms for centroid molecular dynamics. *J. Chem. Phys.*, 101(7):6168–6183, 1994.

[175] J. Cao and G.A. Voth. the formulation of quantum statistical mechanics based on the feynman path centroid density. v. quantum instantaneous normal mode theory of liquids. *J. Chem. Phys.*, 101(7):6184–6192, 1994.

[176] Michael J Gillan, Dario Alfe, and Angelos Michaelides. Perspective: How good is dft for water? *J. Chem. Phys.*, 144(13):130901, 2016.

[177] Francesco Paesani, Soohaeng Yoo, Huib J Bakker, and Sotiris S Xantheas. Nuclear quantum effects in the reorientation of water. *J. Phys. Chem. Lett.*, 1(15):2316–2321, 2010.

[178] HJ Bakker and JL Skinner. Vibrational spectroscopy as a probe of structure and dynamics in liquid water. *Chem. Rev.*, 110(3):1498–1517, 2010.

[179] Pushp Bajaj, Andreas W Götz, and Francesco Paesani. Toward chemical accuracy in the description of ion–water interactions through many-body representations. i. halide–water dimer potential energy surfaces. *J. Chem. Theory Comput.*, 12(6):2698–2705, 2016.

[180] Marc Riera, Narbe Mardirossian, Pushp Bajaj, Andreas W Götz, and Francesco Paesani. Toward chemical accuracy in the description of ion–water interactions through many-body representations. alkali-water dimer potential energy surfaces. *J. Chem. Phys.*, 147(16):161715, 2017.

[181] Pushp Bajaj, Xiao-Gang Wang, Tucker CarringtonJr, and Francesco Paesani. Vibrational spectra of halide–water dimers: Insights on ion hydration from full-dimensional quantum calculations on many-body potential energy surfaces. *J. Chem. Phys.*, 148(10):102321, 2017.

[182] Marc Riera, Sandra E Brown, and Francesco Paesani. Isomeric equilibria nuclear quantum effects and vibrational spectra of $M^+(H_2O)_n$. *J. Phys. Chem. A*, 122(27):5811–5821, 2018.

[183] Francesco Paesani, Pushp Bajaj, and Marc Riera. Chemical accuracy in modeling halide ion hydration from many-body representations. *Adv. Phys. X*, 4(1):1631212, 2019.

[184] Debbie Zhuang, Marc Riera, Gregory K Schenter, John L Fulton, and Francesco Paesani. Many-body effects determine the local hydration structure of cs^+ in solution. *J. Phys. Chem. Lett.*, 10(3):406–412, 2019.

[185] Pushp Bajaj, Marc Riera, Jason K Lin, Yaira E Mendoza Montijo, Jessica Gazca, and Francesco Paesani. Halide ion microhydration: Structure energetics and spectroscopy of small halide–water clusters. *J. Phys. Chem. Lett.*, 123(13):2843–2852, 2019.

[186] Pushp Bajaj, Jeremy O Richardson, and Francesco Paesani. Ion-mediated hydrogen-bond rearrangement through tunnelling in the iodide–dihydrate complex. *Nat. Chem.*, 11(4):367–374, 2019.

[187] Pushp Bajaj, Debbie Zhuang, and Francesco Paesani. Specific ion effects on hydrogen-bond rearrangements in the halide–dihydrate complexes. *J. Phys. Chem. Lett.*, 10(11):2823–2828, 2019.

[188] Brandon B Bizzarro, Colin K Egan, and Francesco Paesani. Nature of halide–water interactions: Insights from many-body representations and density functional theory. *J. Chem. Theory Comput.*, 15(5):2983–2995, 2019.

[189] Colin K Egan, Brandon B Bizzarro, Marc Riera, and Francesco Paesani. Nature of alkali ion–water interactions: Insights from many-body representations and density functional theory. ii. *J. Chem. Theory Comput.*, 16(5):3055–3072, 2020.

[190] Yaoguang Zhai, Alessandro Caruso, Sicun Gao, and Francesco Paesani. Active learning of many-body configuration space: Application to the cs^+–water mb-nrg potential energy function as a case study. *J. Chem. Phys.*, 152(14):144103, 2020.

[191] Marc Riera, Alan Hirales, Raja Ghosh, and Francesco Paesani. Data-driven many-body models for ch_4/h_2o mixtures. *to be submitted*, 2020.

[192] J. D. Hunter. Matplotlib: A 2d graphics environment. *Comput. Sci. Eng.*, 9(3):90–95, 2007.

[193] A Warshel and M Karplus. Calculation of ground and excited state potential surfaces of conjugated molecules. i. formulation and parametrization. *J. Am. Chem. Soc.*, 94(16):5612–5625, 1972.

[194] Arieh Warshel and Michael Levitt. Theoretical studies of enzymic reactions: Dielectric electrostatic and steric stabilization of the carbonium ion in the reaction of lysozyme. *J. Mol. Biol.*, 103(2):227–249, 1976.

[195] T A Halgren and W Damm. Polarizable force fields. *Curr. Opin. Struct. Biol.*, 11(2):236–242, 2001.

[196] Jay W Ponder and David A Case. Force fields for protein simulations. *Adv. Protein Chem.*, 66:27–85, 2003.

[197] Zhifeng Jing, Chengwen Liu, Sara Y Cheng, Rui Qi, Brandon D Walker, Jean-Philip Piquemal, and Pengyu Ren. Polarizable force fields for biomolecular simulations: Recent advances and applications. *Annu. Rev. Biophys.*, 48(1):371–394, 2019.

[198] Arieh Warshel, Mitsunori Kato, and Andrei V Pisliakov. Polarizable force fields: History test cases and prospects. *J. Chem. Theory Comput.*, 3(6):2034–2045, 2007.

[199] Jiali Gao. Energy components of aqueous solution: Insight from hybrid qm/mm simulations using a polarizable solvent model. *J. Comput. Chem.*, 18(8):1061–1071, 1997.

[200] Stuart R Gooding, Peter J Winn, Richard I Maurer, György G Ferenczy, John R Miller, Jayne E Harris, D Vaughan Griffiths, and Christopher A Reynolds. Fully polarizable qm/mm calculations: An application to the nonbonded iodine–oxygen interaction in dimethyl-2-iodobenzoylphosphonate. *J. Comput. Chem.*, 21(6):478–482, 2000.

[201] Christopher J. R. Illingworth, Stuart R. Gooding, Peter J. Winn, Garth A. Jones, György G. Ferenczy, and Christopher A. Reynolds. Classical polarization in hybrid qm/mm methods. *J. Phys. Chem. A*, 110(20):6487–6497, 2006.

[202] C.J.R. Illingworth, K.E. Parkes, C.R. Snell, S. Marti, V. Moliner, and C.A. Reynolds. the eeffect of mm polarization on the qm/mm transition state stabilization: Application to chorismate mutase. *Mol. Phys.*, 106(12-13):1511–1515, 2008.

[203] Eric G Kratz, Alice R Walker, Louis Lagardère, Filippo Lipparini, Jean-Philip Piquemal, and G Andrés Cisneros. Lichem: A qm/mm program for simulations with multipolar and polarizable force fields. *J. Comput. Chem.*, 37(11):1019–1029, 2016.

[204] Hatice Gökcan, Erik Antonio Vázquez-Montelongo, and G Andrés Cisneros. Lichem 1.1: Recent improvements and new capabilities. *J. Chem. Theory Comput.*, 15(5):3056–3065, 2019.

[205] Carles Curutchet, Aurora Muñoz-Losa, Susanna Monti, Jacob Kongsted, Gregory D. Scholes, and Benedetta Mennucci. Electronic energy transfer in condensed phase studied by a polarizable qm/mm model. *J. Chem. Theory Comput.*, 5(7):1838–1848, 2009.

[206] Stefano Caprasecca, Sandro Jurinovich, Lucas Viani, Carles Curutchet, and Benedetta Mennucci. Geometry optimization in polarizable qm/mm models: The induced dipole formulation. *J. Chem. Theory Comput.*, 10(4):1588–1598, 2014.

[207] Jacek Dziedzic, Yuezhi Mao, Yihan Shao, Jay Ponder, Teresa Head-Gordon, Martin Head-Gordon, and Chris-Kriton Skylaris. Tinktep: A fully self-consistent mutually polarizable qm/mm approach based on the amoeba force field. *J. Chem. Phys.*, 145(12):124106, 2016.

[208] Jacek Dziedzic, Teresa Head-Gordon, Martin Head-Gordon, and Chris-Kriton Skylaris. Mutually polarizable qm/mm model with in situ optimized localized basis functions. *J. Chem. Phys.*, 150(7):074103, 2019.

[209] Daniele Loco, Etienne Polack, Stefano Caprasecca, Louis Lagardère, Filippo Lipparini, Jean-Philip Piquemal, and Benedetta Mennucci. A qm/mm approach using the amoeba polarizable embedding: From ground state energies to electronic excitations. *J. Chem. Theory Comput.*, 12(8):3654–3661, 2016.

[210] Jógvan Magnus Haugaard Olsen and Jacob Kongsted. *Molecular Properties Through Polarizable Embedding*, pages 107–143. Elsevier, 2011.

[211] Jogvan Magnus Olsen, Kestutis Aidas, and Jacob Kongsted. Excited states in solution through polarizable embedding. *J. Chem. Theory Comput.*, 6(12):3721–3734, 2010.

[212] Daniele Loco, Louis Lagardère, Stefano Caprasecca, Filippo Lipparini, Benedetta Mennucci, and Jean-Philip Piquemal. Hybrid qm/mm molecular dynamics with amoeba polarizable embedding. *J. Chem. Theory Comput.*, 13(9):4025–4033, 2017.

[213] Daniele Loco, Sandro Jurinovich, Lorenzo Cupellini, Maximilian FSJ Menger, and Benedetta Mennucci. The modeling of the absorption lineshape for embedded molecules through a polarizable qm/mm approach. *Photochem. Photobiol. Sci.*, 17(5):552–560, 2018.

[214] Richard A. Bryce, Robert Buesnel, Ian H. Hillier, and Neil A. Burton. a solvation model using a hybrid quantum mechanical/molecular mechanical potential with fluctuating solvent charges. *Chem. Phys. Lett.*, 279(5–6):367–371, 1997.

[215] Filippo Lipparini, Chiara Cappelli, Giovanni Scalmani, Nicola De Mitri, and Vincenzo Barone. Analytical first and second derivatives for a fully polarizable qm/classical hamiltonian. *J. Chem. Theory Comput.*, 8(11):4270–4278, 2012.

[216] Filippo Lipparini, Chiara Cappelli, and Vincenzo Barone. Linear response theory and electronic transition energies for a fully polarizable qm/classical hamiltonian. *J. Chem. Theory Comput.*, 8(11):4153–4165, 2012.

[217] Tommaso Giovannini, Alessandra Puglisi, Matteo Ambrosetti, and Chiara Cappelli. Polarizable qm/mm approach with fluctuating charges and fluctuating dipoles: The qm/fqfμ model. *J. Chem. Theory Comput.*, 15(4):2233–2245, 2019.

[218] Filippo Lipparini, Chiara Cappelli, and Vincenzo Barone. a gauge invariant multiscale approach to magnetic spectroscopies in condensed phase: General three-layer model computational implementation and pilot applications. *J. Chem. Phys.*, 138(23):234108, 2013.

[219] Chiara Cappelli. Integrated qm/polarizable mm/continuum approaches to model chiroptical properties of strongly interacting solute–solvent systems. *Int. J. Quantum Chem.*, 116(21):1532–1542, 2016.

[220] Zhenyu Lu and Yingkai Zhang. Interfacing ab initio quantum mechanical method with classical drude osillator polarizable model for molecular dynamics simulation of chemical reactions. *J. Chem. Theory Comput.*, 4(8):1237–1248, 2008.

[221] Abir Ganguly, Eliot Boulanger, and Walter Thiel. Importance of mm polarization in qm/mm studies of enzymatic reactions: Assessment of the qm/mm drude oscillator model. *J. Chem. Theory Comput.*, 13(6):2954–2961, 2017.

[222] Gerhard König, Frank C. Pickard, Jing Huang, Walter Thiel, Alexander D. MacKerell, Bernard R. Brooks, and Darrin M. York. a comparison of qm/mm simulations with and without the drude oscillator model based on hydration free energies of simple solutes. *Mol.*, 23(10):2695, 2018.

[223] Saleh Riahi and Christopher N. Rowley. the charmm–turbomole interface for efficient and accurate qm/mm molecular dynamics free energies and excited state properties. *J. Comput. Chem.*, 35(28):2076–2086, 2014.

[224] Christopher N. Rowley and Benoıt Roux. the solvation structure of na^+ and k^+ in liquid water determined from high level ab initio molecular dynamics simulations. *J. Chem. Theory Comput.*, 8(10):3526–3535, 2012.

[225] Sudhir K. Sahoo and Nisanth N. Nair. Interfacing the core-shell or the drude polarizable force field with car-parrinello molecular dynamics for qm/mm simulations. *Front. Chem.*, 6:275, 2018.

[226] Hao Hu, Zhenyu Lu, and Weitao Yang. Qm/mm minimum free-energy path: Methodology and application to triosephosphate isomerase. *J. Chem. Theory Comput.*, 3(2):390–406, 2007.

[227] Hiroshi Nakano and Takeshi Yamamoto. Variational calculation of quantum mechanical/molecular mechanical free energy with electronic polarization of solvent. *J. Chem. Phys.*, 136(13):134107, 2012.

[228] Mark S. Gordon, Dmitri G. Fedorov, Spencer R. Pruitt, and Lyudmila V. Slipchenko. Fragmentation methods: A route to accurate calculations on large systems. *Chem. Rev.*, 112(1):632–672, 2012.

[229] Jiali Gao, Donald G Truhlar, Yingjie Wang, Michael J M Mazack, Patrick Löffler, Makenzie R Provorse, and Pavel Rehak. Explicit polarization: A quantum mechanical framework for developing next generation force fields. *Acc. Chem. Res.*, 47(9):2837–2845, 2014.

[230] Christian B Nielsen, Ove Christiansen, Kurt V Mikkelsen, and Jacob Kongsted. Density functional self-consistent quantum mechanics/molecular mechanics theory for linear and nonlinear molecular properties: Applications to solvated water and formaldehyde. *J. Chem. Phys.*, 126(15):154112, 2007.

[231] Stefano Caprasecca, Sandro Jurinovich, Louis Lagardère, Benjamin Stamm, and Filippo Lipparini. Achieving linear scaling in computational cost for a fully polarizable mm/continuum embedding. *J. Chem. Theory Comput.*, 11(2):694–704, 2015.

[232] Filippo Lipparini. General linear scaling implementation of polarizable embedding schemes. *J. Chem. Theory Comput.*, 15(8):4312–4317, 2019.

[233] Mattia Bondanza, Lorenzo Cupellini, Filippo Lipparini, and Benedetta Mennucci. the multiple roles of the protein in the photoactivation of orange carotenoid protein. *Chem*, 6(1):187–203, 2020.

[234] Daniele Loco, Louis Lagardère, Gérardo A. Cisneros, Giovanni Scalmani, Michael Frisch, Filippo Lipparini, Benedetta Mennucci, and Jean-Philip Piquemal. Towards large scale hybrid qm/mm dynamics of complex systems with advanced point dipole polarizable embeddings. *Chem. Sci.*, 10(30):7200–7211, 2019.

[235] Teerakiat Kerdcharoen, Klaus R Liedl, and Bernd M Rode. A qm/mm simulation method applied to the solution of li^+ in liquid ammonia. *Chem. Phys.*, 211(1-3):313–323, 1996.

[236] Rosa E Bulo, Bernd Ensing, Jetze Sikkema, and Lucas Visscher. Toward a practical method for adaptive qm/mm simulations. *J. Chem. Theory Comput.*, 5(9):2212–2221, 2009.

[237] Norio Takenaka, Yukichi Kitamura, Yoshiyuki Koyano, and Masataka Nagaoka. The number-adaptive multiscale qm/mm molecular dynamics simulation: Application to liquid water. *Chem. Phys. Lett.*, 524:56–61, 2012.

[238] Adam W Duster, Chun-Hung Wang, Christina M Garza, Danielle E Miller, and Hai Lin. Adaptive quantum/molecular mechanics: What have we learned where are we and where do we go from here? *WIREs Comput. Mol. Sci.*, 7(5):e1310, 2017.

[239] Teerakiat Kerdcharoen and Keiji Morokuma. Oniom-xs: An extension of the oniom method for molecular simulation in condensed phase. *Chem. Phys. Lett.*, 355(3-4):257–262, 2002.

[240] Noam Bernstein, Csilla Várnai, Ivan Solt, Steven A Winfield, Mike C Payne, István Simon, Mónika Fuxreiter, and Gábor Csányi. Qm/mm simulation of liquid water with an adaptive quantum region. *Phys. Chem. Chem. Phys.*, 14(2):646–656, 2012.

[241] Andreas Heyden, Hai Lin, and Donald G Truhlar. Adaptive partitioning in combined quantum mechanical and molecular mechanical calculations of potential energy functions for multiscale simulations. *J. Phys. Chem. B.*, 111(9):2231–2241, 2007.

[242] Kyoyeon Park, Andreas W Götz, Ross C Walker, and Francesco Paesani. Application of adaptive qm/mm methods to molecular dynamics simulations of aqueous systems. *J. Chem. Theory Comput.*, 8(8):2868–2877, 2012.

[243] Soroosh Pezeshki and Hai Lin. Adaptive-partitioning redistributed charge and dipole schemes for qm/mm dynamics simulations: On-the-fly relocation of boundaries that pass through covalent bonds. *J. Chem. Theory Comput.*, 7(11):3625–3634, 2011.

[244] Rosa E Bulo, Carine Michel, Paul Fleurat-Lessard, and Philippe Sautet. Multiscale modeling of chemistry in water: Are we there yet? *J. Chem. Theory Comput.*, 9(12):5567–5577, 2013.

[245] Mark P Waller, Sadhana Kumbhar, and Jack Yang. A density-based adaptive quantum mechanical/molecular mechanical method. *ChemPhysChem*, 15(15):3218–3225, 2014.

[246] Hiroshi C Watanabe, Tomš Kubař, and Marcus Elstner. Size-consistent multipartitioning qm/mm: A stable and efficient adaptive qm/mm method. *J. Chem. Theory Comput.*, 10(10):4242–4252, 2014.

[247] Jelle M Boereboom, Raffaello Potestio, Davide Donadio, and Rosa E Bulo. Toward hamiltonian adaptive qm/mm: Accurate solvent structures using many-body potentials. *J. Chem. Theory Comput.*, 12(8):3441–3448, 2016.

[248] Min Zheng and Mark P Waller. Adaptive quantum mechanics/molecular mechanics methods. *WIREs Comput. Mol. Sci.*, 6(4):369–385, 2016.

[249] Sebastian Dohm, Eckhard Spohr, and Martin Korth. Developing adaptive qm/mm computer simulations for electrochemistry. *J. Comput. Chem.*, 38(1):51–58, 2017.

[250] Martin J Field. An algorithm for adaptive qc/mm simulations. *J. Chem. Theory Comput.*, 13(5):2342–2351, 2017.

[251] Jelle M Boereboom, Paul Fleurat-Lessard, and Rosa E Bulo. Explicit solvation matters: Performance of qm/mm solvation models in nucleophilic addition. *J. Chem. Theory Comput.*, 14(4):1841–1852, 2018.

[252] Adam W Duster, Chun-Hung Wang, and Hai Lin. Adaptive qm/mm for molecular dynamics simulations: 5. on the energy-conserved permuted adaptive-partitioning schemes. *Molecules*, 23(9):2170, 2018.

[253] Hiroshi C Watanabe and Qiang Cui. Quantitative analysis of qm/mm boundary artifacts and correction in adaptive qm/mm simulations. *J. Chem. Theory Comput.*, 15(7):3917–3928, 2019.

[254] Min Zheng and Mark P Waller. Yoink: An interaction-based partitioning api. *J. Comput. Chem.*, 39(13):799–806, 2018.

[255] Paul N Day, Jan H Jensen, Mark S Gordon, Simon P Webb, Walter J Stevens, Morris Krauss, David Garmer, Harold Basch, and Drora Cohen. An effective fragment method for modeling solvent effects in quantum mechanical calculations. *J. Chem. Phys.*, 105(5):1968–1986, 1996.

[256] Wei Chen and Mark S Gordon. The effective fragment model for solvation: Internal rotation in formamide. *J. Chem. Phys.*, 105(24):11081–11090, 1996.

[257] Mark S Gordon, Mark A Freitag, Pradipta Bandyopadhyay, Jan H Jensen, Visvaldas Kairys, and Walter J Stevens. The effective fragment potential method: A qm-based mm approach to modeling environmental effects in chemistry. *J. Phys. Chem. A*, 105(2):293–307, 2001.

[258] Debashree Ghosh, Dmytro Kosenkov, Vitalii Vanovschi, Joanna Flick, Ilya Kaliman, Yihan Shao, Andrew TB Gilbert, Anna I Krylov, and Lyudmila V Slipchenko. Effective fragment potential method in q-chem: A guide for users and developers. *J. Comput. Chem.*, 34(12):1060–1070, 2013.

[259] Xin Chen and Jiali Gao. Fragment exchange potential for realizing pauli deformation of interfragment interactions. *J. Phys. Chem. Lett.*, 11(10):4008–4016, 2020.

[260] Claudia I. Viquez Rojas and Lyudmila V. Slipchenko. Exchange repulsion in quantum mechanical/effective fragment potential excitation energies: Beyond polarizable embedding. *J. Chem. Theory Comput.*, page DOI:10.1021/acs.jctc.9b01156, 2020.

[261] Jean-Philip Piquemal and G.Andrés Cisneros. Status of the gaussian electrostatic model a density based. pages 269–300. Pan Stanford Publishing, 2015.

[262] G. Andrés Cisneros, Jean-Philip Piquemal, and T. A. Darden. Quantum mechanics/molecular mechanics electrostatic embedding with. *J. Phys. Chem. B*, 110:13682–13684, 2006.

[263] Hatice Gökcan, Eric Kratz, Thomas A Darden, Jean-Philip Piquemal, and G Andrés Cisneros. Qm/mm simulations with the gaussian electrostatic model: A density-based polarizable potential. *J. Phys. Chem. Lett.*, 9(11):3062–3067, 2018.

[264] Carlo Adamo and Vincenzo Barone. Toward reliable density functional methods without adjustable parameters: The pbe0 model. *J. Chem. Phys.*, 110(13):6158–6170, 1999.

[265] Stefan Grimme, Jens Antony, Stephan Ehrlich, and Helge Krieg. A consistent and accurate ab initio parametrization of density functional dispersion correction (dft-d) for the 94 elements h-pu. *J. Chem. Phys.*, 132(15):154104, 2010.

[266] Thom H Dunning Jr. Gaussian basis sets for use in correlated molecular calculations. i. the atoms boron through neon and hydrogen. *J. Chem. Phys.*, 90(2):1007–1023, 1989.

[267] M. J. Frisch, G. W. Trucks, H. B. Schlegel, G. E. Scuseria, M. A. Robb, J. R. Cheeseman, G. Scalmani, V. Barone, G. A. Petersson, H. Nakatsuji, X. Li, M. Caricato, A. V. Marenich, J. Bloino, B. G. Janesko, R. Gomperts, B. Mennucci, H. P. Hratchian, J. V. Ortiz, A. F. Izmaylov, J. L. Sonnenberg, D. Williams-Young, F. Ding, F. Lipparini, F. Egidi, J. Goings, B. Peng, A. Petrone, T. Henderson, D. Ranasinghe, V. G. Zakrzewski, J. Gao, N. Rega, G. Zheng, W. Liang, M. Hada, M. Ehara, K. Toyota, R. Fukuda, J. Hasegawa, M. Ishida, T. Nakajima, Y. Honda, O. Kitao, H. Nakai, T. Vreven, K. Throssell, J. A. Montgomery, Jr., J. E. Peralta, F. Ogliaro, M. J. Bearpark, J. J. Heyd, E. N. Brothers, K. N. Kudin, V. N. Staroverov, T. A. Keith, R. Kobayashi, J. Normand, K. Raghavachari, A. P. Rendell, J. C.

Burant, S. S. Iyengar, J. Tomasi, M. Cossi, J. M. Millam, M. Klene, C. Adamo, R. Cammi, J. W. Ochterski, R. L. Martin, K. Morokuma, O. Farkas, J. B. Foresman, and D. J. Fox. Gaussian˜16 revision c.01, 2016. Gaussian Inc. Wallingford CT.

[268] Mattia Bondanza, Michele Nottoli, Lorenzo Cupellini, Filippo Lipparini, and Benedetta Mennucci. Polarizable embedding qm/mm: The future gold standard for complex (bio)systems? *Phys. Chem. Chem. Phys.*, 22:14433–14448, 2020.

[269] Carles Curutchet, Lorenzo Cupellini, Jacob Kongsted, Stefano Corni, Luca Frediani, Arnfinn Hykkerud Steindal, Ciro A Guido, Giovanni Scalmani, and Benedetta Mennucci. Density-dependent formulation of dispersioninteractions in hybrid multiscale quantum/molecular mechanics (qm/mm) models. *J. Chem. Theory Comput.*, 14(3):1671–1681, February 2018.

[270] Tommaso Giovannini, Piero Lafiosca, and Chiara Cappelli. a general route to include pauli repulsion and quantum dispersion effects in qm/mm approaches. *J. Chem. Theory Comput.*, 13(10):4854–4870, September 2017.

[271] Eric F Pettersen, Thomas D Goddard, Conrad C Huang, Gregory S Couch, Daniel M Greenblatt, Elaine C Meng, and Thomas E Ferrin. Ucsf chimera—a visualization system for exploratory research and analysis. *J. Comput. Chem.*, 25(13):1605–1612, 2004.

[272] VS Sandeep Inakollu, Daan P Geerke, Christopher N Rowley, and Haibo Yu. Polarisable force fields: What do they add in biomolecular simulations? *Curr. Opin. Struct. Biol.*, 61:182–190, 2020.

[273] Kristof T Schütt, Huziel E Sauceda, P-J Kindermans, Alexandre Tkatchenko, and K-R Müller. Schnet – a deep learning architecture for molecules and materials. *J. Chem. Phys.*, 148(24):241722, 2018.

[274] Oliver T Unke and Markus Meuwly. A reactive scalable and transferable model for molecular energies from a neural network approach based on local information. *J. Chem. Phys.*, 148(24):241708, 2018.

[275] Oliver T Unke and Markus Meuwly. Physnet: A neural network for predicting energies forces dipole moments and partial charges. *J. Chem. Phys.*, 15(6):3678–3693, 2019.

[276] Kristof T Schütt, Farhad Arbabzadah, Stefan Chmiela, Klaus R Müller, and Alexandre Tkatchenko. Quantum-chemical insights from deep tensor neural networks. *Nat. Commun.*, 8(1):1–8, 2017.

[277] Bin Jiang and Hua Guo. Permutation invariant polynomial neural network approach to fitting potential energy surfaces. *J. Chem. Phys.*, 139(5):054112, 2013.

[278] Jun Li, Bin Jiang, and Hua Guo. Permutation invariant polynomial neural network approach to fitting potential energy surfaces. ii. four-atom systems. *J. Chem. Phys.*, 139(20):204103, 2013.

[279] Bin Jiang and Hua Guo. Permutation invariant polynomial neural network approach to fitting potential energy surfaces. iii. molecule-surface interactions. *J. Chem. Phys.*, 141(3):034109, 2014.

[280] Changjian Xie, Xiaolei Zhu, David R Yarkony, and Hua Guo. Permutation invariant polynomial neural network approach to fitting potential energy surfaces. iv. coupled diabatic potential energy matrices. *J. Chem. Phys.*, 149(14):144107, 2018.

[281] Kejie Shao, Jun Chen, Zhiqiang Zhao, and Dong H Zhang. Communication: Fitting potential energy surfaces with fundamental invariant neural network. *J. Chem. Phys.*, 145(7):071101, 2016.

[282] David Rosenberger, Justin S Smith, and Angel E Garcia. Modeling of peptides with classical and novel machine learning force fields: A comparison. *J. Phys. Chem. B*, 2021.

[283] Chen Qu, Paul L Houston, Riccardo Conte, Apurba Nandi, and Joel M Bowman. Breaking the coupled cluster barrier for machine-learned potentials of large molecules: The case of 15-atom acetylacetone. *J. Phys. Chem. Lett.*, 12:4902–4909, 2021.

[284] Apurba Nandi, Chen Qu, Paul L Houston, Riccardo Conte, and Joel M Bowman. δ-machine learning for potential energy surfaces: A pip approach to bring a dft-based pes to ccsd(t) level of theory. *J. Chem. Phys.*, 154(5):051102, 2021.

[285] Jun Li, Zoltan Varga, Donald G Truhlar, and Hua Guo. Many-body permutationally invariant polynomial neural network potential energy surface for n_4. *J. Chem. Theory Comput.*, 16(8):4822–4832, 2020.

[286] Yafu Guan, Changjian Xie, Hua Guo, and David R Yarkony. Neural network based quasi-diabatic representation for s0 and s1 states of formaldehyde. *J. Phys. Chem. A*, 124(49):10132–10142, 2020.

[287] Bin Jiang, Jun Li, and Hua Guo. High-fidelity potential energy surfaces for gas-phase and gas–surface scattering processes from machine learning. *J. Phys. Chem. Lett.*, 11(13):5120–5131, 2020.

[288] Marcos del Cueto, Xueyao Zhou, Linsen Zhou, Yaolong Zhang, Bin Jiang, and Hua Guo. New perspectives on co_2–pt (111) interaction with a high-dimensional neural network potential energy surface. *J. Phys. Chem. C*, 124(9):5174–5181, 2020.

[289] Yuchen Wang, Yafu Guan, Hua Guo, and David R Yarkony. Enabling complete multichannel nonadiabatic dynamics: A global representation of the two-channel coupled 1 2 ^{1}a and 1^3a states of nh_3 using neural networks. *J. Chem. Phys.*, 154(9):094121, 2021.

[290] Tobias Morawietz, Andreas Singraber, Christoph Dellago, and Jörg Behler. How van der waals interactions determine the unique properties of water. *Proc. Natl. Acad. Sci. USA*, 113(30):8368–8373, 2016.

[291] Thuong T Nguyen, Eszter Székely, Giulio Imbalzano, Jörg Behler, Gábor Csányi, Michele Ceriotti, Andreas W Götz, and Francesco Paesani. Comparison of permutationally invariant polynomials neural networks and gaussian approximation potentials in representing water interactions through many-body expansions. *J. Chem. Phys.*, 148(24):241725, 2018.

[292] Kun Yao, John E Herr, David W Toth, Ryker Mckintyre, and John Parkhill. The tensormol-0.1 model chemistry: A neural network augmented with long-range physics. *Chem. Sci.*, 9(8):2261–2269, 2018.

[293] Weiliang Shi, Tian Jia, and Anyang Li. Quasi-classical trajectory analysis with isometric feature mapping and locally linear embedding: Deep insights into the multichannel reaction on an $NH_3^+(^4A)$ potential energy surface. *Phys. Chem. Chem. Phys.*, 22(31):17460–17471, 2020.

[294] Eleftherios Lambros, Filippo Lipparini, Gerardo Andrés Cisneros, and Francesco Paesani. A many-body fully polarizable approach to qm/mm simulations. *J. Chem. Theory Comput.*, 16(12):7462–7472, 2020.

[295] Lin Shen, Jingheng Wu, and Weitao Yang. Multiscale quantum mechanics/molecular mechanics simulations with neural networks. *J. Chem. Theory Comput.*, 12(10):4934–4946, 2016.

[296] Janet Del Bene and JA Pople. Intermolecular energies of small water polymers. *Chem. Phys. Lett.*, 4(7):426–428, 1969.

[297] E Clementi, W Kołos, GC Lie, and G Ranghino. Nonadditivity of interaction in water trimers. *Int. J. Quantum Chem.*, 17(3):377–398, 1980.

[298] KS Kim, Michel Dupuis, GC Lie, and E Clementi. Revisiting small clusters of water molecules. *Chem. Phys. Lett.*, 131(6):451–456, 1986.

[299] Sotiris S Xantheas and Thom H Dunning Jr. Ab initio studies of cyclic water clusters $(h_2o)_n$, $n = 1 - 6$. i. optimal structures and vibrational spectra. *J. Chem. Phys.*, 99(11):8774–8792, 1993.

[300] Sotiris S Xantheas and Thom H Dunning Jr. The structure of the water trimer from ab initio calculations. *J. Chem. Phys.*, 98(10):8037–8040, 1993.

[301] Lars Ojamäe and Kersti Hermansson. Ab initio study of cooperativity in water chains: Binding energies and anharmonic frequencies. *J. Phys. Chem.*, 98(16):4271–4282, 1994.

[302] Riccardo Conte, Chen Qu, and Joel M Bowman. Permutationally invariant fitting of many-body non-covalent interactions with application to three-body methane–water–water. *J. Chem. Theory Comput.*, 11(4):1631–1638, 2015.

[303] Qingfeng Wang and Joel M Bowman. Two-component ab initio potential energy surface for co_2—h_2o extension to the hydrate clathrate $co_2@(h_2o)_20$ and vscf/vci vibrational analyses of both. *J. Chem. Phys.*, 147(16):161714, 2017.

[304] John P Perdew, Robert G Parr, Mel Levy, and Jose L Balduz Jr. Density-functional theory for fractional particle number: Derivative discontinuities of the energy. *Phys. Rev. Lett.*, 49(23):1691, 1982.

[305] Michael G Medvedev, Ivan S Bushmarinov, Jianwei Sun, John P Perdew, and Konstantin A Lyssenko. Density functional theory is straying from the path toward the exact functional. *Science*, 355(6320):49–52, 2017.

[306] Adam Wasserman, Jonathan Nafziger, Kaili Jiang, Min-Cheol Kim, Eunji Sim, and Kieron Burke. The importance of being inconsistent. *Annu. Rev. Phys. Chem.*, 68:555–581, 2017.

[307] Eberhard Engel and Reiner M Dreizler. Exchange-correlation energy functional. pages 109–217. Springer, 2011.

[308] Yingkai Zhang and Weitao Yang. A challenge for density functionals: Self-interaction error increases for systems with a noninteger number of electrons. *J. Chem. Phys.*, 109(7):2604–2608, 1998.

[309] Fenglai Liu, Emil Proynov, Jian-Guo Yu, Thomas R Furlani, and Jing Kong. Comparison of the performance of exact-exchange-based density functional methods. *J. Chem. Phys.*, 137(11):114104, 2012.

[310] Takao Tsuneda and Kimihiko Hirao. Self-interaction corrections in density functional theory. *J. Chem. Phys.*, 140(18):18A513, 2014.

[311] Junwei Lucas Bao, Laura Gagliardi, and Donald G Truhlar. Self-interaction error in density functional theory: An appraisal. *J. Phys. Chem. Lett.*, 9(9):2353–2358, 2018.

[312] Erin R Johnson, Paula Mori-Sánchez, Aron J Cohen, and Weitao Yang. Delocalization errors in density functionals and implications for main-group thermochemistry. *J. Chem. Phys.*, 129(20):204112, 2008.

[313] Aron J Cohen, Paula Mori-Sánchez, and Weitao Yang. Challenges for density functional theory. *Chem. Rev.*, 112(1):289–320, 2012.

[314] Adrienn Ruzsinszky, John P Perdew, and Gabor I Csonka. Binding energy curves from nonempirical density functionals. i. covalent bonds in closed-shell and radical molecules. *J. Phys. Chem. A*, 109(48):11006–11014, 2005.

[315] Min-Cheol Kim, Eunji Sim, and Kieron Burke. Ions in solution: Density corrected density functional theory (dc-dft). *J. Chem. Phys.*, 140(18):18A528, 2014.

[316] Min-Cheol Kim, Hansol Park, Suyeon Son, Eunji Sim, and Kieron Burke. Improved dft potential energy surfaces via improved densities. *J. Phys. Chem. Lett.*, 6(19):3802–3807, 2015.

[317] Min-Cheol Kim, Eunji Sim, and Kieron Burke. Communication: Avoiding unbound anions in density ffunctional calculations. *J. Chem. Phys.*, 134:171103, 2011.

[318] Yeil Kim, Suhwan Song, Eunji Sim, and Kieron Burke. Halogen and chalcogen binding dominated by density-driven errors. *J. Phys. Chem. Lett.*, 10(2):295–301, 2018.

[319] Suhwan Song, Min-Cheol Kim, Eunji Sim, Anouar Benali, Olle Heinonen, and Kieron Burke. Benchmarks and reliable dft results for spin gaps of small ligand fe(ii) complexes. *J. Chem. Theory Comput.*, 14(5):2304–2311, 2018.

[320] John P Perdew and Alex Zunger. Self-interaction correction to density-functional approximations for many-electron systems. *Phys. Rev. B*, 23(10):5048, 1981.

[321] Kushantha PK Withanage, Sharmin Akter, Chandra Shahi, Rajendra P Joshi, Carlos Diaz, Yoh Yamamoto, Rajendra Zope, Tunna Baruah, John P Perdew, Juan E Peralta, and Koblar A. Jackson. Self-interaction-free electric dipole polarizabilities for atoms and their ions using the fermi-löwdin self-interaction correction. *Phys. Rev. A*, 100(1):012505, 2019.

[322] A. D. Becke. Density-functional exchange-energy approximation with correct asymptotic behavior. *Phys. Rev. A*, 38:3098–3100, 1988.

[323] C. Lee, W. Yang, and R. G. Parr. Development of the colle-salvetti correlation-energy formula into a functional of the electron density. *Phys. Rev. B*, 37:785–789, 1988.

[324] J. P. Perdew, K. Burke, and M. Ernzerhof. Generalized gradient approximations made simple. *Phys. Rev. Lett.*, 77:3865–3868, 1996. Erratum: *ibid*. **78**, 1396 (1997).

[325] Narbe Mardirossian, Luis Ruiz Pestana, James C Womack, Chris-Kriton Skylaris, Teresa Head-Gordon, and Martin Head-Gordon. Use of the rvv10 nonlocal correlation functional in the b97m-v density functional: Defining b97m-rv and related functionals. *J. Phys. Chem. Lett.*, 8(1):35–40, 2017.

[326] A. D. Becke. Density-functional thermochemistry. iii. the role of exact exchange. *J. Chem. Phys.*, 98:5648–5652, 1993.

[327] C. Adamo and V. Barone. Toward reliable density functional methods without adjustable parameters: The pbe0 model. *J. Chem. Phys.*, 110:6158–6170, 1999.

[328] Yan Zhao and Donald G Truhlar. The m06 suite of density functionals for main group thermochemistry thermochemical kinetics noncovalent interactions excited states and transition elements: Two new functionals and systematic testing of four m06-class functionals and 12 other functionals. *Theor. Chem. Acc.*, 120(1):215–241, 2008.

[329] N. Mardirossian and M. Head-Gordon. ωb97m-v: A combinatorially optimized range-separated hybrid meta-gga density functional with vv10 nonlocal correlation. *J. Chem. Phys.*, 144:214110:1–23, 2016.

[330] S. Grimme, J. Antony, S. Ehrlich, and H. Krieg. a consistent and accurate initio parameterization of density functional dispersion correction (dft-d) for the 94 elements h–pu. *J. Chem. Phys.*, 132:154104:1–19, 2010.

[331] Y. Shao, Z. Gan, E. Epifanovsky, A. T. B. Gilbert, M. Wormit, J. Kussmann, A. W. Lange, A. Behn, J. Deng, X. Feng, D. Ghosh, M. Goldey, P. R. Horn, L. D. Jacobson, I. Kaliman, R. Z. Khaliullin, T. Kús, A. Landau, J. Liu, E. I. Proynov, Y. M. Rhee, R. M. Richard, M. A. Rohrdanz, R. P. Steele, E. J. Sundstrom, H. L. Woodcock III, P. M. Zimmerman, D. Zuev, B. Albrecht, E. Alguire, B. Austin, G. J. O. Beran, Y. A. Bernard, E. Berquist, K. Brandhorst, K. B. Bravaya, S. T. Brown, D. Casanova, C.-M. Chang, Y. Chen, S. H. Chien, K. D. Closser, D. L. Crittenden, M. Diedenhofen, R. A. DiStasio Jr., H. Do, A. D. Dutoi, R. G. Edgar, S. Fatehi, L. Fusti-Molnar, A. Ghysels, A. Golubeva-Zadorozhnaya, J. Gomes, M. W. D. Hanson-Heine, P. H. P. Harbach, A. W. Hauser, E. G. Hohenstein, Z. C. Holden, T.-C. Jagau, H. Ji, B. Kaduk, K. Khistyaev, J. Kim, J. Kim, R. A. King, P. Klunzinger, D. Kosenkov, T. Kowalczyk, C. M. Krauter, K. U. Lao, A. Laurent, K. V. Lawler, S. V. Levchenko, C. Y. Lin, F. Liu, E. Livshits, R. C. Lochan, A. Luenser, P. Manohar, S. F. Manzer, S.-P. Mao, N. Mardirossian, A. V. Marenich, S. A. Maurer, N. J. Mayhall, C. M. Oana, R. Olivares-Amaya, D. P. O'Neill, J. A. Parkhill, T. M. Perrine, R. Peverati, P. A. Pieniazek, A. Prociuk, D. R. Rehn, E. Rosta, N. J. Russ, N. Sergueev, S. M. Sharada, S. Sharma, D. W. Small, A. Sodt, T. Stein, D. Stück, Y.-C. Su, A. J. W. Thom, T. Tsuchimochi, L. Vogt, O. Vydrov, T. Wang, M. A. Watson, J. Wenzel, A. White, C. F. Williams, V. Vanovschi, S. Yeganeh, S. R. Yost, Z.-Q. You, I. Y. Zhang, X. Zhang, Y. Zhao, B. R. Brooks, G. K. L. Chan, D. M. Chipman, C. J. Cramer, W. A. Goddard III, M. S. Gordon, W. J. Hehre, A. Klamt, H. F. Schaefer III, M. W. Schmidt, C. D. Sherrill, D. G. Truhlar, A. Warshel, X. Xu, A. Aspuru-Guzik, R. Baer, A. T. Bell, N. A. Besley, J.-D. Chai, A. Dreuw, B. D. Dunietz, T. R. Furlani, S. R. Gwaltney, C.-P. Hsu, Y. Jung, J. Kong, D. S. Lambrecht, W. Liang, C. Ochsenfeld, V. A. Rassolov, L. V. Slipchenko, J. E. Subotnik, T. Van Voorhis, J. M. Herbert, A. I. Krylov, P. M. W. Gill, and M. Head-Gordon. Advances in molecular quantum chemistry contained in the q-chem 4 program package. *Mol. Phys.*, 113:184–215, 2015.

[332] F. Neese. Software update: The orca program system version 4.0. *WIREs Comput. Mol. Sci.*, 8:e1327:1–6, 2017.

[333] Christopher W Murray, Nicholas C Handy, and Gregory J Laming. Quadrature schemes for integrals of density functional theory. *Mol. Phys.*, 78(4):997–1014, 1993.

[334] Vyacheslav Ivanovich Lebedev. Quadratures on a sphere. *USSR Comput. Math. & Math. Phys.*, 16(2):10–24, 1976.

[335] S. Dasgupta and J. M. Herbert. Standard grids for high-precision integration of modern density functionals: Sg-2 and sg-3. *J. Comput. Chem.*, 38:869–882, 2017.

[336] Axel D Becke and Erin R Johnson. Exchange-hole dipole moment and the dispersion interaction. *J. Chem. Phys.*, 122(15):154104, 2005.

[337] Erin R Johnson and Axel D Becke. A post-hartree–fock model of intermolecular interactions. *J. Chem. Phys.*, 123(2):024101, 2005.

[338] Erin R Johnson and Axel D Becke. A post-hartree-fock model of intermolecular interactions: Inclusion of higher-order corrections. *J. Chem. Phys.*, 124(17):174104, 2006.

[339] Jing Kong, Zhengting Gan, Emil Proynov, Marek Freindorf, and Thomas R Furlani. Efficient computation of the dispersion interaction with density-functional theory. *Phys. Rev. A*, 79(4):042510, 2009.

[340] Aleksandr V Marenich, Steven V Jerome, Christopher J Cramer, and Donald G Truhlar. Charge model 5: An extension of hirshfeld population analysis for the accurate description of molecular interactions in gaseous and condensed phases. *jctc*, 8(2):527–541, 2012.

[341] Cristóbal Pérez, Matt T Muckle, Daniel P Zaleski, Nathan A Seifert, Berhane Temelso, George C Shields, Zbigniew Kisiel, and Brooks H Pate. Structures of cage prism and book isomers of water hexamer from broadband rotational spectroscopy. *Science*, 336(6083):897–901, 2012.

[342] Yimin Wang, Volodymyr Babin, Joel M Bowman, and Francesco Paesani. The water hexamer: Cage prism or both. full dimensional quantum simulations say both. *J. Am. Chem. Soc.*, 134(27):11116–11119, 2012.

[343] Volodymyr Babin and Francesco Paesani. The curious case of the water hexamer: Cage vs. prism. *Chem. Phys. Lett.*, 580:1–8, 2013.

[344] J Marc Pedulla, Fernando Vila, and KD Jordan. Binding energy of the ring form of $(h_2o)_6$: Comparison of the predictions of conventional and localized-orbital mp2 calculations. *J. Chem. Phys.*, 105(24):11091–11099, 1996.

[345] Jun Cui, Hanbin Liu, and Kenneth D Jordan. Theoretical characterization of the $(h_2o)_21$ cluster: Application of an n-body decomposition procedure. *J. Phys. Chem. B*, 110(38):18872–18878, 2006.

[346] Stefan Vuckovic, Suhwan Song, John Kozlowski, Eunji Sim, and Kieron Burke. Density functional analysis: The theory of density-corrected dft. *J. Chem. Theory Comput.*, 15(12):6636–6646, 2019.

[347] Aron J Cohen, Paula Mori-Sánchez, and Weitao Yang. Insights into current limitations of density functional theory. *Science*, 321(5890):792–794, 2008.

[348] Mark E Tuckerman. Ab initio molecular dynamics: Basic concepts current trends and novel applications. *J. Condens. Matter Phys.*, 14(50):R1297, 2002.

[349] John S Tse. Ab initio molecular dynamics with density functional theory. *Annu. Rev. Phys. Chem.*, 53(1):249–290, 2002.

[350] Paolo Carloni, Ursula Rothlisberger, and Michele Parrinello. the role and perspective of ab initio molecular dynamics in the study of biological systems. *Acc. Chem. Res.*, 35(6):455–464, 2002.

[351] Ali A Hassanali, Jérôme Cuny, Vincenzo Verdolino, and Michele Parrinello. Aqueous solutions: State of the art in initio molecular dynamics. *Philos. Trans. R. Soc. A*, 372(2011):20120482, 2014.

[352] Robert G Parr and W. Yang. *Density Functional Theory of Atoms and Molecules*. Oxford University Press, 1994.

[353] John C Slater. a simplification of the hartree-fock method. *Phys. Rev.*, 81(3):385, 1951.

[354] Axel D Becke. Perspective: Fifty years of density-functional theory in chemical physics. *J. Chem. Phys.*, 140(18):18A301, 2014.

[355] K Laasonen, F Csajka, and M Parrinello. Water dimer properties in the gradient-corrected density functional theory. *Chem. Phys. Lett.*, 194(3):172–174, 1992.

[356] Kari Laasonen, M Parrinello, Roberto Car, Changyol Lee, and David Vanderbilt. Structures of small water clusters using gradient-corrected density functional theory. *Chem. Phys. Lett.*, 207(2-3):208–213, 1993.

[357] AK McMahan and John A Moriarty. Structural phase stability in third-period simple metals. *Phys. Rev. B*, 27(6):3235, 1983.

[358] Frank Herman, John P Van Dyke, and Irene B Ortenburger. Improved statistical exchange approximation for inhomogeneous many-electron systems. *Phys. Rev. Lett.*, 22(16):807, 1969.

[359] David C Langreth and MJ Mehl. Beyond the local-density approximation in calculations of ground-state electronic properties. *Phys. Rev. B*, 28(4):1809, 1983.

[360] John P Perdew. Accurate density functional for the energy: Real-space cutoff of the gradient expansion for the exchange hole. *Phys. Rev. Lett.*, 55(16):1665, 1985.

[361] John P Perdew and Wang Yue. Accurate and simple density functional for the electronic exchange energy: Generalized gradient approximation. *Phys. Rev. B*, 33(12):8800, 1986.

[362] John P Perdew. Density-functional approximation for the correlation energy of the inhomogeneous electron gas. *Phys. Rev. B*, 33(12):8822, 1986.

[363] Axel D Becke. Density-functional exchange-energy approximation with correct asymptotic behavior. *Phys. Rev. A*, 38(6):3098, 1988.

[364] John P Perdew, Kieron Burke, and Matthias Ernzerhof. Generalized gradient approximation made simple. *Phys. Rev. Lett.*, 77(18):3865, 1996.

[365] Katrin Forster-Tonigold and Axel Groß. Dispersion corrected rpbe studies of liquid water. *J. Chem. Phys.*, 141(6):064501, 2014.

[366] Swapan K Ghosh and Robert G Parr. Phase-space approach to the exchange-energy functional of density-functional theory. *Phys. Rev. A*, 34(2):785, 1986.

[367] Troy Van Voorhis and Gustavo E Scuseria. a novel form for the exchange-correlation energy functional. *J. Chem. Phys.*, 109(2):400–410, 1998.

[368] EI Proynov, E Ruiz, A Vela, and DR Salahub. Determining and extending the domain of exchange and correlation functionals. *Int. J. Quantum Chem.*, 56(S29):61–78, 1995.

[369] Axel D Becke. a new inhomogeneity parameter in density-functional theory. *J. Chem. Phys.*, 109(6):2092–2098, 1998.

[370] Narbe Mardirossian and Martin Head-Gordon. Mapping the genome of meta-generalized gradient approximation density functionals: The search for b97m-v. *J. Chem. Phys.*, 142(7):074111, 2015.

[371] Luis Ruiz Pestana, Ondrej Marsalek, Thomas E Markland, and Teresa Head-Gordon. The quest for accurate liquid water properties from first principles. *J. Phys. Chem. Lett.*, 9(17):5009–5016, 2018.

[372] Michael D LaCount and François Gygi. Ensemble first-principles molecular dynamics simulations of water using the scan meta-gga density functional. *J. Chem. Phys.*, 151(16):164101, 2019.

[373] Axel D Becke. a new mixing of hartree–fock and local density-functional theories. *J. Chem. Phys.*, 98(2):1372–1377, 1993.

[374] AD Becke. Density-functional thermochemistry. iii. the role of exact exchange year. *J. Chem. Phys*, 98:5648, 1993.

[375] John P Perdew, Matthias Ernzerhof, and Kieron Burke. Rationale for mixing exact exchange with density functional approximations. *J. Chem. Phys.*, 105(22):9982–9985, 1996.

[376] Kerwin Hui and Jeng-Da Chai. Scan-based hybrid and double-hybrid density functionals from models without fitted parameters. *J. Chem. Phys.*, 144(4):044114, 2016.

[377] Glenn J Martyna, Michael L Klein, and Mark Tuckerman. Nosé–hoover chains: The canonical ensemble via continuous dynamics. *J. Chem. Phys.*, 97(4):2635–2643, 1992.

[378] Glenn J Martyna, Adam Hughes, and Mark E Tuckerman. Molecular dynamics algorithms for path integrals at constant pressure. *J. Chem. Phys.*, 110(7):3275–3290, 1999.

[379] M Allen and D. Tildesley. *Computer Simulations of Liquids*. Oxford University Press, 1987.

[380] J Harris and RO Jones. the surface energy of a bounded electron gas. *J. Phys. F Met. Phys.*, 4(8):1170, 1974.

[381] David C Langreth and John P Perdew. the exchange-correlation energy of a metallic surface. *Solid State Commun.*, 17(11):1425–1429, 1975.

[382] Olle Gunnarsson and Bengt I Lundqvist. Exchange and correlation in atoms molecules and solids by the spin-density-functional formalism. *Phys. Rev. B*, 13(10):4274, 1976.

[383] David C Langreth and John P Perdew. Exchange-correlation energy of a metallic surface: Wave-vector analysis. *Phys. Rev. B*, 15(6):2884, 1977.

[384] J Harris. Adiabatic-connection approach to kohn-sham theory. *Phys. Rev. A*, 29(4):1648, 1984.

[385] Lawrie B Skinner, Congcong Huang, Daniel Schlesinger, Lars GM Pettersson, Anders Nilsson, and Chris J Benmore. Benchmark oxygen-oxygen pair-distribution function of ambient water from x-ray diffraction measurements with a wide q-range. *J. Chem. Phys.*, 138(7):074506, 2013.

[386] Lawrie B Skinner, CJ Benmore, Joerg C Neuefeind, and John B Parise. the structure of water around the compressibility minimum. *J. Chem. Phys.*, 141(21):214507, 2014.

[387] Wolfgang Wagner and Andreas Pruß. the iapws formulation 1995 for the thermodynamic properties of ordinary water substance for general and scientific use. *J. Phys. Chem. Ref. Data*, 31(2):387–535, 2002.

[388] Jeffrey R Errington and Pablo G Debenedetti. Relationship between structural order and the anomalies of liquid water. *Nature*, 409(6818):318–321, 2001.

[389] Jianhang Xu, Zhaoru Sun, Chunyi Zhang, Mark DelloStritto, Deyu Lu, Michael L Klein, and Xifan Wu. Importance of nuclear quantum effects on the hydration of chloride ion. *Phys. Rev. Mater.*, 5(1):L012801, 2021.

[390] Kamal Wagle, Biswajit Santra, Puskar Bhattarai, Chandra Shahi, Mark R Pederson, Koblar A Jackson, and John P Perdew. Self-interaction correction in water-ion clusters. *arXiv:2012.13469*, 2020.

[391] Paola Gallo, Katrin Amann-Winkel, Charles Austen Angell, Mikhail Alexeevich Anisimov, Frederic Caupin, Charusita Chakravarty, Erik Lascaris, Thomas Loerting, Athanassios Zois Panagiotopoulos, John Russo, Jonas Alexander Sellberg, Harry Eugene Stanley, Hajime Tanaka, Carlos Vega, Limei Xu, and Lars Gunnar Moody Pettersson. Water: A tale of two liquids. *Chem. Rev.*, 116(13):7463–7500, 2016.

[392] Philip Ball. Water as an active constituent in cell biology. *Chem. Rev.*, 108(1):74–108, 2008.

[393] Felix Franks. *Water: A Matrix of Life*, volume 21. Royal Society of Chemistry, 2000.

[394] David Eisenberg, Walter Kauzmann, and Walter Kauzmann. *The Structure and Properties of Water*. Oxford University Press, 2005.

[395] Charles Tanford. The hydrophobic effect and the organization of living matter. *Science*, 200(4345):1012–1018, 1978.

[396] William P Jencks. General acid-base catalysis of complex reactions in water. *Chem. Rev.*, 72(6):705–718, 1972.

[397] Phillip E Savage. Organic chemical reactions in supercritical water. *Chem. Rev.*, 99(2), 1999.

[398] Ulf M Lindström. Stereoselective organic reactions in water. *Chem. Rev.*, 102(8):2751–2772, 2002.

[399] Naoko Akiya and Phillip E Savage. Roles of water for chemical reactions in high-temperature water. *Chem. Rev.*, 102(8):2725–2750, 2002.

[400] Chao-Jun Li and Liang Chen. Organic chemistry in water. *Chem. Soc. Rev.*, 35(1):68–82, 2006.

[401] Marc-Olivier Simon and Chao-Jun Li. Green chemistry oriented organic synthesis in water. *Chem. Soc. Rev.*, 41(4):1415–1427, 2012.

[402] Walter Kohn. Nobel lecture: Electronic structure of matter–wave functions and density functionals. *Rev. Mod. Phys.*, 71(5):1253, 1999.

[403] Richard Car and Mark Parrinello. Unified approach for molecular dynamics and density-functional theory. *Phys. Rev. Lett.*, 55(22):2471, 1985.

[404] Robert O Jones. Density functional theory: Its origins rise to prominence and future. *Rev. Mod. Phys.*, 87(3):897, 2015.

[405] David M Ceperley and Berni J Alder. Ground state of the electron gas by a stochastic method. *Phys. Rev. Lett.*, 45(7):566, 1980.

[406] John P Perdew and Yue Wang. Accurate and simple analytic representation of the electron-gas correlation energy. *Phys. Rev. B*, 45(23):13244, 1992.

[407] D Glötzel and AK McMahan. Relativistic effects phonons and the isostructural transition in cesium. *Phys. Rev. B*, 20(8):3210, 1979.

[408] Hans L Skriver. Crystal structure from one-electron theory. *Phys. Rev. B*, 31(4):1909, 1985.

[409] John A Moriarty and AK McMahan. High-pressure structural phase transitions in na mg and al. *Phys. Rev. Lett.*, 48(12):809, 1982.

[410] John P Perdew and Karla Schmidt. Jacob's ladder of density functional approximations for the exchange-correlation energy. volume 577, pages 1–20. American Institute of Physics, 2001.

[411] Chengteh Lee, Weitao Yang, and Robert G Parr. Development of the colle-salvetti correlation-energy formula into a functional of the electron density. *Phys. Rev. B*, 37(2):785, 1988.

[412] Fiona Sim, Alain St. Amant, Imre Papai, and Dennis R Salahub. Gaussian density functional calculations on hydrogen-bonded systems. *J. Am. Chem. Soc.*, 114(11):4391–4400, 1992.

[413] Biswajit Santra, Angelos Michaelides, and Matthias Scheffler. On the accuracy of density-functional theory exchange-correlation functionals for h bonds in small water clusters: Benchmarks approaching the complete basis set limit. *J. Chem. Phys.*, 127(18):184104, 2007.

[414] I-Feng W Kuo, Christopher J Mundy, Matthew J McGrath, J Ilja Siepmann, Joost VandeVondele, Michiel Sprik, Jürg Hutter, Bin Chen, Michael L Klein, Fawzi Mohamed, Matthias Krack, and Michele Parrinello. Liquid water from first principles: Investigation of different sampling approaches. *J. Phys. Chem. B*, 108(34):12990–12998, 2004.

[415] Jeffrey C Grossman, Eric Schwegler, Erik W Draeger, François Gygi, and Giulia Galli. Towards an assessment of the accuracy of density functional theory for first principles simulations of water. *J. Chem. Phys.*, 120(1):300–311, 2004.

[416] Joost VandeVondele, Fawzi Mohamed, Matthias Krack, Jürg Hutter, Michiel Sprik, and Michele Parrinello. The influence of temperature and density functional models in ab initio molecular dynamics simulation of liquid water. *J. Chem. Phys.*, 122(1):014515, 2005.

[417] Jue Wang, Guillermo Román-Pérez, Jose M Soler, Emilio Artacho, and M-V Fernández-Serra. Density structure and dynamics of water: The effect of van der waals interactions. *J. Chem. Phys.*, 134(2):024516, 2011.

[418] John P Perdew, Stefan Kurth, Aleš Zupan, and Peter Blaha. Accurate density functional with correct formal properties: A step beyond the generalized gradient approximation. *Phys. Rev. Lett.*, 82(12):2544, 1999.

[419] Carlo Adamo, Matthias Ernzerhof, and Gustavo E Scuseria. The meta-gga functional: Thermochemistry with a kinetic energy density dependent exchange-correlation functional. *J. Chem. Phys.*, 112(6):2643–2649, 2000.

[420] Jianwei Sun, Richard C Remsing, Yubo Zhang, Zhaoru Sun, Adrienn Ruzsinszky, Haowei Peng, Zenghui Yang, Arpita Paul, Umesh Waghmare, Xifan Wu, Michael L. Klein, and John P. Perdew. Accurate first-principles structures and energies of diversely bonded systems from an efficient density functional. *Nat. Chem.*, 8(9):831, 2016.

[421] Lixin Zheng, Mohan Chen, Zhaoru Sun, Hsin-Yu Ko, Biswajit Santra, Pratikkumar Dhuvad, and Xifan Wu. Structural electronic with dynamical properties of liquid water by ab initio molecular dynamics based on scan functional within the canonical ensemble. *J. Chem. Phys.*, 148(16):164505, 2018.

[422] Aron J Cohen, Paula Mori-Sánchez, and Weitao Yang. Development of exchange-correlation functionals with minimal many-electron self-interaction error. *J. Chem. Phys.*, 126(19):191109, 2007.

[423] Paula Mori-Sánchez, Aron J Cohen, and Weitao Yang. Localization and delocalization errors in density functional theory and implications for band-gap prediction. *Phys. Rev. Lett.*, 100(14):146401, 2008.

[424] Chen Li, Xiao Zheng, Aron J Cohen, Paula Mori-Sánchez, and Weitao Yang. Local scaling correction for reducing delocalization error in density functional approximations. *Phys. Rev. Lett.*, 114(5):053001, 2015.

[425] Eleftherios Lambros, Jie Hu, and Francesco Paesani. Assessing the accuracy of the scan functional for water through a many-body analysis of the adiabatic connection formula. *J. Chem. Theory Comput.*, 17(6):3739–3749, 2021.

[426] Jan Rezac and Pavel Hobza. Describing noncovalent interactions beyond the common approximations: How accurate is the "gold standard" ccsd(t) at the complete basis set limit? *J. Chem. Theory Comput.*, 9(5):2151–2155, 2013.

[427] Roy G Gordon and Yung Sik Kim. Theory for the forces between closed-shell atoms and molecules. *J. Chem. Phys.*, 56(6):3122–3133, 1972.

[428] Gustavo E Scuseria. Comparison of coupled-cluster results with a hybrid of hartree–fock and density functional theory. *J. Chem. Phys.*, 97(10):7528–7530, 1992.

[429] Nevin Oliphant and Rodney J Bartlett. A systematic comparison of molecular properties obtained using hartree–fock a hybrid hartree–fock density-functional-theory and coupled-cluster methods. *J. Chem. Phys.*, 100(9):6550–6561, 1994.

[430] Benjamin G Janesko and Gustavo E Scuseria. Hartree–fock orbitals significantly improve the reaction barrier heights predicted by semilocal density functionals. *J. Chem. Phys.*, 128(24):244112, 2008.

[431] Min-Cheol Kim, Eunji Sim, and Kieron Burke. Understanding and reducing errors in density functional calculations. *Phys. Rev. Lett.*, 111(7):073003, Aug 2013.

[432] Subrata Jana, Abhilash Patra, Szymon Śmiga, Lucian A Constantin, and Prasanjit Samal. Insights from the density functional performance of water and water–solid interactions: Scan in relation to other meta-ggas. *J. Chem. Phys.*, 153(21):214116, 2020.

[433] Suhwan Song, Stefan Vuckovic, Eunji Sim, and Kieron Burke. Density sensitivity of empirical functionals. *J. Phys. Chem. Lett.*, 12(2):800–807, 2021.

[434] Jason D Goodpaster, Taylor A Barnes, Frederick R Manby, and Thomas F Miller III. Density functional theory embedding for correlated wavefunctions: Improved methods for open-shell systems and transition metal complexes. *J. Chem. Phys.*, 137(22):224113, 2012.

[435] Diptarka Hait and Martin Head-Gordon. Delocalization errors in density functional theory are essentially quadratic in fractional occupation number. *J. Phys. Chem. Lett.*, 9(21):6280–6288, 2018.

[436] Donghyung Lee, Filipp Furche, and Kieron Burke. Accuracy of electron affinities of atoms in approximate density functional theory. *J. Phys. Chem. Lett.*, 1(14):2124–2129, 2010.

[437] Golokesh Santra and Jan ML Martin. What types of chemical problems benefit from density-corrected dft? a probe using an extensive and chemically diverse test suite. *J. Chem. Theory Comput.*, 17(3):1368–1379, 2021.

[438] Donghyung Lee and Kieron Burke. Finding electron affinities with approximate density functionals. *Mol. Phys.*, 108(19-20):2687–2701, 2010.

[439] Seungsoo Nam, Suhwan Song, Eunji Sim, and Kieron Burke. Measuring density-driven errors using kohn–sham inversion. *J. Chem. Theory Comput.*, 16(8):5014–5023, 2020.

[440] Debashree Manna, Manoj K Kesharwani, Nitai Sylvetsky, and Jan ML Martin. Conventional and explicitly correlated ab initio benchmark study on water clusters: Revision of the begdb and water27 data sets. *J. Chem. Theory Comput.*, 13(7):3136–3152, 2017.

[441] Mark R Pederson, Adrienn Ruzsinszky, and John P Perdew. Communication: Self-interaction correction with unitary invariance in density functional theory. *J. Chem. Phys.*, 140(12):121103, 2014.

[442] Eric W. Lemmon, Mark O. McLinden, and Daniel G. Friend. Thermophysical properties of fluid systems. National Institute of Standards and Technology, Gaithersburg (MD).

[443] Manfred Holz, Stefan R Heil, and Antonio Sacco. Temperature-dependent self-diffusion coefficients of water and six selected molecular liquids for calibration in accurate ^{1}h nmr pfg measurements. *Phys. Chem. Chem. Phys.*, 2(20):4740–4742, 2000.

[444] Allan J Easteal, William E Price, and Lawrence A Woolf. Diaphragm cell for high-temperature diffusion measurements. tracer diffusion coefficients for water to 363 k. *J. Chem. Soc., Faraday Trans. 1*, 85(5):1091–1097, 1989.

[445] R Mills. Self-diffusion in normal and heavy water in the range 1-45^{o}. *J. Phys. Chem.*, 77(5):685–688, 1973.

[446] Linfeng Zhang, Han Wang, Roberto Car, and E Weinan. Phase diagram of a deep potential water model. *Phys. Rev. Lett.*, 126(23):236001, 2021.

[447] Mb-fit: Software infrastructure for data-driven many-body potential energy functions. https://github.com/paesanilab/MB-Fit.

[448] Mbx: A many-body energy and force calculator. http://paesanigroup.ucsd.edu/software/mbx.html.

[449] I-pi: A universal force engine. http://ipi-code.org.

[450] Lammps molecular dynamics simulator. http://lammps.sandia.gov.

[451] Eleftherios Lambros, Saswata Dasgupta, Etienne Palos, Steven Swee, Jie Hu, and Francesco Paesani. General many-body framework for data-driven potentials with arbitrary quantum mechanical accuracy: Water as a case study. *J. Chem. Theory Comput.*, pages In press, DOI: 10.1021/acs.jctc.1c00541.

[452] Maria Carolina Muniz, Thomas E Gartner III, Marc Riera, Christopher Knight, Shuwen Yue, Francesco Paesani, and Athanassios Z Panagiotopoulos. Vapor–liquid equilibrium of water with the mb-pol many-body potential. *J. Chem. Phys.*, 154(21):211103, 2021.

[453] Evgeny Epifanovsky, Andrew T. B. Gilbert, Xintian Feng, Joonho Lee, Yuezhi Mao, Narbe Mardirossian, Pavel Pokhilko, Alec F. White, Marc P. Coons, Adrian L. Dempwolff, Zhengting Gan, Diptarka Hait, Paul R. Horn, Leif D. Jacobson, Ilya Kaliman, Jörg Kussmann, Adrian W. Lange, Ka Un Lao, Daniel S. Levine, Jie Liu, Simon C. McKenzie, Adrian F. Morrison, Kaushik D. Nanda, Felix Plasser, Dirk R. Rehn, Marta L. Vidal, Zhi-Qiang You, Ying Zhu, Bushra Alam, Benjamin J. Albrecht, Abdulrahman Aldossary, Ethan Alguire, Josefine H. Andersen, Vishikh Athavale, Dennis Barton, Khadiza Begam, Andrew Behn, Nicole Bellonzi, Yves A. Bernard, Eric J. Berquist, Hugh G. A. Burton, Abel Carreras, Kevin Carter-Fenk, Romit Chakraborty, Alan D. Chien, Kristina D. Closser, Vale Cofer-Shabica, Saswata Dasgupta, Marc de Wergifosse, Jia Deng, Michael Diedenhofen, Hainam Do, Sebastian Ehlert, Po-Tung Fang, Shervin Fatehi, Qingguo Feng, Triet Friedhoff, James Gayvert, Qinghui Ge, Gergely Gidofalvi, Matthew Goldey, Joe Gomes, Cristina E. González-Espinoza, Sahil Gulania, Anastasia O. Gunina, Magnus W. D. Hanson-Heine, Phillip H. P. Harbach, Andreas Hauser, Michael F. Herbst, Mario Hernández Vera, Manuel Hodecker, Zachary C. Holden, Shannon Houck, Xunkun Huang, Kerwin Hui, Bang C. Huynh, Maxim Ivanov, Ádám Jász, Hyunjun Ji, Hanjie Jiang, Benjamin Kaduk, Sven Kähler, Kirill Khistyaev, Jaehoon Kim, Gergely Kis, Phil Klunzinger, Zsuzsanna Koczor-Benda, Joong Hoon Koh, Dimitri Kosenkov, Laura Koulias, Tim Kowalczyk, Caroline M. Krauter, Karl Kue, Alexander Kunitsa, Thomas Kus, István Ladjánszki, Arie Landau, Keith V. Lawler, Daniel Lefrancois, Susi Lehtola, Run R. Li, Yi-Pei Li, Jiashu Liang, Marcus Liebenthal, Hung-Hsuan Lin, You-Sheng Lin, Fenglai Liu, Kuan-Yu Liu, Matthias Loipersberger, Arne Luenser, Aaditya Manjanath, Prashant Manohar, Erum Mansoor, Sam F. Manzer, Shan-Ping Mao, Aleksandr V. Marenich, Thomas Markovich, Stephen Mason, Simon A. Maurer, Peter F. McLaughlin, Maximilian F. S. J. Menger, Jan-Michael Mewes, Stefanie A. Mewes, Pierpaolo Morgante, J. Wayne Mullinax, Katherine J. Oosterbaan, Garrette Paran, Alexander C. Paul, Suranjan K. Paul, Fabijan Pavošević, Zheng Pei, Stefan Prager, Emil I. Proynov, Ádám Rák, Eloy Ramos-Cordoba, Bhaskar Rana, Alan E. Rask, Adam Rettig, Ryan M. Richard, Fazle Rob, Elliot Rossomme, Tarek Scheele, Maximilian Scheurer, Matthias Schneider, Nickolai Sergueev, Shaama M. Sharada, Wojciech Skomorowski, David W. Small, Christopher J. Stein, Yu-Chuan Su, Eric J. Sundstrom, Zhen Tao, Jonathan Thirman, Gábor J. Tornai, Takashi Tsuchimochi, Norm M.

Tubman, Srimukh Prasad Veccham, Oleg Vydrov, Jan Wenzel, Jon Witte, Atsushi Yamada, Kun Yao, Sina Yeganeh, Shane R. Yost, Alexander Zech, Igor Ying Zhang, Xing Zhang, Yu Zhang, Dmitry Zuev, Alán Aspuru-Guzik, Alexis T. Bell, Nicholas A. Besley, Ksenia B. Bravaya, Bernard R. Brooks, David Casanova, Jeng-Da Chai, Sonia Coriani, Christopher J. Cramer, György Cserey, A. Eugene DePrince, Robert A. DiStasio, Andreas Dreuw, Barry D. Dunietz, Thomas R. Furlani, William A. Goddard, Sharon Hammes-Schiffer, Teresa Head-Gordon, Warren J. Hehre, Chao-Ping Hsu, Thomas-C. Jagau, Yousung Jung, Andreas Klamt, Jing Kong, Daniel S. Lambrecht, WanZhen Liang, Nicholas J. Mayhall, C. William McCurdy, Jeffrey B. Neaton, Christian Ochsenfeld, John A. Parkhill, Roberto Peverati, Vitaly A. Rassolov, Yihan Shao, Lyudmila V. Slipchenko, Tim Stauch, Ryan P. Steele, Joseph E. Subotnik, Alex J. W. Thom, Alexandre Tkatchenko, Donald G. Truhlar, Troy Van Voorhis, Tomasz A. Wesolowski, K. Birgitta Whaley, H. Lee Woodcock, Paul M. Zimmerman, Shirin Faraji, Peter M. W. Gill, Martin Head-Gordon, John M. Herbert, and Anna I. Krylov. Software for the frontiers of quantum chemistry: An overview of developments in the q-chem 5 package. *J. Chem. Phys.*, 155(8):084801, 2021.

[454] James W Furness, Aaron D Kaplan, Jinliang Ning, John P Perdew, and Jianwei Sun. Accurate and numerically efficient r^2scan meta-generalized gradient approximation. *J. Phys. Chem. Lett.*, 11(19):8208–8215, 2020.

[455] Thomas B Adler, Gerald Knizia, and Hans-Joachim Werner. A simple and efficient ccsd(t)-f12 approximation. *J. Chem. Phys.*, 127(22):221106, 2007.

[456] Shijun Zhong, Ericka C Barnes, and George A Petersson. Uniformly convergent *n*-tuple-ζ augmented polarized (nzap) basis sets for complete basis set extrapolations. i. self-consistent field energies. *J. Chem. Phys.*, 129(18):184116, 2008.

[457] Trygve Helgaker, Wim Klopper, Henrik Koch, and Jozef Noga. Basis-set convergence of correlated calculations on water. *J. Chem. Phys.*, 106(23):9639–9646, 1997.

[458] Kazim E Yousaf and Kirk A Peterson. Optimized auxiliary basis sets for explicitly correlated methods. *J. Chem. Phys.*, 129(18):184108, 2008.

[459] Kazim E Yousaf and Kirk A Peterson. Optimized complementary auxiliary basis sets for explicitly correlated methods: Aug-cc-pvnz orbital basis sets. *Chem. Phys. Lett.*, 476(4-6):303–307, 2009.